Julius-Maximilians-Universität Würzburg
Graduate School of Science and Technology

Physikalisches Institut - Experimentelle Physik V

Quantitative Characterization of Lung Tissue Using Proton MRI

Quantitative Charakterisierung des Lungengewebes
Mithilfe von Proton-MRT

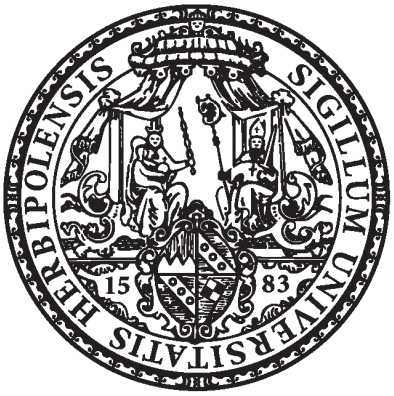

Dissertation zur Erlangung
des naturwissenschaftlichen Doktorgrades (Dr. rer. nat.)
der Julius-Maximilians-Universität Würzburg

vorgelegt von

Flavio Carinci

Würzburg 2016

Eingereicht am 22.07.2016
bei der Graduate School of Science and Technology der Julius-Maximilians-Universität Würzburg

Mitgliedern des Promotionskomitees
1. Primary Advisor: Prof. Dr. Peter M. Jakob
2. Advisor (second): Prof. Dr. Bert Hecht
3. Advisor (third): Prof. Dr. Dr. Wolfgang R. Bauer

Vorsitzender des Promotionskomitees: Prof. Dr. Tobias Hertel

Tag des Promotionskolloquiums: 23.02.2017

Contents

Introduction

Motivation

The lungs are vital organs for the human body. Their primary function is to permit the gas exchange between blood and air, thus enabling the delivery of fresh oxygen to cells. Due to this key role of the lungs for life, pathologies such as emphysema, Chronic Obstructive Pulmonary Disease (COPD), lung tumors, cystic fibrosis, interstitial lung disease or pulmonary vascular diseases can represent serious life-threatening conditions. According to the World Health Organization (WHO), lung pathologies are the second leading cause of death worldwide at present following cardiac diseases, with a trend of continuous increase [1]. For this reason, lung diagnostics represents a field of high and growing importance in the clinical practice, where an early and accurate diagnosis is essential for the treatment and the prognosis of the patient. In this regard, it is of primary interest for both the diagnosis and the characterization of lung pathologies to obtain spatially resolved information about lung morphology, functionality and microstructure.
In the field of diagnostic imaging, Computed Tomography (CT) is currently the gold standard modality for the assessment of most lung diseases. This is mainly due to the possibility of visualizing the lung morphology in detail by means of the acquisition of three-dimensional high-resolution images of the whole lung, with sub-millimeter voxel size, in one breath-hold [2]. Another imaging technique that is widely used in the clinical routine is the perfusion-ventilation scan. This approach allows to obtain spatially resolved information about the perfusion-ventilation ratio, a characteristic parameter of the lung that describes its functionality. The perfusion-ventilation scan can be performed by using either Single Photon Emission Computed Tomography (SPECT) or Positron Emission Tomography (PET) [3]; both SPECT and PET are based on the injection of radioactive tracers which, like CT, expose the patient to ionizing radiations.
In the field of lung imaging, Magnetic Resonance Imaging (MRI) represents an attractive and expanding modality which offers the possibility to obtain spatially resolved information about lung morphology, functionality and microstructure without the need for ionizing radiations [2, 3, 4, 5, 6, 7, 8, 9, 10, 11]. For this reason, MRI is a potential alternative to CT and nuclear medicine in this field. Furthermore, it could also serve as a source of additional diagnostic information for the clinicians.

The Role of MRI in Medicine

Nowadays, MRI is a fundamental tool in medicine along with a number of other diagnostic imaging modalities including digital radiography and ultrasound besides the above men-

tioned CT, SPECT and PET [12]. As previously remarked, one of the major advantages of MRI is the lack of ionizing radiations, which makes it a preferred modality in some groups of patients that should not be exposed to radiations, such as children and pregnant women. Another characteristic of MRI is its flexibility. Thanks to its sensitivity to several tissue properties and physiological mechanisms, in fact, MRI can be used for multiple purposes. In principle, several nuclear species can be used to generate MR images. Nevertheless, only protons play a relevant role for clinical applications due to the particular abundance of water in the human body. Proton MRI can be used to generate multiple kinds of image contrast which are unique in the field of medical imaging, thus providing different diagnostic information in comparison to the other modalities [12]. The image contrast of proton MRI is especially useful to characterize soft tissues and is dictated by the following contrast parameters: proton density and magnetization relaxation times T_1, T_2 and T_2^*. Besides these conventional contrast parameters, MRI can also be used to assess, either qualitatively or quantitatively, a number of other parameters, such as molecular diffusion, flow, tissue oxygenation, magnetization transfer, chemical composition of tissues, magnetic susceptibility, tissue elasticity or volume fractions occupied by different tissue compartments. In addition to this, MRI can be used in combination with the intravenous injection of contrast agents, typically gadolinium compounds, which allow to depict blood vessels (angiography) and provide information about blood delivery to tissues (perfusion).
According to the features described above, MRI enables the diagnosis and characterization of a wide range of anatomical and functional diseases and gives access to the knowledge of several physiological processes. Currently, MRI is used as the gold standard modality for the investigation of a variety of medical conditions in neurology, orthopedics, cardiology and oncology. For some applications, such as functional MRI (fMRI), Chemical Shift Imaging (CSI), Susceptibility Weighted Imaging (SWI), MR Elastography (MRE), diffusion and flow imaging, MRI represents the only option available.
Despite the many advantages of MRI, there are also several drawbacks. In comparison to the other imaging modalities, the major problems consist in the relatively long acquisition times and the high costs. The typical acquisition times in MRI vary from a few seconds to several minutes. For this reason, MRI is particularly sensitive to any kind of motion that could lead to unwanted image artifacts. This includes the involuntary movements of the patient during the scan as well as physiological motion. An additional consequence of the relatively long acquisition times is represented by the limit imposed on the spatial resolution and the Signal-to-Noise Ratio (SNR) of the image, which are both inversely proportional to the acquisition times for most applications.

Short Overview of the Development of MRI

The start of the continuous progress in the development of MRI dates back to 1946 when the works of Felix Bloch [13, 14] and Edward Purcell [15] led to the discovery of Nuclear Magnetic Resonance (NMR). Since then, remarkable breakthroughs have been achieved in this field. In 1973 Paul Lauterbur [16] and Peter Mansfield [17] proposed to integrate NMR with an imaging technique in order to obtain spatially resolved information and generate images of a sample. One year later, Allen Garroway [18] introduced the concept of slice selective excitation, which allowed to generate two-dimensional (2D) images

of a thin slice of the sample. In 1975 Richard Ernst [19] proposed the application of the Fourier-transform to reconstruct MR images. This still represents the fundamental MRI reconstruction approach nowadays. The first MRI scanners were built at the end of the 1970s by the research groups of Raymond Damadian and William Edelstein [20]. In the same period, the first MR images of the human body were produced.
Subsequent developments mainly concerned image acquisition and reconstruction techniques as well as hardware improvements which allowed to reduce the acquisition times to clinically acceptable values and to improve the image quality. A fundamental step for the spread of MRI to the clinical field has been marked by the development of fast image acquisition techniques in the 1980s. Significant examples are the Fast Low Angle SHot (FLASH) proposed by Axel Haase [21] and the Rapid Acquisition with Relaxation Enhancement (RARE) proposed by Jürgen Hennig [22]. The latter method is also known as Turbo Spin-Echo (TSE) and is based on the spin-echo phenomenon discovered by Erwin Hahn in 1950 [23]. During the same years, MRI started to be progressively used in the clinical routine, and the bases for the continuous development of clinical applications were created [20]. This process is still ongoing.
Within the past three decades, the trend of hardware development has been characterized by the use of: 1) magnets with higher magnetic field strengths, 2) Radio-Frequency (RF) antennas with a larger number of independent elements and corresponding signal receive channels as well as 3) stronger and better performing gradient coils. The introduction of multi-channel RF-coils allowed the development of several acquisition acceleration techniques since the end of the 1990s which are known as parallel imaging. These techniques are nowadays widely used in the clinical routine [24, 25, 26, 27]. Among them, SENSitivity Encoding (SENSE), proposed by Klaas Pruessmann [25], and Generalized Autocalibrating Partially Parallel Acquisitions (GRAPPA), proposed by Mark Griswold [26], are worth mentioning.

MRI of the Lung

Historically, lung MRI has not played a leading role in human lung imaging [8]. Due to several factors, in fact, lung imaging represents a very challenging branch of MRI. These are [28, 29]:

- the low proton density of the lung tissue, due to the presence of air in the alveoli, which makes up more than the half of the total lung volume;
- the short signal decay times (T_2 and T_2^*), which are caused by the magnetic susceptibility difference between lung tissue and air in the alveoli;
- the various sources of physiological motion in the lungs including respiration, blood flow in the pulmonary vessels and cardiac beat.

These factors have a direct impact on the image quality of lung MRI. The low proton density and the short signal decay times are responsible for poor SNR in comparison to other organs; moreover, the presence of physiological motion can result in image artifacts. This especially concerns patients with very limited breath-holding times and uncooperative patients.

In the clinical practice, CT is usually preferred to lung MRI due to the higher achievable image resolution, the better SNR and the shorter acquisition times, which make it less sensitive to physiological motion. Besides the image quality issues that hamper the spread of lung MRI in the clinical field, however, there are also other factors to consider. The key feature of lung MRI is the additional diagnostic information that it can provide in comparison to the other imaging modalities thanks to its unique contrast and flexibility. MRI, in fact, can be used to evaluate different aspects of lung physiology that are particularly relevant both to characterize lung diseases and to improve the understanding of patho-physiological events that occur in the lung [2, 30, 31, 32]. In this regard, MRI offers the unique possibility to spatially resolve and to non-invasively investigate several lung properties such as perfusion, ventilation (delivery of fresh gas to the lung), gas exchange and microstructure at the alveolar level [2, 3, 4, 5, 6, 7, 8, 9, 10, 11, 31, 32].
Thanks to the development of new image acquisition techniques and to hardware improvements, the field of lung MRI has remarkably expanded within the last two decades. These allowed both to improve the image quality and to broaden the spectrum of clinical applications of MRI. For example, the Half-Fourier Acquisition Single-shot Turbo spin-Echo (HASTE) [33, 34] and the Ultrashort Echo Time (UTE) [35, 36, 37] pulse sequences permitted to reduce the influence of both physiological motion and short signal decay times on lung MRI [5, 6]. Furthermore, the use of motion compensation techniques, including respiratory gating and cardiac triggering, offered the possibility to reduce image artifacts and to acquire the signal during free breathing [4, 31, 38]. The use of MRI in combination with contrast agents allowed to assess lung perfusion, to depict the pulmonary vascular tree as well as to characterize lung tumors [39, 40, 41]. In addition to this, the introduction of parallel imaging techniques made it possible to shorten the acquisition times, thus reducing the sensitivity of MRI to motion and improving the image quality of lung MRI [4, 31].
Thanks to these advances, proton MRI has become in the last years a comparable alternative to CT for several applications, namely [2, 31, 42]: the detection of large pulmonary nodules (with diameter > 1 cm), the staging of lung tumors and the assessment of pulmonary vascular diseases. Another important field of application for proton MRI is the diagnosis of lung diseases that alter the water content of the lung. Most lung diseases, in fact, are associated with either an increase or a decrease of water per unit volume and hence of the proton density [31, 32]. The accumulation of fluids or tissues in the interstitial and alveolar spaces, for example, increases the proton density while other phenomena such as hyperinflation or tissue destruction reduce it [31, 32]. For the detection of such diseases, T_2 weighted imaging has proved to be superior to CT in terms of image contrast and diagnostic impact [30, 32]. Nevertheless, CT remains the gold standard modality for the visualization of small morphological lesions and anatomical details.
Besides the above mentioned applications, in which lung MRI is an alternative to CT, research is still ongoing on a variety of applications that refer exclusively to proton MRI. These are:

- Oxygen-enhanced MRI. Quantitative T_1 and T_2^* mapping, in combination with the delivery of different oxygen concentrations to the patient, allow to obtain information about ventilation and perfusion, based on the dependence of the signal relaxation times on the oxygen concentration [43, 44, 45].

- Fourier-decomposition. Morphological images acquired with a high temporal resolution of the order of a few hundred ms allow, with proper post-processing, to assess perfusion and ventilation without the need for contrast agents [46, 47].

- Non-contrast-enhanced perfusion. Besides Fourier-decomposition, several techniques such as Arterial Spin Labeling (ASL) [48] and Spin-Echo Entrapped Perfusion imAGE (SEEPAGE) [49] allow to obtain qualitative or quantitative information about lung perfusion without requiring contrast agents.

- Non-conventional contrasts, such as magnetization transfer [50, 51] and Diffusion Weighted Imaging (DWI) [52], enabled the further characterization of lung nodules and tumors.

Another lung MRI technique which has remarkably expanded in the last years is hyperpolarized gas MRI [7, 53]. With this approach, the MR images are not generated by protons but by the nuclei of a gas, typically ^{3}He or ^{129}Xe. The patient inhales the gas, which has been previously subjected to the hyperpolarization procedure in order to increase the generated MR signal, which otherwise would be too low due to the relatively low density of gases. The images obtained with this method show the spatial distribution of the inhaled gas within the lungs. Moreover, advanced methodologies based on hyperpolarized gas MRI permit to obtain additional information [7, 53]. For example, 1) the evaluation of the wash-in and wash-out times of the gas by means of dynamic image acquisition and analysis provides information about lung ventilation [54]; 2) the quantification of the diffusion coefficient of the gas, which is related to the environment in which the gas diffuses, provides information about the alveolar size [55, 56, 57]; 3) the time-dependence of the T_1 of the gas gives information about the perfusion-ventilation ratio [53, 58]; 4) the fraction between the amount of dissolved gas in blood and the gas in the alveoli, which can be detected by exploiting the different resonance frequency of the two components, gives a measure of the gas exchange rate [7, 53].
Despite the impressive amount of diagnostic information that hyperpolarized gas MRI can potentially provide, this technique has not yet established in the clinical field as it requires the use of dedicated hyperpolarizing systems and of complex clinical workflows.

Goals of This Thesis

The aim of this doctoral thesis is to resume the work performed in approximately three and a half years on the topic of proton MRI of the lung. The work was performed between September 2011 and December 2014 at the Research Center Magnetic Resonance Bavaria (MRB) in Würzburg as part of the European project "Pulmonary Imaging NETwork (π-NET)" funded by the 7th Framework Program of the European Commission (grant number PITN-GA-2010-264864). Part of the obtained results have been presented at international conferences and published on peer-reviewed journals, as indicated in the list of publications at the end of the thesis.
The focus of the work concerned the development of a series of MRI techniques that were specifically designed and optimized to obtain quantitative and spatially resolved information about characteristic parameters of the lung. Three image acquisition techniques were

developed. Each of them allows to quantify a different parameter of relevant diagnostic interest for the lung, as further described below:

1. The blood volume fraction, which represents the amount of lung water in the intravascular compartment expressed as a fraction of the total lung water. This parameter is related to lung perfusion [59, 60, 61].

2. The magnetization relaxation time $T_{2,\text{diff}}$, which represents the component of T_2 associated with the diffusion of water molecules through the internal magnetic field gradients of the lung [62]. Because the amplitude of these internal gradients is related to the alveolar size [63], $T_{2,\text{diff}}$ can be used to obtain information about the microstructure of the lung [64, 65].

3. The broadening of the NMR spectral line of the lung. This parameter depends on lung inflation and on the concentration of oxygen in the alveoli [63, 66]. For this reason, the spectral line broadening can be regarded as a fingerprint for lung inflation [67]; furthermore, in combination with oxygen enhancement, it provides a measure for lung ventilation.

All proposed techniques represent further developments of existing methodologies that were adapted for in-vivo lung imaging application. One of the requirements to make them suitable for clinical studies on patients with lung diseases as well as for the clinical routine was to develop relatively fast acquisition techniques. For this reason, a common feature of all techniques is the use of the HASTE sequence, in different variants, for data acquisition. The basic approaches which have been used are briefly described below:

1. The blood volume fraction was quantified by using the Intra-Voxel Incoherent Motion (IVIM) approach proposed by Le-Bihan [59, 60, 61], which is based on DWI. In this work, the possibility to exploit the internal gradients of the lung to reduce signal losses induced by the short T_2 and, at the same time, to avoid technical difficulties such as the violation of the Carr-Purcell-Meiboom-Gill (CPMG) conditions [68, 69] as well as the sensitivity of DWI to motion is investigated.

2. $T_{2,\text{diff}}$ was quantified by exploiting the well-known dependence of T_2 on the interpulse time in TSE-based sequences [64, 65, 70]. In this thesis, a novel technique is proposed, which allows to quantify $T_{2,\text{diff}}$ of the human lung in-vivo in a single breath-hold. Furthermore, the possibility to exploit the knowledge of $T_{2,\text{diff}}$ for the quantification of the alveolar size is explored.

3. The spectral line broadening was quantified by using the Asymmetric Spin-Echo (ASE) approach [71]. Normally, this technique requires relatively long acquisition times that are not suitable for in-vivo applications. In this work, the ASE module was integrated in the HASTE sequence in order to reduce the acquisition times to a single breath-hold. It is shown how the deriving violations of the CPMG conditions can be overcome.

For each technique, dedicated studies were designed and performed in order to: 1) explore the performance of the proposed techniques with regard to the quantification of the mentioned parameters, 2) evaluate the reproducibility of the quantification in-vivo and 3) investigate the corresponding lung properties.

Structure of the Thesis

The thesis is structured as follows: Chapter 1 gives an overview of the basic concepts of NMR and MRI; Chapter 2 describes the main characteristics of lung morphology and functionality along with their implications on proton MRI of the lung; Chapter 3 presents the materials and methods of general interest for this thesis; Chapters 4, 5 and 6 focus on the core of the work. Each of these chapters is dedicated to the quantification of a different parameter, as indicated in the previous section; the development of the pulse sequences, the performed experiments and the corresponding results are described in detail and discussed.

Chapter 1

Basic Principles of MRI

This chapter briefly describes the basic concepts of NMR and MRI by following the descriptions of Abragam [72], Bernstein et al. [73], Callaghan [74], Haacke et al. [75] and Levitt [76], to which the interested reader is referred for a more detailed discussion.

1.1 The Physics of Nuclear Magnetic Resonance

NMR is based on the interaction of the nuclear spin with an external static magnetic field. Besides MRI, one of its main research applications is NMR spectroscopy, which can be used to investigate molecular structures, chemical compositions and concentrations as well as physical and chemical properties of matter.

The Nuclear Spin

The spin is an intrinsic property of particles and represents the quantum mechanical equivalent of the classical intrinsic angular momentum. The spin of a nucleus (or nuclear spin) is described by the operator $\hat{I} = (\hat{I}_x, \hat{I}_y, \hat{I}_z)$, which is given by the sum of the total angular moments $\hat{j}_i$ of the single nucleons (protons and neutrons) that compose it [77]. The quantum state of nuclear spin is characterized by the quantum number I, which is obtained from the following eigenvalues equation of the squared norm operator $\hat{I}^2$:

$$\langle \hat{I}^2 \rangle = \hbar^2 I\,(I+1) \tag{1.1}$$

where $\hbar$ is the Planck's constant. For a given nucleus, the value of I depends on the quantum energetic configuration of its nucleons. For most of the stable nuclides, the following rules hold, as derived from the shell model of the nucleus [78]:

1. if the number of protons and the number of neutrons are both even, then $I = 0$;

2. if the number of protons is odd and the number of neutrons is even, or vice versa, then the nuclear spin is a half integer number $I = j_k$, corresponding to the total angular momentum of the unpaired nucleon;

3. if the number of protons and the number of neutrons are both odd, then the nuclear spin is an integer number $|j_p - j_n| \leq I \leq |j_p + j_n|$, where j_p and j_n are the total angular moments of the unpaired proton and neutron, respectively.

The nuclei of interest for NMR and MRI are those isotopes with $I > 0$, belonging to the groups 2 and 3 described above. An overview of interesting nuclear species is reported in Table 1.1. Some of the most common nuclides such as ^{12}C and ^{16}O are omitted because they belong to group 1 and are not observable with NMR and MRI.

Nuclide	Spin	μ/μ_N	$\gamma/2\pi$ (MHz/T)	Natural abundance (%)	Atomic percent in the human body (%)
^{1}H	1/2	2.79	42.6	100	62
^{13}C	1/2	0.702	10.7	1.11	12
^{14}N	1	0.404	3.08	99.6	1.1
^{17}O	5/2	-1.89	-5.77	0.04	24
^{19}F	1/2	2.63	40.1	100	0.012
^{23}Na	3/2	2.22	11.3	100	0.037
^{31}P	1/2	1.13	17.2	100	0.22

Table 1.1: List of selected nuclear species of interest in NMR and MRI. Values of their nuclear spin quantum number I, magnetic dipole moment μ, gyromagnetic ratio γ, natural abundance and atomic percent of the corresponding chemical element in the human body are reported. Data retrieved from references [75, 79, 80].

Magnetic Dipole Moments

Nuclei with $I > 0$ present an intrinsic magnetic dipole moment $\vec{\mu}$ of amplitude:

$$\mu = \gamma \hbar \sqrt{I\,(I+1)} \tag{1.2}$$

where the proportionality factor γ is called nuclear gyromagnetic ratio and is a characteristic parameter of each nuclear species (see Table 1.1).
The order of magnitude of a magnetic dipole moment is obtained by multiplying the orbital gyromagnetic ratio of protons $e/2m_p$ by a quantum of angular momentum $\hbar$:

$$\mu_N = \frac{e\hbar}{2m_p} \simeq 5.05 \cdot 10^{-27}\,\mathrm{JT}^{-1} \tag{1.3}$$

where μ_N is called nuclear magneton.
The magnetic dipole moment is not directly related to the electrical charge of particles: both protons and neutrons have a spin quantum number $I = 1/2$ and hence a magnetic dipole moment. The experimental values of their respective magnetic dipole moments are [81]:

$$\mu_p \simeq 2.79\,\mu_N \tag{1.4}$$

$$\mu_n \simeq -1.91\,\mu_N \tag{1.5}$$

Because the nuclear spin is determined by the unpaired nucleons, the magnetic dipole moment is of the order of μ_N for most nuclear species (see Table 1.1).

Spins in a Static Magnetic Field

The interaction of a magnetic dipole with a static magnetic field $\vec{B}$ is classically expressed by:

$$E = -\vec{\mu} \cdot \vec{B} \tag{1.6}$$

where E is the potential energy. The corresponding Hamiltonian operator is [77]:

$$\hat{H} = -\gamma B_0 \, \hat{I}_z \tag{1.7}$$

where B_0 is the magnetic field strength and $\hat{I}_z$ represents the component of the nuclear spin in the direction of the magnetic field (conventionally the z-axis). The eigenvalues equation for $\hat{I}_z$ is [77]:

$$\langle \hat{I}_z \rangle = \hbar m \tag{1.8}$$

where m is the secondary quantum number of nuclear spin and can assume one of the $2I + 1$ values $(-I, -I + 1, ..., I)$. This means that the energy levels of the accessible quantum states for a nuclear spin in a magnetic field are:

$$E_m = \langle \hat{H} \rangle = -\gamma \hbar B_0 \, m \tag{1.9}$$

In the absence of an external magnetic field, the energy levels are degenerate. The application of a static magnetic field breaks the degeneracy, causing the split of the levels. This is known as Zeeman effect [77]. The energy difference between these levels is given by:

$$\Delta E = \hbar \omega_0 \tag{1.10}$$

where

$$\omega_0 = \gamma B_0 \tag{1.11}$$

is called Larmor (or resonance) frequency.
In a static magnetic field, a system of nuclei with $I > 0$ can be excited with an electromagnetic field oscillating at angular frequency ω_0. Because the strength of the static magnetic fields that are used in NMR and MRI is typically of the order of a few tesla, the corresponding resonance frequency is in the range of the RF span of the electromagnetic spectrum. For protons:

$$\frac{\gamma}{2\pi} = \frac{\omega_0}{2\pi B_0} \simeq 42.6 \text{ MHz T}^{-1} \tag{1.12}$$

Population of a System of Spin $1/2$

For a nucleus with spin quantum number $I = 1/2$, only two energy levels are accessible: $E_{+1/2}$ and $E_{-1/2}$, corresponding to $m = +1/2$ and $-1/2$ respectively. If $\gamma > 0$, the state of lower energy, which is called ground state, is $E_{+1/2}$ and corresponds to the parallel alignment of the spin to the magnetic field; $E_{-1/2}$, instead, is the excited state and corresponds to the anti-parallel spin alignment (see Figure 1.1).

When considering a system made of a large number of nuclei, it is necessary to introduce ensemble averages in order to describe the state of the system. According to the Boltzmann distribution, the ratio between the population of the ground state N_+ and that of the excited state N_- is:

$$\frac{N_+}{N_-} = \exp\left(\frac{\triangle E}{k_B T}\right) \tag{1.13}$$

where T is the absolute temperature in kelvin and k_B is the Boltzmann constant. The population ratio always fulfills the condition $N_+ > N_-$ and increases with lower temperatures and higher magnetic field strengths according to equation (1.10). At $T = 300$ K the thermal energy is $k_B T \simeq 25$ meV, while the energy split for protons at 3.0 T is $\triangle E \simeq 525$ neV, meaning that $k_B T \gg \triangle E$ at room temperature. Thus, according to equation (1.13) the two levels have almost the same population. Under this assumption, the first order approximation of equation (1.13) leads to:

$$\frac{N_+}{N_-} \simeq 1 + \frac{\triangle E}{k_B T} \tag{1.14}$$

Hence, the relative excess of particles which occupy the ground level, with respect to the total number of particles, is given by:

$$\frac{\triangle N}{N} = \frac{N_+ - N_-}{N} \simeq \frac{\triangle E}{2 k_B T} \tag{1.15}$$

where $N = N_+ + N_-$ is the total number of particles. For protons at 3.0 T the relative spin excess is about 10^{-5}.

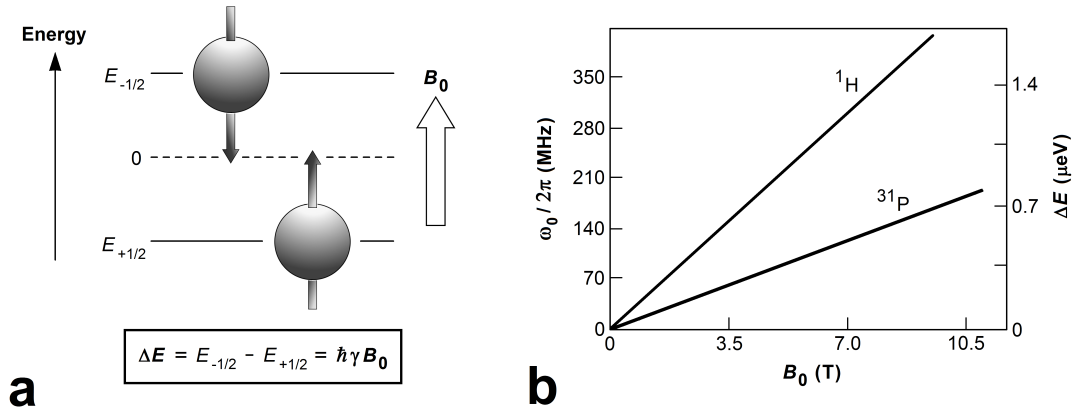

Figure 1.1: a) Representation of the available energy levels for particles with spin quantum number $I = 1/2$ and gyromagnetic ratio $\gamma > 0$ in a magnetic field. b) Dependence of the energy split ΔE on the magnetic field strength B_0 for two different nuclear species (^{1}H and ^{31}P). Reproduced with permission from reference [82], with adaptions.

The Magnetization Vector

The behavior of a system composed of a large number of nuclei can be studied in terms of the macroscopic magnetization vector $\vec{M} = (M_x, M_y, M_z)$, which is defined as the

total magnetic dipole moment per unit volume. This vector is obtained from the sum of the magnetic dipole moments of all the particles of the system. Due to the linear proportionality between magnetic dipole moment and nuclear spin [77], the magnetization vector can be expressed as:

$$\vec{M} = \frac{1}{V}\sum_{i=1}^{N}\vec{\mu} = \frac{N}{V}\,\gamma\langle\hat{I}\rangle \tag{1.16}$$

where V is the volume of the sample. The components M_x, M_y and M_z can be obtained by substituting in equation (1.16):

$$\langle\hat{I}_x\rangle = \frac{\hbar}{2}\sin\theta\cos\phi \tag{1.17}$$

$$\langle\hat{I}_y\rangle = \frac{\hbar}{2}\sin\theta\sin\phi \tag{1.18}$$

$$\langle\hat{I}_z\rangle = \frac{\hbar}{2}\cos\theta \tag{1.19}$$

as given by the properties of the Pauli matrices [77] which are normally used to describe $\hat{I}_x$, $\hat{I}_y$ and $\hat{I}_z$. This gives a representation of the magnetization vector in spherical coordinates, with a polar angle θ and an azimuthal angle ϕ. For a system characterized by a population difference ΔN the condition of thermal equilibrium is:

$$\vec{M} \simeq \left(0, 0, \frac{\triangle N}{2N}\,\hbar\rho\gamma\right) \tag{1.20}$$

where $\rho = N/V$ is the density of particles per unit volume, called spin density. In the absence of an external magnetic field, the energy levels are equally populated and the magnetic dipoles are randomly oriented. This results in the reciprocal cancellation of the magnetic dipole vectors and, consequently, in the absence of a macroscopic magnetization. If an external magnetic field is applied, a population difference between the two energy levels is generated, resulting in a net magnetization.
Equation (1.20) states that the equilibrium position of the magnetization is parallel to the external magnetic field. Its magnitude can be derived from the combination of equations (1.15) and (1.20), such that:

$$M_0 = \frac{\gamma^2\hbar^2}{4k_BT}\,\rho B_0 \tag{1.21}$$

A net magnetization can be macroscopically observed even with the very small spin excess at room temperature due to the relatively large total number of nuclei in a sample, which is proportional to the Avogadro constant $N_A = 6.022 \cdot 10^{23}$ particles/mol.

The Bloch-Equation

In 1946 Felix Bloch proposed a set of first order differential equations, which were derived from phenomenological arguments, in order to describe the dynamics of the magnetization in an external magnetic field [13].

The Bloch-Equation is based on the following assumptions:

1. The evolution of a magnetic dipole moment $\vec{\mu}$ in a static magnetic field of strength B_0 is a free precession about the direction of the magnetic field, with angular frequency $\omega_0 = \gamma B_0$. Therefore, the motion of the magnetization vector $\vec{M}$ can be described by:

$$\frac{d\vec{M}}{dt} = \gamma \vec{M} \times \vec{B} \tag{1.22}$$

this represents a precession of $\vec{M}$ about $\vec{B}$ with frequency ω_0, as shown in Figure 1.2 a.

2. The return of the magnetization towards its equilibrium, which is called relaxation, is described by two exponential decays through equations:

$$\frac{dM_z}{dt} = -\frac{M_z - M_0}{T_1} \tag{1.23}$$

$$\frac{dM_{xy}}{dt} = -\frac{M_{xy}}{T_2} \tag{1.24}$$

where M_z and M_{xy} represent the longitudinal and transverse components of the magnetization with respect to the magnetic field. T_1 and T_2 are called longitudinal and transverse relaxation times, respectively, and represent the characteristic time constants of the exponential decays.

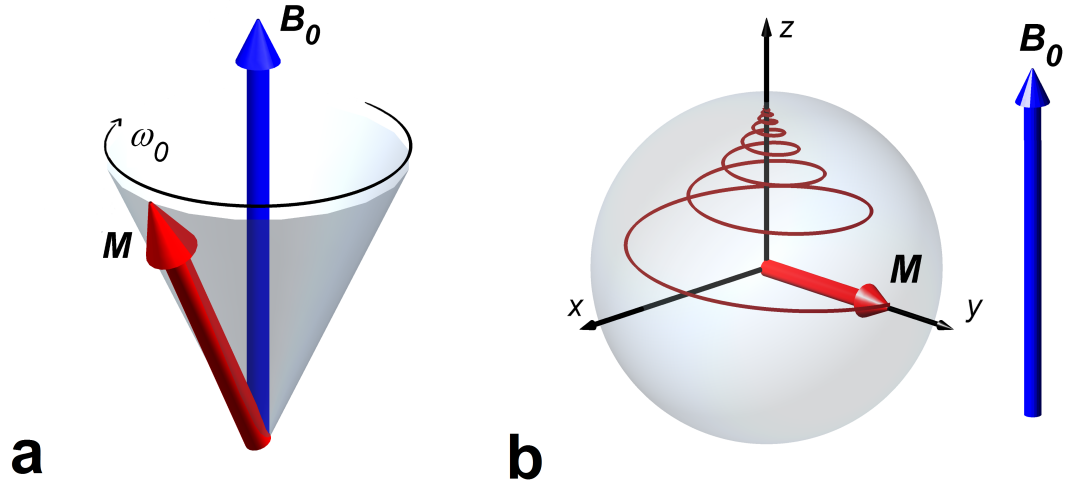

Figure 1.2: a) Precession of the magnetization vector $\vec{M}$ about an external magnetic field of strength B_0. The sense of rotation is clockwise if $\gamma > 0$, counter-clockwise otherwise. The angular frequency of precession is $\omega_0 = \gamma B_0$. b) Trajectory of the magnetization vector $\vec{M}$ during the relaxation process. The return to equilibrium of the longitudinal and transverse components of the magnetization is combined with the precession about the external magnetic field, as it results from the Bloch equation (1.25).

The motion of the magnetization results from the combination of free precession and relaxation, such that:

$$\frac{d\vec{M}}{dt} = \gamma\vec{M} \times \vec{B} - \frac{M_x\vec{x} + M_y\vec{y}}{T_2} - \frac{M_z - M_0}{T_1}\vec{z} \tag{1.25}$$

where $\vec{x}$, $\vec{y}$ and $\vec{z}$ are the unit vectors in the three coordinate directions. The use of the Bloch-equation is very useful to describe the dynamics of the spin system in macroscopic terms and provides a correct description of the phenomena of precession and relaxation. An example of the trajectory of $\vec{M}$ which results from the combination of precession and relaxation is shown in Figure 1.2 b.

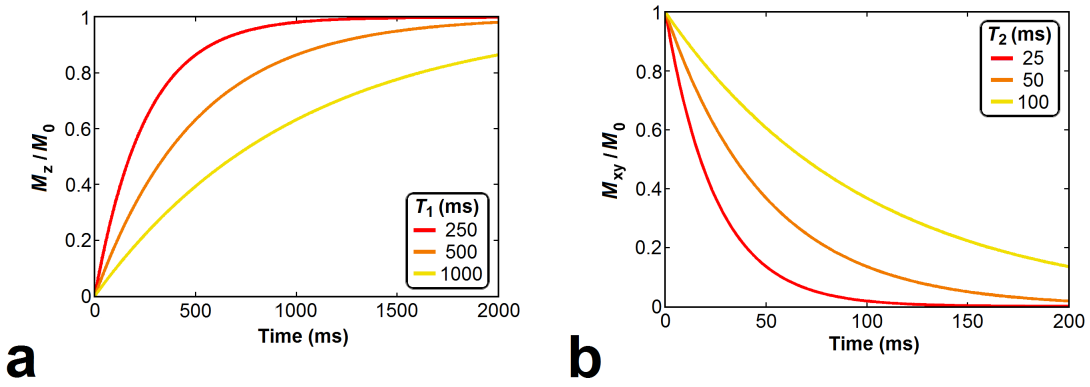

Figure 1.3: a) Effect of different values of the relaxation time T_1 on the exponential recovery of the longitudinal magnetization M_z towards its equilibrium value M_0. b) The exponential decay of the transverse magnetization M_{xy} is characterized by a silimar effect when using different values of T_2. In both shown examples (a and b) the initial condition is represented by the magnetization vector lying on the transverse xy-plane.

Magnetization Relaxation

Equation (1.25) has the only stable solution $\vec{M} = (0, 0, M_0)$. When the magnetization is in a different configuration, the system is excited and the magnetization tends to re-align to the magnetic field, in order to reach the equilibrium position. The motion of $\vec{M}$ during the relaxation process is given by the following solution of the Bloch-equation:

$$M_{xy}(t) = M_{xy}(0)\, e^{-t/T_2}\, e^{i(-\omega_0 t + \phi_0)} \tag{1.26}$$

$$M_z(t) = M_z(0)\, e^{-t/T_1} + M_0 \cdot \left[1 - e^{-t/T_1}\right] \tag{1.27}$$

where $M_{xy}(t)$ is expressed in complex notation and ϕ_0 represents its phase at $t = 0$.
The longitudinal relaxation corresponds, microscopically, to the spin transitions from the excited state to the ground state. Such transitions can occur through interactions between the spins and the surrounding environment, which allow for energy exchanges of the spins with atoms and molecules [15] (spin-lattice interactions).

The transverse relaxation is due to a loss of phase coherence of the magnetization at the microscopic level, which is caused by interactions between spins (spin-spin interactions). The magnetic dipole moments of particles, in fact, reciprocally affect their precession frequencies. This results, over time, in a phase dispersion among the dipole moments of the system and hence, in a reduced amplitude of the magnetization vector [83]. Because the transitions from the excited state to the ground state also imply a loss of phase coherence, the values of the relaxation times always fulfill the condition $T_2 < T_1$.
The relaxation times T_1 and T_2 are characteristic parameters of matter. The human body consists of a multitude of different types of tissue, each with its specific relaxation times. Their values for different tissues of the human body are reported in Table 1.2. Examples of relaxation curves obtained with different values of the relaxation times are shown in Figure 1.3, for both the transverse and the longitudinal magnetization components.

Tissue	T_1 (ms)	T_2 (ms)
Gray Matter	950	100
White Matter	600	80
Muscle	900	50
Cerebrospinal Fluid	4500	2200
Fat	250	60
Blood	1200	100-200

Table 1.2: Representative values of the magnetization relaxation times T_1 and T_2 of protons for different tissues of the human body at $B_0 = 1.5$ T and $T = 37$ °C. Reproduced with permission from reference [75].

Magnetic Field Inhomogeneities

The decay of the transverse magnetization can be accelerated by the presence of static magnetic field inhomogeneities throughout the sample. These are defined as:

$$\Delta B_0 = B_z - B_0 \tag{1.28}$$

where B_z is the actual magnetic field strength and B_0 is the nominal field strength. These field inhomogeneities result in a shift of the Larmor frequency, as indicated by equation (1.11). Therefore, if the static magnetic field is not homogeneous throughout the whole sample, a further loss of phase coherence would affect the transverse magnetization, similarly to the effect of the spin-spin interactions. In this case, the transverse relaxation time can be obtained from the following formula:

$$\frac{1}{T_2^*} = \frac{1}{T_2} + \frac{1}{T_2'} \tag{1.29}$$

where T_2^* is the overall transverse relaxation time and T_2' represents the signal decay constant associated to the presence of field inhomogeneities. T_2' contributes to shorten the transverse relaxation time, such that $T_2^* < T_2$. In contrast to the T_2 decay, which is irreversible, the relaxation mechanism associated with the presence of magnetic field inhomogeneities can be recovered by using spin-echo based techniques, as further described later in this chapter.

Excitation and Rotating Reference Frame

Excitation of the sample is performed by means of a transmit (TX) antenna (or RF-coil) operating at the resonance frequency ω_0 of the nucleus of interest. The magnetic component of the generated electromagnetic RF-field, indicated with $\vec{B}_1$, flips the magnetization from its equilibrium position. This effect can be described by a generalized version of the Bloch-equation.
Consider a magnetic field $\vec{B}_1$ perpendicular to the static magnetic field $\vec{B}$ and oscillating with circular polarization at a generic angular frequency ω_{RF} such that:

$$\vec{B}_1(t) = \left[B_1(t)\cos\left(-\omega_{\mathrm{RF}}t + \phi_{\mathrm{RF}}\right), B_1(t)\sin\left(-\omega_{\mathrm{RF}}t + \phi_{\mathrm{RF}}\right), 0\right] \tag{1.30}$$

where ϕ_{RF} is the phase of $\vec{B}_1$ in the complex plane at $t = 0$.
In the presence of $\vec{B}_1$, a transformation of the coordinates system simplifies the description of the dynamics of the magnetization [84]. In the coordinate system $\{x', y', z'\}$, which rotates about the z-axis with angular frequency ω_{RF}, the first term of the Bloch-equation becomes:

$$\frac{d\vec{M}'}{dt} = \gamma\vec{M}' \times \vec{B}_{\mathrm{eff}}(t) \tag{1.31}$$

where $\vec{M}'$ is the representation of the magnetization vector in the rotating reference frame. The relaxation terms are usually negligible during excitation as the RF-field is typically applied for a duration in time which is much shorter than T_1 and T_2. The effect of $\vec{B}_1$ in the rotating reference frame is described by an effective field $\vec{B}_{\mathrm{eff}}$. This is given by:

$$\vec{B}_{\mathrm{eff}}(t) = \left[B_1(t)\cos\phi_{\mathrm{RF}}, B_1(t)\sin\phi_{\mathrm{RF}}, B_0 - \frac{\omega_{\mathrm{RF}}}{\gamma}\right] \tag{1.32}$$

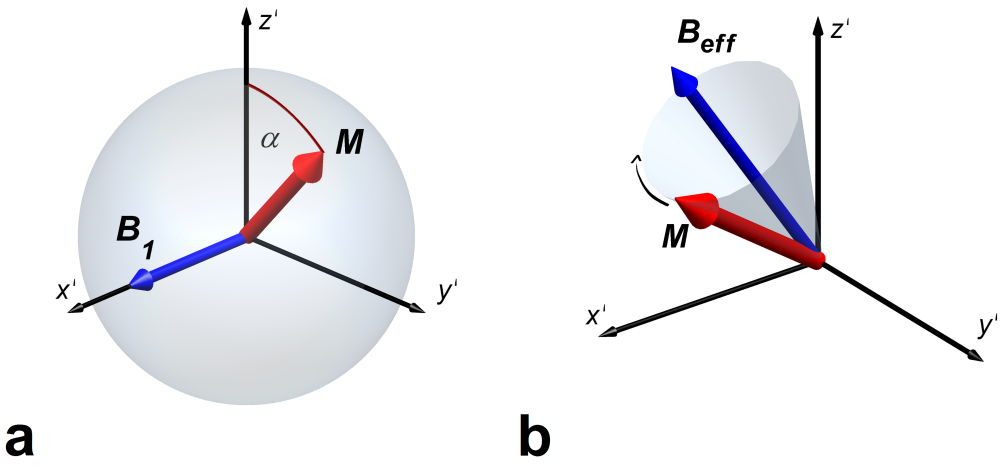

Figure 1.4: a) Time evolution of the magnetization vector in the rotating reference frame during the excitation with an on-resonance RF-field $\vec{B}_1$. b) Precession of the magnetization vector about the effective magnetic field $\vec{B}_{\mathrm{eff}}$ in the rotating reference frame in the presence of an off-resonance RF-field.

When the RF-field is applied at frequency $\omega_{\mathrm{RF}} = \omega_0$, it is said to be "on-resonance". In this case, $\vec{B}_{\mathsf{eff}}$ has no z-component. The solution of equation (1.31) is, by analogy with the free precession term in the Bloch-equation (1.25), a precession of $\vec{M}'$ about $\vec{B}_1$ with angular frequency $\gamma B_1(t)$, as shown in Figure 1.4 a. If a RF-pulse of duration τ_{RF} is applied, the angle accumulated by the magnetization at the end of the excitation, which is called flip-angle, is given by:

$$\alpha = \gamma \int_0^{\tau_{\mathrm{RF}}} B_1(t)\, dt \tag{1.33}$$

If the magnetization is initially parallel to the z-axis, a RF-pulse with $\alpha = 90°$ (named 90°-pulse) flips the magnetization into the transverse xy-plane.
When the RF-field is applied at frequency $\omega_{\mathrm{RF}} \neq \omega_0$, it is said to be "off-resonance". In this case, $\vec{B}_{\mathsf{eff}}$ presents also a z-component. The solution of equation (1.31) is a precession of $\vec{M}'$ about $\vec{B}_{\mathsf{eff}}$ with angular frequency $\gamma|\vec{B}_{\mathsf{eff}}(t)|$, as shown in Figure 1.4 b.
The effect of the possible presence of static magnetic field inhomogeneities ΔB_0 on the excitation is analogous to the use of an off-resonance RF-field, as this would contribute to create a z-component of $\vec{B}_{\mathsf{eff}}$ as it is stated by equation (1.32).

Signal Detection

Signal detection is performed by means of a receive (RX) RF-coil. When the RF-coil is placed near to the excited sample, with its winding axis perpendicular to the static magnetic field, the precessing transverse magnetization $M_{xy}(t)$ will induce an alternating voltage at the ends of the loop due to the Faraday's law of induction [79], as shown in Figure 1.5. The induced voltage (s) is given by the variation of the concatenated magnetic flux over time, such that:

$$s(t) \propto \frac{d}{dt}\left[\vec{B}_1^{-} \cdot \vec{M}_{xy}(t)\right] \tag{1.34}$$

where $\vec{B}_1^{-}$ is the RX coil sensitivity, which is defined from the principle of reciprocity as the magnetic field per unit current that the coil would generate at the position of the sample [79].
The temporal dependence of $\vec{M}_{xy}(t)$ is given by equation (1.26). Thus, the NMR signal, which is also called Free Induction Decay (FID), is given by:

$$s(t) \propto \omega_0 M_0 V B_1^{-} \sin\alpha\, e^{-t/T_2}\, e^{i(-\omega_0 t + \phi_0 - \phi_{RF})} \tag{1.35}$$

as it results from equations (1.26) and (1.34).
In practice, the detected signal is sampled in a discrete number of points by an Analog-to-Digital Converter (ADC) and amplified. According to equation (1.35), the NMR signal decays exponentially in time with decay constant T_2 and oscillates at the resonance frequency ω_0, as expressed by the modulation of the signal with the factor $e^{i\omega_0 t}$. In order to remove this phase modulation, which does not provide any valuable information, the sampled signal is usually retrospectively demodulated by multiplication with the factor $e^{-i\omega_0 t}$.

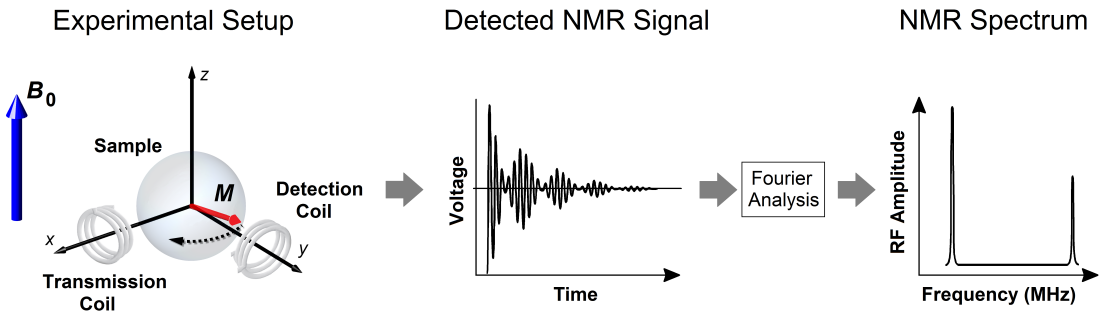

Figure 1.5: Experimental setup of a NMR experiment: the sample is placed in a static magnetic field of strength B_0 and is excited with the RF-field generated by the TX coil. The preceding magnetization induces a time-dependent voltage on the RX coil during the relaxation process. The frequency spectrum of the detected NMR signal, which is given by its inverse Fourier transform, can be used to investigate the concentration of different nuclear species in the sample. Reproduced with permission from references [76] and [82], with adaptions.

NMR Spectroscopy

Equation (1.35) holds in the limit of small and homogeneous samples, where all parameters in the equation can be assumed to be single-valued constants. However, this condition is not always fulfilled. In this section, the influence of a heterogeneous distribution of resonance frequencies on the time course of the NMR signal is briefly discussed. This represents the basis of NMR spectroscopy.
The resonance frequency can present a heterogeneous distribution within the sample due to several factors, such as: 1) spatial variations of the static magnetic field, 2) differences in the resonance frequency of a given nuclear species when bounded to different chemical compounds (chemical shift) and 3) presence of multiple nuclear species, which have different gyromagnetic ratios. Due to the precession about the static magnetic field, the phase of the transverse magnetization linearly increases with time, as indicated by the factor $e^{i\omega_0 t}$ in equation (1.35). In the presence of resonance frequency heterogeneities, a residual phase accrual could still be observed after signal demodulation, due to the difference between the actual resonance frequency and the nominal resonance frequency. This is given by:

$$\phi = -(\omega - \omega_0)\, t \tag{1.36}$$

where ω is the actual resonance frequency and ω_0 is the nominal resonance frequency. If the resonance frequency is heterogeneously distributed within the sample, the time course of the FID signal is given by a weighted superposition of multiple dephasing signal components. Each of them presents the form of equation (1.35). Neglecting the time independent variables in equation (1.35), the time evolution of the FID signal can be expressed by:

$$s(t) \propto e^{-t/T_2} \int P(\omega)\, e^{-i(\omega-\omega_0)t} d\omega \tag{1.37}$$

where $P(\omega)$ is the probability density distribution of resonance frequencies in the NMR frequency spectrum.

Equation (1.37) represents the basic equation of NMR spectroscopy and states that the time course of the FID signal is given by the Fourier-transform of $P(\omega)$ [85], modulated by the exponential transverse decay. Information about the different nuclear species and chemical compounds in the sample can be obtained by acquiring the FID signal at different time points and performing an inverse Fourier transformation, as shown in Figure 1.5. The different signal components would appear like peaks in the NMR spectrum.
The possible presence of spatial inhomogeneities in the static magnetic field would spread the NMR spectral peaks over a broader range of frequencies, accelerating the signal decay. This concept was already introduced in this chapter by means of the decay time T_2' in equation (1.29) and will be discussed in more detail in the next chapter.

Nuclide	Molarity (mol/l)	$\mathcal{R}_i/\mathcal{R}(^1\mathrm{H})$
^{1}H	88	1.0
^{17}O	$16 \cdot 10^{-3}$	$5.4 \cdot 10^{-6}$
^{19}F	$4 \cdot 10^{-6}$	$3.8 \cdot 10^{-8}$
^{23}Na	$80 \cdot 10^{-3}$	$8.5 \cdot 10^{-5}$
^{31}P	$75 \cdot 10^{-3}$	$5.7 \cdot 10^{-5}$

Table 1.3: Values of the molarity in the gray matter of the human brain for a list of selected nuclides of interest in MRI and relative signal intensity $\mathcal{R}$ produced at $B_0 = 1.5$ T compared to protons. Reproduced with permission from reference [75].

1.2 General Overview of MRI Concepts

MRI is an application of the NMR principles which is aimed at the production of images of the sample. The key idea of MRI, developed in the 1970's by Paul Lauterbur [16] and Peter Mansfield [17, 86, 87], consists in the application of magnetic fields which vary linearly in space (or magnetic field gradients) to generate a spatially dependent precession frequency within the sample. Thereby, information about the spatial distribution of the magnetization is encoded in the frequency of the signal. An inverse Fourier transformation can then be used to extract the frequency content of the acquired signal and to reconstruct the MR image [19].
MRI finds its main application in medicine, where it is used to generate images of the human body for diagnostic purposes. The image contrast is generated by the difference in some physical properties of tissues, which are called contrast parameters. Examples of these are: the spin density ρ and the relaxation times T_1, T_2 and T_2^*. The diagnosis is based on the fact that the contrast parameters can assume different values in healthy and pathological tissues, thus resulting in a visual contrast on the MR image [88].
In principle, all nuclei with $I > 0$ can be used for MRI. However, only a few species play an important role in clinical and experimental MRI, because a sufficiently high abundance is necessary to obtain a measurable signal. An example of the relative signal strength $\mathcal{R}$ generated by different nuclear species in the human brain is reported in Table 1.3 and clarifies why protons are more commonly used in MRI than any other nuclei, especially for clinical applications. Nevertheless, MRI based on the use of other nuclei, such as

hyperpolarized gas MRI with ^{3}He or ^{129}Xe, can provide valuable additional information [53], as already discussed.

Magnetic Field Gradients

The basic principle to achieve spatial information about the spins in a sample is to superimpose a magnetic field gradient (here simply called "gradient") to the static field $\vec{B}$. A gradient $\vec{G}$ is a magnetic field parallel to $\vec{B}$, with a linearly varying magnitude in a certain direction in space. This is expressed by:

$$\vec{G} = \left(\frac{\partial B_z}{\partial x}, \frac{\partial B_z}{\partial y}, \frac{\partial B_z}{\partial z} \right) \tag{1.38}$$

If a gradient $\vec{G}(t)$ is applied, the resulting resonance frequency within the sample would be spatially dependent. This is given by:

$$\omega\left(\vec{r}, t\right) = \gamma \left[B_0 + \vec{G}\left(t\right) \cdot \vec{r} \right] \tag{1.39}$$

This simple equation is the basis of the imaging principle. It states that the application of a gradient after excitation of the sample induces the magnetization to precess with a frequency that depends on its spatial position. Therefore, the frequency of the signal contains spatial information.

The k-Space Formalism

The mathematical description of image reconstruction from the NMR signal is called k-space formalism. The total signal arising from a volume V of the sample is given by the complex sum of multiple oscillating components. Each of them is characterized by a different resonance frequency, similarly to what was already discussed for NMR spectroscopy. Neglecting the possible spatial variations of B_1^-, ω_0 and α as well as relaxation effects in equation (1.35), the MR signal can be expressed as:

$$s\left(t\right) \propto \int_V \rho\left(\vec{r}\right) \, e^{i\phi_G(\vec{r},t)} \, d^3r \tag{1.40}$$

where $\phi_G\left(\vec{r}, t\right)$ represents the phase which is accumulated by the transverse magnetization at the time of signal acquisition t due to the presence of the gradient. This is given by:

$$\phi_G\left(\vec{r}, t\right) = -\int_0^t \omega\left(\vec{r}, t\right) dt \tag{1.41}$$

with $\omega\left(\vec{r}, t\right)$ as in equation (1.39). After demodulation, the signal can be rewritten as:

$$S(\vec{k}) \propto \int_V \rho\left(\vec{r}\right) \, e^{-i\,2\pi\vec{k}\cdot\vec{r}} \, d^3r \tag{1.42}$$

where

$$\vec{k} = \frac{\gamma}{2\pi} \int_0^t \vec{G}\left(t'\right) dt' \tag{1.43}$$

The sum of oscillating terms in equation (1.42) assumes the form of the Fourier-transform of the spatial distribution of the spin density $\rho(\vec{r})$. In order to highlight this feature, the use of the vector $\vec{k}$ was introduced, which can be thought as the zeroth moment of the function $\vec{G}(t)$ at the time of signal acquisition t, multiplied by the constant factor $\gamma/2\pi$. The vector space of spatial frequencies $\vec{k}$, which is reciprocal with respect to the image space, is called k-space.
Equations (1.42) and (1.43) are the fundamental relations of MRI and state that the acquired signal $S(\vec{k})$ and the spin density $\rho(\vec{r})$ are mutually conjugate, through a Fourier-transform. Thus, an image of the sample can be reconstructed by applying an inverse Fourier transformation on the k-space representation of the acquired signal, according to:

$$\rho(\vec{r}) \propto \int_K S(\vec{k})\, e^{+i\,2\pi\vec{k}\cdot\vec{r}}\, d^3k \tag{1.44}$$

The Principle of Spatial Encoding

If a magnetic field gradient $\vec{G}(t)$ is applied after the excitation of the sample, the k-space is traversed in the conjugate direction of the gradient starting from the k-space center, as indicated by equation (1.43). The distance traveled in the k-space is linearly proportional to the zeroth moment of $\vec{G}(t)$. This means that the MR signal acquired during or after application of a magnetic field gradient corresponds to a specific location in the k-space. In order to reconstruct a MR image, several k-space points must be acquired, depending on

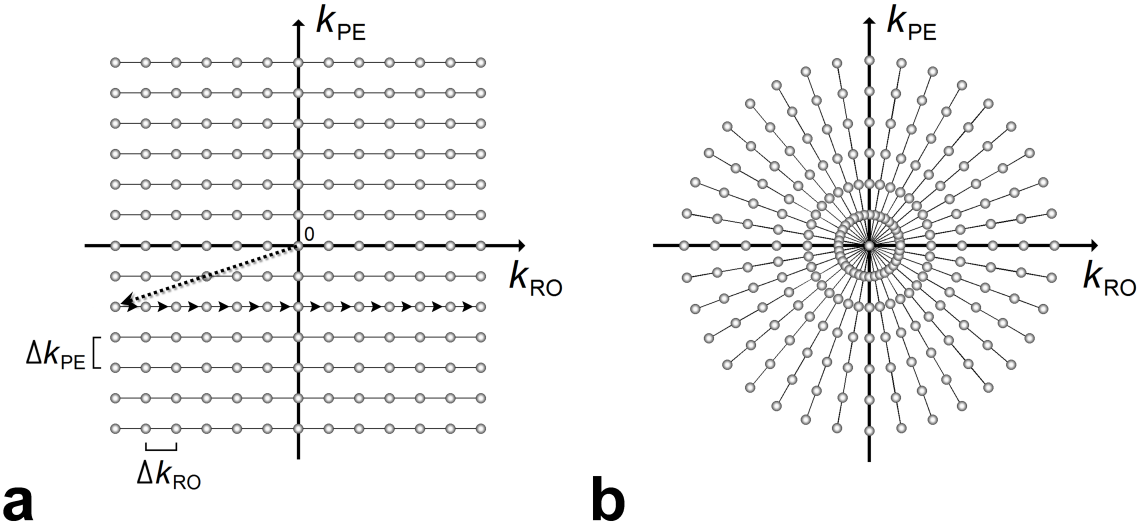

Figure 1.6: Example of Cartesian (a) and radial (b) coverage of a 2D k-space. Signal acquisition in the presence of G_{RO} allows to acquire one line of the k-space, as indicated by the arrows. The tip of each arrow corresponds to a sampled point. The dotted line indicates the initial values of k_{RO} and k_{PE}, which are regulated by the zeroth moments of the PE and of the prefocusing gradients, as shown later in Figure 1.12.

the desired resolution and dimensionality of the image. The number of k-space dimensions corresponds to the number of dimensions of the desired image such that to spatially resolve 2 or 3 dimensions, a series of respectively 2 or 3 gradients must be applied in orthogonal directions (2D or 3D imaging).
There are several strategies to sample the k-space. This represents an important aspect of MRI, as it has a direct impact on the image properties and on the acquisition time. The simplest and most common strategy of k-space sampling is represented by the Cartesian grid, as shown in Figure 1.6 a. Another interesting approach is radial sampling, as shown Figure 1.6 b.
When the signal is sampled in the presence of a gradient which has a constant amplitude in time, the acquired k-space points are equally distributed on a k-space line, as indicated by the arrows in Figure 1.6 a. Such gradient is called Read-Out (RO), or frequency-encoding, gradient. The RO gradient has the effect to spatially modulate the precession frequency as shown in Figure 1.7 b. The k-space in the conjugate RO direction k_{RO} is discretized by the ADC. The distance between two neighboring k-space points is:

$$\Delta k_{\mathrm{RO}} = \frac{\gamma}{2\pi} G_{\mathrm{RO}} \Delta t_{\mathrm{RO}} \tag{1.45}$$

where Δt_{RO} is the sampling step of the ADC, which is also called "d-well time", while G_{RO} is the amplitude of the RO gradient. Radial sampling of the k-space can be performed by acquiring several k-space lines while circularly changing the spatial direction of the RO gradient.

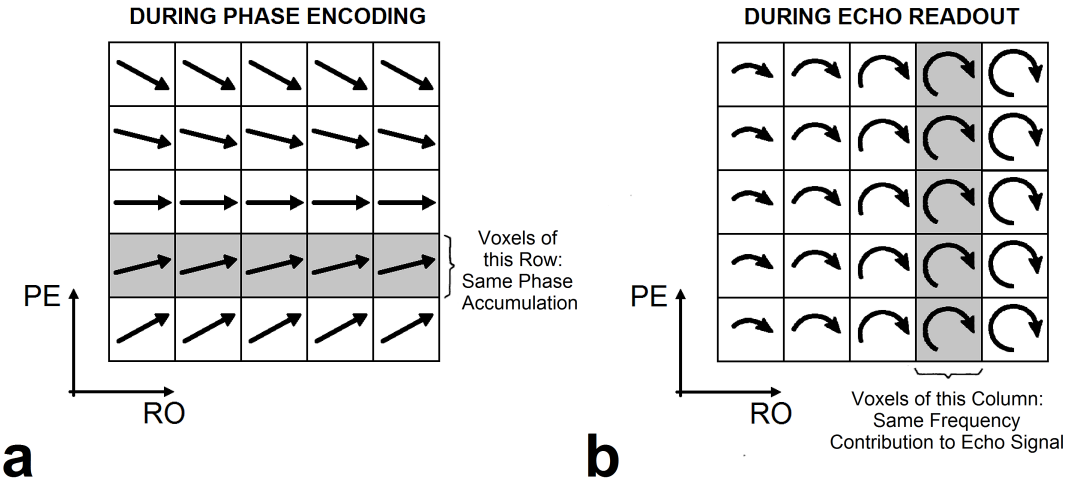

Figure 1.7: Graphical representation of the spatial encoding principle. a) After the application of a phase-encoding gradient G_{PE}, a phase accrual is induced in the transverse magnetization, depending on its spatial position in the PE direction. b) During the application of a read-out gradient G_{RO}, the precession frequency of the transverse magnetization depends on its spatial position in the RO direction. Reproduced with permission from reference [82], with adaptions.

Alternatively to radial sampling, Cartesian coverage of the k-space can be achieved by applying a second gradient, called Phase-Encoding (PE) gradient, before actual signal sampling. The directions of the PE and RO gradients must be orthogonal to each other. The effect of the PE gradient is to generate a spatial modulation of the phase of the magnetization in the direction of the gradient, as shown in Figure 1.7 a. The k-space in the corresponding conjugate direction k_{PE} is discretized as follows:

$$k_{\mathrm{PE}} = \frac{\gamma}{2\pi} \int_0^{\tau_{\mathrm{PE}}} G_{\mathrm{PE}}(t')dt' \tag{1.46}$$

where G_{PE} is the amplitude of the PE gradient and τ_{PE} is its duration. This means that by properly changing the zeroth moment of the PE gradient it is possible to acquire different rows in the Cartesian grid of Figure 1.6 a. In order to completely sample the k-space, several k-space lines must be acquired with different values of k_{PE}.
Reconstruction of a 3D image requires the acquisition of a three-dimensional k-space. The third dimension $k_{3\mathrm{D}}$ can be sampled with the application of a second phase-encoding gradient of amplitude $G_{3\mathrm{D}}$ in the direction orthogonal to both the RO and the PE gradients. $G_{3\mathrm{D}}$ and G_{PE} can be applied simultaneously before signal acquisition. Because the total acquisition time of a MRI scan is proportional to the number of acquired k-space lines, 3D imaging typically requires much longer acquisition times than 2D imaging.

Image Properties

Due to the discrete nature of the k-space, the Fourier-transform that is commonly used for image reconstruction is discretized as well. Therefore, the MR image can be obtained from an inverse Fast Fourier-Transform (FFT) of the k-space. In the case of 2D imaging, this is given by:

$$\rho\left(r_{\mathrm{RO}}, r_{\mathrm{PE}}\right) \propto \sum_{n=0}^{N_{\mathrm{RO}}-1} \sum_{m=0}^{N_{\mathrm{PE}}-1} S\left(n\Delta k_{\mathrm{RO}}, m\Delta k_{\mathrm{PE}}\right) e^{i\,2\pi(n\Delta k_{\mathrm{RO}} r_{\mathrm{RO}} + m\Delta k_{\mathrm{PE}} r_{\mathrm{PE}})} \tag{1.47}$$

where N_{RO} and N_{PE} indicate the number of acquired k-space points in the RO and PE directions, respectively. The MR image can be thought as a matrix of cubical voxels which constitute a Cartesian grid. r_{RO} and r_{PE} in equation (1.47) are the spatial coordinates of the centers of the image voxels. The properties of the reconstructed image and those of the k-space are correlated through the properties of the Fourier-transform. These can be resumed as follows:

1. The number of image voxels (N) in each spatial direction is equal to the number of acquired points in the corresponding k-space direction.

2. The distance in space displayed by the MR image in each direction, which is called Field-Of-View (FOV), is related by means of the following equation to the distance between neighboring points (Δk) in the corresponding k-space direction:

$$\mathrm{FOV} = \frac{2\pi}{\Delta k} \tag{1.48}$$

this is also known as Nyquist criterion.

3. The size of a voxel (Δr) in each spatial direction is given by:

$$\Delta r = \frac{\text{FOV}}{N} = \frac{2\pi}{k_{\max}} \tag{1.49}$$

where $k_{\max} = \Delta k N$. The voxel size is also known as spatial resolution. To obtain a higher spatial resolution (or a smaller voxel size) in a given spatial direction, a larger number of k-space points must be acquired in the corresponding conjugate direction.

4. Information about image features that vary with low spatial frequencies, such as the image contrast, is provided by the central region of the k-space, while information about small details is given by the outer part of the k-space.

Slice Selection

Alternatively to the excitation of the whole volume, MRI offers also the possibility to selectively excite the magnetization in a slice of the sample. In this case, only the MR signal that is generated within the slice is detected, such that the reconstruction of a 2D image would depict the spin density distribution on the plane of the slice. This is of great advantage for some MR applications because of the much shorter acquisition times which are normally required by 2D imaging techniques, in comparison to 3D imaging.
Slice selection, like spatial encoding, is based on the application of magnetic field gradients, as proposed by Garroway et al. in 1974 [18]. When a gradient is applied, the resonance frequency varies linearly in space along the direction of $\vec{G}$, while it remains constant over the orthogonal planes, as indicated by equation (1.39). Slice selection is achieved by applying a magnetic field gradient, called Slice-Selection (SS) gradient, simultaneously with a proper RF-pulse.

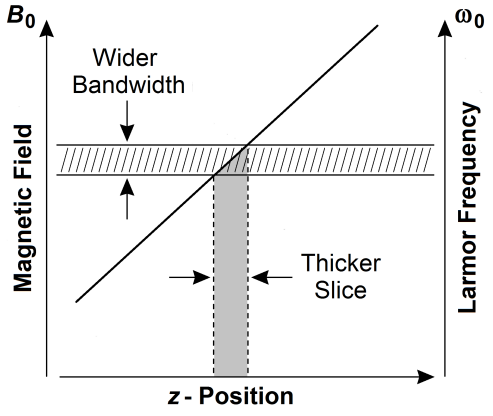

Figure 1.8: Representation of the frequency and bandwidth required by a RF-pulse for slice-selective excitation. The position and the thickness of the excited slice are linearly proportional to the frequency and bandwidth of the RF-pulse, respectively. Reproduced with permission from reference [82].

The time course of the RF-pulse, or pulse shape, defines the spatial profile of the slice. For example, in order to obtain a uniform slice profile, the resonance frequencies within a given interval of width $\Delta\omega$ must be uniformly excited. For small flip-angles ($\alpha < 10°$) the slice profile is approximated by the Fourier-transform of the RF-pulse shape [89]. Hence, a uniform slice profile can be achieved by means of the so called SINC-pulse. Its pulse-shape is given by:

$$B_1(t) \propto \text{sinc}\left(\frac{\Delta\omega}{2}t\right) \tag{1.50}$$

which represents the Fourier-transform of a boxcar-function of width $\Delta\omega$. Because the RF-pulse must have a finite duration, the SINC-pulse is usually truncated in time. Therefore, the corresponding slice profile cannot be a perfect box-function, as shown in Figure 1.9. Due to the linear relationship between resonance frequency and spatial position in the presence of the SS gradient, the slice thickness Δr_{SS} and the position of the slice center r_{SS} are respectively given by:

$$\Delta r_{SS} = \frac{\Delta\omega}{\gamma G_{SS}} \tag{1.51}$$

$$r_{SS} = \frac{\omega_{RF}}{\gamma G_{SS}} \tag{1.52}$$

where G_{SS} is the amplitude of the SS gradient and ω_{RF} is the frequency of the RF-pulse. In MRI, several RF-pulse shapes are used, which are specifically designed for different applications. For a more detailed description about RF-pulses, the interested reader is referred to references [73, 89].

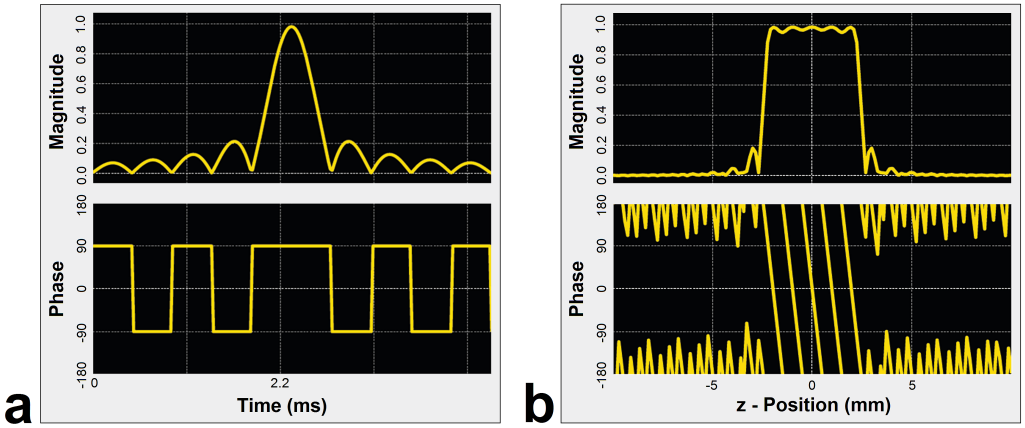

Figure 1.9: a) Timing of a SINC-pulse truncated to five lobes. b) Slice profile obtained by applying the same pulse together with a gradient of 10 mT/m. Due to the truncation, the slice profile is not a perfect box-function. In particular, a typical ringing phenomenon can be observed in proximity of the edges. Furthermore, spin dephasing in the SS direction can be observed. This effect can be overcome by the application of a gradient called refocusing gradient directly after the excitation, as shown later in Figure 1.12. Figure generated with SpinBench (Heartvista Inc., http://www.heartvista.com/spinbench/).

MRI Hardware

A MRI scanner mainly consists of hardware components which generate static or variable magnetic fields and of a signal detecting system. Most of these components are electronically controlled by a console. A detailed description of the hardware components of a MR scanner is out of the scope of this thesis and can be found in reference [79]. A simplified scheme of an MRI scanner is shown in Figure 1.10. Its basic components are:

- The **main magnet**. Its role is to generate the static magnetic field $\vec{B}$ with a possibly uniform distribution throughout the volume of the sample. Depending on the application, permanent, resistive or superconductive magnets may be used [79]. Nowadays, most clinical MRI scanners are made of superconductive material and have field strengths of either 1.5 or 3.0 T. Also the geometry of the magnet is flexible. However, most magnets rely on a cylindrical geometry. The direction of the static magnetic field defines the z-direction which is used as reference for the coordinates system in MRI. In cylindrical magnets, this corresponds to the main axis of the cylinder. The main magnet is often equipped with shim coils of conductive material. Their role is to compensate possible spatial inhomogeneities of the static magnetic field.

- The **gradient coils**. Their role it to generate a linear magnetic field in space, which is superimposed upon the static magnetic field. They typically consist of three systems of coils, which generate the transverse (G_x and G_y) and longitudinal (G_z) magnetic field gradients. They are usually made of conductive material and can be dynamically switched on and off during the MR acquisition. The typical gradient strengths used in MRI range between 10 and 100 mT/m.

- The **RF-coils**. RF-coils are used to either generate RF-pulses or to detect the MR signal. Some RF-coils can be used for both applications. Usually, RF-coils are specifically designed to operate at a certain frequency and present a fixed geometry. TX coils are driven by a transmitter, which is responsible for the shape, duration

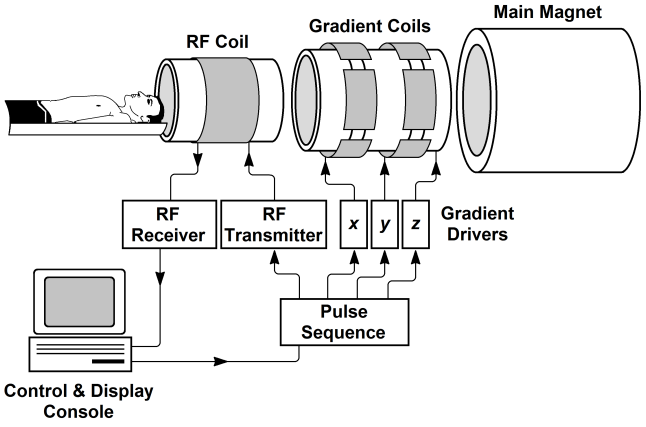

Figure 1.10: Scheme of the basic hardware components of a MRI scanner. Reproduced with permission from reference [82], with adaptions.

and amplitude of the RF-pulses. RX coils are connected to an electronic acquisition chain, which allows for signal sampling and amplification. Modern RX coils consist of multiple receive elements and corresponding signal acquisition channels, which can be separately controlled. Thereby, the sensitivity of each element of the coil is limited to a specific region of the sample, thus offering advantages in terms of SNR and acquisition speed, as further discussed in Chapter 3.

Coordinates System in MRI

Spatial encoding gradients (RO, PE and 3D) and slice-selective gradients (SS) can be applied in any direction in space, such that MR images with any arbitrary orientation can be obtained. This can be achieved by properly combining G_x, G_y and G_z. In most cases, however, MR images are acquired in either the transverse, the coronal or the sagittal orientations. These are defined from the anatomical coordinates system that is universally used in medicine to refer to image orientation, as shown in Figure 1.11. The three coordinate axes of the anatomical coordinates system correspond to the Anterior-Posterior (A-P), Left-Right (L-R) and Head-Feet (H-F) directions. The H-F direction is also known as Superior-Inferior (S-I) direction.

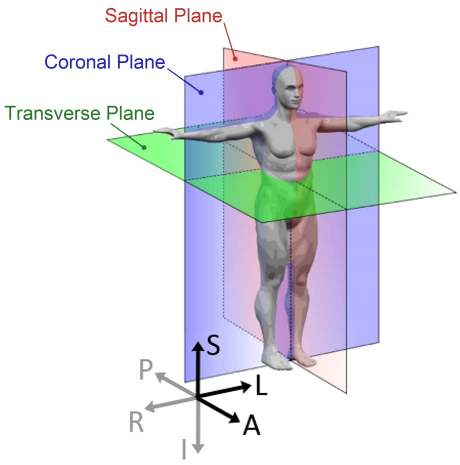

Figure 1.11: Representation of the anatomical coordinates system with the three reference planes (transverse, coronal and sagittal) and the six fundamental directions (anterior-posterior, left-right and superior-inferior). Reproduced from reference [90] in agreement with license [91].

1.3 Basic Pulse Sequences

A typical MR acquisition is based on the application of a series of RF-pulses, magnetic field gradients and signal acquisition events. Their chronological combination in time is called pulse sequence. The purpose of a pulse sequence is to manipulate the magnetization

in order to generate the desired image contrast and, at the same time, to sample the k-space. The most common image contrasts are: ρ, T_1, T_2 and T_2^* weighting, which are used to highlight the differences of the corresponding contrast parameters among tissues. At present, a large number of pulse sequences exist, which allow to generate different kinds of image contrasts and to address several clinical needs. In this regard, two main categories of pulse sequences can be identified: Gradient-Recalled Echo (GRE) and Spin-Echo (SE) based sequences. In general, the basic parameters of a pulse sequence are:

- the **echo time** (TE), which represents the time interval between excitation and signal acquisition;
- the **repetition time** (TR), which is the time interval between two consecutive excitation pulses.

These parameters have a direct impact on the contrast of the MR image and on the total acquisition time, as further discussed below.

Gradient-Recalled Echo

The term GRE refers to a group of pulse sequences, in which the excitation RF-pulse is directly followed by a series of spatial encoding gradients and signal acquisition. A schematic timing diagram of the GRE sequence is shown in Figure 1.12 for both 2D and 3D imaging.
The RF-pulse flips the magnetization from the longitudinal axis by an angle α. In case of 2D imaging, the excitation is performed by a slice-selective RF-pulse, as already discussed. The SS gradient is typically followed by a further gradient lobe, called refocusing gradient, which allows to recover the dephasing of the transverse magnetization which is accumulated between the peak and the end of the RF-pulse. Because this dephasing is due to the presence of the SS gradient itself, the SS and the refocusing gradients must have opposite polarities.
Signal sampling is performed by the ADC, simultaneously with the application of the RO gradient. This allows for the acquisition of a k-space line as indicated by the arrows in Figure 1.6 a. In order to cover the negative region of the k-space in the RO direction, a further gradient lobe, called prefocusing gradient, is applied before signal acquisition. This gradient must have opposite polarity with respect to the RO gradient. The position of the acquired line in the PE direction of the k-space is regulated by the zeroth moment of the PE gradient lobe, which is interposed between excitation and signal acquisition. In case of 3D imaging, a 3D phase-encoding gradient is additionally applied.
In order to acquire a complete MR-image, it is necessary to repeat the scheme of Figure 1.12 several times. At each repetition, a different k-space line is sampled. This is achieved by varying the zeroth moment of the phase-encoding gradients G_{PE} and, if required, G_{3D}. The total acquisition time (TA) of a GRE acquisition is proportional to the number of acquired k-space lines and is given by:

$$\mathrm{TA} = \mathrm{TR} \times N_{\mathrm{PE}} \times N_{\mathrm{3D}} \tag{1.53}$$

where N_{PE} and N_{3D} indicate the number of acquired lines in the PE and 3D directions respectively. In case of 2D imaging, $N_{\mathrm{3D}} = 1$.

In a GRE sequence, the signal amplitude decay and consequently the image contrast are dictated by T_2^*, as no actions are taken to compensate for signal dephasing induced by static magnetic field inhomogeneities. This is expressed by:

$$s(\mathrm{TE}) \propto \exp\left(-\frac{\mathrm{TE}}{T_2^*}\right) \tag{1.54}$$

where TE is the time distance between the peak of the RF-pulse and the center of the signal acquisition window. This means that stronger T_2^*-weighting is achieved with longer TEs.

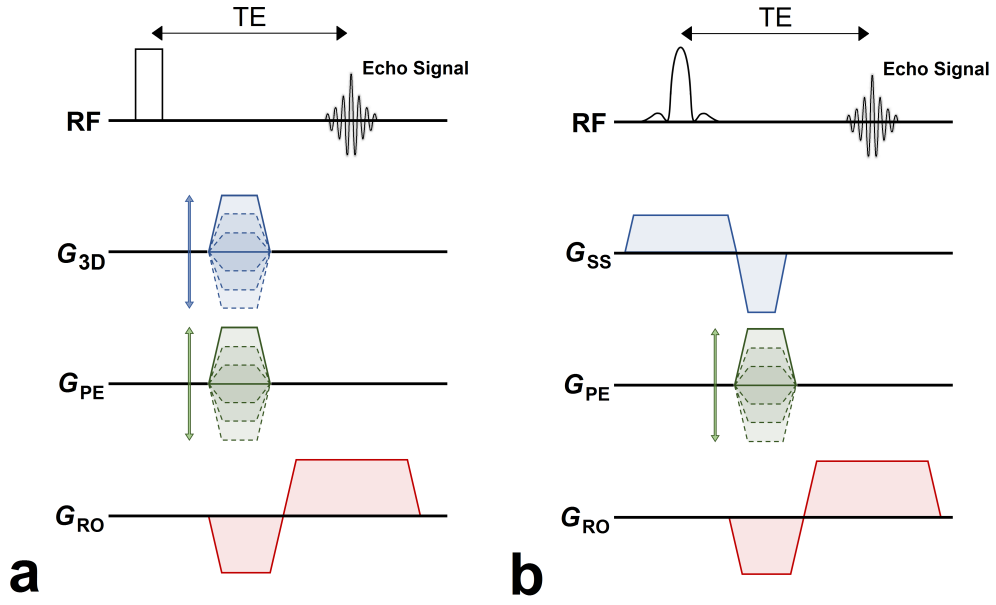

Figure 1.12: Pulse diagrams of 3D (a) and 2D (b) GRE sequences. At each repetition, the zeroth moment of the phase encoding gradients (G_{PE} and G_{3D}) is varied in order to cover the whole k-space, as it has been described in Figure 1.6 a. The negative gradient lobe in the RO direction is the prefocusing gradient and is required to collect the data in the negative region of k_{RO}. In the 2D sequence variant, excitation is performed by a slice-selective RF-pulse. The negative gradient lobe in the SS direction is the refocusing gradient and allows to recover the dephasing of the transverse magnetization which occurs during the excitation, as it has been shown in Figure 1.9 b. Reproduced with permission from reference [82], with adaptions.

Steady-State Sequences

A complete recovery of the magnetization to its equilibrium is obtained at a time $t \gg T_1, T_2$ after excitation. Because $T_1 > T_2$, it can be assumed that a full recovery is achieved for $\mathrm{TR} \geq 5T_1$. In the human body, T_1 can assume values as long as several seconds. Therefore, acquisition times of the order of a few hours would be required to acquire a single image according to equation (1.53). This is not suitable for the clinical routine. To overcome this

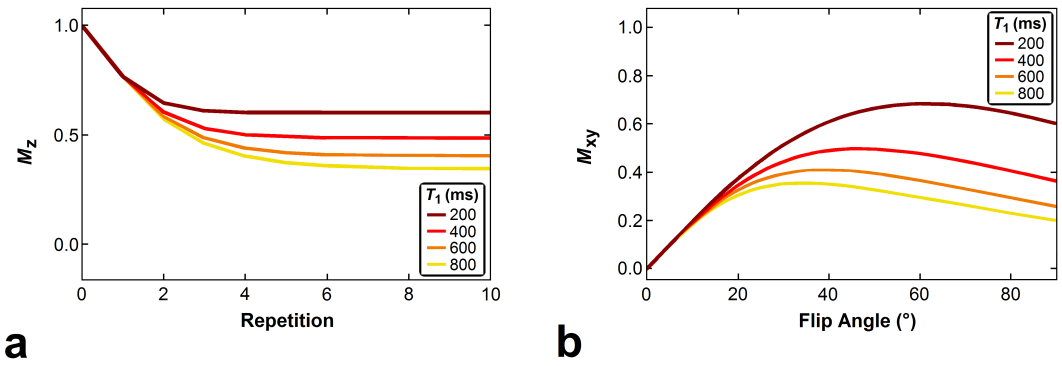

Figure 1.13: a) Plot of the longitudinal magnetization immediately after the excitation $M_z(n)$ as a function of the repetition number n, for different values of T_1. The flip-angle $\alpha = 40°$ and the repetition time TR = 200 ms are common to all curves. A steady-state is reached for $n_{SS} \approx 10$. b) Plot of the transverse magnetization at the steady-state M_{xy}^{SS} as a function of the flip-angle, for different values of T_1. The repetition time TR = 200 ms and the echo time TE = 0 ms are common to all curves. Figure generated with SpinBench (Heartvista Inc., http://www.heartvista.com/spinbench/).

problem, fast sequences called steady-state sequences have been developed in the past.
The basic idea behind steady-state sequences is to exploit the residual magnetization that is still available before a complete recovery of the magnetization. Several steady-state sequences have been proposed. One of the most commonly used for clinical applications is the FLASH sequence introduced by Haase et al. in 1986 [21]. In this section, the principle of spoiled steady-state imaging [92], which represents the basis of the FLASH sequence, is briefly described. For a more detailed description of steady-state imaging, the interested reader is referred to references [73, 93, 94].
Spoiled steady-state imaging is based on the application of a gradient, called spoiling gradient, at the end of each sequence repetition. This gradient produces a dephasing of the transverse magnetization similarly to the T_2^* decay, which allows to start the next repetition with a fully dephased transverse magnetization. Consequently, the residual transverse magnetization does not play any role on the signal formation mechanism, which is fully determined by the residual longitudinal magnetization available before each excitation.
If the repetition time is too short to allow a complete recovery, the longitudinal magnetization would decrease at each repetition, with values given by (see Figure 1.13 a):

$$M_z\left[(n+1)\,\mathrm{TR}\right] = M_z\left(n\,\mathrm{TR}\right)\cos\alpha\, e^{-\mathrm{TR}/T_1} + M_0\left(1 - e^{-\mathrm{TR}/T_1}\right) \tag{1.55}$$

where n is the index of the repetition.
A steady-state value for M_z and M_{xy} is reached when $n > n_{SS}$, with $n_{SS} \approx 10 - 200$ repetitions, depending on α, T_1 and TR. The steady-state values, for both the longitudinal and the transverse magnetization are:

$$M_z^{SS} = M_0\,\frac{1 - e^{-\mathrm{TR}/T_1}}{1 - e^{-\mathrm{TR}/T_1}\,\cos\alpha} \tag{1.56}$$

$$M_{xy}^{SS} = M_z^{SS}\sin\alpha\, e^{-\mathrm{TE}/T_2^*} \tag{1.57}$$

Equation (1.56) states that $M_z^{\mathrm{SS}} < M_0$. This phenomenon is known as saturation of the longitudinal magnetization and indicates a loss of signal amplitude with respect to a non-steady-state sequence. This is, in general, the cost of faster imaging when using steady-state sequences.
The main characteristic of steady-state sequences is the introduction of T_1-weighting in the signal, which is expressed by the dependence of M_z^{SS} on the ratio TR/T_1. This means that the use of short TRs, relatively to T_1, introduces a T_1 contrast in the image. The smaller the ratio TR/T_1, the lower the signal amplitude and the stronger the T_1-weighting. Equation (1.56) also demonstrates a dependence of the signal amplitude on the flip-angle α, which indicates that the extent of T_1-weighting increases with the flip-angle. As demonstrated by Figure 1.13 b, the signal amplitude presents a maximum value at a certain flip-angle α_{E} given by:

$$\alpha_{\mathrm{E}} = \arccos\left(e^{-\mathrm{TR}/T_1}\right) \tag{1.58}$$

which is called Ernst-angle.

Spin-Echoes

The SE phenomenon discovered by Erwin Hahn in 1950 [23] is a signal formation mechanism that allows to recover the dephasing of the transverse magnetization which is induced by static magnetic field inhomogeneities. This effect is responsible for the relaxation time component T_2' in equation (1.29).
The key approach for the formation of a spin-echo (or Hahn-echo) is the use of a 180°-pulse, which is called refocusing pulse. A schematic diagram of the SE pulse sequence is given in Figure 1.14 a. The initial 90°-pulse flips the longitudinal magnetization into the transverse plane. The refocusing pulse is placed in the middle between the excitation pulse and the signal acquisition window, at a time distance TE/2 from both of them. During the first time period TE/2, the transverse magnetization dephases, due to both spin-spin interactions and static magnetic field inhomogeneities. The attenuation of the transverse magnetization during this time period is dictated by T_2^*. When the refocusing pulse is applied, the phase of the transverse magnetization is reversed. During the second time period TE/2, the dephasing caused by the presence of static magnetic field inhomogeneities is recovered, as the phase shifts accumulated before and after the application of the refocusing pulse are equal and opposite. Thus, a fully refocused signal is formed at time distance TE from the application of the excitation pulse, as shown in Figure 1.14 b. The dephasing which is induced by spin-spin interactions, instead, is further accumulated during the whole TE period. Therefore, the signal amplitude decay at TE is dictated by T_2, such that:

$$s(\mathrm{TE}) \propto \exp\left(-\frac{\mathrm{TE}}{T_2}\right) \tag{1.59}$$

The SE pulse sequence can be used for several purposes in both MRI and NMR spectroscopy. The principle of spatial encoding for a SE sequence is the same as for a GRE sequence. However, it must be considered that the zeroth gradient moments which are accumulated before and after the application of the refocusing pulse have opposite signs, like the phase of the transverse magnetization. This means that all gradients applied after the refocusing pulse must have opposite polarity, with respect to the polarity that they

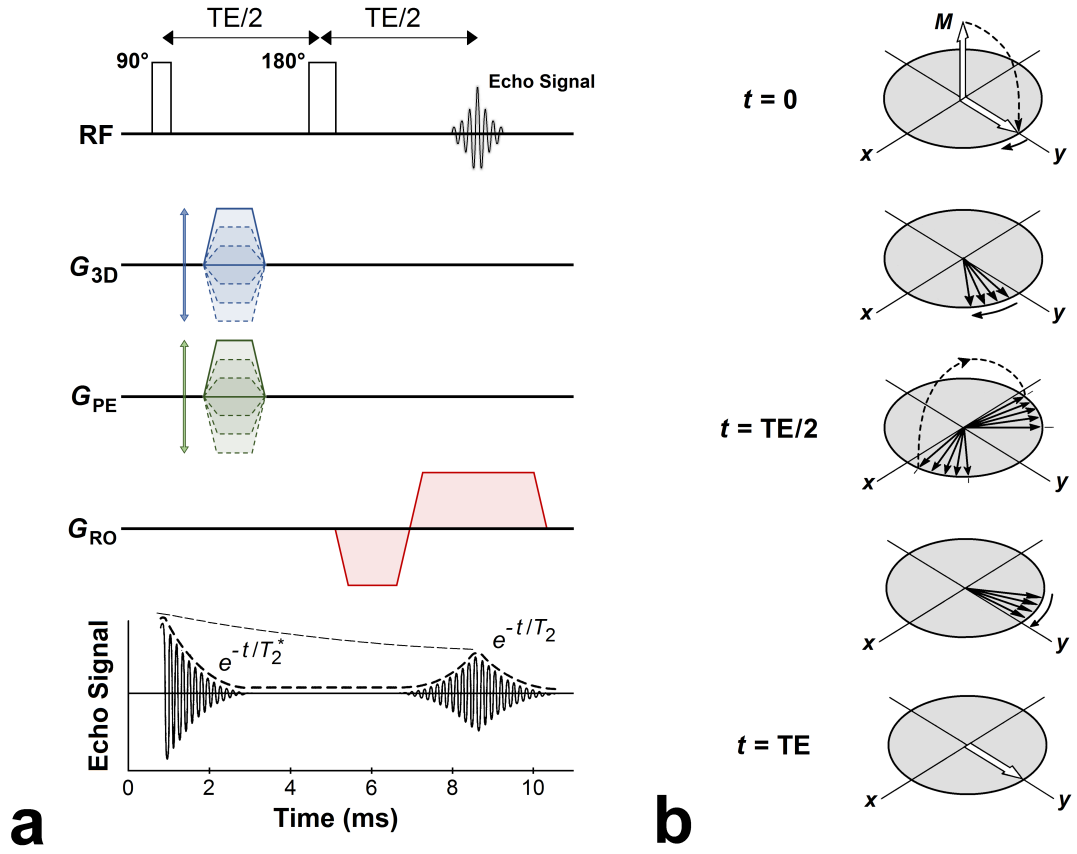

Figure 1.14: a) Pulse diagram of a SE sequence. b) Time evolution of components of the transverse magnetization, which have different precession frequencies due to the presence of static magnetic field inhomogeneities. Before the refocusing pulse the transverse magnetization dephases. The refocusing pulse flips the magnetization by 180°. This starts to rephase by accumulating an opposite phase shift. At the echo time TE a fully refocused signal is formed. Reproduced with permission from reference [82], with adaptions.

would normally have in a GRE sequence. A pair of gradient lobes called crushing gradients are normally placed at each side of the refocusing pulse, in order to cancel the unwanted signal contribution which is due to the FID of the pulse itself. The SE pulse sequence can be used for both 2D and 3D imaging. For the 2D variant, the refocusing and the excitation pulses are usually slice-selective.

Stimulated-Echoes

A further signal formation mechanism is the so called stimulated-echo. This refers to any kind of signal echo which is generated by the magnetization that after an initial excitation is first stored in the longitudinal axis and then re-excited [95]. The formation mechanism of a stimulated-echo requires the application of at least three RF-pulses, as shown in Figure 1.15. The first RF-pulse flips the magnetization away from the longitudinal

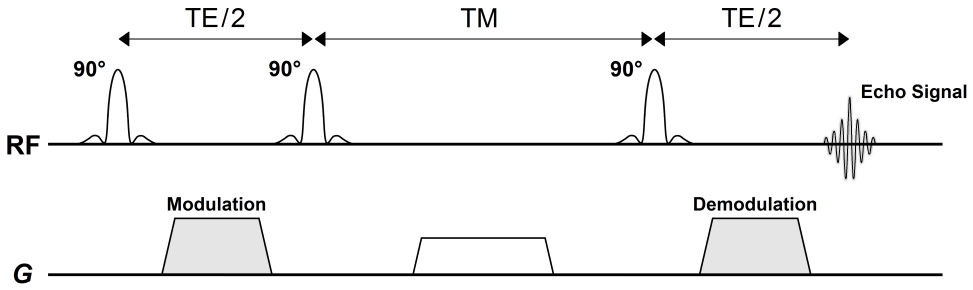

Figure 1.15: Pulse sequence diagram of the STimulated Echo Acquisition Mode (STEAM).

axis. The excited transverse magnetization is subsequently dephased by the application of a gradient lobe called modulation gradient (shaded in dark gray). This generates a spatially dependent phase-modulation throughout the sample. After a time period TE/2 the second RF-pulse stores part of the excited magnetization back in the longitudinal axis. The phase-modulation which has been generated by the modulation gradient is preserved and transferred to the longitudinal magnetization. During the subsequent middle time (TM) interval the longitudinal magnetization is subject to T_1 relaxation, while the residual transverse magnetization is fully dephased by the application of a crushing gradient. The available longitudinal magnetization at the end of the time interval TM is finally refocused by the third RF-pulse in combination with a demodulation gradient lobe which has same zeroth moment as the modulation gradient. A stimulated-echo is produced after a time interval TE/2 from the application of the third RF-pulse. The crushing gradient and the demodulation gradient also have the role to cancel the signal contributions deriving from the FIDs of the second and the third RF-pulses respectively. During the two TE/2 periods, the transverse magnetization is subject to T_2^* relaxation. However, because the phase of the magnetization is fully refocused at the time of signal acquisition, the overall signal amplitude decay is dictated by T_2.
In contrast to the SE, the stimulated-echo carries information which regards not only the transverse but also the longitudinal relaxation, due to the T_1 relaxation during the time interval TM. This is expressed by the following signal amplitude attenuation:

$$s(\mathrm{TE}, \mathrm{TM}) \propto \exp\left(-\frac{\mathrm{TE}}{T_2}\right) \exp\left(-\frac{\mathrm{TM}}{T_1}\right) \tag{1.60}$$

One of the characteristics of the stimulated-echo is that only a fraction of the excited magnetization actually contributes to the acquired signal, as the magnetization which is dephased by the crushing gradient during the interval TM is not refocused. Even though RF-pulses with any arbitrary flip-angles can lead to the formation of a stimulated-echo, the maximum signal amplitude is obtained with three 90°-pulses. In this case, approximately half of the initially excited magnetization contributes to the signal amplitude of the stimulated-echo.
One of the first MRI applications that made use of stimulated-echoes is the STimulated Echo Acquisition Mode (STEAM) pulse sequence, which was proposed by Frahm et al. in 1985 [96, 97]. With this technique, multiple stimulated echoes are repeatedly acquired

after the time interval TM by means of a series of RF-pulses with small flip-angles, each followed by a demodulation gradient. Thereby, several k-space lines are filled with a single excitation pulse.

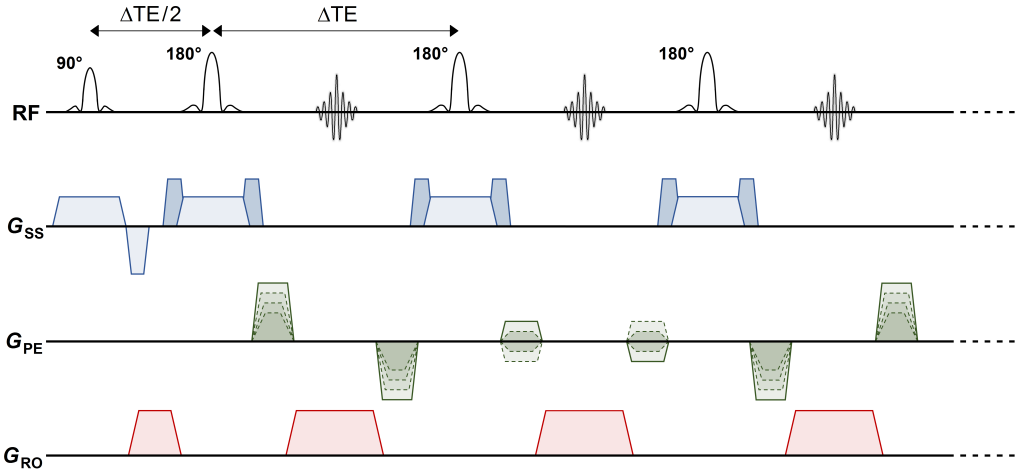

Figure 1.16: Pulse diagram of a 2D TSE sequence.

The TSE Sequence

The TSE sequence was introduced by Hennig et al. in 1986 [22] and represents a variant of the SE sequence. The basic idea of this sequence is to acquire several k-space lines with a single excitation and multiple refocusing pulses. This way, a smaller number of repetitions is required to fill the whole k-space and faster image acquisition is achieved. The TSE sequence can be used for both 2D and 3D imaging. A timing diagram of the 2D variant of the TSE sequence is shown in Figure 1.16.
Excitation with a 90°-pulse is followed by a train of refocusing pulses called pulse-train. The refocusing pulses produce a series of signals called echo-train, which are repeatedly acquired at the middle times between two consecutive pulses. Each echo is distinctively phase-encoded, in order to fill different k-space lines. The time distance between two consecutive refocusing pulses (ΔTE), which is called inter-pulse time (or inter-echo time), is uniform throughout the whole pulse-train and is equal to the time distance between two consecutive echoes. ΔTE is twice the time distance between the excitation pulse and the first refocusing pulse. With respect to the conventional SE sequence, the acquisition time is reduced by a factor equal to the number of refocusing pulses, which is called Turbo-Factor (TF). TF is also equal to the number of echoes in one echo-train.

Signal Composition and the CPMG conditions
Generation of pure spin-echo signals with a TSE sequence is achieved only in the ideal case of refocusing pulses with exactly 180° flip-angle. In practice, however, the actual flip-angle often deviates from 180°, due to spatial inhomogeneities of the B_1 field and to imperfections of the slice profile of the refocusing pulses. For this reason, at each refocusing pulse

the magnetization can be 1) partially refocused, 2) partially tipped into the longitudinal axis and 3) partially left intact, such that the signal generated with a TSE sequence is a complex mixture of multiple components. These are:

- primary spin-echoes, which are generated by direct refocusing of the transverse magnetization at each refocusing pulse;
- secondary spin-echoes, which represent the transverse magnetization that is actually refocused after several refocusing pulses;
- stimulated-echoes, which consist in the magnetization that is first returned to the longitudinal axis by imperfect refocusing and then re-excited by a subsequent refocusing pulse.

In general, each of these signal components can have different phase. Moreover, their temporal positions do not necessarily coincide. When echoes with phase inconsistencies overlap, they can cause constructive or destructive signal interference phenomena, which would result in oscillations of the signal pathway along the echo-train. This would lead to image artifacts, as further described in the next section.
In order to ensure that both spin-echoes and stimulated-echoes only occur at the signal sampling positions (mid-point between two refocusing pulses) and with identical phases, the so called Carr-Purcell-Meiboom-Gill (CPMG) conditions must be fulfilled [68, 69]. These consist in the following two criteria:

1. the RF-phase of the refocusing pulses must be constant throughout the whole refocusing pulse-train and shifted by $\pi/2$ with respect to the RF-phase of the excitation pulse;
2. the phase accumulated by the magnetization between any two consecutive refocusing pulses must be uniform throughout the pulse-train and half compared to the phase accumulated between the excitation and the first refocusing pulses.

Fulfillment of the CPMG conditions would guarantee that spin-echoes and stimulated-echoes constructively interfere, such that strong signal oscillations along the echo-train are avoided.
Because the phase accrual of the magnetization depends on both the sequence timing, through equation (1.36), and the zeroth moments of the spatial encoding gradients, through equations (1.39) and (1.41), the second CPMG condition has implications on both sequence timing and gradient moments. In brief, the second CPMG condition states that both 1) the inter-pulse time and 2) the zeroth moments of the gradients applied between two consecutive refocusing pulses must be constant throughout the whole refocusing pulse-train. Furthermore, they must respectively correspond to: 1) half the time distance and 2) half the zeroth gradient moments, which are applied between the excitation pulse and the first refocusing pulse.
Due to the phase reversal action of the refocusing pulses, as already discussed for the conventional SE sequence, the polarity of the RO gradients must be identical for all lobes in the sequence. In order to fulfill the second CPMG condition, the prefocusing gradient lobe must be applied only once, between the excitation pulse and the first refocusing pulse, and with the same polarity as the actual RO gradients.

The PE gradients must be applied after each refocusing pulse, before signal acquisition. Rewinding gradients with the same zeroth moment as the PE gradients but with opposite polarity must be applied after signal acquisition, in order to fulfill the second CPMG condition.
In the case of 2D imaging, the refocusing pulses are slice-selective and, therefore, they are applied simultaneously with SS gradients. These gradients are usually combined with a pair of crushing gradients placed at each side of the refocusing pulse, in order to cancel unwanted FID signals, which are generated by the refocusing pulses due to deviations of the flip-angle from the ideal 180°. The crushing gradients and the slice selection gradients must have a constant zeroth moment throughout the whole pulse-train.

k-Space Reordering and the Point Spread Function
During the echo-train, the signal amplitude decays approximately like e^{-t/T_2}. This means that each phase-encoded line presents a different signal amplitude, due to the different T_2-weighting. This has the following implications on the image [98]:

1. Because the image contrast is mainly determined by the central k-space lines, the TE in a TSE sequence is usually defined as the time distance between excitation and acquisition of the k-space central line. The value of TE in a TSE sequence is regulated by ΔTE, TF and by the reordering scheme which is used for the acquisition of the phase-encoded lines. This defines how the different echoes in the echo-train are assigned to different positions in the k-space. The most common schemes are centric and linear reordering.
   With centric reordering, the k-space center is acquired at the beginning of the echo-train. The outer lines are acquired by progressively traveling the k-space towards the peripheral regions with an alternating pattern between the negative and positive regions. In this case, TE = ΔTE and the image contrast presents less T_2-weighting but larger signal amplitude. With linear reordering, the k-space lines are acquired starting from one end of the k-space and progressively moving towards the other end, such that the k-space center is acquired later in the echo-train. In this case, TE = ΔTE $\cdot$ TF/2 and the image contrast presents stronger T_2-weighting but lower signal amplitude.

2. The T_2 decay acts as a weighting function on the k-space lines which are acquired at different positions in the echo-train. This is given by:

$$W\left(k_{\mathrm{PE}}\right) = \exp\left[-n\left(k_{\mathrm{PE}}\right)\frac{\Delta\mathrm{TE}}{T_2}\right] \tag{1.61}$$

   where $n(k_{\mathrm{PE}})$ is the index that indicates the position in the echo-train at which the line k_{PE} is acquired. This depends on the reordering scheme adopted.
   The acquired k-space can be thought as the multiplication of the actual k-space with $W(k_{\mathrm{PE}})$. From the properties of the Fourier-transform, the resulting image is the convolution of the ideal image with the Fourier-transform of $W(k_{\mathrm{PE}})$. This is called point spread function. Due to the spreading effect of the convolution, the T_2 decay typically results in image blurring.
   Each tissue has a different point spread function, due to the different T_2. Stronger blurring is produced by tissues with shorter T_2. Centric reordering results in more

blurring in comparison to linear reordering, due to the larger presence of short-lived signal components at shorter TEs as well as to the doubled time interval between the acquisitions of two adjacent k-space lines, which derives from the alternation between the positive and negative regions of the k-space.

The concept of point spread function does not only apply to the T_2 decay but also to other signal inconsistencies that can occur during the acquisition, due to other factors. Typical examples in a TSE acquisition are:

- Physiological motion. Due to the relatively long repetition times which are required to recover the longitudinal magnetization, signal inconsistencies among different repetitions (or inter-view inconsistencies) can be induced by physiological motion.
- Violations of the CPMG conditions. If the CPMG conditions are violated, the different echoes in the echo-train do not have the same phase and amplitude due to constructive and destructive interference, as already discussed (intra-view inconsistencies).

In these cases, the typical consequence of the point spread function is the generation of image artifacts, usually in the form of so called "ghosts".

Contrast	TR	TE
ρ	as long as possible	as short as possible
T_1	of the order of T_1	as short as possible
T_2 (T_2^*)	as long as possible	of the order of T_2 (T_2^*)

Table 1.4: General set of rules which should be used in order to optimize the image contrast. Reproduced with permission from reference [75].

Image Quality Parameters

The image quality in MRI is usually defined in terms of three parameters: SNR, spatial resolution and contrast [12, 99, 101, 100]. These are determined by the imaging parameters and other factors, as further described below:

1. The **SNR** is defined as the ratio between signal amplitude s and background noise σ_s. Neglecting the relaxation effects, equations (1.21) and (1.35) state that the detected signal amplitude in MRI is proportional to the static magnetic field strength, the gyromagnetic ratio, the proton density and the total imaged volume according to:

$$s \propto \rho \, \gamma^3 \, B_0^2 \, V \tag{1.62}$$

The noise is determined by random thermal fluctuations in the sample and in the receive coil electronics. At field strengths higher than 0.05 T the dependence of the noise on the field strength can be assumed to be linear, which means that [99]:

$$\mathrm{SNR} = \frac{s}{\sigma_s} \propto B_0 \tag{1.63}$$

2. The **spatial resolution** is defined as the size of the image voxels in all spatial dimensions ($\Delta r_{\mathrm{RO}} \times \Delta r_{\mathrm{PE}} \times \Delta r_{\mathrm{3D}}$). Because the ability to separate different objects in the image depends on both the signal amplitude and the noise, the parameter SNR/voxel is often used to define the smallest voxel size (or the highest image resolution) that allows to distinguish details in the image. In the image domain, the signal amplitude is proportional to the volume of the voxel, while the noise detected by the receiver is rescaled by the square root of the number of acquired samples ($N_{\mathrm{RO}} \times N_{\mathrm{PE}} \times N_{\mathrm{3D}}$). In addition to this, the noise is inversely proportional to $\sqrt{\Delta t_{\mathrm{RO}}}$, as the use of smaller values of the signal sampling step Δt_{RO} corresponds to an increase of the bandwidth of detected noise frequencies. Hence, if all the other imaging parameters are fixed, then [101]:

$$\frac{\mathrm{SNR}}{\mathrm{voxel}} \propto \Delta r_{\mathrm{RO}} \Delta r_{\mathrm{PE}} \Delta r_{\mathrm{3D}} \sqrt{\frac{N_{\mathrm{PE}} N_{\mathrm{3D}}}{\mathrm{BW}_{\mathrm{RO}}}} \tag{1.64}$$

where

$$\mathrm{BW}_{\mathrm{RO}} = \frac{1}{N_{\mathrm{RO}} \Delta t_{RO}} \tag{1.65}$$

This parameter is called receive bandwidth and is measured in the units of Hz/voxel. Besides the parameter SNR/voxel, another limiting factor for the spatial resolution is blurring, through the point spread function [100]. This, in fact, spreads the local spatial information over a broader region, thus reducing the actual image resolution. Such effect is particularly relevant for tissues with short T_2^*, as the T_2^* decay modulates the signal during the read-out window. A similar effect occurs for tissues with short T_2 when using TSE-based sequences, as already discussed.

3. The **contrast** is defined as the absolute signal difference between different tissues and is determined by several sequence parameters including TE, TR and α. The basic rules which define how to choose TE and TR in order to obtain the desired image contrast are listed in Table 1.4.

In MRI, the imaging parameters can be adjusted to optimize one or more of the image quality factors described above depending on the specific requirements of the investigation.

Chapter 2

MRI of the Lung

In this chapter, a brief overview of the morphological, functional and microstructural properties of the human lung is provided, following the descriptions of Beachey [102], Larsen et al. [103], Schwartzstein et al. [104] and Tortora et al. [105] to which the interested reader is referred for a more detailed discussion. In addition to this, the major issues concerning the application of proton MRI in the lung are discussed. In particular, the consequences which the inhomogeneous distribution of magnetic fields within the lung has on the transverse relaxation mechanisms are described.

2.1 Morphology and Physiology of the Human Lung

The lungs are respiratory organs. In humans, they are essential for life. Their main function is to transport oxygen (O_2) from the atmosphere into the bloodstream and to release carbon dioxide (CO_2) from the bloodstream into the atmosphere. This gas exchange is accomplished within millions of small and closely-packed air sacs, called alveoli. The whole process of oxygen transport can be divided into the following three steps:

1. the physical movement of air in and out of the alveoli (ventilation);
2. the microcirculation of blood in the lung capillaries (perfusion);
3. the gas exchange between the alveoli and the pulmonary capillaries (diffusion).

Short Description of the Human Lungs

Humans have two lungs, a right lung and a left lung, which are located in the thoracic cavity on either side of the heart and are protected by the rib cage. A graphical representation of the human lungs is shown in Figure 2.1. The lungs are not identical: the left lung is slightly smaller, due to the presence of the heart. Both of them are separated into lobes, with three lobes in the right lung (upper, middle and lower lobes) and two in the left lung (upper and lower lobes).
The lungs are the largest organs of the respiratory system and belong to the lower respiratory tract, which includes also: trachea, bronchi and bronchioles. The lower respiratory tract presents a tree-like structure called respiratory tree. This can be described as follows: the trachea divides into two bronchi, which branch to the left and to the right lungs where

they progressively divide; at each division one airway branches into two or more smaller airways. After multiple divisions the bronchi give rise to a series of bronchioles, terminal bronchioles, alveolar ducts, alveolar sacs and, finally, to the alveoli. The lungs can be thought as a bunch of alveoli resulting from the latest divisions of the respiratory tree. Correspondingly, the lung parenchyma refers to the functional and connective tissues that constitute the alveolar walls.

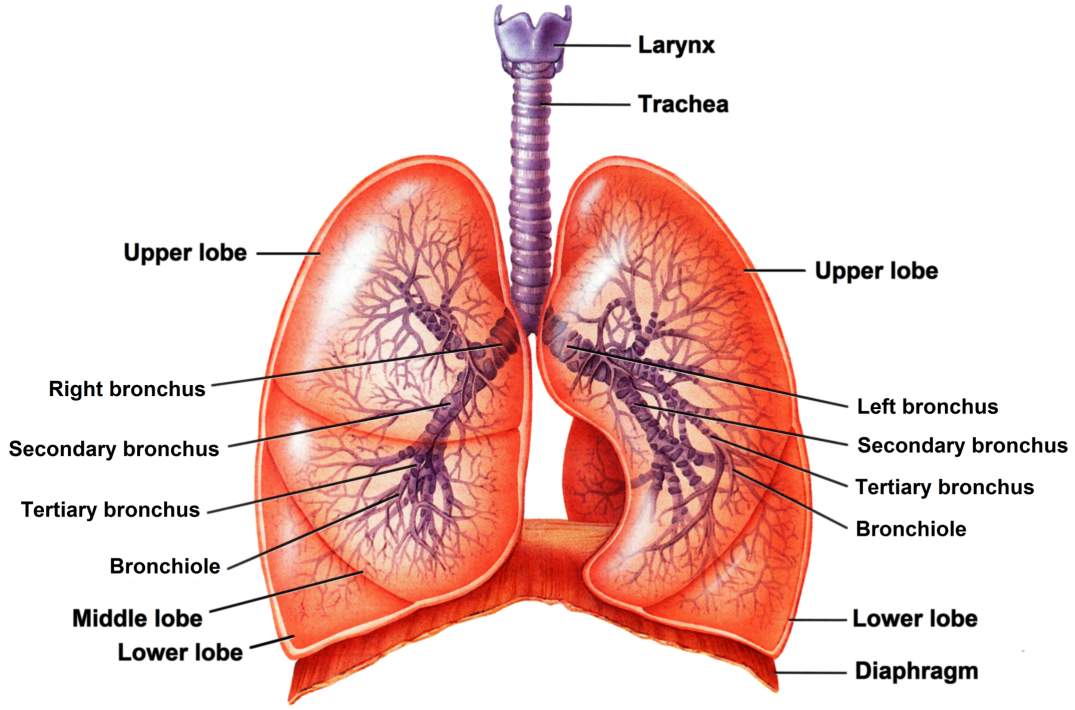

Figure 2.1: Graphical representation of the human lungs. Reproduced with permission from reference [105], with adaptions.

The Respiratory Cycle

The passage of air from the atmosphere into the lungs is called inspiration (or inhalation), while the passage of air out of the lungs is called expiration (or exhalation). The cyclical process during which the lungs expand and compress due to inspiration and expiration is collectively known as respiration (or breathing).
Respiration is driven by muscular action, mainly of the diaphragm, a thin muscle located at the base of the thoracic cavity between the lungs and the abdomen. The driving forces for gas flow between the lungs and the atmosphere are the pressure differences. During inspiration, contraction of the diaphragm pulls the bottom of the thoracic cavity downward, increasing its volume. This causes the internal pressure of the chest to decrease, resulting in a flow of air into the airways up to the alveoli. Vice versa, during expiration the diaphragm relaxes and a positive pressure is generated in the thorax, causing the air to rush out of

the alveoli. The rib cage is also able to expand and contract to some degree and support breathing, through the action of the intercostal muscles.

Lung Capacities

The lung capacities refer to the volumes of air in the lungs which are associated with different phases of the respiratory cycle, as shown in Figure 2.2. During non-forced breathing, in rest conditions, the lung volume changes periodically between the end-expiratory and the end-inspiratory states. This is called tidal breathing. The respiratory state, however, can also be forced to maximum lung expansion or compression. The degree of expansion of the lungs is called inflation. The lung capacities associated to different levels of inflation can be resumed as follows:

- Tidal Volume (TV): difference of air volume in the lungs between end-inspiration and end-expiration during tidal breathing.
- Residual Volume (RV): volume of air in the lungs after a maximal exhalation.
- Functional Residual Capacity (FRC): volume of air in the lungs at the end-expiratory position.
- Total Lung Capacity (TLC): volume of air in the lungs at maximal inflation.

The average TLC of an adult human male is about 5.8 l, whereas the average FRC is 2.3 l. Only a small fraction of these volumes, about 0.5 l, is used during tidal breathing.

Pulmonary Ventilation

Pulmonary ventilation ($\dot{V}$) is defined as the volume of air that flows into or out of the lungs per unit time and is usually measured in the units of l/min. This is expressed by:

$$\dot{V} = \left| \frac{dV_{\text{air}}}{dt} \right| \tag{2.1}$$

In rest conditions, the total pulmonary ventilation of the both lungs is given by the product between TV and the respiratory rate, in number of breaths per minute. The average respiratory rate in an adult human male is about 12 breaths per minute, which results in $\dot{V} \approx 6.0$ l/min, considering the typical tidal volume mentioned above. Because only the inhaled gas that reaches the alveoli actually contributes to gas exchange, another parameter called alveolar ventilation is often used to describe ventilation. This is given by the volume of air that flows into or out of the alveoli per unit time. In humans, the alveolar ventilation is approximately 4.2 l/min. In MRI, regional lung ventilation can be assessed, either qualitatively or quantitatively, on a voxel-by-voxel basis. To this end, techniques such as the Fourier-decomposition method proposed by Bauman et al. [46], oxygen-enhanced MRI [43] or hyperpolarized gas MRI [7, 53, 54] can be used.

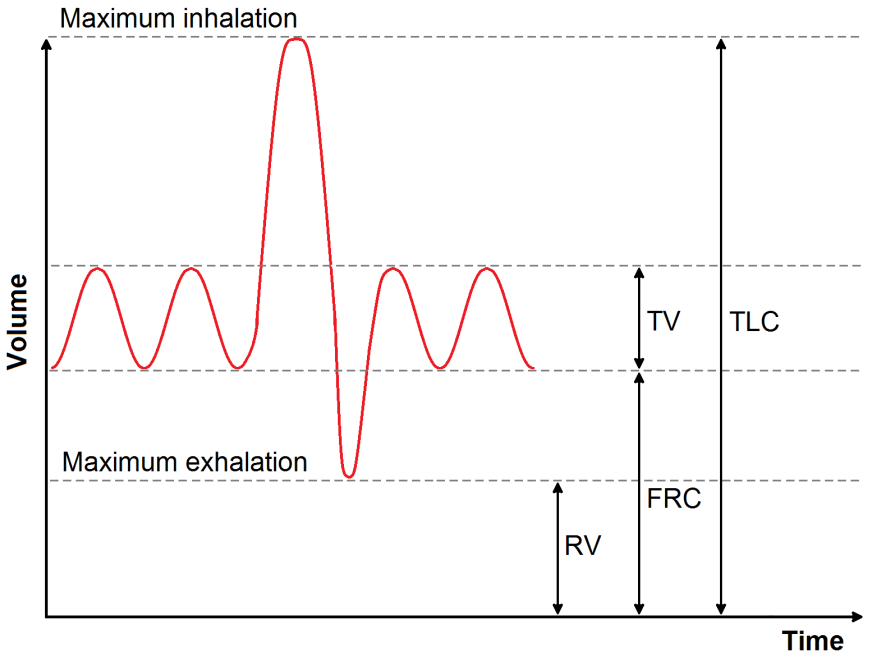

Figure 2.2: Diagram of the lung volumes and capacities. Reproduced with permission from reference [105], with adaptions.

Lung Perfusion

Perfusion is the process of blood delivery to a capillary bed. In the lungs this is performed by pulmonary circulation. The pulmonary circulatory system is a net of vessels organized in a tree-like structure, similarly to the respiratory tree. The main vessels (arteries and veins) progressively divide in smaller vessels (arterioles and venules) until the form of the smallest capillaries is reached. The vessels of the pulmonary circulatory system follow the branches of the respiratory tree up to the alveoli, which are surrounded by a network of capillaries, called alveolar capillaries. The role of pulmonary circulation is to carry deoxygenated blood away from the heart to the lungs, through the pulmonary arteries (one for each lung), and to return oxygenated blood back to the heart, through the pulmonary veins, where it is ready for delivery to the rest of the body. O_2 is exchanged with CO_2 at the level of the pulmonary capillaries.
Perfusion ($\dot{Q}$) is commonly defined as the absolute blood volume that reaches a certain region of the body per unit time and is measured in the units of l/min. This is expressed by:

$$\dot{Q} = \left| \frac{dV_{\text{blood}}}{dt} \right| \tag{2.2}$$

The total perfusion of the both lungs is equal to the cardiac output of the right ventricle (product between blood volume per stroke and heart rate). This is typically $4 - 8$ l/min. In MRI, however, several different parameters are used to describe regional lung perfusion. These include: blood flow, blood volume, mean transit time, blood volume fraction and

pseudo-diffusion coefficient. These parameters can be quantified on a voxel-by-voxel basis using techniques such as contrast-enhanced MRI [40, 41], Arterial Spin Labeling (ASL) [48] and Intra-Voxel Incoherent Motion (IVIM) [59, 60]. For a more detailed description about perfusion parameters, acquisition techniques and quantification, the interested reader is referred to Hatabu et al. [40], Ohno et al. [41] and Le-Bihan et al. [61]. For the scope of this work, only the blood volume fraction and the pseudo-diffusion coefficient are of interest, as further discussed later in this chapter.

Alveoli and Gas Exchange

Gas exchange occurs in later divisions of the respiratory tree, which include terminal bronchioles, alveolar ducts, alveolar sacs and alveoli. Nevertheless, about 90 % of gas exchange takes place in the alveoli. A graphical representation of the alveoli is shown in Figure 2.3 a. As already mentioned, the alveoli can be regarded as the basic structural unit of the lung. Each human lung contains approximately 300 million alveoli measuring $200-300$ μm in diameter, with a total surface area of $50-100$ m^2 [29]. The net of alveolar capillaries, in which they are wrapped, covers about 70 % of their area.
Gas exchange is a diffusion process which is due to the different concentration of O_2 and CO_2 in blood (in the alveolar capillaries) and air (in the alveoli). Although oxygen diffusion is impeded by the low solubility of oxygen in water, the exceptionally thin air/blood barriers of about 1.5 μm thickness, which are called alveolar membranes, allow gases in the alveoli to diffuse into the blood and vice versa. A schematic representation of the gas exchange process in the alveoli is shown in Figure 2.3 b.

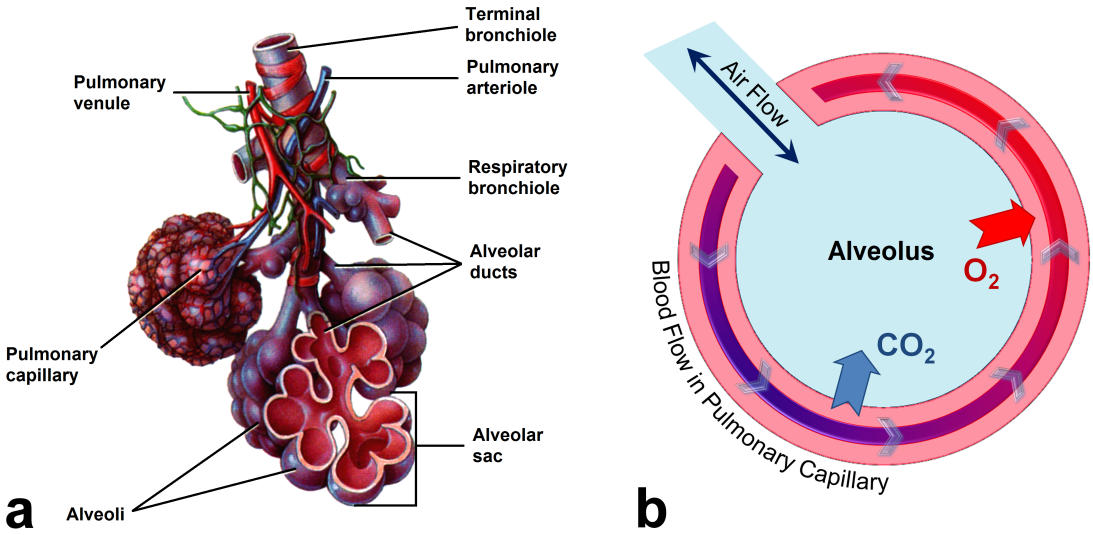

Figure 2.3: a) Graphical representation of the latest divisions of the respiratory tree including bronchioles, alveolar sacs and alveoli. Reproduced with permission from reference [105], with adaptions. b) Graphical representation of the gas exchange mechanism in the alveolus.

2.2 General Aspects of Lung MRI

Challenges in Lung MRI

Application of proton MRI in the lung is hampered by several factors, due to the unique morphology and physiology of the lung. These can be resumed as follows [28, 29, 30]:

1. Low proton density. The lung has inherently low proton density due to its heterogeneous composition, which consists of both air and lung tissue. Because the air-filled alveoli make up a considerable fraction of the total lung volume, the overall density of the lung is significantly lower than any other organ in the human body: approximately $20-30$ % compared to other soft tissues. For this reason, the lungs produce a weaker MR signal in comparison to other organs and appear darker on conventional MR images. This also results in a lower SNR. The lung density depends on the level of inflation: at FRC the average mass and volume of the pair of lungs are about 1 kg and 3.4 l, resulting in a density of about 0.3 g/cm^3. This decreases to about 0.15 g/cm^3 at TLC.

2. Short transverse relaxation times (T_2 and T_2^*). The heterogeneity of the lung is not only responsible for its low proton density but also for the relatively short transverse relaxation times, which further hamper the MR signal detection. Lung tissue and air, in fact, have a different magnetic susceptibility. This results in relatively strong internal magnetic field inhomogeneities and in corresponding magnetic field gradients within the lung space. Such magnetic field variations typically present a quasi-

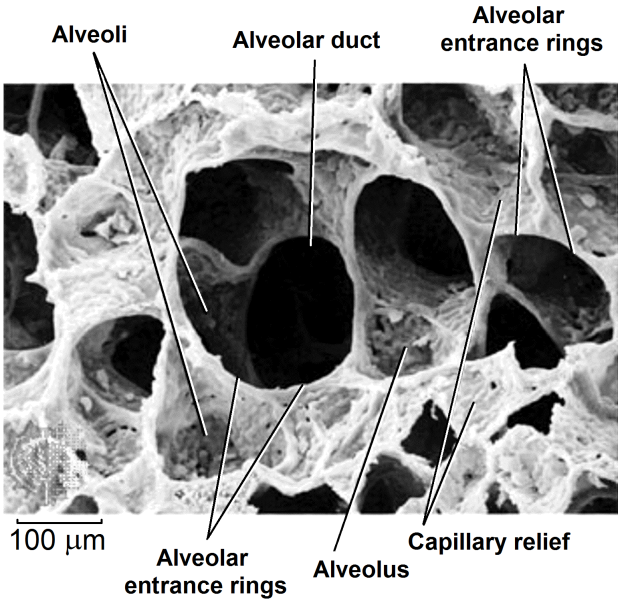

Figure 2.4: Electron micrograph scan (SEM) of alveoli and alveolar walls in a healthy and adult human lung. Reproduced with permission of S. Karger AG [107] from reference [108], with adaptions.

periodic modulation pattern at the level of the alveolar length scale. The amplitude of the magnetic field inhomogeneities is larger in correspondence of the multiple air/tissue interfaces that characterize the lung microstructure, as shown in Figure 2.4. This peculiar characteristic of the lung tissue affects the transverse magnetization by enhancing its loss of phase coherence within the voxel (intravoxel dephasing). The MR signal decay is consequently accelerated, as further discussed later in this chapter. The typical values of the transverse relaxation times of the lung at $B_0 = 1.5$ T are of the order of a few ms for T_2^* [45, 109, 110, 111] and of several tens of ms for T_2 [70, 112, 113]. Both T_2 and T_2^* of the lung decrease with the magnetic field strength [113, 114].

3. Physiological motion. Depending on the acquisition strategy adopted, signal variations can be induced during the acquisition by respiration, cardiac beat and blood flow in the pulmonary vessels. This would result in image artifacts, unless proper solutions are adopted.

Acquisition Strategies in Lung MRI

In order to face the difficulties described above, appropriate image acquisition techniques must be used in lung MRI. One of the basic approaches to acquire signal from the lung, with its short transverse relaxation times, is to use relatively short echo times. The pulse sequences that are most commonly used for lung imaging can be divided into the following two categories:

1. Spoiled GRE-based sequences with radial k-space sampling and short or Ultrashort Echo Times (UTE) for T_1-weighted imaging [35, 36, 37, 115]. In this case the use of the shortest possible TE is beneficial because the signal decay is dictated by T_2^*, which is typically of the order of a few ms. In this regard, the UTE sequence represents one of the most suitable approaches [36, 109].

2. TSE-based sequences with large turbo-factors and short inter-echo times for T_2-weighted imaging. With this approach, the multiple refocusing pulses minimize the influence of susceptibility differences on the signal decay, which is dictated by T_2. Large turbo-factors and short inter-echo times help to reduce TE as well as the sensitivity to physiological motion. In this regard, the HASTE sequence described in the next chapter is one of the most suitable approaches for lung MRI [33, 34].

Many acquisition strategies can be used in combination with the pulse sequences mentioned above in order to reduce the problems related with physiological motion. These are:

- Breath-holding. Data are acquired in one or multiple breath-holds of the duration of several seconds, depending on the possibility of the patient/volunteer.

- Respiratory and/or cardiac triggering. Data are acquired at specific time intervals. The position and duration of these intervals are prospectively defined according to the signal generated by an external device which detects physiological motion. An example of this is the electrocardiograph (ECG).

- Navigators. Intrinsic variations of the MR signal are used to either prospectively control the acquisition [116], similarly to cardiac and respiratory triggering, or to retrospectively gate the continuously acquired data. In the latter case, only a fraction of the acquired data is actually used for image reconstruction.

- Motion compensation. The acquired data are retrospectively corrected either in the image space or in the k-space. To this end, image registration algorithms can be used as well as the signal generated by navigators or external devices.

2.3 Static Magnetic Fields in the Lung

The magnetic susceptibility difference between lung tissue and gas in the alveoli is an intrinsic property of the lung, which is responsible for both the inhomogeneous distribution of the static magnetic field within the lung space and the relatively short transverse relaxation times T_2 and T_2^*. In the next sections, the basic physical principles underlying the internal distribution of static magnetic fields in the lung are described.

Internal Magnetic Fields in Matter

In the majority of substances the magnetism is induced, meaning that the magnetization appears only when an external magnetic field is applied. In a magnetized material, each infinitesimal volume of matter can be thought as a magnetic dipole, which alters the local magnetic field in the surrounding space and contributes to the generation of a spatially distributed internal magnetic field $\vec{B}(\vec{r})$. The main contribution to this effect arises from the alignment of the magnetic dipole moments of atomic electrons. The two main mechanisms that account for the induced magnetization in matter are [75, 76]:

- Paramagnetism. The magnetic dipole moments associated with the spins of unpaired electrons tend to align parallel to the external magnetic field. This results in a net magnetization, similarly to the already discussed formation of the nuclear magnetization. The corresponding magnetic field contributes to increase the external field. The contribution of the nuclear magnetization is negligible for paramagnetism, as the gyromagnetic ratio of electrons γ_e and the corresponding magnetic moment are much larger than those of nuclei (for protons $|\gamma_e|/\gamma \simeq 658$).

- Diamagnetism. The electric currents associated with the orbital angular moments of electrons generate magnetic dipole moments which tend to align anti-parallel to the applied magnetic field, similarly to the Faraday's law of induction. The resulting magnetization generates a magnetic field which opposes to the external field.

An example of the magnetic field distortion which is caused by paramagnetic and diamagnetic objects is shown in Figure 2.5. Diamagnetism is a much weaker effect than paramagnetism, which normally dominates. However, most materials in nature are diamagnetic due to the fact that electron spins pair up and cancel their magnetic dipole moments. In this case, paramagnetism is absent and no longer dominates the omnipresent diamagnetism.

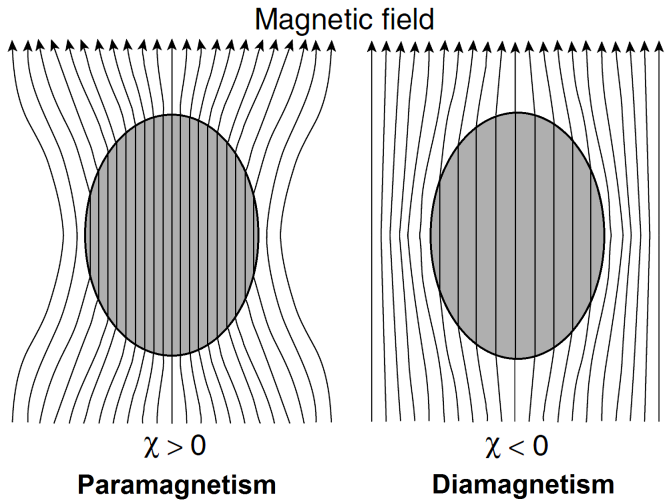

Figure 2.5: Magnetic field lines in the presence of diamagnetic and paramagnetic objects. Reproduced with permission from reference [76].

Nuclear spins experience a magnetic field that results from the superposition of the externally applied field and the induced internal fields. This can be expressed by [117]:

$$\vec{B}(\vec{r}) = \mu_0 \left[\vec{H}(\vec{r}) + \vec{M}_a(\vec{r}) \right] \tag{2.3}$$

where μ_0 is the magnetic permeability in vacuum, $\vec{M}_a(\vec{r})$ is the local atomic magnetization and $\vec{H}(\vec{r})$ is the local magnetizing field strength, expressed in the same units as the magnetization. In vacuum, $\vec{M}_a = 0$ and consequently $\vec{B}(\vec{r}) = \mu_0 \vec{H}(\vec{r})$.
Paramagnetic and diamagnetic materials are also called linear materials, as the induced magnetization $\vec{M}_a$ is linearly proportional to the local magnetizing field $\vec{H}$. This is mathematically expressed by the following equation [117]:

$$\vec{M}_a(\vec{r}) = \chi \vec{H}(\vec{r}) \tag{2.4}$$

where χ is a dimensionless number, called magnetic susceptibility, which describes how the material responses to an applied magnetic field. The magnetic susceptibility is positive for paramagnetic materials and negative for diamagnetic materials. Pure water is diamagnetic with $\chi \simeq -9.05 \cdot 10^{-6}$, considering the units of measurement of the international system. The local magnetic field in linear materials is given by [117]:

$$\vec{B}(\vec{r}) = \mu_0 (1 + \chi) \vec{H}(\vec{r}) \tag{2.5}$$

If χ is homogeneous in space, then the magnetic field in the material is proportional to the externally applied field. In MRI, this is expressed by:

$$\vec{B} = B_0 (1 + \chi) \vec{z} \tag{2.6}$$

According to equation (1.28), the magnetic field in the material is shifted by $\Delta B_0 = \chi B_0$ with respect to the externally applied field.

When materials with different magnetic susceptibilities are placed in an external magnetic field, χ in equation (2.5) becomes spatially dependent. This concept can be described by means of the function $\chi = \chi(\vec{r})$. In this case, the spatial distribution of the magnetic field $\vec{B}(\vec{r})$ depends on the specific geometry of the magnetized objects and on their respective magnetic susceptibilities. $\vec{B}(\vec{r})$ is given by the solution of the Maxwell's equations for static magnetic fields:

$$\nabla \cdot \vec{B}(\vec{r}) = 0 \tag{2.7}$$

$$\nabla \times \vec{H}(\vec{r}) = 0 \tag{2.8}$$

The calculation of the magnetic field distribution in bodies with arbitrary shapes may need to be carried out with numerical methods [117, 118, 119, 120]. As a general rule, it can be stated that stronger magnetic field inhomogeneities occur at the interfaces between materials with different magnetic susceptibility. The amplitude of these inhomogeneities increases linearly with both the magnetic field strength B_0 and the susceptibility difference $\Delta\chi$, such that:

$$\Delta B_0 \propto \Delta\chi B_0 \tag{2.9}$$

In the human body, the presence of magnetic field inhomogeneities is mainly observed at the interfaces between different tissues. The sources of these field inhomogeneities can be either macroscopic, if they act over the typical dimensions of a voxel, or microscopic, if they act over distances which are much smaller than the size of a voxel. In the lung, magnetic field inhomogeneities occur at a microscopic level on the alveolar length scale. They originate from the susceptibility difference between the air in the alveoli and the lung tissue, which is typically of the order of 10^{-5} [45, 121].

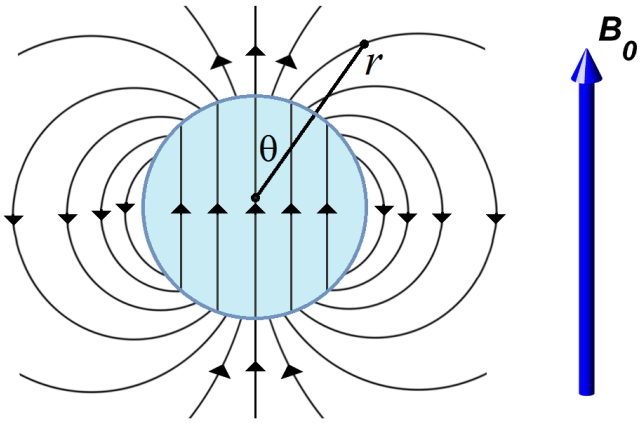

Figure 2.6: Magnetic field lines of the internal field which is generated by a spherical body in the presence of an external field $B_0\vec{z}$.

Spherical Body in a Magnetic Field

A simple geometry, which is often used to model the pulmonary alveolus and to calculate the distribution of the internal magnetic fields in the lung, is a homogeneous sphere with

radius R embedded in a medium with different susceptibility. The susceptibility difference between the sphere and the surrounding medium is $\Delta\chi$. Both of them are subject to a uniform external magnetic field $B_0\vec{z}$.
In this case, the spatial distribution of the magnetic field can be analytically obtained from the solution of equations (2.7) and (2.8), which is results in [30, 75, 117]:

$$\vec{B}(\vec{r}) = \frac{3(1+\Delta\chi)}{3+\Delta\chi} B_0\vec{z} \qquad \text{for } |\vec{r}| < R \tag{2.10}$$

$$\vec{B}(\vec{r}) = B_0\vec{z} + \frac{\Delta\chi}{3+\Delta\chi} R^3 B_0 \frac{3(\vec{z}\cdot\vec{r})\,\vec{r} - |\vec{r}|^2\,\vec{z}}{|\vec{r}|^5} \qquad \text{for } |\vec{r}| \geq R \tag{2.11}$$

Inside the sphere the magnetic field is uniform while outside the sphere it presents a dipolar distribution, as graphically shown in Figure 2.6. Assuming that $\Delta\chi << 1$, the amplitude of the magnetic field inhomogeneities in the direction of the external field can be approximated as follows [30, 67]:

$$\Delta B_0 = \frac{2}{3}\Delta\chi B_0 \qquad \text{for } |\vec{r}| < R \tag{2.12}$$

$$\Delta B_0 = \frac{1}{3}\Delta\chi B_0 \left(\frac{R}{|\vec{r}|}\right)^3 \left(3cos^2\theta - 1\right) \qquad \text{for } |\vec{r}| \geq R \tag{2.13}$$

The inverse proportionality between ΔB_0 and $|\vec{r}|$ in equation (2.13) states that stronger magnetic field inhomogeneities occur at the interface between the sphere and the surrounding space, where $|\vec{r}| = R$. These inhomogeneities progressively decrease when moving away from the surface of the sphere.

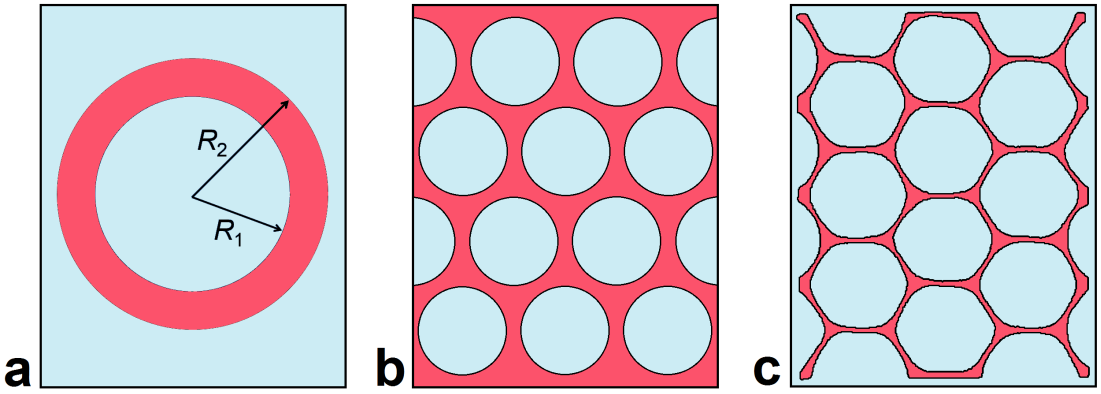

Figure 2.7: Two dimensional cross sections of the spherical shell model (a), of the spherical foam model (b) and of the Wigner-Seits model of the lung parenchyma. Reproduced with permission from references [67, 120], with adaptions.

Lung Models

The inflated lung can be thought as a collection of air cavities (the alveoli) embedded in a diamagnetic medium (the lung tissue) [67]. When an external magnetic field is applied,

each cavity acts approximately like a magnetic dipole which generates spatial magnetic field inhomogeneities in the surrounding lung tissue. Several models of the lung microstructure have been proposed in order to calculate the spatial distribution of internal magnetic fields and to assess the NMR properties of the lung tissue. These models include [30, 67, 117, 120]:

- Spherical-shell model [67, 117, 118]. A single spherical shell of inner radius R_1 and outer radius R_2 is used to model the alveolus, as shown in Figure 2.7 a. The space between the inner and the outer spheres represents the alveolar walls, which are characterized by a susceptibility difference $\Delta\chi$ with respect to the rest of the volume. The magnetic field distribution within the shell is given by the difference between the magnetic fields induced in the two spheres of radii R_1 and R_2 separately, such that [30, 117]:

$$\Delta B_0 = \Delta\chi B_0 \left[\frac{2}{3} - \frac{1}{3}\left(\frac{R_1}{|\vec{r}|}\right)^3 \left(3cos^2\theta - 1\right)\right] \tag{2.14}$$

- Spherical-foam model [67, 118]. The alveoli are modeled as a dense packing of non-penetrating spheres of radius R placed at the vertices of a hexagonal structure, as shown in Figure 2.7 b. The space between the spheres represents the lung tissue. The internal magnetic field is calculated at each point in the tissue as a linear superposition of the fields generated by each individual sphere as [30, 122]:

$$\vec{B}\left(\vec{r}\right) \approx B_0\vec{z} + \frac{1}{3}R^3\Delta\chi B_0 \sum_i \frac{3\left[\vec{z}\cdot\left(\vec{r}-\vec{r}_i\right)\right]\left(\vec{r}-\vec{r}_i\right) - \left|\vec{r}-\vec{r}_i\right|^2\vec{z}}{\left|\vec{r}-\vec{r}_i\right|^5} \tag{2.15}$$

  where $\vec{r}_i$ indicates the positions of the sphere centers. The result provided by equation (2.15) represents a first order approximation of the actual field, which highly simplifies the calculation of the magnetic field distribution.

- Wigner-Seitz model [118, 120, 123]. The alveolus is modeled as a polyhedral air cell, as shown in Figure 2.7 c. The magnetic field distribution can be calculated by using an approach based on the principle of linear superposition of dipolar fields which is used for the spherical-foam model, in combination with a Monte Carlo technique. A more detailed description of this procedure can be found in Christman et al. [120]. This model better simulates the actual shape of the alveoli, at the cost of a more complex calculation of the internal magnetic field distribution [30].

For a more detailed description of lung models and of internal magnetic field calculations, the interested reader is referred to references [30, 67, 117, 118, 119, 120].

2.4 Magnetic Resonance Properties the Lung Tissue

The inhomogeneous distribution of internal magnetic fields is a peculiar characteristic of the lung tissue, which makes it very different from all other tissues in the body with regard to MRI. This is usually considered as a drawback for lung MRI, as it represents the origin of the relatively short transverse relaxation times of the lung tissue. However, it also offers the possibility to assess interesting properties of the lung, as further discussed in the next sections.

The NMR Spectral Line of the Lung

The spatial distribution of internal magnetic fields in the lung generates a relatively broad distribution of resonance frequencies in the NMR spectrum. The shape of the resulting NMR spectral line can be described by a probability density function in the resonance frequency domain, which is indicated here as $P(\omega)$. Examples of NMR line shapes are shown in Figure 2.8 a.
The properties of the NMR spectral line of the lung have been studied by means of both numerical calculations [67, 117, 119, 120] and experiments [43, 45, 66, 109, 120, 124]. Numerical calculations were used in combination with the lung models described above, in order to obtain the spatial distribution of the internal magnetic fields and to generate a histogram which approximates $P(\omega)$. Experiments were conducted using either NMR spectroscopy [66, 120, 124] or oxygen-enhanced MRI [43, 44, 45, 109]. The results found with both numerical and experimental approaches indicate that the NMR spectral line of the lung is related to morphological, functional and microstructural properties of the lung tissue, as further described below:

- Numerical calculations have shown a dependence of the NMR line shape on the lung model used, suggesting that the line shape of the lung is an indicator of its microstructural geometry [67, 117, 119, 120]. For the healthy lung tissue, the experimentally obtained line shape is very well approximated by the Wigner-Seitz model [30, 120].

- Both numerical calculations and experiments with NMR spectroscopy demonstrated that the NMR spectral line of inflated lungs is significantly broader in comparison to other tissues as well as to airless lungs [63, 66, 67, 71, 118, 120, 125, 126]. This has been attributed to the presence of strong and broadly distributed internal magnetic fields in the inflated lungs, as discussed above. Moreover, a significant increase of the line broadening was observed with the volume of air in the lung, which indicates a dependence of the line broadening on the level of lung inflation.

- Experiments with oxygen-enhanced MRI have shown that the spectral line broadening of the lung increases with the concentration of oxygen in the breathing gas [45, 109]. This has been attributed to an increase of the susceptibility difference between lung tissue and breathing gas with the oxygen concentration. Experiments indicated an increase of $\Delta\chi$ of about 10% between room air (21% O_2) and pure oxygen (100% O_2) [45, 109].

Spectral Line Broadening in the Lung

The spectral line broadening is defined from the second moment of $P(\omega)$. This is given by:

$$\langle\omega^2\rangle = \int P(\omega)\,(\omega - \langle\omega\rangle)^2\,d\omega \tag{2.16}$$

where ω is resonance frequency which is associated with the local internal magnetic field. According to the definition used in references [67, 120, 125], the line broadening is given by $\sqrt{\langle\omega^2\rangle}$. In absolute terms, the line broadening is proportional to the statistical dispersion of ΔB_0 within the lung. According to equation (1.11), in fact, stronger magnetic field inhomogeneities spread the resonance frequencies over a broader interval. This means

that the spectral line broadening increases linearly with both B_0 and $\Delta\chi$, as indicated by equation (2.9). These effects have been theoretically described by Yablonskiy et al. [127] and by Stables et al. [128] and experimentally confirmed in the lung by several investigators [45, 109, 114].
In order to remove its dependence on the magnetic field strength B_0, the line broadening is usually expressed in ppm by means of the normalization with the nominal resonance frequency [67, 120, 125], such that:

$$\text{line broadening} = \frac{\sqrt{\langle\omega^2\rangle}}{\gamma B_0} \tag{2.17}$$

The spectral line broadening increases with the fractional volume of air in the lung (η). This parameter is given by:

$$\eta = \frac{V_{\text{air}}}{V_{\text{air}} + V_{\text{tissue}}} \tag{2.18}$$

where V_{air} is the total volume of air, which depends on the level of inflation, and V_{tissue} is the volume of lung tissue. η represents a quantitative measure for lung inflation. In the lung models described above, different values of η have been used to numerically simulate different levels of lung inflation [67, 118, 120], as shown in the example of Figure 2.8. For the spherical shell model, η depends on the relative sizes of the inner and outer spheres according to:

$$\eta = \left(\frac{R_1}{R_2}\right)^3 \tag{2.19}$$

For the other models, η depends on the size of the spheres (or cells) and on their packing density. The results of several investigators showed that η has a negligible influence on the NMR line shape of the lung, but it strongly regulates the line broadening [30, 67, 118, 120]. This is due to the fact that ΔB_0 uniformly scales with η, as indicated by equations (2.9) and (2.14). The mechanism of spectral line broadening in the lung can be resumed as follows [30]: for $\eta = 0$ (airless lung) the alveoli are collapsed and there are no air/tissue interfaces; as inflation occurs, alveoli open generating a surface of air/tissue interfaces proportional to η, which leads to a broadening of the spectral line.
An example of the dependence of the line broadening on η, which has been obtained by Case et al. [67] from the spherical-foam model, is shown in Figures 2.8 a and 2.8 b. The line broadening monotonically increases with η. Similar results were obtained by Christman et al. [120] as well as by Durney et al. [118] using the Wigner-Seitz model. In all cases, the results seem to indicate that the spectral line broadening increases in good approximation with the square root of η, such that:

$$\frac{\sqrt{\langle\omega^2\rangle}}{\gamma B_0} \propto \Delta\chi\sqrt{\eta} \tag{2.20}$$

In the lung, a monotonic increase of the line broadening with the level of inflation has been experimentally observed by several investigators [63, 66, 124, 125]. Typical values of the spectral line broadening range between 1.0 ppm and 2.5 ppm for air fractions between 20 % and 90 % [67, 120, 125]. A further increase of the line broadening has been observed with the concentration of O_2 in the breathing gas by using oxygen-enhanced MRI. This effect is due to the increase of $\Delta\chi$ with the oxygen concentration [45, 109].

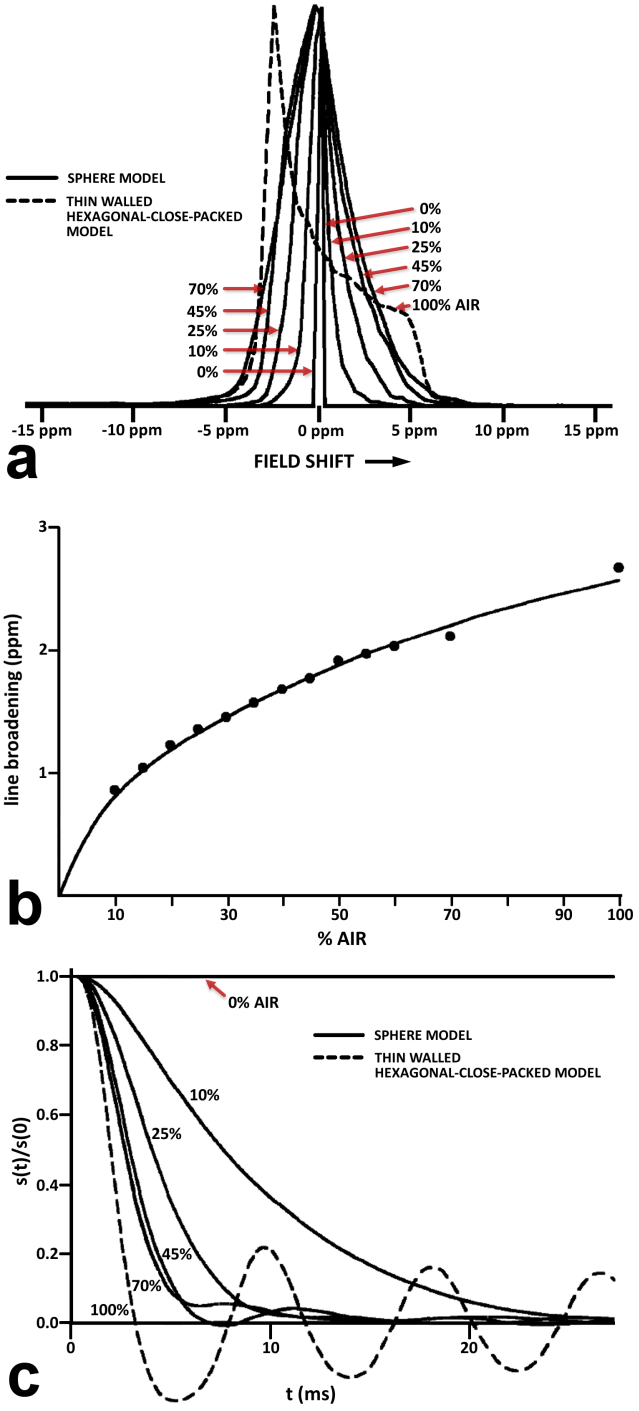

Figure 2.8: a) Spectral line shapes calculated by Case et al. [67] using the spherical-foam model in combination with different air percentages up to 74 % air, at which neighboring spheres touch. The case 100 % air was obtained from the Wigner-Seitz model with infinitely thin walls. b) Spectral line broadening at different air percentages. c) Corresponding FID signals at $B_0 = 0.94$ T. Reproduced with permission from reference [67], with adaptions.

Internal Magnetic Field Gradients

The air volume fraction η and the corresponding line broadening can be thought as measures of lung inflation. As such, they represent good indicators for the relative distances that characterize the lung microstructure. According to equations (2.11) and (2.15), in fact, if all distance variables would be rescaled by an equal factor while maintaining the overall geometry, the spatial profile and amplitude of the internal magnetic fields would not change: they would be simply redistributed on a region of space rescaled by the same factor [122, 129]. Hence, also the line broadening would not change. The same principle holds for η in equations (2.18) and (2.19). In order to characterize the lung microstructure in absolute terms, another parameter is of interest: the internal magnetic field gradients [130, 131].
Associated with the internal field inhomogeneities there is also a spatial distribution of internal magnetic field gradients (G_{int}) which are locally defined, like the external gradients, by equation (1.38). In contrast to the external gradients, however, the internal gradients are not uniform in space and present a broad statistical distribution, similarly to the magnetic field inhomogeneities from which they originate [122, 130, 132, 133]. The local amplitude of the internal gradients is given by [131, 132, 133]:

$$G_{\text{int}} = \sqrt{\left(\frac{\partial B_z}{\partial x}\right)^2 + \left(\frac{\partial B_z}{\partial y}\right)^2 + \left(\frac{\partial B_z}{\partial z}\right)^2} \tag{2.21}$$

The main peculiarity, which differentiates the internal gradients from the magnetic field inhomogeneities, is their dependence on the absolute size of the magnetic field perturbers. In the case of the lung, these are represented by the alveoli. Figure 2.9 graphically illustrates an example of the spatial distribution of the internal magnetic fields and of the corresponding gradients in a system of packed spheres. The spatial variations of the internal magnetic fields primarily occur on the length scale of the sphere diameter, with a quasi periodic modulation pattern [30]. Therefore, the corresponding internal gradients given by equation (2.21) depend on both the relative distance between the spheres, which regulates the amplitude of the static magnetic field inhomogeneities, and on the absolute radius of the spheres [64, 122, 129].
In general, the statistical distribution of internal gradients depends on the specific microstructural geometry of the considered system [130, 134], similarly to what has been discussed above for the spectral line shape. In most cases, however, the influence of the size of the magnetic field perturbers on the mean amplitude of the internal gradients can be resumed in an inverse proportionality. In the case of a single magnetized sphere, this relationship is given by [64]:

$$\sqrt{\langle G_{\text{int}}^2 \rangle} = \frac{\Delta\chi B_0}{3R}\sqrt{\frac{36}{5}\eta\frac{\eta^{5/3}-1}{\eta-1}} \tag{2.22}$$

as found by Ziener et al. [64]. The dependence of the mean internal gradient on the sphere radius R in equation (2.22) introduces an additional information of microstructural nature with respect to the information which is provided by the magnetic field inhomogeneities and by the corresponding line broadening.

In the case of the lung, considering a typical value of the alveolar diameter of 200 μm [29, 135, 136, 137], the air volume fraction in expiration $\eta \approx 0.5$, the susceptibility difference between air and lung tissue $\Delta\chi \approx 10^{-5}$ [45] and a static magnetic field $B_0 = 1.5$ T, the mean internal gradient results to be approximately: $\sqrt{\langle G_{\text{int}}^2 \rangle} \approx 100$ mT/m. This is even larger than the maximum amplitude achievable by a conventional system of magnetic field gradients used on clinical MR-scanners, which is about 50 mT/m.

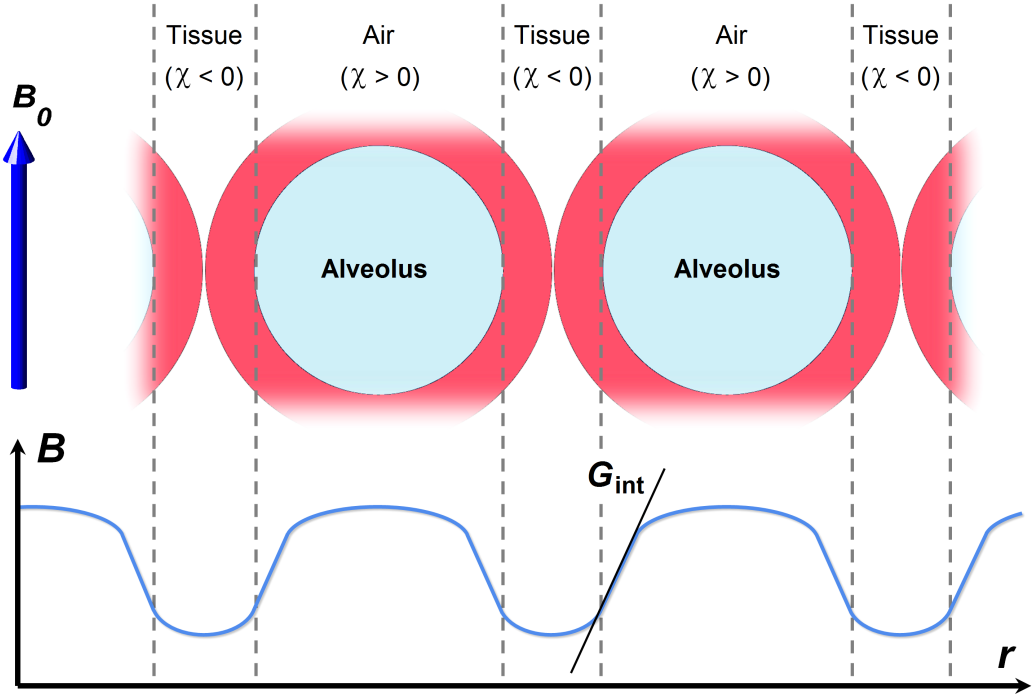

Figure 2.9: Graphical representation of the distribution of the internal magnetic fields in the lung. The internal magnetic fields change on the length scale of the alveolar diameter [30]. The corresponding internal gradients (G_{int}) are directly proportional to the amplitude of the internal magnetic fields and inversely proportional to the alveolar diameter.

2.5 Transverse Relaxation Mechanisms in the Lung

The relaxation of the transverse magnetization is determined by a loss of phase coherence. This can be due to several factors, including spin-spin interactions and static magnetic field inhomogeneities, as indicated by equation (1.29). In proton MRI of the lung, the MR signal is generated in the thin alveolar walls that characterize the lung tissue, where relatively strong magnetic field inhomogeneities occur, as described above. Because the typical voxel size which is used in MRI, of the order of several millimeters, is much larger than the diameter of the alveoli, the internal magnetic field inhomogeneities and the corresponding magnetic field gradients are broadly distributed within the image voxel. This intravoxel

dispersion of magnetic fields has a profound influence on the transverse relaxation mechanisms in the lung tissue.
In general, the influence of the internal magnetic fields on the transverse relaxation of the lung can be resumed in a shortening of the relaxation times T_2 and T_2^*. The mechanisms which contribute to this effect are [28]:

1. static signal dephasing due to the presence of internal magnetic field inhomogeneities;
2. diffusion and perfusion through the internal magnetic field gradients.

In this section, the mechanisms that determine the transverse relaxation in the lung are discussed, together with their dependencies on morphological, functional and microstructural properties of the lung tissue. This aspect is particularly interesting for lung MRI, as it could be exploited to better characterize the lung tissue as well as to achieve key information for the diagnosis of lung diseases which alter the intrinsic properties of the lung.

Static Signal Dephasing

Studies on the distribution of internal magnetic fields in the lung and on the corresponding line broadening started with the observation that the FID signal is much shorter in inflated lungs than in fully collapsed (or airless) lungs [66, 71, 126]. This is a direct consequence of the broadly distributed magnetic field inhomogeneities within the lung. In the presence of magnetic field inhomogeneities, in fact, the transverse magnetization dephases linearly with time according to equation (1.36). This effect is called static signal dephasing and can be recovered by means of signal refocusing in spin-echo based sequences. The time course of the FID signal is the Fourier transform of the NMR spectral line $P(\omega)$, as stated by equation (1.37). From the properties of the Fourier transform, a broader spectral line is characterized by an FID with shorter decay time and vice versa. This means that the frequency domain (spectral line) and the time domain (FID) are both expressions of the intravoxel dispersion of magnetic field inhomogeneities which characterizes the inflated lungs.
The time course of the FID signal depends on the specific line shape of the considered system. In most biological tissues, including airless lung, the transverse relaxation is well approximated by an exponential function with decay time T_2' [123, 138], as described by equation (1.29). This is due to the fact that in most tissues the line shape is well approximated by the Lorentzian function [139]:

$$P(\omega) = \frac{1}{\pi} \frac{T_2'}{1 + (\omega T_2')^2} \tag{2.23}$$

This approximation holds if the volume occupied by the magnetic field perturbers is much smaller than the total volume, meaning that $\eta << 1$. In the lung, where $0.5 < \eta < 0.9$, a different time course of the FID signal can be observed. Figure 2.8 c shows the calculated FIDs for the spherical-foam model obtained by Case et al. [67] with different values of η. The result clearly shows a deviation from the exponential model. Furthermore, as expected, the FID is shortened when increasing η, due to the already discussed increase of the line broadening. The same behavior has been experimentally observed in the lung, where the

FID gets shorter with increasing levels of inflation [45, 66, 63, 109, 111, 125, 138, 140]. It was also demonstrated that the decay time in the lung linearly decreases with the field strength B_0 [114] and with the oxygen concentration in the breathing gas, due to the increase of $\Delta\chi$ [43, 45, 109].

Molecular Diffusion

In order to better understand the other transverse relaxation mechanisms in the lung, it is necessary to first discuss the phenomenon of molecular diffusion.

Microscopic Description
Diffusion is the process of mass transport within a fluid which is due to the microscopic motion of atoms and molecules. Microscopically, diffusion is described by the so called Brownian motion. This can be thought as a random motion of the particles in a fluid, which results from their collisions with the surrounding environment. A graphical representation of diffusing particles is given in Figure 2.10. The Brownian motion is often modeled as a random walk. In this model, motion is divided in discrete steps. Each step is characterized by an equal duration in time (τ), called mean free time, which represents the average time distance between two consecutive collisions. During the mean free time, particles move with a constant velocity of amplitude v, which is proportional to the temperature. The corresponding distance traveled by a particle in one step is $\lambda = v\tau$. This is called mean free path. At each step, the direction in space in which the particle moves is randomly determined, as the direction of diffusive motion randomly changes after each collision. After several steps, a particle which was initially localized on a specific spatial position will be characterized by a probability distribution to be found in each point in space. The variance of this probability distribution, which represents the mean square displacement of diffusing particles, increases with time (i.e. with the number of steps in the random walk).

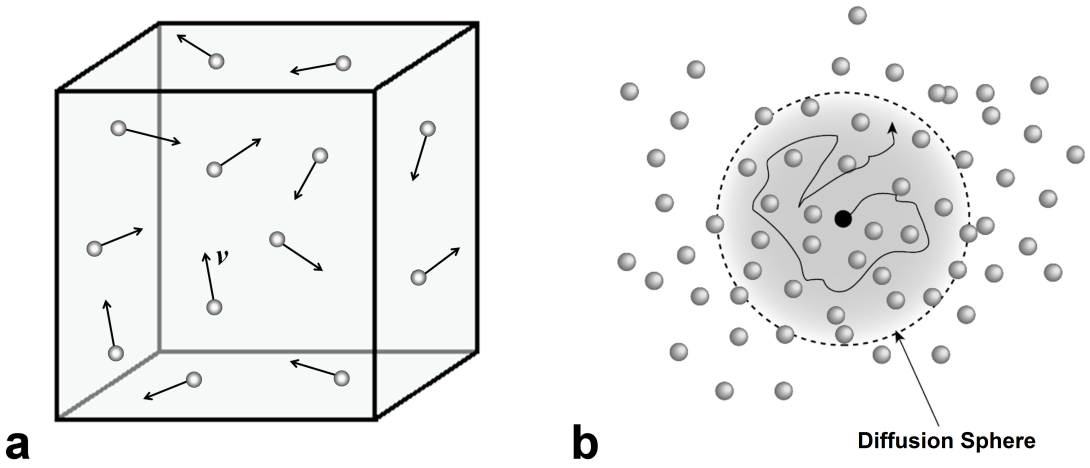

Figure 2.10: a) Graphical representation of diffusing particles. b) Example of the random motion of one particle in a 2D plane. Reproduced with permission from reference [76].

Diffusive motion is characterized by a parameter called diffusion coefficient (D), which describes the mobility of particles. This is given by:

$$D = \frac{v\lambda}{6} \tag{2.24}$$

which is measured in the units of mm^2/s. D can also be thought as the rate at which the mean square displacement of diffusing particles increases with time. In pure water at 300 K, the diffusion coefficient is $D_w \approx 2.3 \cdot 10^{-3}$ mm^2/s. In biological tissues, the diffusion coefficient of water molecules is typically lower than D_w. This is due to the higher viscosity and to the effect of geometrical restriction which is exercised by biological structures such as cell membranes, extracellular structures and other physical barriers on the diffusive motion of molecules [30, 141]. This forces the water molecules to move within a bounded region of space, reducing their mobility. This phenomenon is known as restricted diffusion. In MRI restricted diffusion is observed when the mean square displacement of the excited magnetization achieves values of the order of the spatial separation between the biological barriers that characterize the microstructure of a tissue, such as the diameter of cells.

Macroscopic Description
Macroscopically, the dynamics of diffusing particles is regulated by the Fick's laws. The Fick's first law postulates that a net flux of particles occurs in the presence of a concentration gradient. This is expressed by:

$$\vec{j} = -D\vec{\nabla}\rho \tag{2.25}$$

where $\vec{j}$ is the flux in number of particles per unit time and area, while ρ is the concentration in number of particles per unit volume. Equation (2.25) states that the particles move from regions of high concentration to regions of low concentration, with a velocity that is proportional to the concentration gradient and to the diffusion coefficient. In the absence of a concentration gradient there is no net flux but the diffusion process is still present. This means that the sum of the random diffusive motions of particles cancel each other.
The Fick's second law is a partial differential equation, which predicts how the concentration of particles changes with time. This is given by:

$$\frac{\partial \rho(\vec{r}, t)}{\partial t} = D\nabla^2\rho \tag{2.26}$$

In the case of unrestricted diffusion, equation (2.26) can be analytically solved. Suppose that the initial concentration of particles at time $t = 0$ is given by the delta function $\rho(\vec{r}, 0) = \delta(\vec{r} - \vec{r}_0)$. The function which describes how $\rho(\vec{r}, 0)$ evolves with time is called diffusion propagator. This is given by:

$$\rho(\vec{r}, t) = \frac{1}{\sqrt{(4\pi D t)^q}} \exp\left(-\frac{|\vec{r} - \vec{r}_0|^2}{4Dt}\right) \tag{2.27}$$

where $1 \leq q \leq 3$ is the dimensionality of the problem. Equation (2.27) states that an initial concentration of particles localized in a well defined position in space $\vec{r}_0$ evolves by

spreading in the surrounding space with a Gaussian distribution of increasing variance, as shown in Figure 2.11. The variance increases linearly with time according to:

$$\langle r^2 \rangle = 2qDt \tag{2.28}$$

This effect is analogous to the increase of the mean square displacement in a random walk. In the case of an arbitrary initial concentration of particles $\rho(\vec{r}, 0)$, the solution of the Fick's second law can be generalized as the convolution between $\rho(\vec{r}, 0)$ and the diffusion propagator. This is expressed by:

$$\rho(\vec{r}, t) = \rho(\vec{r}, 0) \otimes \frac{1}{\sqrt{(4\pi Dt)^q}} \exp\left(-\frac{|\vec{r} - \vec{r}_0|^2}{4Dt}\right) \tag{2.29}$$

Diffusion can have either an isotropic or an anisotropic nature. In isotropic diffusion, the mobility of particles and the corresponding diffusion coefficient are equal in any spatial direction. In anisotropic diffusion, the mobility depends on the spatial direction, due to geometrical restrictions. In this case, the diffusion coefficient is described by a tensor. The effects of diffusion anisotropy are out of the scope of this work. For a more detailed discussion on this topic, the interested reader is referred to references [74, 141, 142, 143].

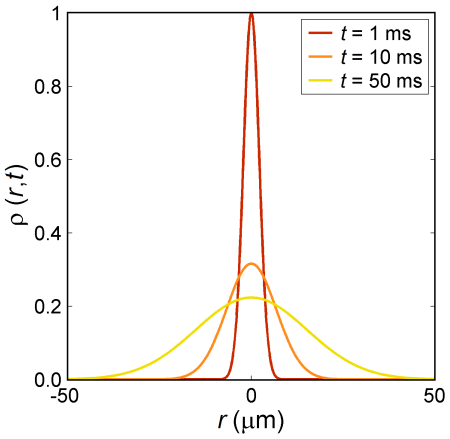

Figure 2.11: Time evolution of the particle concentration $\rho(\vec{r}, t)$ in the presence of Gaussian diffusion, assuming $D = D_w = 2.3 \cdot 10^{-3}$ mm/s^2.

Motion in a Magnetic Field Gradient

In the presence of a magnetic field gradient, motion contributes to dephase the transverse magnetization. The influence of motion on the magnetization depends on its directional coherence, as described below.

Coherent motion
In a magnetic field gradient $\vec{G}$, any kind of directionally coherent motion, such as flow or bulk translational motion, induces a phase shift in the transverse magnetization. Such

phase shift is linearly proportional to the velocity component in the direction of the gradient. In order to demonstrate this concept, consider a magnetization vector moving with velocity $\vec{v}$. Its position at time t is given by:

$$\vec{r}(t) = \vec{r}_0 + \vec{v}t \tag{2.30}$$

Due to the gradient, the resonance frequency at each point in space depends on the amplitude and direction of the gradient according to equation (1.39). The corresponding phase shift accumulated by the transverse magnetization during motion can be obtained by combining equations (1.39), (1.41) and (2.30). This results in:

$$\phi_G(\vec{r}, t) = -\gamma \left[\vec{m}_0 \cdot \vec{r}_0 + \vec{m}_1 \cdot \vec{v}\right] \tag{2.31}$$

where $\vec{m}_0$ and $\vec{m}_1$ are the zeroth and the first moments of the gradient respectively. They are given by:

$$\vec{m}_0 = -\int_0^t \vec{G}\, dt' \tag{2.32}$$

$$\vec{m}_1 = -\int_0^t \vec{G}\, t' dt' \tag{2.33}$$

For static spins ($\vec{v} = 0$), the phase accrual of the transverse magnetization is proportional to $\vec{m}_0$. This effect is used for spatial encoding, as indicated by equation (1.43). When spins move, an additional phase shift occurs, which is linearly proportional to the amplitude of $\vec{m}_1$ and to the velocity component in the direction of the gradient. This means that coherent motion does not directly affect the amplitude of the transverse magnetization but it simply induces a phase shift. However, if a given voxel contains spins with distributed velocity vectors, which means that either different directions of motion and/or different velocity amplitudes are present, then an intravoxel dispersion of phase shifts would result. This loss of phase coherence at the voxel level generates a signal attenuation. Such condition applies, for example, to laminar or turbulent motion as well as to diffusion.

Diffusion
Due to the incoherent nature of diffusive motion, molecular diffusion in the presence of a magnetic field gradient contributes to further attenuate the amplitude of the transverse magnetization [23, 68]. The influence of diffusion on the magnetization is described by the Bloch-Torrey equation [144]. This is obtained by adding a diffusion term given by the second Fick's law (2.26) to the Bloch-equation (1.25), which results in the following partial differential equation:

$$\frac{\partial \vec{M}(\vec{r}, t)}{\partial t} = \gamma \vec{M}(\vec{r}, t) \times \vec{B}(\vec{r}, t) - \frac{M_x \vec{x} + M_y \vec{y}}{T_2} - \frac{M_z - M_0}{T_1} \vec{z} + D\nabla^2 \vec{M}(\vec{r}, t) \tag{2.34}$$

where $\vec{B}(\vec{r}, t) = [B_0 + \vec{G}(t) \cdot \vec{r}]\, \vec{z}$. The solution of equation (2.34) for the transverse magnetization is given by [142, 145]:

$$M_{xy}(\vec{r}, t) = M_{xy}(\vec{r}, 0)\, e^{-t/T_2 - b(t)D}\, e^{i[\phi_G(\vec{r}, t) + \phi_0]} \tag{2.35}$$

The first exponential term in equation (2.35) describes the attenuation of the transverse magnetization which is due to both T_2 relaxation and diffusion, while the second exponential term describes the phase shift, as discussed above by means of equation (2.31).

Stronger attenuation is obtained for larger diffusion coefficients and larger values of the parameter b, which is called b-value. The b-value is a characteristic parameter of the applied magnetic field gradient. It depends on the shape, amplitude and duration of the gradient and describes its sensitivity to diffusion. Its value is given by:

$$b(t) = \gamma^2 \int_0^t \left[\int_0^{t'} G(t'')\, dt'' \right]^2 dt' \tag{2.36}$$

In the absence of a magnetic field gradient, the solution of the Bloch-Torrey equation is the convolution of the diffusion propagator with equations (1.26) and (1.27). This condition always applies to the longitudinal magnetization, as $\vec{M}_z \times \vec{B} = 0$ independently from the presence of a magnetic field gradient. Such effect, however, is usually neglected because the molecular displacement induced by diffusion during TE is typically much smaller than the size of a voxel.

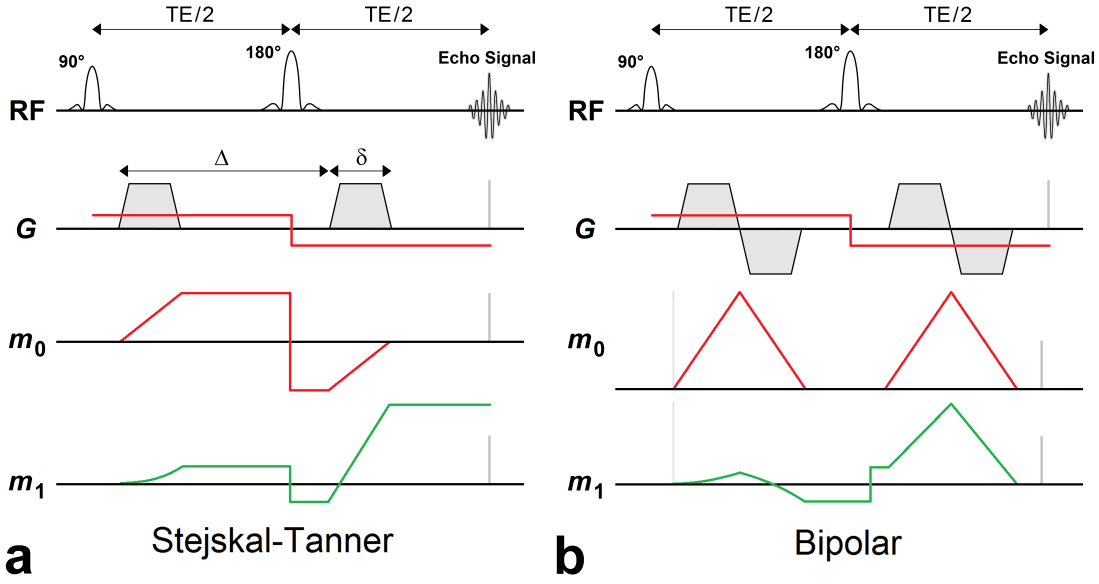

Figure 2.12: Diffusion weighted SE sequence with different diffusion weighting gradient configurations and their corresponding gradient moments (red: m_0, green: m_1). a) Stejskal-Tanner gradient configuration; b) Bipolar gradient configuration. Reproduced from reference [146], in agreement with license [147], with adaptions.

Diffusion Weighted Imaging

Besides spatial encoding and slice selection, magnetic field gradients can also be used to generate diffusion contrast on the MR images, as stated by equations (2.35) and (2.36). This application is called Diffusion Weighted Imaging (DWI).
Diffusion weighting is achieved by incorporating diffusion sensitizing gradients into the pulse sequence [68, 145]. These typically consist of two or more gradient lobes, which are placed between excitation and signal read-out. The simplest configuration of diffusion

sensitizing gradients consists of two lobes of equal $\vec{m}_0$, which are applied one after each other as shown in Figure 2.12 a. In GRE-based sequences, the two lobes must have opposite polarity (bipolar gradients), such that the overall $\vec{m}_0$ of the pair of diffusion sensitizing gradients is nulled before signal read-out and does not affect the spatial encoding. In SE-based sequences, the same effect is achieved with two lobes of same polarity placed at each side of the first refocusing pulse, due to the phase reversal effect of the refocusing pulse. This gradient configuration was originally proposed by Stejskal and Tanner in 1965 [145] and is also known as Stejskal-Tanner gradients. If the two lobes are identical and rectangular-shaped, the b-value obtained from equation (2.36) is [145]:

$$b = \gamma^2 G^2 \delta^2 \left(\Delta - \frac{\delta}{3} \right) \tag{2.37}$$

where δ is the duration of a single gradient lobe and Δ is the separation time between the two lobes, as shown in Figure 2.12 a.
In the presence of the first diffusion sensitizing gradient lobe, both static and diffusing spins dephase. The dephasing of static spins is fully recovered with the application of the second gradient lobe, similarly to the recovery of static signal dephasing in a SE sequence. The dephasing induced by diffusion is not recovered, because of the random spin displacement in time. The degree of signal attenuation which is induced by diffusion on a MR image (or diffusion weighting) is expressed by [142, 145, 148]:

$$s(b) \propto \exp(-bD) \tag{2.38}$$

DWI is not only used to generate a diffusion contrast but also to quantify the diffusion coefficient. To this end, several images can be acquired with identical sequence parameters but different b-values. The signal amplitude of the different images is then fitted on a voxel-by-voxel basis using equation (2.38). The diffusion coefficient obtained from the fit describes the molecular mobility in the direction of the applied gradient.
Diffusion weighting gradients are also sensitive to bulk motion. The Stejskal-Tanner gradients, in fact, have a first moment $m_1 = G\delta\Delta$, as indicated by equation (2.33). This means that the presence of bulk motion and/or flow would induce a phase shift in the transverse magnetization. Because physiological motion is typically much faster than diffusion, sequences which make use of diffusion sensitizing gradients are highly sensitive to motion and might be subject to image artifacts. These have usually the form of either ghosting artifacts or signal cancellations which are due to the intravoxel phase dispersion. In order to reduce such problems, gradient shapes consisting of multiple lobes with alternated polarities can be used for diffusion weighting, as shown in Figure 2.12 b. This allows to reduce the sensitivity to bulk motion ($m_1 \approx 0$) while maintaining the sensitivity to diffusion ($b > 0$), at the cost of an increased duration of the diffusion sensitizing block and, consequently, of an increased TE.

Diffusion through Internal Gradients

Diffusion plays an important role in lung MRI, as it strongly affects the transverse relaxation time T_2. Signal attenuation owing to diffusion, in fact, is not only determined by the application of external magnetic field gradients but it can also be induced by the internal gradients. The effect of diffusion through the internal magnetic field gradients consists

in the enhanced loss of phase coherence in the transverse magnetization [68, 130, 149], which manifests itself in a shortening of T_2. This phenomenon is particularly relevant in microscopically heterogeneous media, such as the lung tissue, which are characterized by the presence of relatively strong internal gradients.
The initial evidence for the influence of diffusion through the internal gradients on the transverse relaxation of the lung tissue was the observation of the dependence of T_2 on the measurement method [70, 113]. It was found, in fact, that the T_2 values of the lung tissue which are measured with the single spin-echo (or Hahn-echo) sequence are considerably shorter than those obtained with the multi-echo CPMG sequence [69]. The difference in the T_2 values obtained with the two measurement methods is larger in inflated lungs than in airless lungs [30, 70], indicating that the effect is enhanced by inflation. This observation suggested that the T_2 of the lung is determined by both spin-spin interactions and diffusion through the internal gradients. For this reason, the transverse relaxation of the lung tissue and of other microscopically heterogeneous media can be expressed as [64, 150]:

$$\frac{1}{T_2} = \frac{1}{T_{2,0}} + \frac{1}{T_{2,\mathrm{diff}}} \tag{2.39}$$

where $T_{2,0}$ is the intrinsic transverse relaxation time, which is due to spin-spin interactions, and $T_{2,\mathrm{diff}}$ is the additional transverse relaxation time, which is due to diffusion through the internal gradients. The two relaxation mechanisms are further described in the next sections.

Spin-Spin Interactions

The signal attenuation which is associated with spin-spin interactions and dictated by the relaxation time $T_{2,0}$ is due to random fluctuations of the magnetic field at the sites of the nuclear spins. The magnetic dipole moments of atoms and molecules, in fact, perturb the magnetic field in the surrounding space. Due to diffusion, the magnetic field experienced by each spin randomly fluctuates in time, as shown in Figure 2.13. In this section, a simplified model of spin-spin interactions is presented, as reported in references [74, 75]. For a more detailed description of this phenomenon, the interested reader is referred to references [30, 76, 83].
Suppose that the motion of a given spin can be described as a random walk characterized by a mean free time τ_2. Due to random fluctuations, the magnetic field B_z experienced by the spin is time-dependent and randomly changes value at each step of the random walk. B_z is typically characterized by:

$$\langle B_z \rangle = 0 \tag{2.40}$$
$$\langle B_z^2 \rangle > 0 \tag{2.41}$$

Consequently, the phase accumulated by a spin after a large number of steps N is [74, 75]:

$$\langle \phi \rangle = -\gamma N \tau_2 \langle B_z \rangle = 0 \tag{2.42}$$
$$\langle \phi^2 \rangle = \gamma^2 N \tau_2^2 \langle B_z^2 \rangle > 0 \tag{2.43}$$

This means that spin-spin interactions induce a phase dispersion $\langle \phi^2 \rangle$ in the transverse magnetization, but no net phase shift.

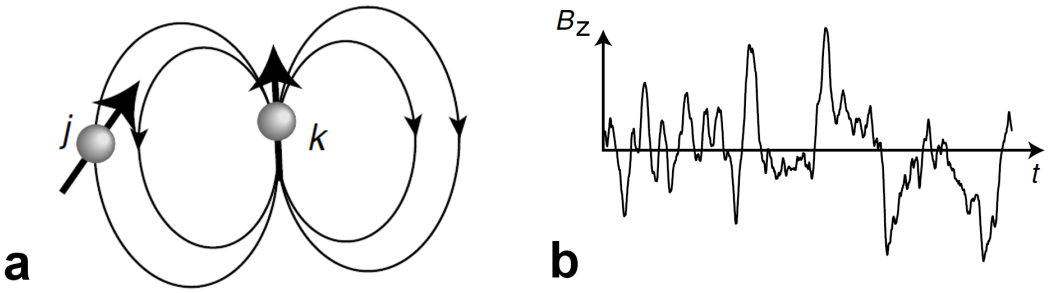

Figure 2.13: a) Influence of the magnetic field generated by a microscopic dipole "k" at the site of a nuclear spin "j" which diffuses in its proximity. b) Corresponding fluctuations of the magnetic field experienced by the spin "j"; the time frequency of the fluctuations is regulated by τ_2. Reproduced with permission from reference [76], with adaptions.

At time $t = N\tau_2$, the transverse magnetization is given by the weighted sum of distributed phase components according to:

$$\frac{M_{xy}(t)}{M_{xy}(0)} = \int e^{i\phi} e^{-\phi^2/2\langle\phi^2\rangle} d\phi = e^{-\langle\phi^2\rangle/2} = e^{-\gamma^2\tau_2\langle B_z^2\rangle\, t/2} \tag{2.44}$$

This corresponds to an exponential attenuation characterized by the relaxation time:

$$T_{2,0} = \frac{2}{\gamma^2\langle B_z^2\rangle\tau_2} \tag{2.45}$$

The attenuation of the transverse magnetization which is due to spin-spin interactions is mainly determined by the characteristics of the magnetic field fluctuations. Shorter $T_{2,0}$ is either due to stronger amplitude of the fluctuations, which is described by $\langle B_z^2\rangle$, or to slower fluctuations, through τ_2.
Due to the multi-compartmental nature of the lung tissue, $T_{2,0}$ in the lung is broadly distributed over a range of values between 15 and 200 ms [70, 112]. The mean value in the healthy lung tissue is about 80 ms [113].

The Carr-Purcell Mechanism

When molecules diffuse through internal magnetic field gradients, the transverse relaxation is enhanced, as suggested by equations (2.37) and (2.38). The Carr-Purcell mechanism described by Carr and Purcell in 1954 [68] explains the dependence of this relaxation enhancement on the pulse sequence used. The basic principle of the Carr-Purcell mechanism is that the signal attenuation which is due to diffusion through the internal gradients can be reduced by increasing the number of refocusing pulses applied between excitation and signal read-out.
Even though the internal gradients are typically inhomogeneously distributed in space, it is useful to consider for the moment the case of a uniform and constant gradient active during the whole pulse sequence, in order to demonstrate the Carr-Purcell mechanism. Under this condition, the Hahn-echo experiment is equivalent to a diffusion-weighted acquisition with

the diffusion sensitizing gradient characterized by $\Delta = \delta = \mathrm{TE}/2$. The b-value for this gradient configuration obtained from equation (2.37) is:

$$b_{\mathrm{Hahn}} = \gamma^2 G^2 \frac{\mathrm{TE}^3}{12} \tag{2.46}$$

The CPMG sequence, instead, is equivalent to an acquisition with a number N of consecutive gradient lobes, which is equal to the number of refocusing pulses. The resulting b-value is given by the sum of the b-values of each individual gradient pair, such that:

$$b_{\mathrm{CPMG}} = \gamma^2 G^2 \frac{\mathrm{TE}^3}{12\,N^2} \tag{2.47}$$

According to equation (2.38), the signal loss which is owing to diffusion is given by:

$$s\,(\mathrm{TE}) \propto \exp\left(-\gamma^2 G^2 \frac{\mathrm{TE}^3}{12N^2} D\right) \tag{2.48}$$

where the Hahn-echo case corresponds to $N = 1$, while the CPMG case is given by $N > 1$.

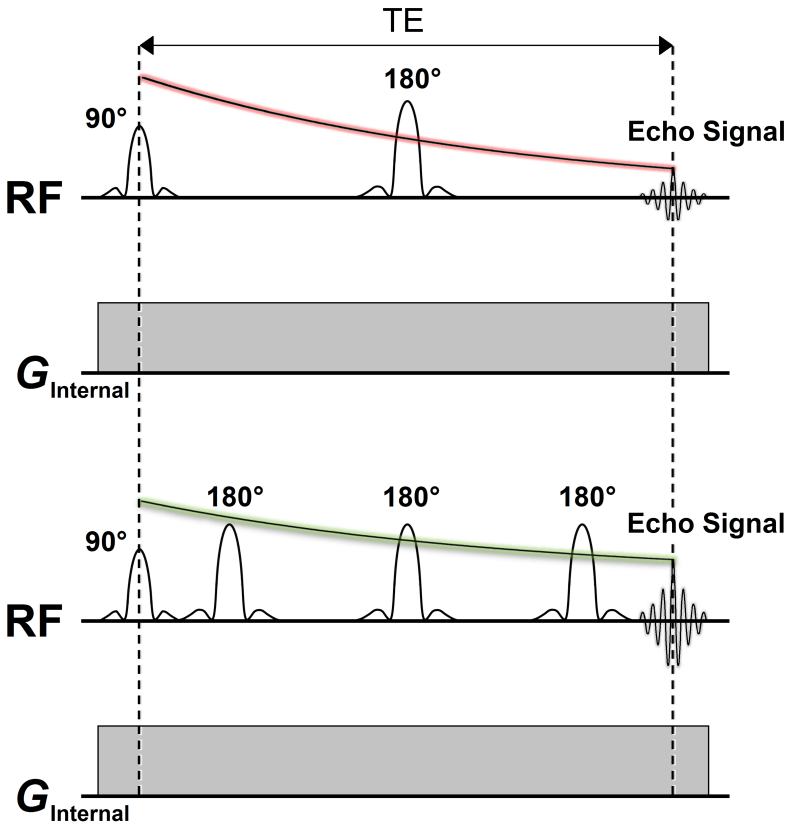

Figure 2.14: Graphical representation of the Carr-Purcell mechanism. In the presence of a gradient, the diffusion-induced signal attenuation at a given echo time is reduced when increasing the number of refocusing pulses between excitation and signal acquisition.

Equation (2.48) states that the diffusion-induced signal attenuation at a fixed TE is reduced by a factor N^2 when using multiple refocusing pulses, as graphically shown in Figure 2.14. This means that in a CPMG sequence the signal attenuation which is due to diffusion through the internal gradients can be reduced by decreasing the inter-pulse time.
The Carr-Purcell mechanism explains the difference which is observed in the T_2 of the lung with the CPMG sequence and the Hahn-echo sequence [70]. However, the transverse relaxation enhancement in the lung is not very well described by equation (2.48), which holds in the case of a spatially uniform gradient. In contrast to the external gradients, in fact, the internal magnetic field gradients of the lung present spatial variations and are broadly distributed [131, 133, 151], as discussed above. In order to better describe the phenomenon of diffusion through the internal gradients in the lung, the concept of diffusion regime must be introduced.

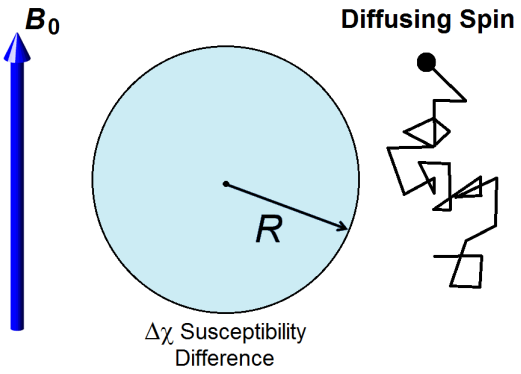

Figure 2.15: Sketch of a spin diffusing, with a diffusion coefficient D, about a magnetized sphere of radius R and equatorial field $\delta\omega$ (in the units of angular frequency). Reproduced with permission from reference [152], with adaptions.

Diffusion Regimes

In general, for heterogeneous media such as the lung, the transverse relaxation enhancement which is induced by diffusion through the internal gradients depends on the following factors: 1) the microstructural geometry of the considered system, 2) the pulse sequence used and 3) the diffusion regime, as previously described by Hürlimann [130, 151]. The concept of diffusion regime is used to describe the relationship between the space in which the molecules diffuse and the diffusion time. In MRI, it can be used to characterize both diffusion through the internal magnetic field gradients and diffusion through uniform external gradients in the presence of spatial restrictions to motion. Here, the diffusion regimes which characterize diffusion through the internal gradients in the presence of spherical magnetic field perturbers is discussed, following the description of Yung [152]. For a more general discussion on the topic of diffusion regimes, the interested reader is referred to references [130, 153, 154, 155].
A simple model, which can be used to describe the phenomenon of diffusion through the internal gradients of the lung, is a spin diffusing around a magnetized sphere of radius R,

as shown in Figure 2.15. In this model, the sphere represents the pulmonary alveolus. The diffusion regime of such a system depends on the interplay of the following parameters [152]:

1. the time $\tau = R^2/D$ which is necessary for a spin to diffuse by a length R;
2. the frequency offset at the equator of the sphere $\delta\omega = \gamma\Delta\chi B_0/3$.

Based upon the relative magnitude of τ and $\delta\omega$, the relaxation behavior can be categorized in the following two diffusion regimes:

- Slow (or free) diffusion regime. It applies when $1/\tau < \delta\omega$. In this case, the spins diffuse small distances compared to the length scale on which the internal gradients change, which is of the order of R. Hence, the magnetic field gradient experienced by each spin is approximately constant during TE. Due to the broad distribution of internal gradients, the signal decay is given by a weighted superposition of multiple exponential components characterized by different relaxation rates. Each of them corresponds to a different value of G_{int}, according to equation (2.48). This is mathematically expressed by [131, 134, 151, 156]:

$$s\,(\text{TE}) \propto \int p\,(G_{\text{int}}) \exp\left(-\gamma^2 G_{\text{int}}^2 D \frac{\text{TE}^3}{12\,N^2}\right) dG_{\text{int}} \tag{2.49}$$

  where $p(G_{\text{int}})$ is the probability density function associated with the internal gradients. In general, the signal decay curve of equation (2.49) depends on the specific distribution of internal gradients and, thus, on the microstructural geometry of the considered system. Nevertheless, Weisskoff et al. [157] experimentally found that the signal amplitude decay for a system of densely packed spheres similar to the lung model used by Case et al. [67], can be well approximated by a mono-exponential decay. The corresponding transverse relaxation time $T_{2,\text{diff}}$ for the Hahn-echo sequence has been empirically found by Yung [152]. This is given by:

$$\frac{1}{T_{2,\text{diff}}} = \beta \frac{\eta}{R} \sqrt{\gamma \frac{\Delta\chi}{3} B_0 D} \tag{2.50}$$

  where $\beta \simeq 3.8$ is a dimensionless constant of proportionality and η is the fraction of volume which is occupied by the spheres. In the lung, this corresponds to the fractional volume of air, as discussed above.

- Fast diffusion (or motional averaging) regime. It applies when $1/\tau > \delta\omega$. In this case, the spins diffuse large distances compared to R and, therefore, they experience a broad spectrum of magnetic field gradients during TE. These are averaged out by motion. Because of this averaging effect, the spatial distribution of the internal gradients and the corresponding probability density function do not have any influence on the signal behavior [152]. In this case, the signal amplitude decays exponentially with a decay rate [152]:

$$\frac{1}{T_{2,\text{diff}}} = \alpha\,\eta \frac{\gamma^2 \Delta\chi^2 B_0^2 R^2}{D} \tag{2.51}$$

  where $\alpha \simeq 0.48$ is a dimensionless constant of proportionality. An example of motional averaging is represented by spin-spin interactions, as indicated by equation (2.45) [30].

In the case of the lung, considering the typical values of the alveolar radius and of the susceptibility difference, as previously mentioned, in combination with the diffusion coefficient of water D_w and with a static magnetic field $B_0 = 1.5$ T, the parameters which determine the diffusion regime are: $\tau \approx 4.35$ s and $\delta\omega \approx 1340$ s^{-1}. This means that the condition $1/\tau < \delta\omega$ is fulfilled and, thus, the slow diffusion regime holds.

Intravoxel Incoherent Motion

In MRI, the expression Intra-Voxel Incoherent Motion (IVIM) designates any kind of microscopic and directionally incoherent motion that occurs within a voxel. In biological tissues, this includes essentially molecular diffusion and blood microcirculation in the capillary network [59, 60]. The basic concept of IVIM, introduced by Le Bihan in 1986 [59], is that blood microcirculation mimics a diffusion process due to the pseudorandom organization of the capillary network within the voxel. Therefore, in the presence of a magnetic field gradient, the spin displacement which is due to perfusion produces a phase dispersion in the transverse magnetization, similarly to molecular diffusion. This loss of phase coherence at the voxel level is responsible for a further attenuation of the signal amplitude of flowing blood, in addition to that which is caused by spin-spin interactions and by conventional diffusion. The signal attenuation which is induced by blood microcirculation is proportional to the velocity of blood and, therefore, is typically one order of magnitude larger compared to molecular diffusion. For this reason, the relative contributions of diffusion and perfusion to the signal decay are significantly different and can be separated from each other [59].

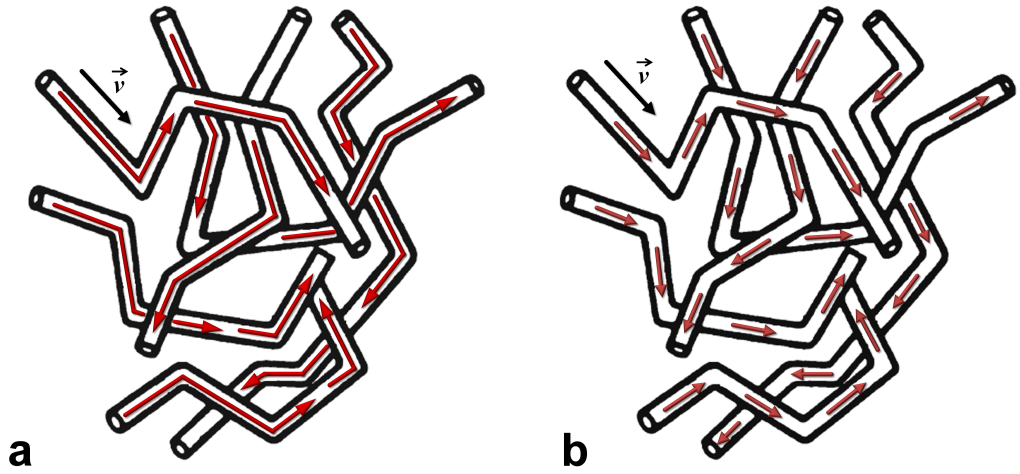

Figure 2.16: Example of the two models of IVIM. a) Blood flow changes capillary segment several times during TE, such that the movement of spins mimics a diffusion process with pseudo-diffusion coefficient D^*. b) Blood flow does not change capillary segment during TE; in this case, signal attenuation is due to the random orientation of the capillaries at the voxel level. Reproduced with permission from reference [60], with adaptions.

In order to describe the signal attenuation owing to blood microcirculation, a two-compartmental model of biological tissues is used. In this model, the water molecules are divided up into an intravascular and an extravascular compartment. The intravascular compartment represents the flowing blood, whereas the extravascular compartment represents the parenchymal tissue. In a spin-echo sequence, the overall signal attenuation is described by [60]:

$$s\left(\mathrm{TE}, b\right) = \exp\left(-\frac{\mathrm{TE}}{T_2}\right) \exp\left(-bD\right) \left[fF + (1-f)\right] \tag{2.52}$$

where f represents the fraction of spins in the intravascular compartment (flowing spins) while $1-f$ is the remaining fraction of spins in the extravascular compartment (diffusing spins). Both compartments experience signal attenuations which are due to spin-spin interactions as well as to diffusion. These depend respectively on TE and on the b-value of the applied gradients. The intravascular compartment experiences an additional signal attenuation, which is expressed by means of the flow attenuation factor F.
The value of F can be calculated on a statistical basis, due to the large amount of capillaries in a voxel (5700 mm^{-3} in the brain [60]). Assuming that the capillary network can be modeled as a series of straight capillary segments, the expression for F will depend on the average length of the segments (l) and on the mean velocity of blood in the capillaries (v) [60]. Depending on the interplay of l, v and TE, the following two models can be applied (see Figure 2.16):

1. In the first model, blood flow changes capillary segment and direction several times during TE. In this case, the movement of spins in the capillary network can be assimilated to a diffusion process. The expression for F is thus:

   $$F = e^{-bD^*} \tag{2.53}$$

   where D^* is called pseudo-diffusion coefficient and represents the effective diffusion coefficient associated with blood microcirculation. Its value can be approximated with $D^* \approx lv/6$, by analogy with the diffusion coefficient in equation (2.24). Assuming typical values for $l \approx 57$ μm and $v \approx 2.1$ mm/s [60], the expected D^* is about $2.0 \cdot 10^{-2}$ mm^2/s. This value is about one order of magnitude greater than the diffusion coefficient of water, which means that perfusion induces a much faster signal attenuation than diffusion. With this model, equation (2.52) results in a bi-exponential decay.

2. In the second model, blood flow does not change capillary segment during TE, either because flow is relatively slow or because TE is relatively short. Nevertheless, each spin in the voxel accumulates a different phase shift due to the different direction of flow with respect to the applied gradients, according to equation (2.31). In this case, F is determined by the following weighted superposition of dephased signal components:

   $$F = \int e^{-i\,\gamma\,\vec{m}_1 \cdot \vec{v}} p\left(\vec{v}\right) d^3v \tag{2.54}$$

   where $p\left(\vec{v}\right)$ is the probability density function of spins with a certain velocity.

The IVIM imaging approach is usually based on the acquisition of several images with different b-values. An example of the typical signal attenuation curve which is obtained with

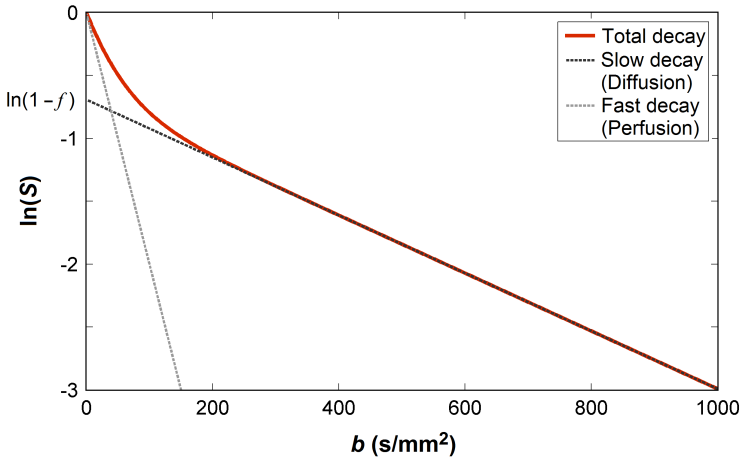

Figure 2.17: Example of the typical signal attenuation curve for IVIM imaging: at small b-values the signal attenuation is prevalently induced by perfusion, while at large b-values it is mainly dictated by diffusion in the extravascular compartment [60].

this approach is shown in Figure 2.17. In the region of small b-values, signal attenuation is prevalently induced by perfusion, due to the higher mobility of flowing blood with respect to diffusing molecules. At larger b-values, the blood signal is completely suppressed and signal attenuation is dictated by diffusion in the extravascular compartment.
The data acquired with the IVIM approach can be used to quantify the fractional volume of water in the intravascular compartment f, which is also known as blood volume fraction, as well as the pseudo-diffusion coefficient of blood D^*. These represent quantitative indicators for regional perfusion [61]. In order to quantify f or D^*, the acquired data are fitted with the model of equation (2.52) using the appropriate value of F.

Chapter 3

Materials and Methods

In this work, three image acquisition techniques based on proton MRI are presented, which allow to quantify characteristic parameters of the lung tissue. These are: 1) the blood volume fraction f, 2) the transverse relaxation time $T_{2,\text{diff}}$ which is due to diffusion through the internal gradients and 3) the spectral line broadening. Furthermore, the possibility to exploit the knowledge of $T_{2,\text{diff}}$ for the quantification of the alveolar diameter is investigated. All techniques are based on the use of the same pulse sequence: the single shot turbo spin-echo with half-Fourier acquisition (HASTE) [33, 34]. Nevertheless, each technique is characterized by the use of a different magnetization preparation module. In this chapter, the experimental methods of image acquisition and reconstruction that are of general interest for this work are described. These include partial Fourier reconstruction, parallel imaging as well as technical aspects regarding the HASTE sequence. A more detailed description of each of the proposed techniques is provided in the next three chapters, together with the results obtained from the experiments.

3.1 Image Acquisition and Reconstruction Techniques

The HASTE Sequence

The HASTE is a variant of the TSE sequence characterized by the fact that the data which is required for the reconstruction of a 2D image is acquired within a single echo-train (i.e. with a single excitation). The advantages of the HASTE sequence, with respect to the conventional TSE, are: 1) the reduced acquisition times and, consequently, 2) the reduced sensitivity to motion. With the TSE sequence, in fact, image acquisition requires the application of multiple excitation pulses, each with the corresponding echo-train. These are also known as "shots". The different shots are typically separated by a repetition time of the order of several seconds, in order to allow for the recovery of the longitudinal magnetization. Because respiration, cardiac motion and blood flow are typically modulated on time scales of the order of seconds, they might generate image artifacts with the conventional TSE sequence, as already discussed in Chapter 1. With the HASTE sequence, instead, the image is acquired in a single shot, with a total acquisition time of the order of a few hundred milliseconds. This is of great advantage for lung imaging, due to the possibility to acquire multiple artifact-free images in a single breath-hold. Furthermore, like in the conventional TSE sequence, the use of refocusing pulses

reduces the signal losses which are induced by magnetic field inhomogeneities. This aspect is of primary importance for lung imaging because of its relatively short T_2^*.
Thanks to the features described above, the HASTE sequence is one of the most commonly used pulse sequences for lung imaging [34]. Nevertheless, because of the relatively long echo-trains which are required to acquire the whole k-space in a single shot, this technique is sensitive to other effects such as: signal losses induced by the T_2 decay and, consequently, image blurring, as discussed in Chapter 1. Because both of these effects can be reduced by means of shorter echo-train lengths, the inter-echo time of a HASTE sequence should be as short as possible. For this reason, relatively short refocusing pulses are commonly used, at the cost of a degraded slice profile and increased RF-power deposition, together with relatively high receive bandwidths. Another characteristic of the HASTE sequence is that the k-space is only partially sampled in the PE direction and image reconstruction is performed using a dedicated algorithm, as further described in the next section.
The characteristic parameters of the HASTE sequence are: the Partial-Fourier Factor (PFF), which represents the fraction of k-space lines that are actually acquired as compared to a full k-space acquisition, and the echo-train length, which corresponds to the total number of acquired k-space lines. This parameter depends on the matrix size in the PE direction and on PFF.

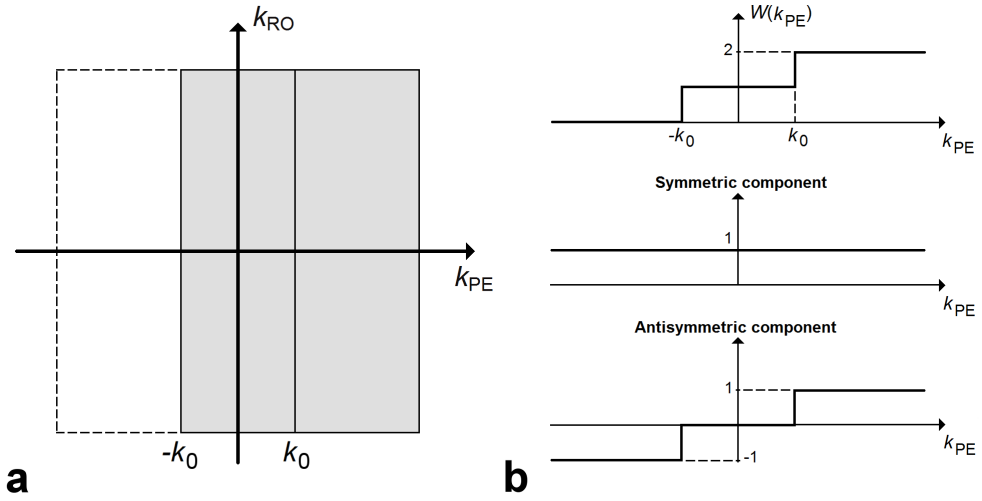

Figure 3.1: a) Example of k-space sampling pattern which is used for partial-Fourier acquisition in the PE direction. b) Example of the filter $W(k)$ which is used to reconstruct a partially acquired k-space, together with its symmetric and antisymmetric components. These generate the real and imaginary parts of the point spread function, respectively.

Partial-Fourier Acquisition and Reconstruction

Partial-Fourier techniques, such as the HASTE, are based on the partial acquisition of the k-space. This is symmetrically sampled around the center, in the low frequency region, and asymmetrically sampled over the high frequencies, as shown in Figure 3.1 a. Image reconstruction from an asymmetrically sampled k-space can be performed by exploiting the symmetry properties of the Fourier transform. In fact, even though MRI images can depict the spatial distribution of both amplitude and phase of the magnetization, for most applications only the amplitude is of interest, as it provides the conventional image contrasts (T_1, T_2, T_2^*, ρ, diffusion, etc.). In order to obtain the required information about the signal amplitude, the reconstruction of a real-valued image, in alternative to a conventional complex image, would be sufficient [73]. The basic principle behind partial-Fourier imaging is that real-valued functions present a Hermitian symmetry in the k-space. This is mathematically expressed by [73]:

$$S(-\vec{k}) = S^*(\vec{k}) \tag{3.1}$$

where * denotes complex conjugation. With this assumption, only half of the data need to be collected, in principle, in order to reconstruct a real-valued image, while the uncollected data could be synthesized by conjugate reflection across the origin. Unfortunately, many sources of phase shift can cause the magnetization to present a complex pattern throughout the FOV such that, in practice, the real-valued assumption is often violated. These phase shift sources include [73]: magnetic field inhomogeneities, motion, eddy currents and spatially inhomogeneous phase of the RF-coils sensitivity. As a result, additional information is required before applying conjugate reflection. This information is typically provided by the strip of data which is symmetrically sampled in the region of the k-space center.
A number of different algorithms for partial-Fourier reconstruction have been proposed in the past [158, 159]. In this section, the basic principles of a technique called homodyne processing will be discussed, following the description of Bernstein et al. [73].
The simplest way to reconstruct a partial k-space data set is to simply fill the uncollected data with zeroes. The standard FFT-based reconstruction can then be used to obtain a magnitude image. This approach, called zero-filling, results normally in poor image quality, as it does not synthesize the missing data. In the assumption of a real-valued function, the conjugate reflection technique is equivalent to calculating the real part of the image which results from a zero-filled k-space multiplied by the following weighting function (see Figure 3.1 b):

$$W(k) = \begin{cases} 0 & k \leq -k_0 \\ 1 & -k_0 \leq k \leq k_0 \\ 2 & k \geq k_0 \end{cases} \tag{3.2}$$

where k_0 is the lower limit of the partially acquired region of k-space. Direct image reconstruction from the weighted k-space, through an inverse FFT, would normally generate image blurring in the direction with partial k-space coverage as well as ringing near sharp

edges, which is known as Gibbs ringing. The reason for these effects can be identified by considering that the reconstructed image is the convolution between the native image and the point spread function which is associated with $W(k)$, as described in Chapter 1. The antisymmetric component of $W(k)$, which is shown in Figure 3.1 b, generates a broad and oscillating imaginary part of the point spread function. Therefore, in the presence of undesired phase shifts, the signal is spread over the whole image. The real part of the point spread function, instead, results from the constant symmetric component of $W(k)$ and presents a sharp peak which does not contribute to signal spreading.
In order to reduce image blurring and Gibbs ringing, phase correction must be applied before the k-space symmetry can be exploited. The whole image reconstruction process can be resumed as follows:

1. A low resolution phase-image ϕ_{LR} is reconstructed from the inverse Fourier transform of the central and symmetrically sampled k-space data.

2. The partially acquired k-space data is preweighted using the filter $W(k)$ and inverse Fourier transformed to produce an image S_{PF}.

3. Phase correction is performed by multiplying image S_{PF} by $e^{-i\,\phi_{\mathrm{LR}}}$. Because phase variations usually present a low frequency pattern, the low resolution phase-image is usually sufficient to achieve acceptable phase correction.

4. The final image is obtained as the real part of the phase-corrected image, which can be expressed by:
$$S = \Re\left[S_{\mathrm{PF}}\, e^{-i\,\phi_{\mathrm{LR}}}\right] \tag{3.3}$$

In order to generate a point spread function that minimizes residual blurring and Gibbs ringing in the final image, the use of smoother (or apodized) filters instead of that in equation (3.2) might be beneficial, as proposed by Margosian et al. [158, 159]. In principle, partial-Fourier acquisition can be performed in any direction of the k-space. In the HASTE sequence, the PE direction is used with the aim to shorten the echo-train length and to reduce both signal losses which are due to the T_2 decay and image blurring.

Parallel Imaging

Parallel imaging is based on the use of multi-channel RF-coils for signal detection. These consist of multiple RF-elements that can be simultaneously used for signal acquisition. The original purpose of parallel imaging was to increase SNR [73]. In high field MRI ($B_0 > 0.2$ T), in fact, the detected noise comes predominantly from fluctuations in the sample and, therefore, is modulated by the sensitivity profile of the coil [73]. This is indicated as B_1^- in equation (1.42). In a multi-channel coil, each element is sensitive to the signal which is generated in a small region of space relatively to the whole FOV. Therefore, the noise which is induced on each coil element is reduced in comparison to a coil that is sensitive to the whole volume of the sample. The images obtained from the different coil

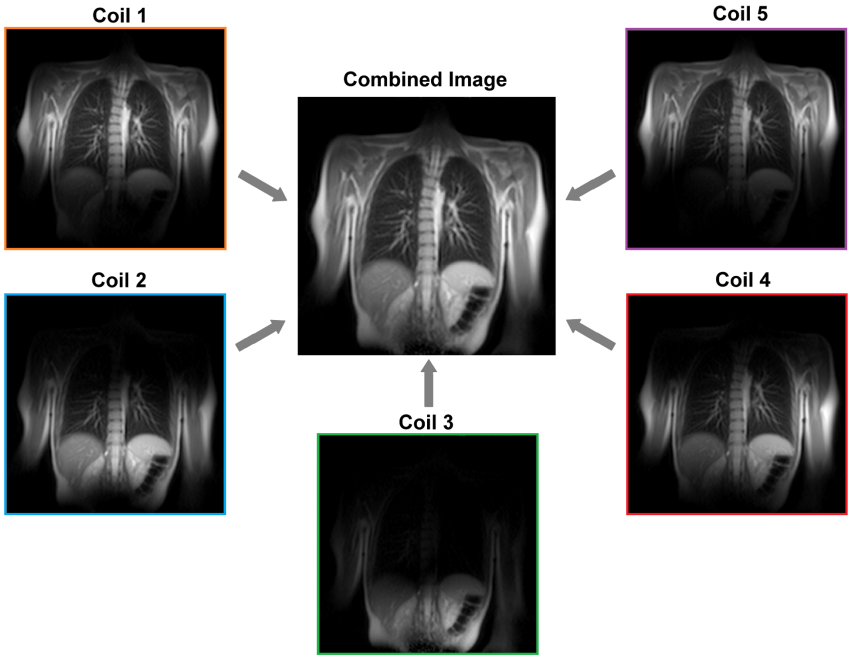

Figure 3.2: Example of coronal images of the human lung obtained from different elements of a multi-channel RF-coil (indicated as Coil 1-5) and corresponding image resulting from the combination (sum of squares) of all coil elements.

elements are then combined by using the sum of squares or other strategies, in order to generate a homogeneous image, as illustrated in Figure 3.2.
In the last two decades, the further application of parallel imaging to accelerate the data acquisition has been proposed and largely investigated. This is possible by exploiting the spatial information which is provided by the sensitivity profiles $B_1^-(\vec{r})$ of the elements of a multi-channel coil. Each coil element, in fact, has a different spatial sensitivity and, thus, a different view of the object, which is given by the product between $B_1^-(\vec{r})$ and the signal generated in the sample.
Several parallel imaging techniques have been developed in the last years [24, 25, 26, 27]. All of them are based on the same idea of undersampling the k-space by skipping the acquisition of a certain fraction of k-space lines. In the case of the HASTE sequence, the use of parallel imaging allows to reduce image blurring in the PE direction as well as its sensitivity to physiological motion, thanks to the shorter echo-trains required.
All parallel imaging techniques are characterized by an Acceleration Factor (AF), which is defined as the ratio between the number of lines of a fully sampled k-space and the number of actually acquired lines. An example of the typical k-space sampling pattern which is used for 2D parallel imaging is shown in Figure 3.3: the acquisition of a number of k-space lines

is regularly skipped, proportionally to AF. Such sampling pattern is equivalent to acquiring an image with FOV reduced by a factor AF in comparison to the actually desired FOV, as stated by the Nyquist criterion of equation (1.48). When directly reconstructing the MR image with an inverse FFT from the undersampled k-space, image aliasing is typically observed. This consists in the in-folding of the signal which is generated outside the actual FOV into the image, in the form of a series of image replicas shifted by a distance factor FOV/AF from each other. An example of aliasing is shown in Figure 3.3.
The different parallel imaging techniques make use of different reconstruction algorithms. Depending on which approach is used, two main categories can be identified: algorithms operating in the image space, which allow to unfold aliasing, and algorithms operating in the k-space, which provide a full k-space. For all parallel imaging techniques, information about the coil sensitivity profiles is necessary. This can be achieved by using either a dedicated separate scan, or by fully sampling the inner region of the k-space according to the Nyquist criterion while undersampling the outer part.

GRAPPA Reconstruction

In this section, the basic principles of Generalized Autocalibrating Partially Parallel Acquisitions (GRAPPA) are described. GRAPPA was proposed in 2002 by Griswold et al. [26] and belongs to the category of parallel imaging methods which operate in the k-space. For each receive channel, a full k-space data set is generated by synthesizing the missing k-space points (target points) from the available acquired data (source points).
According to equation (1.42), the MR signal at a certain location of the k-space for a given coil element is given by:

$$S_j(\vec{k}) \propto \int_V \rho\left(\vec{r}\right) C_j\left(\vec{r}\right) \, e^{-i\,2\pi\vec{k}\cdot\vec{r}}\, d^3r \tag{3.4}$$

where j is the index that denotes the coil element and $C_j\left(\vec{r}\right) \propto B_1^-\left(\vec{r}\right)$ is a dimensionless weighting function that reflects its sensitivity profile. The basic idea of GRAPPA reconstruction is to calculate the value of a target point as a linear superposition of the values of a set of source points. The block of source points, which are used for this calculation, is called GRAPPA kernel. An example of GRAPPA kernel is shown in Figure 3.4: in order to reconstruct a single target point, a superposition of the six closest points across all channels is used.
With the assumption mentioned above, the value of a target point can be expressed as:

$$S_j(\vec{k}) = \sum_{l=1}^{N_c} \sum_{m=1}^{N_{sp}} S_l(\vec{k}_m)\, w_{j,l,m} \tag{3.5}$$

where N_c is the number of coil elements (or receive channels) used, N_{sp} is the number of source points in the GRAPPA kernel and $w_{j,l,m}$ are the weighting factors of the linear combination, which are called GRAPPA weights.

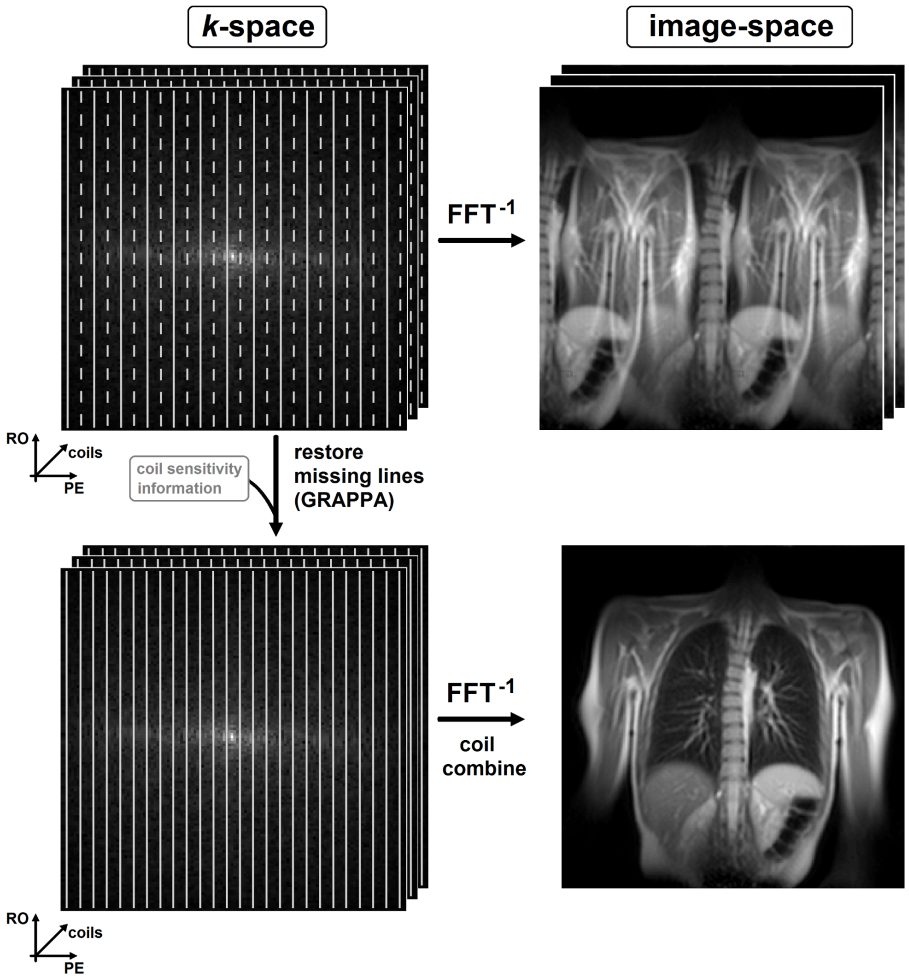

Figure 3.3: Top left: Example of k-space sampling pattern which is used for parallel imaging acquisition, with AF = 2; the dashed lines represent the skipped k-space lines; every second line is regularly skipped. Top right: Corresponding image reconstructed from the undersampled k-space by means of an inverse FFT; the image is affected by the typical aliasing artifact, which consists in two replicas of the image shifted by FOV/2 from each other. Bottom left: GRAPPA allows to restore the missing k-space lines. Bottom right: Image reconstructed after application of GRAPPA; aliasing is completely unfolded.

The key feature behind GRAPPA reconstruction is that the GRAPPA weights do not depend on the k-space coordinate of the target point, but only on the relative distances in the k-space between target point and source points, which are given by $\Delta\vec{k}_m = \vec{k}_m - \vec{k}$.

This can be demonstrated by substituting equation (3.4) in (3.5), which results in:

$$\sum_{l=1}^{N_c} \sum_{m=1}^{N_{sp}} w_{j,l,m}\, C_l\left(\vec{r}\right)\, e^{-i\,2\pi\Delta\vec{k}_m\cdot\vec{r}} = C_j\left(\vec{r}\right) \tag{3.6}$$

Thanks to this feature, the GRAPPA problem reduces to finding the correct GRAPPA weights for all coil elements and all source points in a given GRAPPA kernel. Due to the regularity of the k-space sampling pattern, the same GRAPPA kernel can then be used in combination with the corresponding GRAPPA weights for the calculation of several target points by means of equation (3.5).
The calculation of the GRAPPA weights is performed by means of an Auto-Calibration Scan (ACS). The ACS consists in the acquisition of a small region of k-space, usually about the k-space center, with full Nyquist sampling. The ACS can be either integrated in the imaging scan, or separately acquired. In the latter case, the image contrast of the ACS must not be necessarily identical to the imaging scan. The GRAPPA weights are

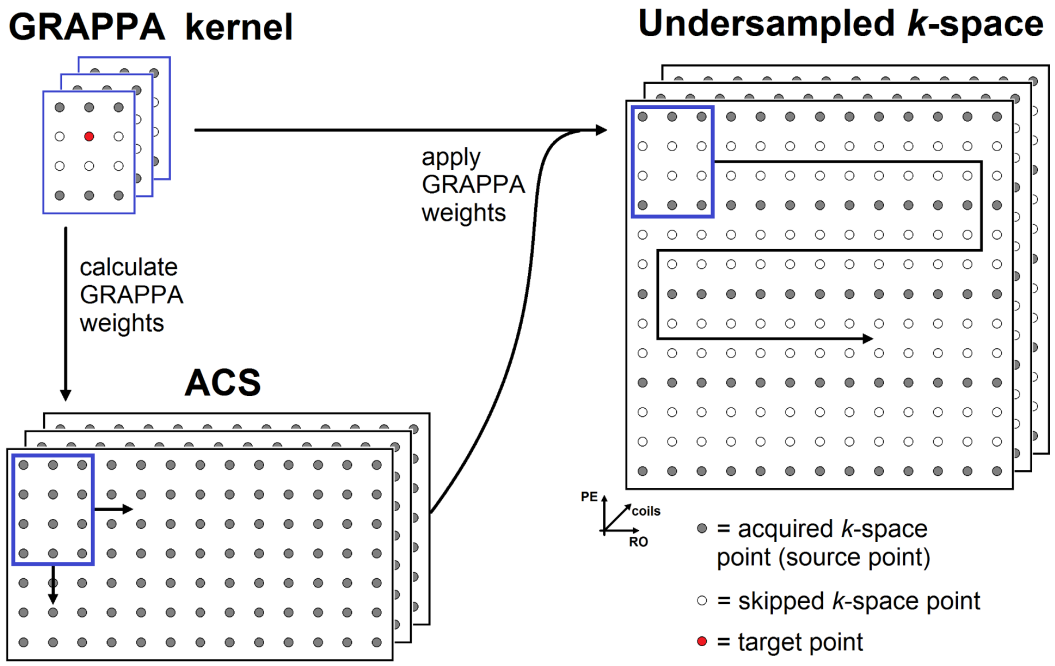

Figure 3.4: Schematic representation of GRAPPA reconstruction: the GRAPPA kernel is first used to calculate the GRAPPA weights by exploiting the multiple repetitions of the kernel in the ACS data; the obtained GRAPPA weights are then applied on the undersampled k-space to restore the missing points.

obtained from the ACS data. For this purpose, equation (3.5) is used to form a set of linear equations, in which the GRAPPA weights are the only unknown parameters. This can be expressed in matrix form for each coil element j and each GRAPPA kernel by:

$$\mathbf{s}_j = \hat{S}_j \cdot \mathbf{w}_j \tag{3.7}$$

where $\mathbf{s}_j$ is an array of size N_{tp}, which includes all target points $S_j(\vec{k})$ in the ACS that are used as reference for the calibration. $\hat{S}_j$ is a matrix consisting of N_{tp} lines and $N_c \times N_{sp}$ columns; each element of the matrix corresponds to a source point of the GRAPPA kernel, with value $S_l(\vec{k}_m)$. For each target point in the ACS, one line of the matrix $\hat{S}_j$ is filled using all source points in the GRAPPA kernel and all coil elements. To obtain multiple matrix lines, several different repetitions of the GRAPPA kernel within the ACS are used, as shown in Figure 3.4. Finally, $\mathbf{w}_j$ is a column array of size $N_c \times N_{sp}$; its elements are the unknown GRAPPA weights.
The GRAPPA weights are obtained by inverting equation (3.7). In order to solve the system, the number of equations must be large enough. This means that the ACS data must fulfill the condition $N_{tp} \geq N_c \times N_{sp}$. In practice, a number of equations larger than $N_c \times N_{sp}$ is commonly used to increase the stability of the solution against noise. This results in an overdetermined system, which is solved with a least squares approximation.

SNR Considerations in Parallel Imaging

The main drawback of parallel imaging techniques is a loss of SNR in the reconstructed image, as compared to the image which would be obtained from a fully sampled k-space [25]. This loss of SNR is usually spatially varying and increases with AF. Two factors contribute to this effect. The first one is the reduced number of acquired k-space lines which generates a loss of SNR proportional to $\sqrt{\mathrm{AF}}$, as indicated by equation (1.64). The second factor is intrinsic to the reconstruction algorithm and originates from the sensitivity profiles of the coil elements. In order to effectively remove aliasing and obtain better SNR, in fact, the coil elements must have possibly different sensitivities. In practice, this condition cannot be fulfilled for all locations in space, such that in the regions where the coil sensitivities are similar, residual aliasing and SNR reduction can occur. This additional loss of SNR is described by means of the so called geometry factor $g(\vec{r})$. The geometry factor depends on the specific sensitivity profiles of the coil elements and represents a measure for the suitability of the coil configuration for parallel imaging applications; it can be calculated for each image voxel and typically increases with AF. When considering both effects described above, the SNR of an image reconstructed with parallel imaging techniques ($\mathrm{SNR}_{parallel}$) can be expressed as a function of the SNR which is obtained with a fully sampled k-space (SNR_{full}) as [73, 25]:

$$\mathrm{SNR}_{parallel}(\vec{r}) = \frac{\mathrm{SNR}_{full}(\vec{r})}{g(\vec{r}) \cdot \sqrt{\mathrm{AF}}} \tag{3.8}$$

In theory, for an ideal combination of coil sensitivities, the maximum acceleration factor achievable is given by N_c. In practice, due to the loss of SNR, acceleration factors between 2 and 6 are normally used for clinical applications.

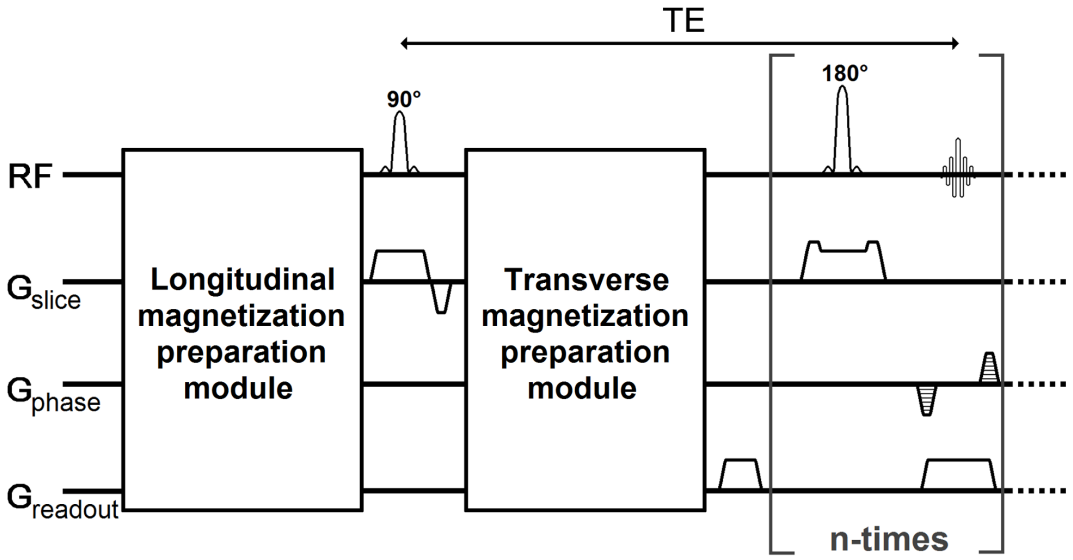

Figure 3.5: Example of the timing diagram of a HASTE sequence with magnetization preparation of both the longitudinal and transverse components.

Magnetization Preparation

The HASTE sequence can be used in combination with several magnetization preparation modules. These can be imagined as a series of RF-pulses and gradient lobes that are applied before data acquisition and allow for the manipulation of the image contrast. The position of the preparation module in the HASTE sequence typically depends on which component of the magnetization shall be prepared. As shown in Figure 3.5, preparation modules that act on the longitudinal magnetization are normally placed in front of the sequence, before the excitation pulse, whereas preparation modules that act on the transverse magnetization are placed between excitation and signal readout. Examples of longitudinal and transverse magnetization preparation modules of interest for this work are, respectively:

- Inversion recovery. It consists of a 180° RF-pulse followed by spoiling gradients, as shown in Figure 3.12 [73, 75]. The aim of the 180° pulse is to fully invert the direction of the longitudinal magnetization. The subsequent spoiling gradients serve to cancel the unwanted residual transverse magnetization, which possibly results from imperfections in the flip-angle of the RF-pulse. The time distance between the peak

of the inversion pulse and the peak of the excitation pulse is called inversion time (TI) and can be arbitrarily chosen. During TI, the longitudinal magnetization tends to recover its equilibrium position according to:

$$M_z\,(\mathrm{TI}) = M_0\left[1 - 2\exp\left(-\frac{\mathrm{TI}}{T_1}\right)\right] \tag{3.9}$$

The available longitudinal magnetization at the time of excitation is then flipped in the transverse plane and the generated signal is acquired. TI regulates the T_1 contrast in the resulting image according to equation (3.9), as shown in the curve of Figure 3.12.

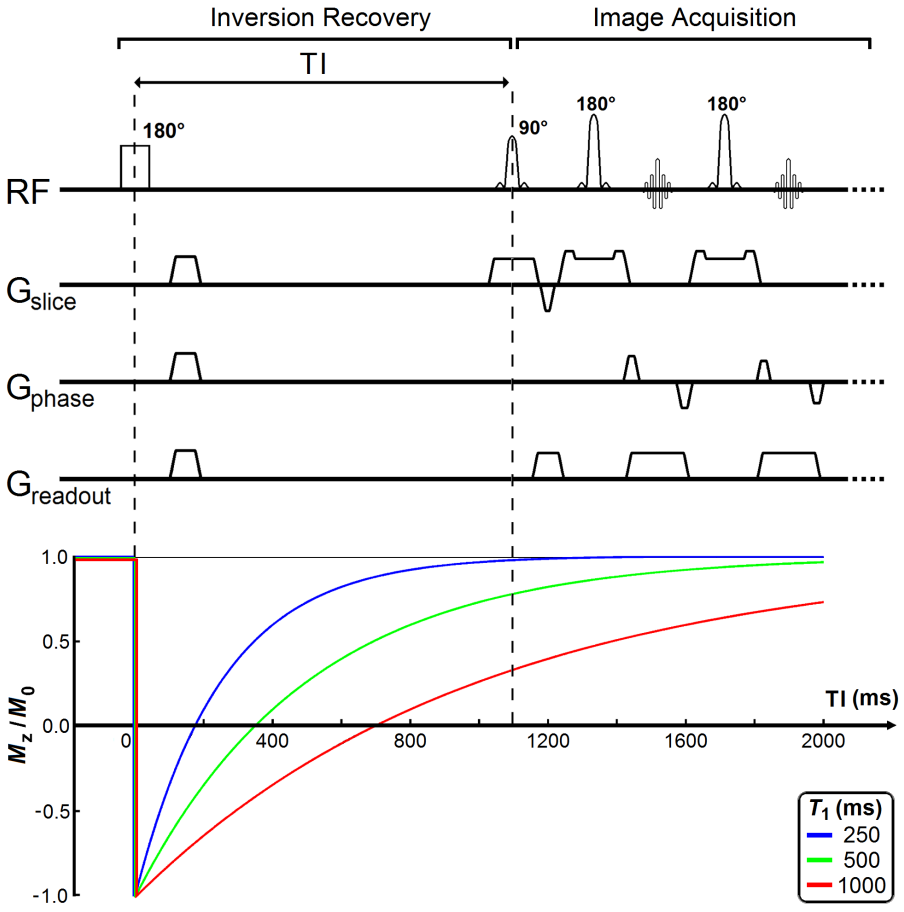

Figure 3.6: Diagram of the inversion recovery preparation module (top) and corresponding relaxation curves for the longitudinal magnetization (bottom).

- Diffusion. As discussed in Chapter 2, diffusion preparation consists in a series of gradient lobes placed between excitation and signal readout. In the HASTE sequence, diffusion weighting is typically achieved by placing a pair of diffusion sensitizing gradients at each side of the first refocusing pulse (Stejskal-Tanner configuration), as shown in Figure 2.12 a. The introduction of diffusion sensitizing gradients in the HASTE sequence can result in violations of the CPMG conditions that need to be addressed, as further discussed in the next section.

Violation of the CPMG Conditions

In the HASTE sequence, violations of the CMPG conditions can occur in the presence of transverse magnetization preparation modules [73]. Diffusion preparation contributes to violate both CPMG conditions, as described below:

1. According to the first CPMG condition, the RF-phase of the excitation pulse must be shifted by $\pi/2$ with respect to the RF-phase of the refocusing pulses. This means that the excited magnetization and the RF-phase of the refocusing pulses must be aligned. The diffusion sensitizing gradients can induce unwanted phase shifts in the transverse magnetization due to motion, violating the CPMG condition.

2. According to the second CPMG condition, the phase accumulated by the transverse magnetization between two consecutive refocusing pulses must be equal throughout the whole the pulse-train. This means that the inter-pulse time must be constant. This condition is usually violated by diffusion preparation, as the duration of its gradient lobes, of the order of several tens of milliseconds, is much larger than the typical inter-pulse times of a HASTE sequence, which is of the order of a few milliseconds.

In the case of violations of the second CPMG condition, the residual longitudinal magnetization which is available at the end of the preparation module would generate stimulated echoes later in the echo-train. These typically have a different phase with respect to the primary spin-echoes [73, 160, 161, 162]. This effect would result in signal cancellations in the image, as shown in the example of Figure 3.7. Such problem can be addressed by using different zeroth moments for the crushing gradients of the refocusing pulses that are applied in the preparation module and those that are applied in the subsequent echo-train [163, 164]. This approach avoids that the residual longitudinal magnetization which is available at the end of the preparation module can be refocused by the subsequent RF-pulses. In the Stejskal-Tanner configuration, this issue is usually addressed by the diffusion sensitizing gradients themselves, which typically have a much larger zeroth moment compared to the crushing gradients of the refocusing pulse train.
Violations of the first CPMG condition require more complex solutions. In TSE-based sequences, such as the HASTE, the transverse magnetization can be split into two components [165, 166, 167]:

1. the in-phase component ($M_{\parallel}$), which is the transverse magnetization aligned with the RF-phase of the refocusing pulses and, thus, satisfies the first CPMG condition;

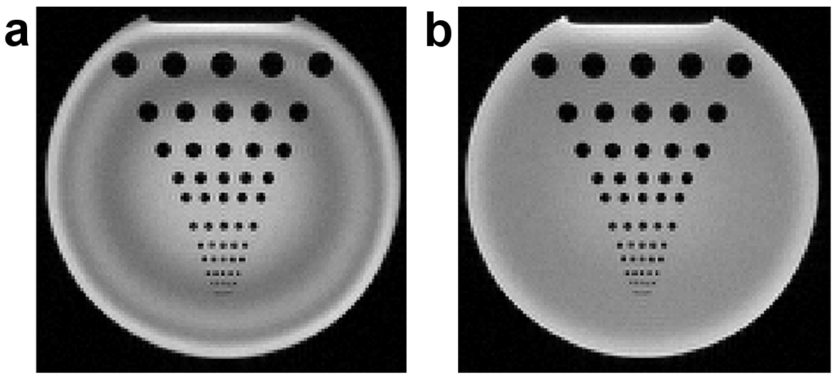

Figure 3.7: a: Example of image artifacts which are generated by the violation of the second CPMG condition in a conventional TSE sequence with Stejskal-Tanner diffusion preparation ($b = 0$ s/mm^2). b: The artifacts are removed by using a different gradient moment for the refocusing pulse of the diffusion preparation module, as compared to the refocusing pulses of the echo train.

2. the out-of-phase component ($M_\perp$), which is the transverse magnetization perpendicular to the RF-phase of the refocusing pulses and, thus, violates the first CPMG condition.

The behavior of $M_\parallel$ and $M_\perp$ during the echo-train is very different from each other, as demonstrated by several investigators using either numerical simulations of the Bloch equations [165, 166, 167] or phase-graphs (graphical representation of the phase evolution of spin-echoes and stimulated-echoes in the echo-train) [160, 161, 162]. The result which has been obtained by Le-Roux [165] by numerically simulating the dynamics of the magnetization with different values of the flip-angle of the refocusing pulses in a conventional HASTE sequence is shown in Figure 3.8. This can be resumed as follows:

- $M_\parallel$ achieves a steady-state after a few refocusing pulses (about 5), independently from the flip-angle (Figure 3.8 a). The signal amplitude increases as soon as the flip-angle approaches the ideal 180°. At the steady-state, a balance between the signal contributions of spin-echoes and stimulated-echoes is reached. As the flip-angle approaches 180°, the signal contribution of spin-echoes increases while the signal contribution of stimulated-echoes decreases and vice versa [166, 168, 169, 170].

- $M_\perp$ is stable only with a flip-angle of exactly 180°. In practice, this condition cannot be achieved throughout the entire FOV due to spatial inhomogeneities of both the transmit RF-field $\vec{B}_1$ and the slice profile. With different flip-angles, the magnetization strongly oscillates during the echo-train (Figure 3.8 b), as the total signal amplitude is the complex sum of spin-echoes and stimulated-echoes which are not in-phase [163, 165, 166, 171].

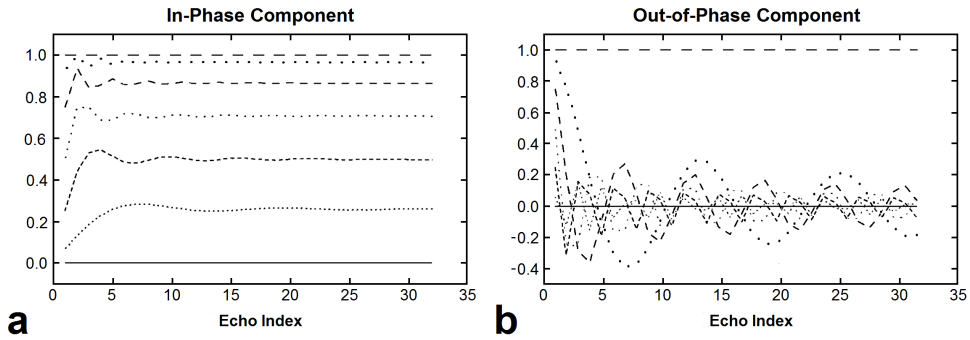

Figure 3.8: Evolution of the transverse magnetization in the echo train of a CPMG experiment. Echo index values (i) are between 1 and 32. The different curves correspond to different flip angles of the refocusing pulse, which range from 0° to 180° with a step of 30°. The magnetization is rescaled to the amplitude of the initial magnetization, which is assumed to be completely flipped in the transverse plane. a: In-phase component $M_{\parallel}$. b: Out-of-phase component $M_{\perp}$; in this case, the magnetization has been multiplied by $(-1)^i$. Reproduced with permission from reference [165].

When the first CPMG condition is violated, the oscillations of $M_{\perp}$ would result in signal inconsistencies among different k-space lines. This would cause image artifacts such as signal voids and ghosting, due to the effect of the point spread function. An example of the artifacts which are induced by physiological motion in a diffusion-prepared HASTE sequence is shown in Figure 3.9 b. To overcome this problem, several solutions can be adopted. However, none of them is free from drawbacks in comparison to the conventional HASTE sequence. These include (see Figure 3.10):

- The use of crushing gradients with different zeroth moments at the two sides of the refocusing pulse (unbalanced gradients) [163, 171, 172] (Figure 3.10 a). With this approach, the amplitude and phase of the acquired signal is approximately constant during the echo-train independently from the initial phase of the transverse magnetization. However, due to the unbalanced crushing gradients, only half of the available signal is actually rephased. For this reason, the signal amplitude is reduced by a factor 2 compared to the conventional HASTE sequence [165].

- The acquisition of two distinct echo signals for each k-space line by means of a readout gradient of doubled length compared to a conventional acquisition [173] (Figure 3.10 b). This approach, known as split-echo acquisition of fast spin-echo signals (SPLICE), represents a variant of the method described above in which the readout gradients play the same role as the unbalanced crushing gradients. However, thanks to the sum of the two acquired echoes, the overall signal loss is reduced to a factor $\sqrt{2}$ [171]. The acquisition of the two echoes requires the increase of both the inter-pulse time and the total echo-train duration. Because the two readout windows

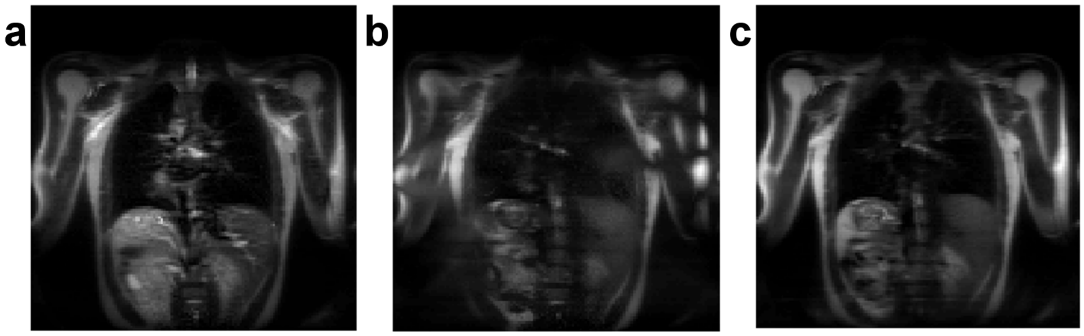

Figure 3.9: Example of coronal images of the human lung acquired in-vivo with different variants of the diffusion-prepared HASTE sequence. a: Conventional HASTE sequence with $b = 0$ s/mm^2. b: Conventional HASTE sequence with $b = 200$ s/mm^2, showing ghosting artifacts and signal voids. c: Non-CPMG HASTE sequence, based on the quadratic increase of the RF-phase of the refocusing pulses [165], with $b = 200$ s/mm^2.

cannot be both perfectly centered between two refocusing pulses, the signal is slightly affected by T_2' decay.

- The use of crushing gradients with variable zeroth moment along the refocusing pulse-train (Figure 3.10 c). With this approach, stimulated-echoes are not rephased such that only the primary spin-echoes contribute to the acquired signal [160, 164, 174]. Also in this case, a loss of signal amplitude occurs in comparison to the conventional HASTE sequence. The amount of this signal loss depends on the flip-angle of the refocusing pulses.

- The use of either 1) special modulation patterns of the RF-phase of the refocusing pulses along the pulse-train [165, 167, 175, 176] (Figure 3.10 d) or 2) multiple acquisitions in which the RF-phase of the refocusing pulses is shifted by a certain value (phase-cycling) [166, 171]. These techniques do not comport a signal loss with respect to the conventional HASTE sequence. However, techniques belonging to the first group are usually sensitive to deviations of the flip-angle of the refocusing pulses from the ideal 180°, while techniques based on phase-cycling require multiple acquisitions (longer scan times) and are sensitive to signal inconsistencies among them, which can be induced by motion.

The non-CPMG HASTE Sequence

In this work, a conventional HASTE sequence was used in combination with different magnetization preparation modules for most experiments. However, in order to perform perfusion imaging in the lung by means of the IVIM approach described in Chapter 2, a

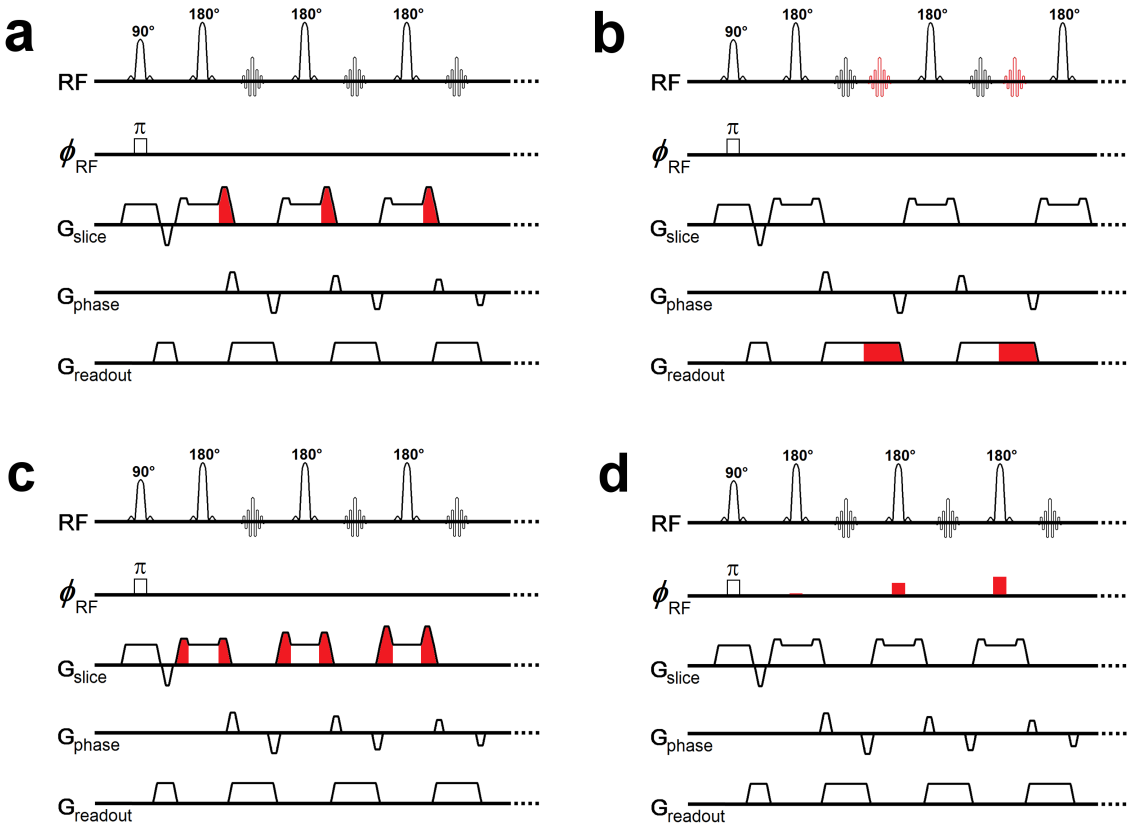

Figure 3.10: Sequence diagrams used by different TSE-based techniques to overcome the violations of the CPMG conditions. The differences in comparison to a conventional TSE sequence are depicted in red. a: Unbalanced crushing gradients [163]. b: Acquisition of two signal echoes by increasing the duration of the readout gradient [173]. c: Crushing gradients with variable zeroth moment [164]. d: RF-phase pattern along the refocusing pulse train [165, 167].

non-CPMG HASTE sequence was used. To this end, the technique proposed by Le-Roux in 2002 [165] was adopted in order to overcome the violation of the CPMG conditions. The basic idea of this technique is to quadratically increase the RF-phase of the refocusing pulses during the echo-train according to [165, 177]:

$$\phi_{\mathrm{RF}}(i) = 73.47^{\circ} \cdot i^2 \tag{3.10}$$

where i is the index that indicates the position of the RF-pulse within the pulse-train. Because the refocusing pulses have a variable RF-phase along the echo-train, the effectiveness of signal refocusing is similar for both $M_{\parallel}$ and $M_{\perp}$, as shown in Figure 3.11. For a range of

values of the flip-angle, between approximately 140° and 180°, both $M_{\parallel}$ and $M_{\perp}$ reach a steady-state after a few pulses (about 7). Within this range of flip-angles, the signal oscillations observed with the CPMG sequence for $M_{\perp}$ are avoided. For smaller flip-angles, both $M_{\parallel}$ and $M_{\perp}$ strongly oscillate, meaning that flip-angles close to 180° should be used. Even in this case, the first few echoes should not be used to fill k-space lines for imaging, due to the strong signal oscillations at the beginning of the echo-train shown in Figure 3.11. The phase of $M_{\perp}$, which is not depicted in Figure 3.11, is reversed at each refocusing pulse. For this reason, odd and even echoes must be separately used to fill two distinct k-spaces, such that an echo-train of double length is required as compared to the conventional HASTE sequence. The magnitude images obtained from the separate reconstruction of the two k-spaces (odd and even lines) are finally added in order to improve the overall SNR.
The choice of using this technique is due to several factors. Some of the approaches described above, in fact, present the drawback of a loss of signal amplitude with respect to the conventional HASTE sequence [165, 173]. This is particularly disadvantageous in the lung, due its low proton density. In addition to this, the SPLICE approach requires an increase of the inter-pulse time. This is a drawback because of the T_2 shortening effect, which is induced in the lung by diffusion through the internal gradients, as described in Chapter 2. The use of unbalanced gradients in some of the mentioned techniques [163, 172, 173], instead, increases their sensitivity to bulk motion and flow. This might result in further signal losses and artifacts in the lung. Techniques based on multiple acquisitions with RF-phase cycling [166], finally, are prone to phase inconsistencies among the different acquisitions. These are induced by physiological motion in the presence of diffusion sensitizing gradients. The main advantage of the approach which has been described here is that it does not comport any signal losses in comparison to the conventional HASTE sequence, nor the use of unbalanced gradients. An example of images of the human lung acquired with both the conventional and the non-CPMG HASTE sequences in combination with diffusion sensitizing gradients is shown Figure 3.9. The images demonstrate the benefits of this technique for DWI. The main drawbacks of this approach are the sensitivity to flip-angle inhomogeneities and the longer echo-trains required by the separate use of odd and even echoes.

Cardiac Triggering

Heart pulsation plays an important role in lung MRI, mainly for two reasons: 1) the proximity of the cardiac muscle to the lungs and 2) the blood flow in the pulmonary vessels. Thanks to its single shot capability and to its short acquisition times, the HASTE sequence allows to freeze most of the physiological motions, including heart pulsation. Nevertheless, due to the relatively long echo-trains, of the order of a few hundred milliseconds, the acquisition may be influenced by blood flow in- and outside of the imaged slice (inflow and outflow) [38]. For this reason, cardiac triggering is key in lung MRI, when using the HASTE sequence.

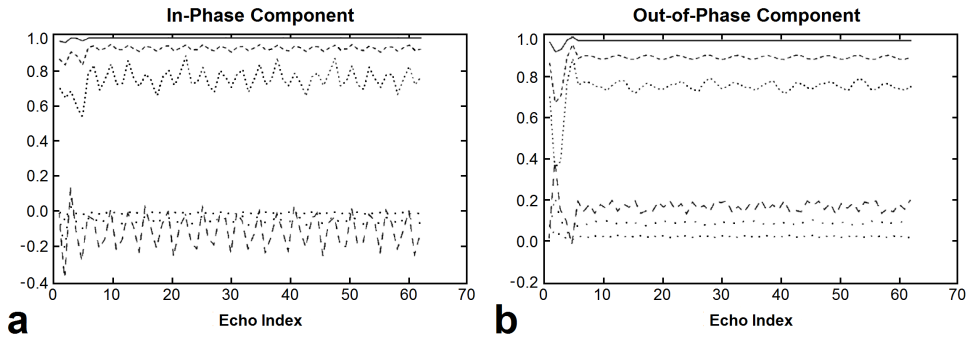

Figure 3.11: Evolution of the transverse magnetization during the echo train of the non-CPMG experiment with quadratic RF-phase modulation. The different curves correspond to different flip angles of the refocusing pulse, which are 160°, 140° and 115°. a: In-phase component $M_{\parallel}$. b: Out-of-phase component $M_{\perp}$; in this case, the magnetization has been multiplied by $(-1)^i$. Reproduced with permission from reference [165].

Cardiac motion can be thought as a quasi-periodic cycle consisting of several phases. These include: atrial systole, atrial diastole, ventricular systole and ventricular diastole. The characteristic frequency of the cardiac cycle, which is called heart rate, is typically between 50 and 100 beats/min in rest conditions [178].
The activity of the heart over time can be non-invasively detected by means of electrocardiography (ECG). With this technique, a series of electrodes are placed on the patient's body in the region of the heart, in order to detect the electrical changes that arise on the skin of the patient from the geometrical polarization and depolarization of the cardiac muscle. The variation of the electric potential in the electrodes is collected, processed and recorded by a dedicated device. The graph of voltage versus time is known as electrocardiogram. A representation of a typical period of the electrocardiogram is shown in Figure 3.12. This can be thought as a series of time intervals, called waves, which are characterized by a specific duration and shape of the electric potential. The different waves are identified by alphabetical letters (P, R, Q, S, T). Each of them corresponds to a different state of polarization of the heart and, therefore, to a different phase of the cardiac cycle. These can be resumed as follows [178]:

- Cardiac diastole. During this stage, the whole heart is relaxed, including both ventricles (ventricular diastole) and atria (atrial diastole), and it refills with blood. In the electrocardiogram, cardiac diastole corresponds to the period of time between the T-wave and the P-wave.

- Atrial systole. In this stage, the atria contract and blood flows from the atria to the ventricles. In the electrocardiogram, this corresponds to the period of time between the P-wave and the R-wave.

- Cardiac (or ventricular) systole. In this stage, the ventricles contract and blood flows from the right ventricle to the pulmonary arteries and from the left ventricle to the aorta. In the electrocardiogram, cardiac systole corresponds to the period of time between the R-wave and the T-wave.

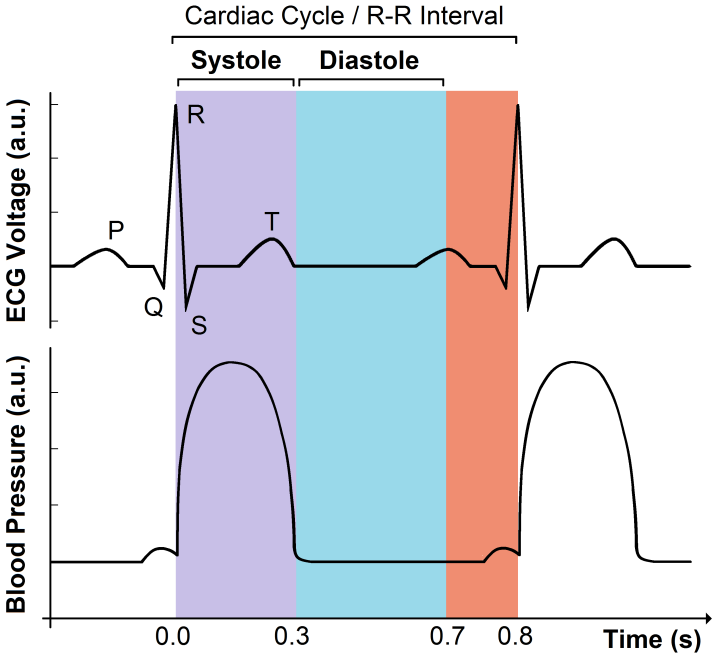

Figure 3.12: Example of a typical ECG signal (top) and of the corresponding blood pressure in the aorta (bottom). Reproduced with permission from reference [105], with adaptions.

The total period of the cardiac cycle is measured as the time distance between two consecutive R waves. This is also known as R-R interval. Throughout the cardiac cycle, blood velocity in the vessels increases and decreases due to the change of blood pressure, as shown in Figure 3.12. In MRI, ECG is used in order to 1) trigger the acquisition at the desired cardiac phase, 2) improve the MR-signal consistency among different acquisitions and 3) reduce image artifacts. Moreover, with ECG also the influence of blood flow on the image contrast can be reduced. This is particularly important in lung MRI, when using the HASTE sequence, as the signal amplitude can strongly change due to blood in- and out- flow. Knight-Scott et al. [38] demonstrated that these variations can be as large as 30 % during the cardiac cycle. The maximum signal amplitude is typically achieved during diastole, thanks to the slower blood flow in the pulmonary vessels and to the reduced effect of blood outflow [38]. An example of this effect is shown in Figure 3.13.

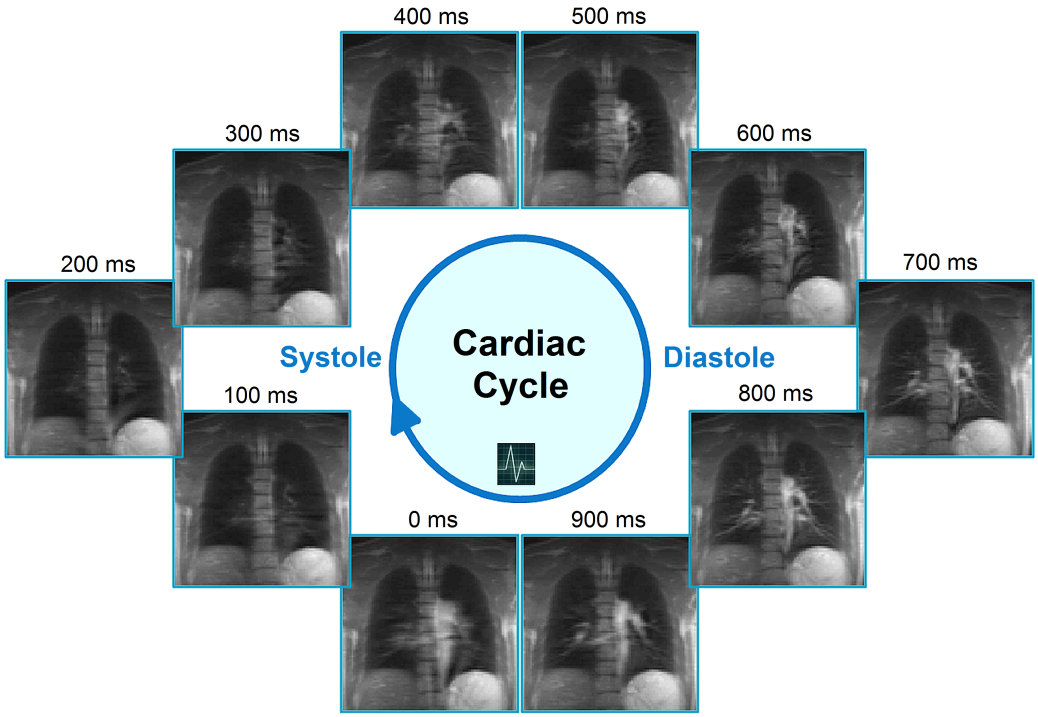

Figure 3.13: Coronal images of the human lung acquired at different cardiac phases using a HASTE sequence with ECG synchronization. The delay between the peak of the ECG signal (R-wave) and image acquisition is indicated in ms above each image.

3.2 Hardware and Software

Experimental Setup

Experiments were performed at 1.5 T on a clinical MR-scanner (Avanto, Siemens Healthcare, Erlangen, Germany). The scanner relies on a standard cylindrical geometry, as shown in Figure 3.14 a, with a bore diameter of 60 cm and a length of 160 cm, and is equipped with a gradient system providing a maximum amplitude of 45 mT/m and a minimum rise time of 200 T/m/s.
Experiments were performed on both phantoms and humans. In-vivo, a six element receiver body array coil was used for signal detection, in combination with an eight channel spine matrix (Siemens Healthcare). The experimental setup used for in-vivo experiments is the following: the volunteer lies in either the supine or prone position on the patient table of the scanner, which is equipped with the spine matrix; the body coil is placed on the chest of the volunteer, in correspondence of the lungs. An example of the experimental

setup used for in-vivo experiments is shown in Figure 3.14 b. Informed written consent was obtained from each volunteer or patient before performing the in-vivo studies.
All in-vivo experiments were performed in breath-hold. For some experiments, comparison measurements between different breathing gases (room air and pure oxygen) were performed. This technique, known as oxygen enhancement, was proposed by Edelmann et al. in 1996 for lung MRI [43] and has been widely used in recent years to observe the dependence of the magnetization relaxation times on the oxygen concentration, in both air in the alveoli (T_2^*) and blood (T_1) [44, 179, 45, 109]. In order to perform oxygen-enhanced imaging, a breathing mask connected to a dedicated system that allows to dynamically switch between the different breathing gases, was used for gas delivery to the volunteers.
For phantom experiments, both the coil setting described above and a four channel head array coil (Siemens Healthcare) were used.

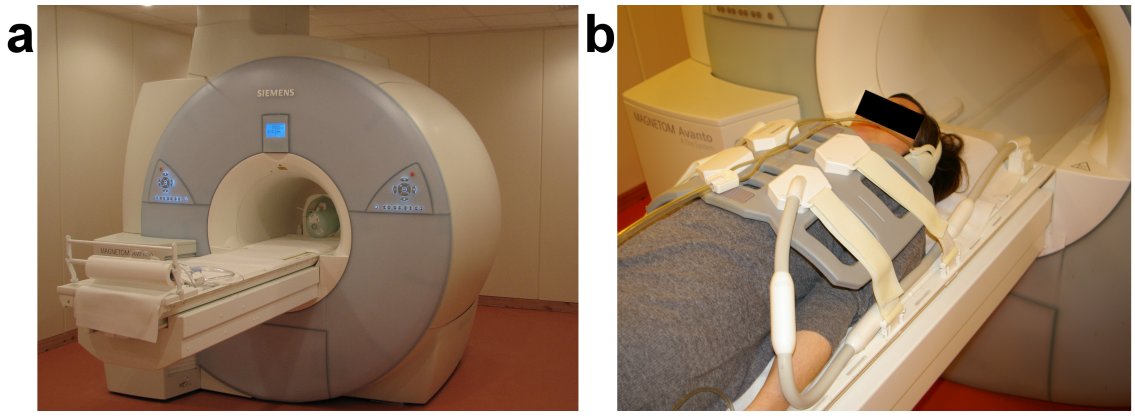

Figure 3.14: a: Whole body MR-scanner used for the experiments. b: Example of the experimental setup which was used for the in-vivo experiments.

Pulse Sequence Development

A HASTE sequence with several different magnetization preparation modules was implemented using IDEA (Siemens Healthcare): the pulse sequence programming tool used on Siemens scanners, which based on the C++ language. The basic scheme of the pulse sequence is shown Figure 3.5. A unique and flexible sequence was implemented; the characteristic parameters of the pulse sequence and of the magnetization preparation modules could be selected by the user, by means of a user-interface.
The refocusing pulses of the HASTE readout were kept as short as possible, in order to minimize the inter-pulse time and reduce signal losses which are induced by transverse relaxation, as well as image blurring. Crushing gradients at each side of the refocusing pulses were applied in both the RO and SS directions. Cardiac triggering, based on ECG, was used in-vivo in order to acquire the signal at the desired cardiac phase.

Data Post-Processing

MATLAB (MathWorks Inc, Natick, USA) was used to generate all graphs and histograms presented in this work, as well as for data post-processing. This includes statistical analysis of data, quantifications, data fitting, image reconstruction and image processing.
Figures in this work were generated using either MATLAB or GIMP (GNU Image Manipulation Program) [180], except where differently indicated.

Chapter 4

Quantification of the Blood Volume Fraction

Part of the work presented in this chapter has been published on a peer-reviewed journal and presented at international conferences, as indicated by references [A1,A5,A8] in the list of publications.

4.1 Introduction

The knowledge of regional perfusion parameters of the lungs is of primary interest for the assessment of pulmonary functionality as well as for the diagnosis and characterization of a large variety of lung diseases. Pulmonary perfusion, in fact, may be altered by several diseases such as [2, 3, 11, 30, 52, 179, 181, 182, 183]:

- pulmonary embolism, pulmonary hypertension or obstructive vascular diseases due to the decrease of blood flow in large or medium sized pulmonary vessels;
- lung tumors and pulmonary fibrosis owing to the destruction or displacement of the capillary bed;
- Chronic Obstructive Pulmonary Disease (COPD), emphysema or cystic fibrosis due to the phenomenon of hypoxic vaso-constriction, which causes a reduction of perfusion in non-ventilated regions of the lung.

In the presence of such diseases, perfusion imaging can be useful not only for the diagnosis but, in some cases, also for the assessment of the severity and the causes of the disease. Another clinical application of perfusion imaging is the prediction of post-operative lung function, in order to improve surgery planning in patients with lung tumors and emphysema, as well as the subsequent treatment monitoring [11, 52].
In this regard, MRI has shown to be a versatile diagnostic tool, as it can be used for the quantification of several pulmonary perfusion parameters. Dynamic contrast-enhanced

MRI [39] is the methodology of reference at present and has been widely used to assess the following parameters [40, 41]: blood flow, blood volume and mean transit time. Quantification of the pulmonary blood flow with non-contrast-enhanced MRI has also been proposed and investigated by means of Arterial Spin Labeling (ASL) [48], Spin-Echo Entrapped Perfusion imAGE (SEEPAGE) [49] and Fourier-decomposition [46, 47].
Another interesting perfusion parameter of the lung is the blood volume fraction (f), which represents the fraction of spins in the intravascular compartment [184, 185, 186]. This parameter can be defined by using a two compartmental model of the lung. In this model, the Total Lung Water (TWL) is divided up into the Intra-Vascular Lung Water (IVLW) and the Extra-Vascular Lung Water (EVLW). The blood volume fraction is defined as:

$$f = \frac{\text{IVLW}}{\text{TLW}} \tag{4.1}$$

The remaining fraction of spins in the extravascular compartment is given by $1 - f = \text{EVLW/TLW}$.
Besides the already mentioned applications of perfusion imaging, quantification of the blood volume fraction may be useful for the detection of lung diseases which pathologically alter the water balance between the intra- and extravascular compartments, such as interstitial lung diseases [32] and edema [52, 184, 186, 187]. Apart from that, it has also been demonstrated by several investigators [188, 189] that the knowledge of the fraction of EVLW can improve the accuracy in the diagnosis of Acute Lung Injury (ALI). In this case, the blood volume fraction can serve also as a good indicator for the severity of the disease [188, 189]. Furthermore, the knowledge of the blood volume fraction aids in the further characterization of the pulmonary water compartments [112]. In particular, it can help to assess the magnetization relaxation times T_1 and T_2 as well as the magnetization transfer ratio of the intra- and extravascular compartments separately [112, 185, 190].
In the past several investigators quantified the blood volume fraction of the lung by means of contrast-enhanced MRI [184, 186, 191]. To this end, either MR angiography [184, 186] or T_1 mapping [191] are performed both before and after the administration of contrast agent. However, clinical applications of these techniques to the human lung can be rarely found in literature. A non-contrast-enhanced method based on T_1 mapping has been recently proposed by Gaass et al. [185]. This approach uses a two-compartmental signal decay model in order to separate the signal components of the different tissue compartments based on their longitudinal relaxation times. A potential drawback of this method is the dependence of T_1 of the lung on the echo time, as recently demonstrated by Triphan et al. [192]. This might affect the quantification. Furthermore, this technique requires multiple breath-holds for image acquisition and therefore it is sensitive to motion.
Here, an alternative non-contrast-enhanced technique is proposed in order to quantify the blood volume fraction of the human lung in-vivo. The technique requires the acquisition of two images only: one reference image (which reflects the TLW) and one blood suppressed image (which reflects the EVLW). The image acquisition can be accomplished in a single breath-hold of approximately 10 s duration, making the proposed technique attractive for

clinical applications.
The underlying principle of the presented technique is inspired by the IVIM method [59, 60, 61] described in Chapter 2. The IVIM approach is based on the sensitivity of DWI to blood microcirculation in the capillaries. The separation between the intra- and extravascular signal components can be achieved by exploiting the different spin velocities in the different compartments, as the IVLW consists mainly of flowing (i.e. "fast-moving") spins while the EVLW is composed of diffusing (i.e. "slowly-moving") spins. Application of the conventional IVIM technique to lung imaging is challenging for several reasons, such as: 1) the low proton density and the short transverse relaxation times of the lung tissue, 2) the relatively long TE required by the diffusion sensitizing gradients, which are accompanied by signal losses due to T_2 relaxation, as well as 3) the high sensitivity of DWI to bulk motion.
The aim of the work presented in this chapter was to develop a robust technique based on the theoretical principles of IVIM in order to quantify the blood volume fraction of the human lung in a single breath-hold and without the use of contrast agents. It is shown here how the presence of internal magnetic field gradients in the lungs can be used to achieve this goal.

4.2 Materials and Methods

4.2.1 IVIM and Blood Volume Fraction

The basic idea of the IVIM approach to obtain the blood volume fraction is to acquire two or more images which show different signal attenuation of the blood signal. In the presence of a bipolar gradient, the spin displacement which is due to perfusion produces a loss of phase coherence at the voxel level. This results in an attenuation of the signal amplitude of flowing blood. The two compartmental model of equation (2.52) describes this signal attenuation in a spin-echo sequence [59]. The model assumes that the two water compartments have similar transverse relaxation time T_2 and diffusion coefficient D. Implications of possible violations of this assumption are discussed later in this chapter.
The blood volume fraction can be obtained by acquiring two images (S_1 and S_2) and using the following formula which derives from equation (2.52):

$$f = 1 - \frac{S_2}{S_1} \exp(bD) \tag{4.2}$$

where S_1 is a reference image acquired without applying the diffusion-sensitizing gradients, such that $F \approx 1$; and S_2 is a blood-suppressed image acquired with a large enough b-value, such that $F \approx 0$. If $D << 1/b$, the exponential term in equation (4.2) can be neglected, otherwise acquisition of a third image with a different b-value is required, in order to quantify D.
In the lungs, the blood signal attenuation is not only dictated by the externally applied gradients, but also by the presence of the internal magnetic field gradients that originate

from the magnetic susceptibility difference between lung tissue and gas in the alveoli. The underlying idea of the presented technique is to take advantage of this intrinsic property of the lung in order to suppress the blood signal in the pulmonary capillaries and to obtain the blood volume fraction by using the IVIM principle. To this end, an ECG-synchronized HASTE sequence is used in combination with a magnetization preparation module based on the pulse scheme of the stimulated-echo imaging (STEAM) experiment [96, 97]. The STEAM module, in fact, introduces a modulation of the transverse magnetization which depends on the amplitude of the internal magnetic field gradients, as demonstrated by Song et al. [129, 193].

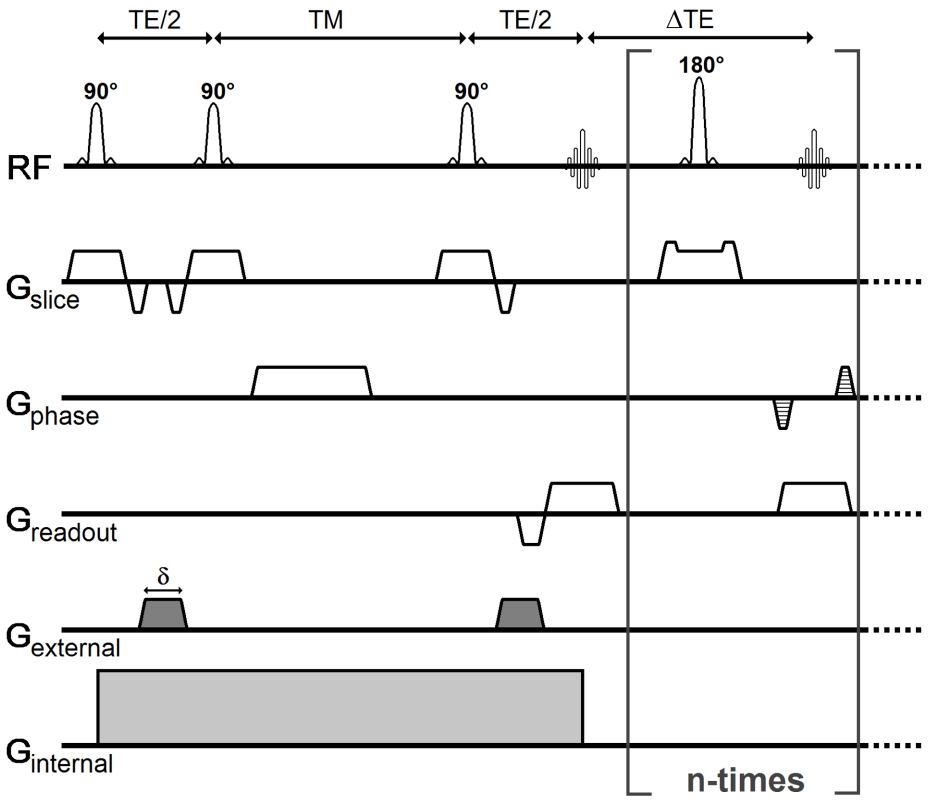

Figure 4.1: Timing diagram of the STEAM-prepared HASTE pulse sequence used for blood volume fraction imaging. The three 90° slice selective RF-pulses prepare the transverse magnetization for the stimulated echo acquisition (STEAM). The following train of 180° refocusing pulses allows for the readout the full k-space in a single shot (HASTE). TE = echo time of the stimulated echo, TM = middle time interval, δ = duration of the external gradient pulse, n = number of repetitions of the readout block. Reproduced with permission from reference [A1].

4.2.2 Pulse Sequence

A timing diagram of the STEAM-prepared HASTE sequence is shown in Figure 4.1. The magnetization preparation module consists of three slice selective RF-pulses with 90° flip angles. The subsequent HASTE readout is composed of a train of 180° refocusing pulses, which allows for the readout of the full k-space in a single shot.
Formation of unwanted echoes from the preparation block was prevented by applying a crushing gradient in the PE direction during the TM interval. Centric reordering of the phase-encoding steps was used together with partial Fourier acquisition. Image reconstruction was accomplished by using the Margosian algorithm [158]. The sequence includes also ECG synchronization, as the resulting signal in the lungs strongly depends on the cardiac phase [34, 38].

4.2.3 Blood Signal Attenuation Mechanisms

Attenuation of Macroscopic Blood Flow
The external gradient lobes which are applied during the two TE/2 periods have a zeroth moment $m_0 \approx G_{\text{etx}} \cdot \delta$ each, where G_{etx} is the gradient amplitude and δ its duration. The two gradient lobes act on the transverse magnetization like a bipolar gradient which has first moment $m_1 \approx m_0 \cdot (\text{TM} + \delta)$. This property can be used to attenuate the signal from flowing spins according to the mechanism described below:

- The first gradient lobe generates an intravoxel dephasing in the transverse magnetization.
- During the separation time between the two gradient lobes, flowing spins move in the direction of the external gradient depending on the spin velocity $\vec{v}$.
- The second gradient lobe refocuses the transverse magnetization of static spins. An intravoxel phase dispersion $\Delta\phi = \gamma \cdot m_1 \cdot \Delta v$ remains for flowing spins [194, 195], where Δv is the velocity dispersion in the direction of the gradient.

This loss of phase coherence is responsible for the blood signal attenuation described by the factor F in equation (2.52). Full signal suppression is obtained if $\Delta\phi > 2\pi$ (i. e. $m_1 > 2\pi/\gamma/\Delta v$). This principle has been widely used to suppress the signal of flowing blood [196, 197]. The velocity dispersion Δv is given by turbulent or laminar flow [195] in the large and medium sized vessels and by incoherent motion in the capillaries [59]. In the larger vessels the blood signal is efficiently suppressed with a gradient first moment $m_1 > 100$ mT·ms^2/m [194], due to the fast flow condition.

Attenuation of Microscopic Blood Flow
Blood suppression at the capillary level is more challenging, due to the fact that the blood velocity is much smaller than in the large vessels. The typical velocity in the capillaries is $v \approx 2$ mm/s [59, 198, 199, 200], which results in a velocity dispersion $\Delta v \approx 2v$

(considering that the projection in the direction of the external gradient includes both positive and negative values of v). According to the model described above, a first moment $m_1 > 6000$ mT·ms^2/m is required for full blood suppression. Such gradient moments are typical of diffusion sensitizing gradients. This is, in fact, the basic idea of the IVIM technique, which makes use of strong diffusion sensitizing gradients in order to suppress the blood signal at the capillary level. However, such gradient moments require rather long gradient lobes, of the order of several tens of ms with conventional gradient systems, which implies strong T_2-weighting and increased sensitivity to bulk motion. This is especially problematic in the lungs due to the relatively short T_2 [112] and to the proximity of the heart.
The central idea of this work is to exploit the signal attenuation enhancement in the lung capillaries, which is due to the presence of internal magnetic field gradients around the alveoli, as indicated by the gradient shaded in light gray in Figure 4.1. This intrinsic characteristic of the lung allows for the suppression of the blood signal in the capillaries without the need for strong external diffusion sensitizing gradients. The corresponding signal attenuation mechanism can be described as follows:

- During the first time interval TE/2 the transverse magnetization is dephased by the internal magnetic field gradients, which periodically occur within the lung space on the length scale of the alveolar diameter with a mean amplitude of the order of $\langle G_{\text{int}} \rangle \approx 100$ mT/m at 1.5 T, as discussed in Chapter 2 (equation (2.21)).

- During the separation time between the two TE/2 periods, the spins displace incoherently.

- During the second time interval TE/2 the phase accumulated from static spins is refocused, due to phase reversal. An intravoxel phase dispersion $\Delta\phi \approx \gamma \cdot \langle G_{\text{int}} \rangle \cdot \text{TE}/2 \cdot (\text{TM}+\text{TE}/2) \cdot \Delta v$ remains for flowing spins, similarly to the case of the external gradient lobes. Blood signal suppression is obtained if $\Delta\phi > 2\pi$, which means:

$$\left(\text{TM} + \frac{\text{TE}}{2}\right) \cdot \frac{\text{TE}}{2} > \frac{2\pi}{\gamma \langle G_{\text{int}} \rangle \Delta v} \tag{4.3}$$

At 1.5 T, blood signal suppression at the capillary level is obtained for $(\text{TM} + \text{TE}/2) \cdot \text{TE}/2 > 60$ ms^2, considering the typical value of $\langle G_{\text{int}} \rangle$ mentioned above.

4.2.4 Signal Decay Model and Quantification

During the TM interval, the magnetization is subject to the T_1 decay. This must be taken into account by introducing an exponential term for the T_1 decay in the model of equation (2.52):

$$S(\text{TE}, \text{TM}) \propto \exp\left(-\frac{\text{TM}}{T_1}\right) \exp\left(-\frac{\text{TE}}{T_2}\right) \exp\left(-bD\right) \left[fF + (1-f)\right] \tag{4.4}$$

Like the conventional IVIM method, the presented technique requires the acquisition of at least two images (S_1 and S_2) with different attenuation of the signal of flowing blood. The main difference with respect to the conventional technique is that the signal in the capillaries is suppressed by the internal gradients, whereas the signal in the large vessels is suppressed by a pair of small external gradient lobes instead of strong diffusion sensitizing gradients. In both cases, the blood signal attenuation described by the factor F in equation (4.4) is proportional to TM and to the velocity v, which depends on the cardiac phase. Therefore, the overall sensitivity of the sequence to blood flow and microcirculation can be regulated by changing the value of TM and the cardiac phase used for acquisition. This was achieved by using different TMs for S_1 and S_2 ($\mathrm{TM}_1 << \mathrm{TM}_2$), in combination with different time delays between image acquisition and the ECG peak.
To obtain the desired blood signal attenuation, S_1 was acquired in diastole (slow blood flow) and with $(\mathrm{TM}_1 + \mathrm{TE}/2) \cdot \mathrm{TE}/2 << 60$ ms^2, which results in negligible blood attenuation ($F \approx 1$); S_2 was acquired in end-systole (fast blood flow) with $(\mathrm{TM}_2 + \mathrm{TE}/2) \cdot \mathrm{TE}/2 \simeq 80$ ms^2, which results in full blood suppression ($F \approx 0$) according to equation (4.3). TE/2 was kept constant for both images. Under these conditions, the blood volume fraction can be obtained from:

$$f = 1 - \frac{S_2}{S_1} \exp\left(-\frac{\mathrm{TM}_2 - \mathrm{TM}_1}{T_1}\right) \exp\left[(b_2 - b_1)\, D\right] \tag{4.5}$$

The role of the two exponential terms in equation (4.5) is discussed below:

1. The first exponential term accounts for the different T_1 weighting of the two images, due to the different TM. However, because of the relatively long T_1 of the lung tissue ($T_1 \approx 1000$ ms [201]) the TMs can be chosen in such a way that $\mathrm{TM}_1 << \mathrm{TM}_2 << T_1$. In this case, the T_1-dependent term accounts only for a minor correction in the quantification of f and the explicit knowledge of T_1 is not necessary. A reasonable choice for the TMs which fulfills this condition is the following: $\mathrm{TM}_1 = 2$ ms and $\mathrm{TM}_2 = 40$ ms. In this case the first exponential term is ≈ 1.04, assuming $T_1 = 1000$ ms.

2. The second exponential term accounts for the different diffusion weighting of the two images. The b-value in equation (4.5) consists of two components (b_{ext} and b_{int}), due to the presence of both the external and internal magnetic field gradients, such that $b = b_{\mathrm{ext}} + b_{\mathrm{int}}$. The value of b_{ext} can be calculated from [202]:

$$b_{\mathrm{ext}} \simeq \gamma^2 G_{\mathrm{ext}}^2 \delta^2 \left(\mathrm{TM} + \frac{2}{3}\delta\right) \tag{4.6}$$

   In order to fully attenuate the blood signal in the large vessels, a gradient amplitude $G_{\mathrm{ext}} \approx 19$ mT/m was used for the external gradient lobes, with $\delta \approx 0.4$ ms. This results in: $m_{1,1} \approx 18$ mT·ms^2/m for S_1 and $m_{1,2} \approx 310$ mT·ms^2/m for S_2, consistently with the finding of Newbould et al. [194].

The external b-values are then: $b_{\text{ext},1} \approx 9.4{\cdot}10^{-3}$ s/mm^2 and $b_{\text{ext},2} \approx 1.7{\cdot}10^{-1}$ s/mm^2. The effect of the external gradients in equation (4.5) is therefore negligible, considering that the diffusion coefficient of free water is $D_{\text{w}} \approx 2.3 \cdot 10^{-3}$ mm^2/s and that $(b_{\text{ext},2} - b_{\text{ext},1})^{-1} \approx 6.2$ mm^2/s $>> D_{\text{w}}$.
The overall sensitivity to bulk motion can be expressed by means of the field of speed (FOS) associated to the external gradient lobes. The FOS is defined as the spin velocity which induces a 2π phase accrual [195]. This means that a large FOS indicates low sensitivity to bulk motion. In our case, image S_2 is the most sensitive to bulk motion, with FOS $= 2\pi/\gamma/m_{1,2} \approx 7.6$ cm/s. This means that any physiologic motion occurring at velocities of the order of 10 cm/s, such as cardiac motion, could give rise to an intravoxel dephasing which results in signal voids known as "through-plane deformation artifacts" [203, 204]. However, the sensitivity to bulk motion is significantly reduced compared to conventional diffusion sensitizing gradients, which require a much higher m_1 or, alternatively, a much longer TE for motion compensation.
The value of b_{int} can be calculated by replacing in the previous formula the typical amplitude (see equation (2.21)) and the duration (TE/2) of the internal gradients:

$$b_{\text{int}} \simeq \gamma^2 \langle G_{\text{int}} \rangle^2 \left(\frac{\text{TE}}{2}\right)^2 \left(\text{TM} + \frac{\text{TE}}{3}\right) \tag{4.7}$$

The value of TE/2 required to achieve full blood suppression is given by the positive signed solution of $(\text{TM}_2 + \text{TE}/2) \cdot \text{TE}/2 > 60$ ms^2, as obtained from equation (4.3). This results in TE/2 > 1.5 ms.
The internal b-values are then: $b_{\text{int},1} \approx 5.3$ s/mm^2 and $b_{\text{int},2} \approx 66.5$ s/mm^2 at $B_0 = 1.5$ T, considering the typical value of $\langle G_{\text{int}} \rangle$ mentioned above. The second exponential term is hence ≈ 1.15, when using the diffusion coefficient of free water.

Thus, the blood volume fraction can be obtained by combining the described effects of T_1 and diffusion in equation (4.5). This results in:

$$f = 1 - \left(1.20 \cdot \frac{S_2}{S_1}\right) \tag{4.8}$$

Equation (4.8) relies on specific assumptions made on T_1, b_{int} and D of the lung. If such assumptions are not satisfied, the calculation of f would be affected by an error Δf, which can be estimated by means of the error propagation in equation (4.5):

$$\begin{aligned} \Delta f &= \frac{\partial f}{\partial T_1}\Delta T_1 + \frac{\partial f}{\partial\,(b_2 - b_1)\,D}\Delta T_1 = \\ &= (1-f) \cdot \left[\frac{\text{TM}_2 - \text{TM}_1}{T_1^2}\Delta T_1 + \Delta\,(b_2 - b_1)\,D\right] \end{aligned} \tag{4.9}$$

where ΔT_1 and $\Delta\,(b_2 - b_1)\,D$ are absolute errors.

4.2.5 Experiments in Healthy Volunteers

In-vivo imaging experiments were performed on the human lung. Eight healthy subjects (6 male and 2 female, age range $27 - 38$ years) without any known history of pulmonary disease were investigated.
The two images S_1 and S_2, with $\mathrm{TM}_1 = 2$ ms and $\mathrm{TM}_2 = 40$ ms, were acquired in a single breath-hold of approximately 10 s duration. A separation time of 6 s was included between the two acquisitions, in order to allow for the full recovery of the longitudinal magnetization. The trigger delay between the ECG peak and the first RF-pulse was manually adjusted, in order to acquire the images in the desired cardiac phase. A six element body array coil was used in combination with an eight channel spine matrix for signal detection. The following imaging parameters were used for all experiments: FOV $= 500 \times 500$ mm^2, slice thickness $= 12$ mm, matrix size $= 128 \times 128$ (zero-filled to 256×256), partial Fourier factor $= 5/8$ (corresponding to 80 phase encoding lines), receiver bandwidth $= 3910$ Hz/Px, inter-echo spacing $= 2$ ms. Due to the use of centric reordering, the first five echoes were not used for imaging, as strong signal oscillations may occur here when the flip angle of the refocusing pulse deviates from the ideal 180° [160, 169]. This resulted in an actual echo time at the k-space center of approximately 14 ms.
All images were acquired with the volunteer in the supine position. A Hamming filter was applied to all acquired images, in order to avoid Gibbs ringing. Eight coronal slices of the whole lung and seven sagittal slices of the right lung were acquired for each volunteer in expiratory state, at FRC. A repeatability study was performed to demonstrate the robustness of the presented technique: the acquisition of one coronal slice through the aorta was repeated, in separate breath-holds, for a total of ten measurements in each subject. The dependence of the blood volume fraction on lung inflation was also analyzed by acquiring the same coronal slice in inspiratory state, at TLC.

4.2.6 Image Analysis

Maps of the blood volume fraction f were calculated from the acquired images on a voxel-by-voxel basis using equation (4.8). The results obtained in the lung parenchyma were systematically evaluated, as described below:

1. A region of interest (ROI) was manually drawn on image S_1 around the whole region of the lung parenchyma as shown in Figure 4.2 a. The lung was identified as the region of lower signal amplitude.

2. For each experiment, a signal amplitude threshold was defined. Only the voxels with signal amplitude below the threshold were accepted, in order to discard large vessels and other tissues with high proton density from the ROI and ensure that primarily data from the lung parenchyma are evaluated, as shown in Figure 4.2 b. Because signal amplitude variations with low spatial frequency, such as the coil sensitivity profiles, can alter the image contrast and interfere with image segmentation, a high-

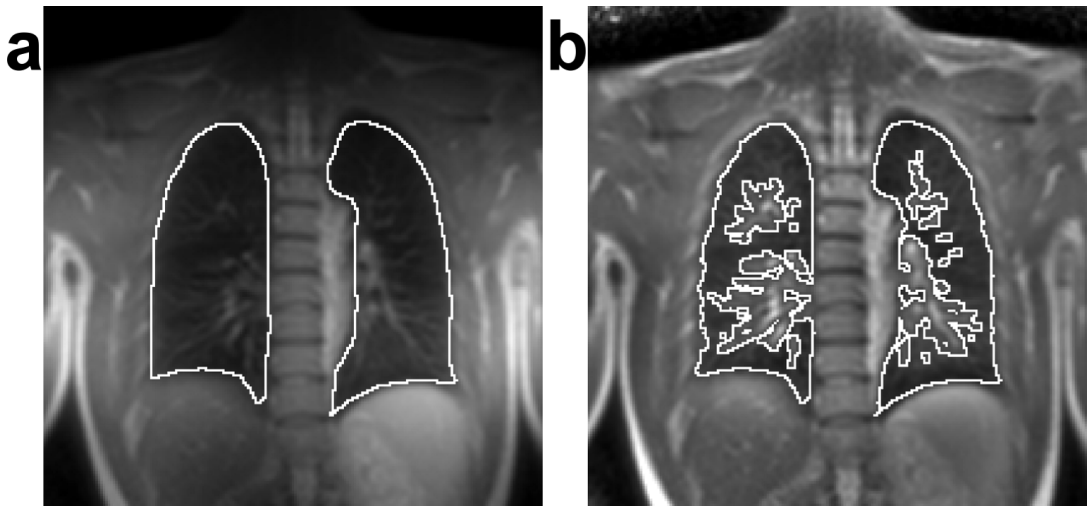

Figure 4.2: Image segmentation procedure used to select the lung parenchyma tissue. a: A ROI which includes the whole region of the lung was manually drawn on image S_1. b: After high-pass filtering, the image presents a better spatial homogeneity and the large vessels can be automatically discarded by applying a threshold. Reproduced with permission from reference [A1].

pass filter was applied to image S_1 before thresholding, as described by Wang et al. in reference [205].

3. Histograms of the statistical distribution of f within the ROI were generated and the corresponding mean values (MV) and standard deviations (STD) were calculated.

MVs and STDs obtained in different volunteers by averaging all slices of the acquired datasets were compared. Coronal and sagittal datasets were separately evaluated. For the repeatability study, the mean value and its standard deviation (σ_{MV}) were calculated over the ten performed measurements. The resulting coefficient of variation (CoV), defined as the ratio $\sigma_{\mathrm{MV}}/\mathrm{MV}$, was used as a measure of reproducibility.
For the analysis of the influence of lung inflation, differential mean values ($\Delta\mathrm{MV} = \mathrm{MV}_{\mathrm{FRC}} - \mathrm{MV}_{\mathrm{TLC}}$) obtained in the same coronal slice at FRC and TLC were calculated. A Student's t-test was performed to assess the statistical significance of the similarity between the two groups ($P_{\mathrm{inflation}}$), in the assumption of homogeneity of variance. The null-hypothesis was rejected for $P_{\mathrm{inflation}} < 0.05$.
The gravitational dependence of the blood volume fraction was also analyzed: maps obtained from the sagittal datasets were averaged in the horizontal direction, assuming that each line of the image represents an isogravitational plane [49]. The result of this calculation was used to generate a plot of the blood volume fraction profile in the A-P direction.

4.2.7 Experiments in Patients with Lung Cancer

A first application of the presented technique in the clinical field was also performed. To this end, five patients with lung cancer were investigated on a clinical 3.0 T MR scanner (Trio, Siemens Healthcare, Erlangen, Germany).
Maps of the blood volume fraction were acquired and examined in order to identify the possible additional information provided by the proposed technique in comparison to a morphological HASTE image. In one of the volunteers, the blood volume fraction map was compared also to a perfusion rate map which was obtained with ASL by using a FAIRER-HASTE sequence, as proposed by Mai et al. [48]. The perfusion rate, in ml of blood/min/100ml of tissue, was calculated by following the description of Schraml et al. [182]. All images were acquired in the transverse orientation. Other imaging parameters were identical to those which have been used for the experiments with volunteers.

4.2.8 Comparison with Conventional IVIM

In addition to the experiments described above, the proposed technique was compared to conventional IVIM [59, 60]. To this end, the non-CPMG HASTE sequence described in Chapter 3 was implemented and used for imaging [165]. A motion-compensated diffusion preparation was used, as shown in Figure 4.3 [207].
Imaging experiments were performed in five healthy volunteers with both techniques. The acquisition strategy used for conventional IVIM was similar to that used for the proposed technique: two images (S_1 and S_2) with different b-values were acquired in a single breath-hold of approximately 10 s duration at different cardiac phases. S_1 was acquired in diastole with $b_{\text{ext}} = 0$ s/mm^2, while S_2 was acquired in systole with $b_{\text{ext}} \simeq 30$ s/mm^2. For each volunteer, coronal images were acquired at FRC in a single slice through the aorta.
In order to minimize the duration of the diffusion preparation, and thus TE, the diffusion sensitizing gradients were applied at maximum amplitude (≈ 27 mT/m in each direction) and on all three directions simultaneously [207]. The basic imaging parameters were identical to the experiments described above, except for the longer echo time at the k-space center which was approximately 35 ms due to the presence of the diffusion preparation module.
Odd and even echoes were separately used for image reconstruction, as described in Chapter 3. Normally, this would require an echo train of double length compared to a conventional HASTE sequence, with the drawback of increased blurring. In order to keep the echo train length equal for both techniques, GRAPPA with AF = 2 was used for experiments with the non-CPMG HASTE. To this end, an additional acquisition of the same coronal slice with full k-space coverage and identical parameters to the actual imaging scan was performed in a separate breath-hold using a FLASH sequence. This acquisition was used as ACS data. Like for the STEAM-prepared HASTE acquisition, centric reordering of the phase-encoded lines was used.

Quantification of the blood volume fraction was performed on a voxel by voxel basis using equation (4.2). Also in this case it was assumed that $D \approx D_w$, which resulted in:

$$f = 1 - \left(1.07 \cdot \frac{S_2}{S_1}\right) \tag{4.10}$$

The MVs of the blood volume fraction obtained with both the STEAM-prepared HASTE and the non-CPMG HASTE sequences within the lung parenchyma were compared after image segmentation. To this end, the relative difference of the MVs obtained with the two techniques, defined as $(\mathrm{MV_{DWI}} - \mathrm{MV_{STEAM}})/\mathrm{MV_{DWI}}$, was calculated.

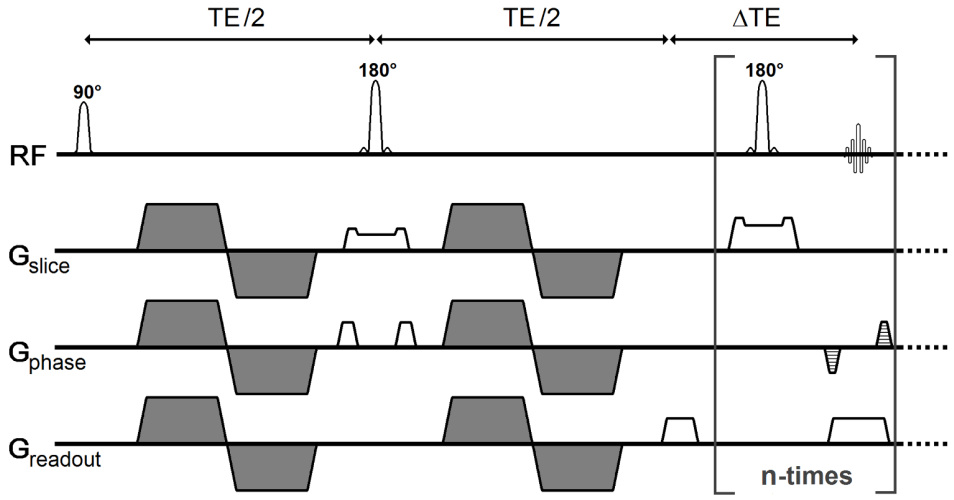

Figure 4.3: Timing diagram of the non-CPMG HASTE pulse sequence, with motion-compensated diffusion preparation, used for standard IVIM to quantify the blood volume fraction. The diffusion sensitizing gradients are applied along the three spatial directions at the same time and with maximum gradient amplitude, in order to minimize the echo time.

4.2.9 Reduction of the Influence of T_1

In order to mitigate the influence of T_1 on the quantification of the blood volume fraction, a variant of the STEAM-prepared HASTE sequence with additional inversion recovery preparation (IR) was implemented. A diagram of the pulse sequence is shown in Figure 4.4. The basic idea to reduce the influence of T_1 is to regulate the TI of the IR preparation in both acquisitions (S_1 and S_2), in addition to TM. The values of $\mathrm{TI_1}$ (for S_1) and $\mathrm{TI_2}$ (for S_2) were chosen in such a way that the difference in the T_1-weighting of the two images is minimized.

With the proposed sequence, T_1 weighting is regulated by both TI and TM according to:

$$S(\mathrm{TI}, \mathrm{TM}) \propto \exp\left(-\frac{\mathrm{TM}}{T_1}\right)\left[1 - 2\exp\left(-\frac{\mathrm{TI}}{T_1}\right)\right] \tag{4.11}$$

Identical T_1-weighting in the two images is obtained if:

$$1 - 2\exp\left(-\frac{\mathrm{TI}_1}{T_1}\right) = \left[1 - 2\exp\left(-\frac{\mathrm{TI}_2}{T_1}\right)\right]\exp\left(\frac{\mathrm{TM}_1 - \mathrm{TM}_2}{T_1}\right) \tag{4.12}$$

Equation (4.12) does not have a general solution that would allow to choose TI_1 and TI_2 independently from T_1. However, if $\mathrm{TI}_1, \mathrm{TI}_2, \mathrm{TM}_1, \mathrm{TM}_2 << T_1$, the exponential terms in equation (4.12) can be expanded in a Taylor series, such that:

$$\mathrm{TI}_1 = \mathrm{TI}_2 + \frac{\mathrm{TM}_2 - \mathrm{TM}_1}{2} \tag{4.13}$$

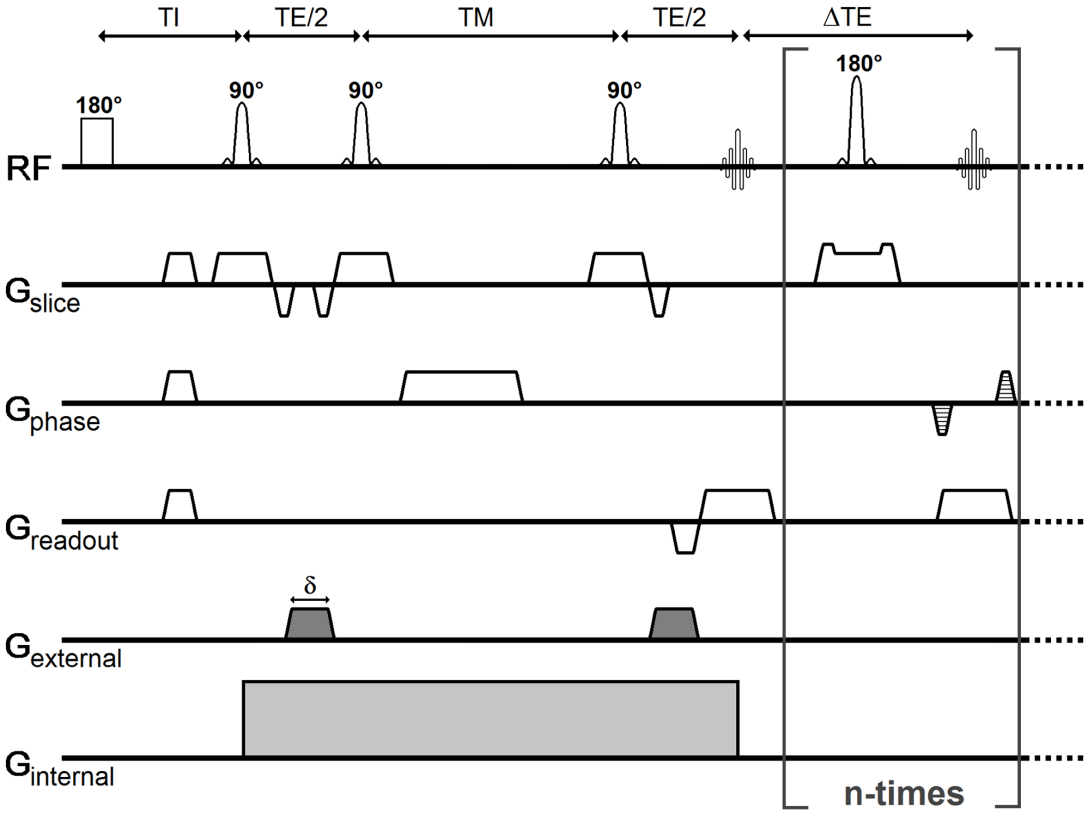

Figure 4.4: Diagram of a variant of the STEAM-prepared HASTE pulse sequence with additional inversion recovery preparation: an inversion pulse with 180° flip-angle, followed by crushing gradient, in placed in front of the sequence in order to regulate the T_1 weighting.

For most tissues, including the lung ($T_1 \approx 1000$ ms [201]), the condition leading to equation (4.13) can be easily fulfilled. In order to minimize the signal losses which are due to the T_1 decay, TI_2 was kept as small as possible, while TI_1 was correspondingly calculated from equation (4.13). This resulted in $TI_2 = 3$ ms and $TI_1 = 22$ ms, as $TM_1 = 2$ ms and $TM_2 = 40$ ms.
Imaging experiments were performed in one of the volunteers with and without IR preparation. Coronal images were acquired at FRC in a single slice through the aorta. The basic imaging parameters were the same as for the experiments described above. The subtraction between images S_1 and S_2 was calculated and used as a qualitative indicator for the influence of T_1. The blood volume fraction was quantified, in both cases, on a voxel by voxel basis. For the sequence variant with IR preparation, the following formula was used:

$$f = 1 - \left(1.15 \cdot \frac{S_2}{S_1}\right) \tag{4.14}$$

which was obtained from equation (4.5), by neglecting the T_1-dependent term.
The MVs of the blood volume fraction obtained with both sequence variants within the lung parenchyma, after image segmentation, were compared and their relative difference was calculated.

4.3 Results

A representative example of the magnitude images S_1 and S_2 which were acquired in one of the volunteers is shown in Figure 4.5, for both the coronal and the sagittal orientations. The same non-linear scaling was applied to all images in order to enhance the visualization of the lung parenchyma. Different attenuation of the blood signal can be observed in S_1 and S_2. In S_1 the blood signal attenuation is negligible, due to slow blood flow in diastole and short TM. In S_2 the blood signal is suppressed, due to fast blood flow in end-systole and long TM, which implies high sensitivity to both blood flow in the large vessels and blood microcirculation in the capillaries. Despite the use of centric reordering, blurring in the phase encoding direction is minimal, due to the use of a very short inter-echo time of 2 ms.
The resulting parametric maps of f are shown in Figures 4.6 and 4.7. Six coronal slices and six sagittal slices acquired in two different subjects are reported. Major blood vessels show higher f with respect to the lung parenchyma. A decrease of f is observed towards the periphery of the lung, where the presence of large and medium sized vessels is reduced. The effect of blood microcirculation outside the lung is not observable, due to the absence of internal magnetic field gradients. However, the large vessels are still visible in the f maps, due to the blood signal attenuation effect which occurs in the presence of the external gradients. It is important to note that the values of f obtained in close proximity of the heart are not reliable because the two images were triggered in different cardiac phases.

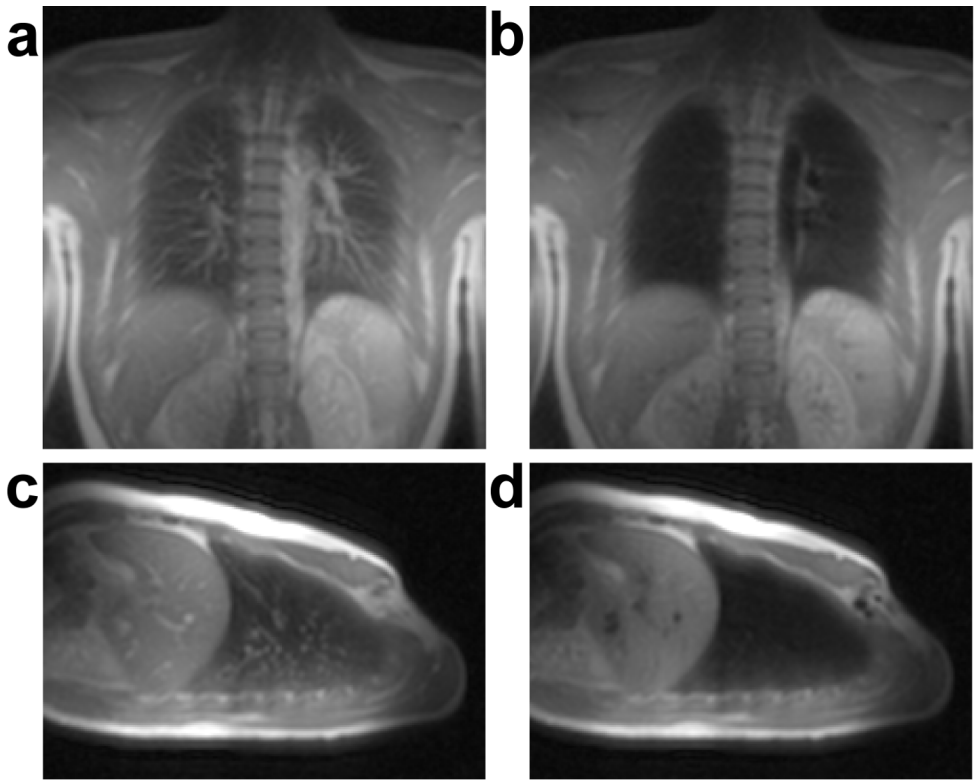

Figure 4.5: Magnitude images of the human lung obtained at 1.5 T using the ECG-synchronized STEAM-prepared HASTE sequence. Both coronal (a,b) and sagittal (c,d) slices are shown. a,c: Reference images (S_1) acquired in diastole with $TM_1 = 2$ ms. b,d: Blood suppressed images (S_2) acquired in end-systole with $TM_2 = 40$ ms. Reproduced with permission from reference [A1].

An example of the ROIs which were obtained after image segmentation is shown in Figure 4.8 a,c for both FRC and TLC. Large vessels are efficiently removed, but contamination from medium sized vessels can still be observed within the ROI. The resulting histograms of the statistical distribution of f within the lung parenchyma are shown in Figure 4.8 b,d. A broad distribution, with values ranging from 0% to 85%, can be observed. For each subject, the corresponding MVs and STDs obtained by averaging all the acquired slices of the coronal and sagittal datasets at FRC are given in Table 4.1. In all cases mean values for f between 32% and 40% were found. The mean calculated over all volunteers is $f \approx 36\%$. The absolute error obtained for this value from equation (4.9) is $\Delta f \approx 5\%$, assuming a relative error as large as 50% on both T_1 and $(b_2 - b_1) \cdot D$. For all volunteers, standard deviations between 13% and 21% were obtained, with an average value of 16%, which indicates a rather wide statistical distribution.

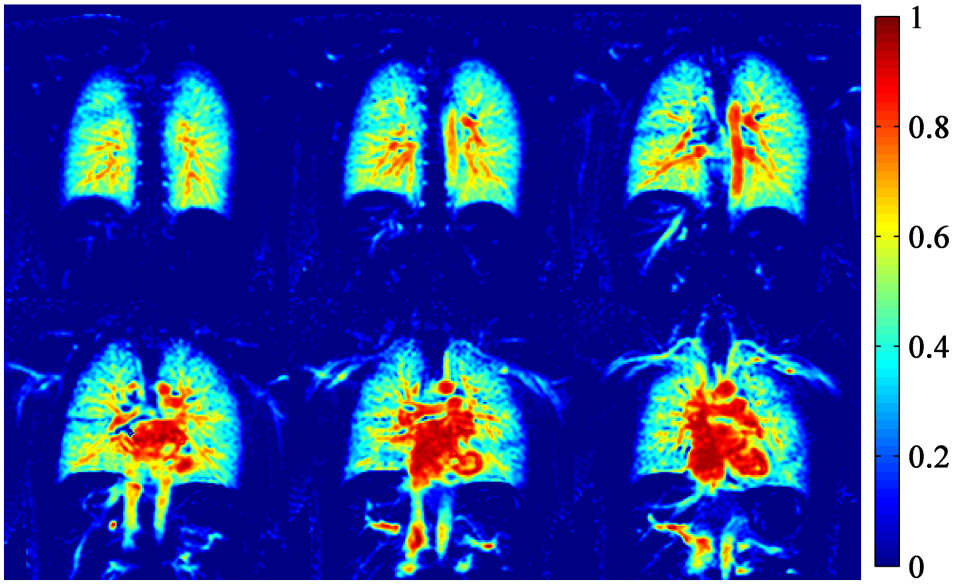

Figure 4.6: Parametric maps of the blood volume fraction f of the human lung obtained at 1.5 T using the STEAM-prepared HASTE sequence. A set of six coronal slices is shown. Reproduced with permission from reference [A1].

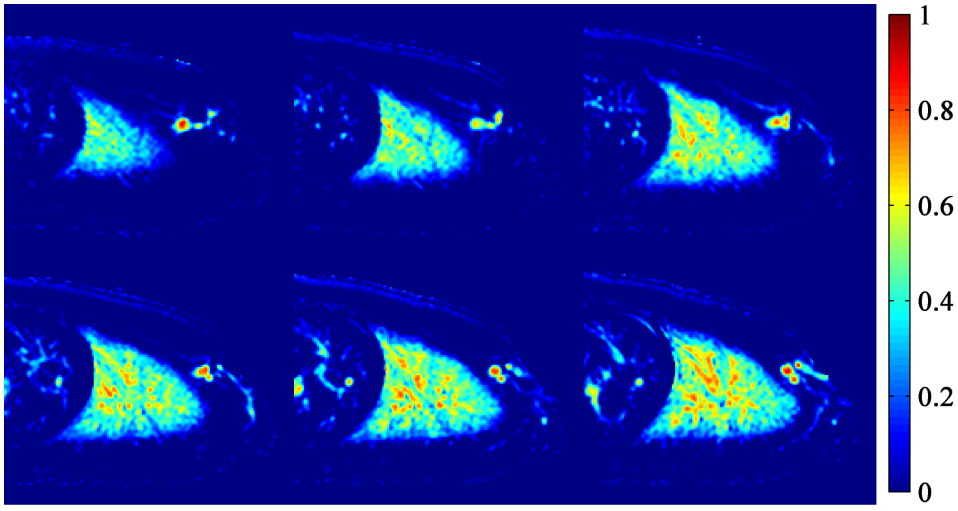

Figure 4.7: Parametric maps of the blood volume fraction f of the human lung obtained at 1.5 T using the STEAM-prepared HASTE sequence. A set of six sagittal slices is shown. Reproduced with permission from reference [A1].

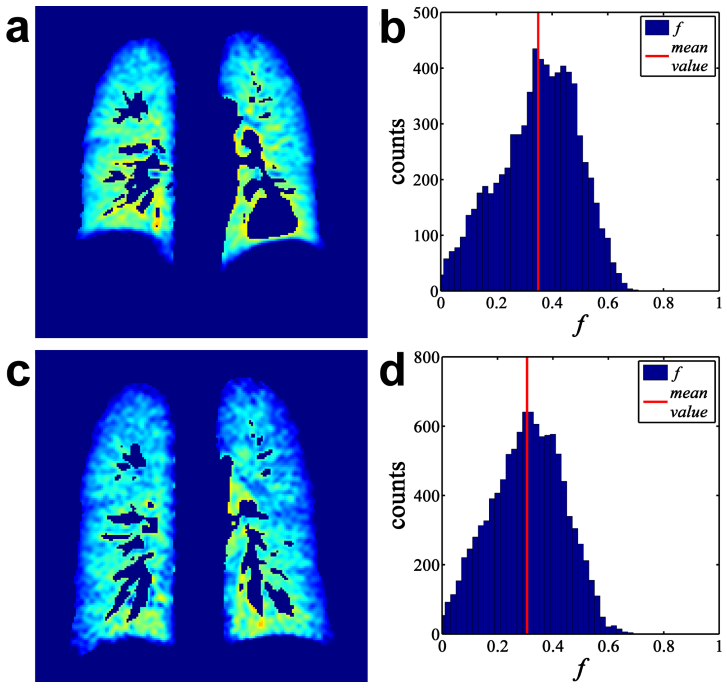

Figure 4.8: a,c: Example of the ROIs which were obtained after segmentation of the lung parenchyma at FRC (a) and TLC (c) in the coronal orientation. b,d: Corresponding histograms of the statistical distribution of the blood volume fraction within the lung parenchyma. Reproduced with permission from reference [A1].

Subject	MV ± STD (%) Coronal	Sagittal
1	35 ± 15	36 ± 13
2	37 ± 16	38 ± 16
3	36 ± 16	37 ± 15
4	37 ± 16	33 ± 15
5	38 ± 16	36 ± 15
6	35 ± 15	36 ± 13
7	32 ± 16	33 ± 14
8	40 ± 19	40 ± 21
Mean	36 ± 16	

Table 4.1: Mean values and standard deviations of the blood volume fraction within the lung parenchyma, obtained after averaging all the acquired slices of the coronal and sagittal data sets. Reproduced with permission from reference [A1].

The results of the repeatability study are reported in Table 4.2, together with the dependence of f on lung inflation. The standard deviation of the mean value σ_{MV} over ten measurements was between 0.39 and 1.10 for all volunteers. The corresponding coefficient of variation $\sigma_{\mathrm{MV}}/\mathrm{MV}$ is below 0.03 in all cases. Comparison between expiration (FRC) and inspiration (TLC) shows a significant reduction of the blood volume fraction with lung inflation ($P_{\mathrm{inflation}} < 0.01$ for all volunteers). However, the difference observed between FRC and TLC is strongly dependent on the volunteer, with values ranging from 0.9% to 8.4%.

	Expiration (FRC)			Inspiration (TLC)		
Subject	MV (%)	σ_{MV} (%)	$\sigma_{\mathrm{MV}}/\mathrm{MV}$	MV (%)	ΔMV (%)	$P_{\mathrm{inflation}}$
1	38.8	0.61	0.016	37.9	0.9	< 0.01
2	35.7	0.50	0.014	29.9	5.8	< 0.0001
3	32.8	0.87	0.027	29.4	3.4	< 0.0001
4	36.8	1.10	0.030	33.8	3.0	< 0.0005
5	33.7	0.94	0.028	27.5	6.2	< 0.0001
6	35.9	0.66	0.018	33.8	2.1	< 0.0005
7	35.0	0.63	0.018	26.6	8.4	< 0.0001
8	41.0	0.36	0.009	38.4	2.6	< 0.0001
Mean	36.2	0.71	0.018	32.2	4.1	< 0.0005

Table 4.2: Reproducibility of the mean values obtained from ten repeated measurements at FRC, together with the dependence of the blood volume fraction on lung inflation. Reproduced with permission from reference [A1].

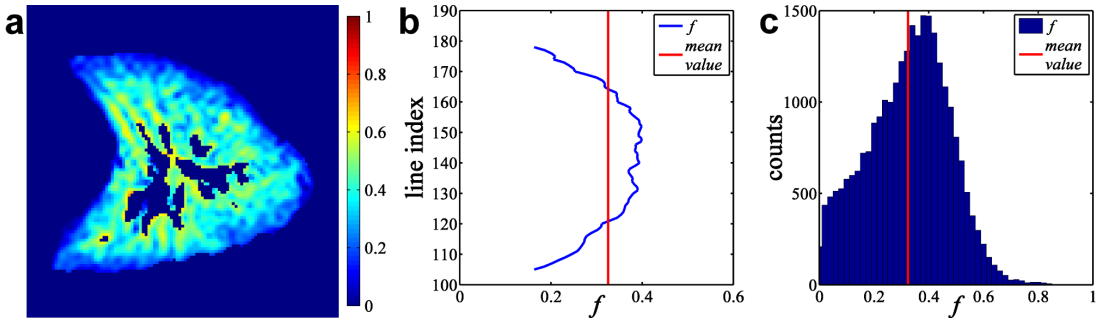

Figure 4.9: a: Example of the ROI which is obtained after segmentation of the lung parenchyma in the sagittal orientation. b: Gravitational dependence of the blood volume fraction obtained by averaging a full sagittal data set in the horizontal direction after image segmentation. c: Histogram of the statistical distribution of the blood volume fraction within the lung parenchyma obtained in a full sagittal data set after image segmentation. Reproduced with permission from reference [A1].

The gravitational dependence of the blood volume fraction obtained for one of the sagittal datasets is shown in Figure 4.9. The distribution of f in the A-P direction demonstrates a higher blood volume fraction in the central region of the lung. The values observed in the anterior and posterior regions are similar. This indicates a minimal influence of gravitation on the blood volume fraction.

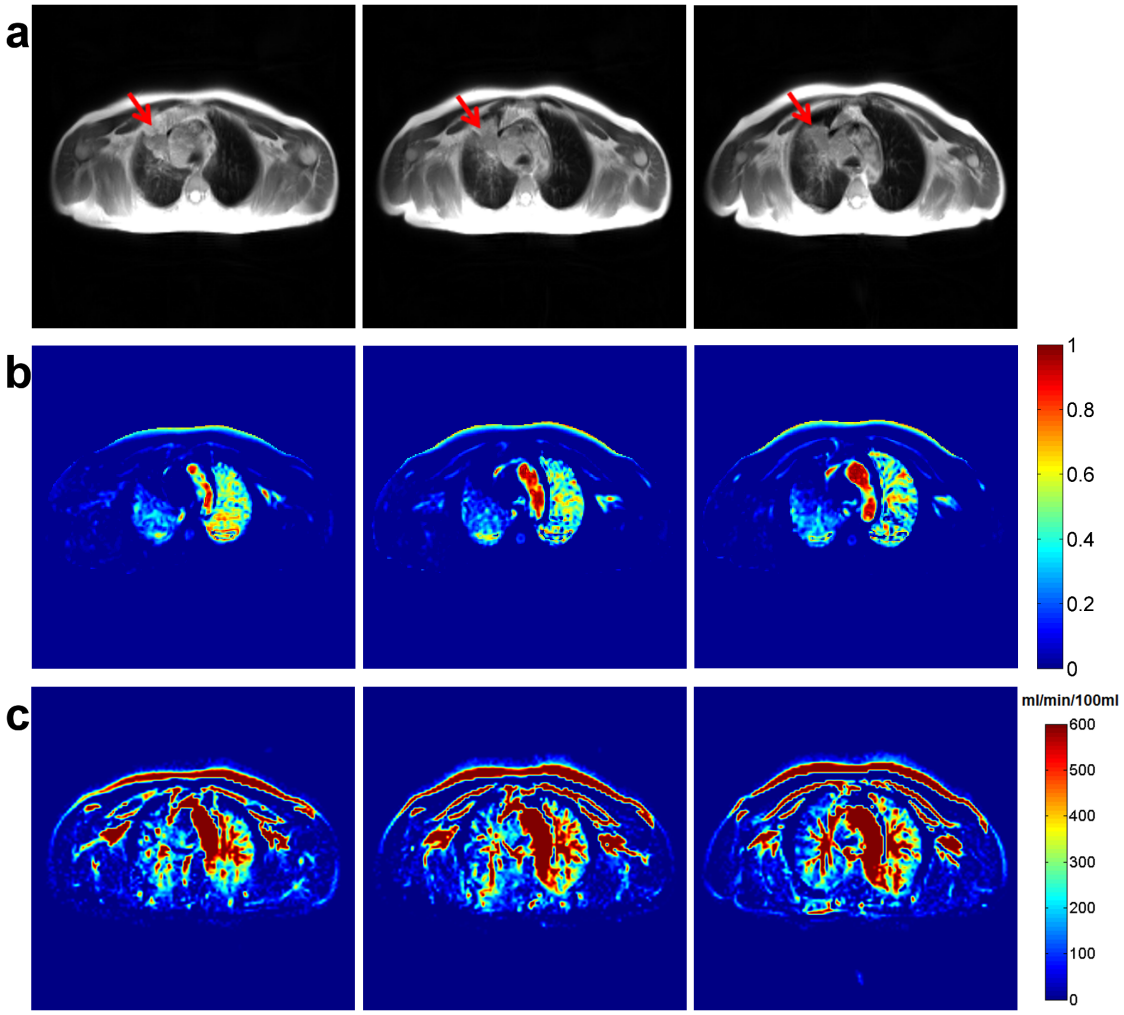

Figure 4.10: Images acquired in a patient with lung carcinoma with different techniques. A set of three transverse slices is shown for each technique. a: Morphological images acquired using a conventional HASTE sequence (the tumor is indicated by the red arrows). b: Maps of the blood volume fraction obtained from the STEAM-prepared HASTE sequence. c: Maps of the perfusion rate acquired using a FAIRER-HASTE sequence. Courtesy of Cord Meyer, Department of Experimental Physics 5, University of Würzburg.

The results obtained in one of the patients with lung cancer by using both IVIM and ASL are shown in Figure 4.10. A comparison between 1) the morphological images acquired with a conventional HASTE sequence, 2) the blood volume fraction maps obtained using the STEAM-prepared HASTE and 3) the perfusion rate maps obtained with the FAIRER-HASTE sequence is shown. A reduced blood volume fraction can be clearly observed in the region of the lung parenchyma which is close to the tumor. This kind of information cannot be retrieved from the morphological image alone, which simply shows an increased signal amplitude in that region indicating an increase of proton density. The two effects together (increased proton density and reduced blood volume fraction) are compatible with edema. This could be induced in the lung parenchyma by the tumor itself or by treatment [187, 211]. A similar effect can be observed in the perfusion rate map, which shows a reduced perfusion in the corresponding region of the lung. However, a different kind of information is provided by the two techniques (ASL and IVIM), as indicated by the different contrast in the blood volume fraction maps and in the perfusion rate maps. The blood volume fraction maps do not provide any information in the region of the tumor, due to the absence of internal gradients, as well as in other tissues with high proton density. This does not hold for ASL, which can be used also to assess the perfusion rate in the tumor itself. The results obtained in other patients using the STEAM-prepared HASTE sequence are shown in Figure 4.11. A reduced blood volume fraction in the region of the

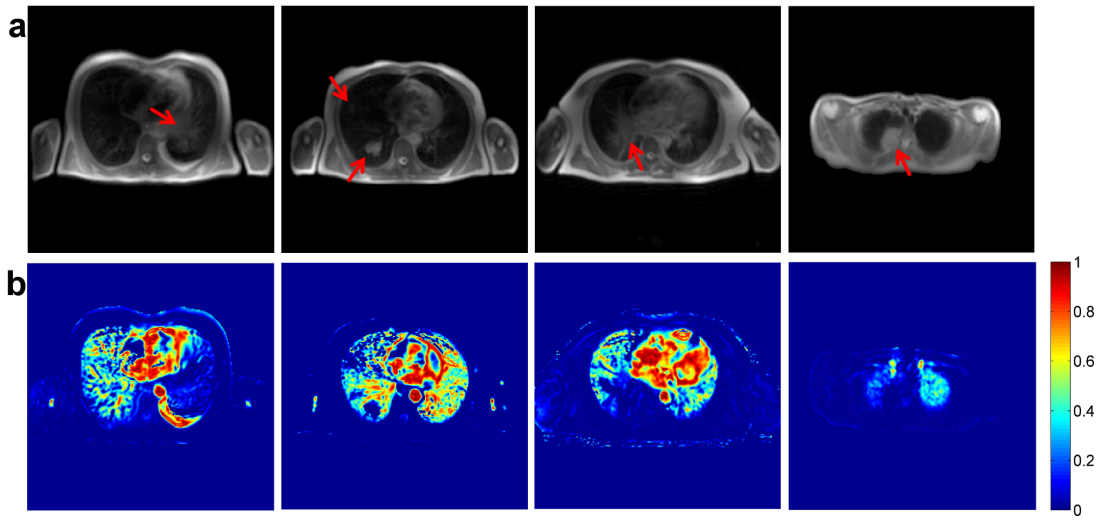

Figure 4.11: Images acquired in different patients with lung carcinoma using the STEAM-prepared HASTE sequence. A single transverse slice in the region of the tumor is shown for each patient. a: Morphological image (S_1) acquired using the STEAM-prepared HASTE sequence (the tumor is indicated by the red arrows). b: Corresponding maps of the blood volume fraction.

lung parenchyma which is close to the tumor can be clearly observed in at least two of the patients.
A comparison between the blood volume fraction maps obtained with conventional IVIM and with the proposed technique is shown in Figure 4.12, together with the corresponding histograms of the distribution of f within the lung parenchyma. The MVs obtained in all volunteers with both techniques are reported in Table 4.3. Similar MVs and STDs were obtained within the lung parenchyma with both techniques. However, systematically larger values were obtained in all subjects with conventional IVIM. The relative difference between the MVs obtained with the two techniques was below 0.2 for all volunteers, with an average calculated over all subjects of approximately 0.096.

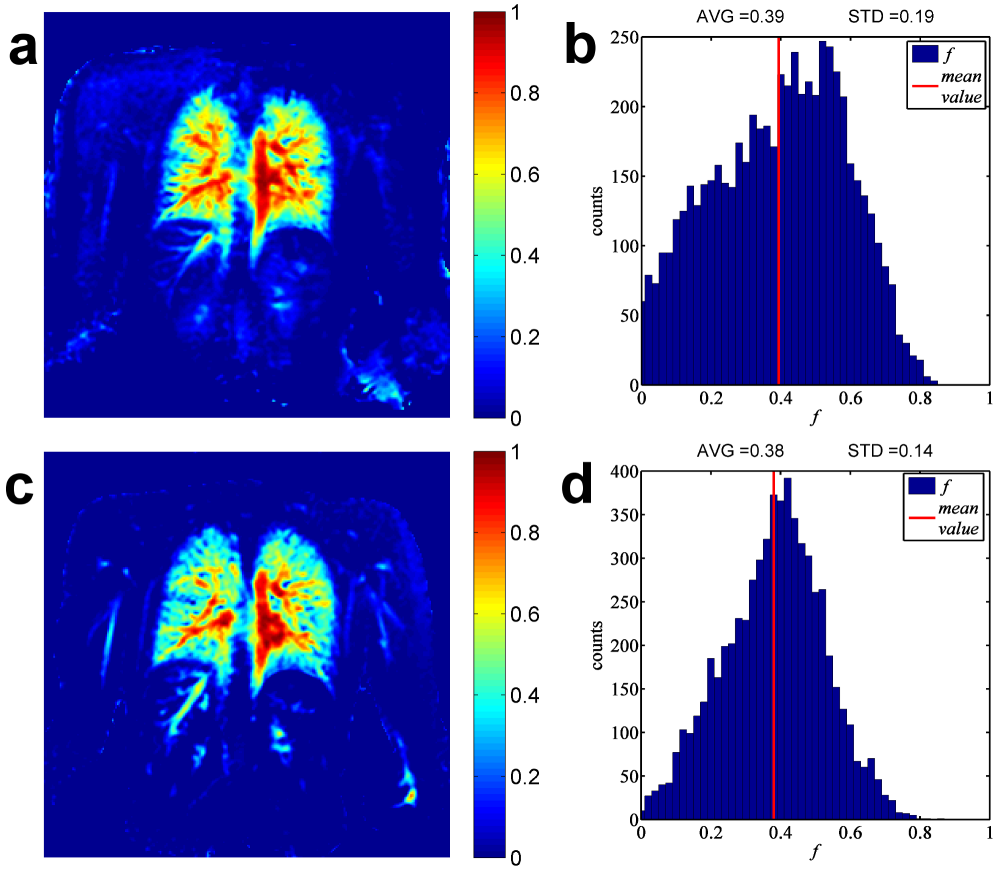

Figure 4.12: Comparison between the results obtained with conventional IVIM, based on DWI (a,b), and with the proposed STEAM-prepared HASTE sequence (c,d). a,c: Blood volume fraction maps. b,d: Corresponding histograms of the statistical distribution within the lung parenchyma.

Subject	MV ± STD (%) DWI	STEAM	$(MV_{DWI} - MV_{STEAM})/MV_{DWI}$
1	32.5 ± 17	32.1 ± 14	0.012
2	38.9 ± 14	31.3 ± 14	0.195
3	37.1 ± 17	33.5 ± 12	0.097
4	34.5 ± 17	29.9 ± 12	0.133
5	39.3 ± 19	38.0 ± 14	0.033
Mean	36.5 ± 17	33.0 ± 13	0.096

Table 4.3: Comparison of the mean values and standard deviations of the blood volume fraction within the lung parenchyma obtained with conventional IVIM, based on DWI, and the proposed technique, based on the STEAM-prepared HASTE.

The results of the comparison between the two sequence variants with and without IR preparation is shown in Figure 4.13. The subtraction between images S_1 and S_2 (Figure 4.13 a,d) shows better suppression of the background signal in the sequence variant with IR preparation, indicating a reduction of the influence of T_1. The blood volume frac-

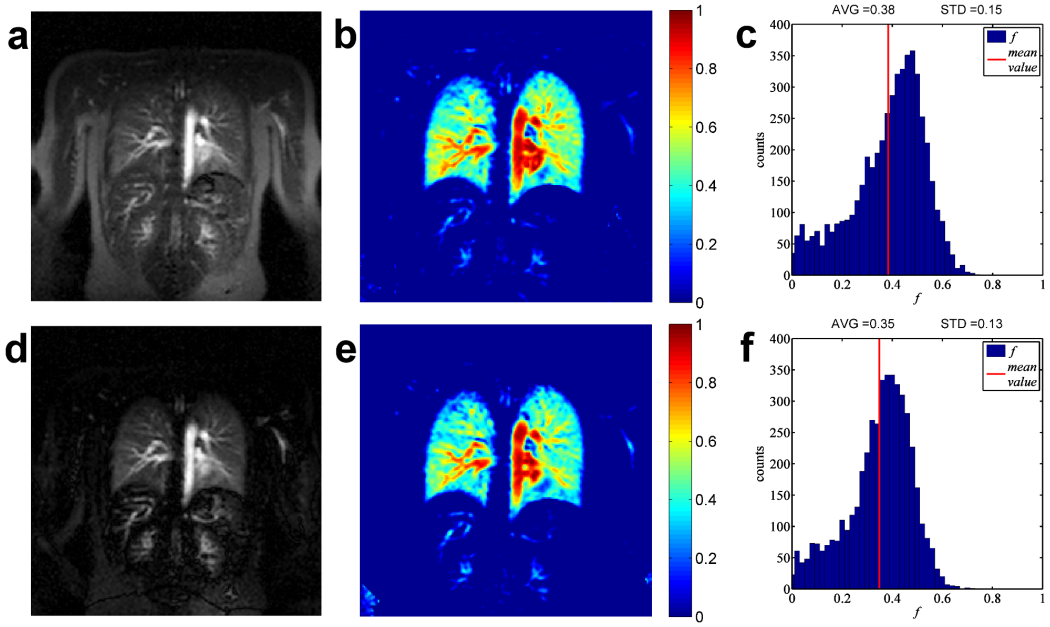

Figure 4.13: Comparison between the results obtained using the two variants of the STEAM-prepared HASTE sequence: with (bottom) and without (top) inversion recovery preparation. a,d: Subtraction between images S_1 and S_2. b,e: Blood volume fraction maps. c,f: Corresponding histogram of the statistical distribution within the lung parenchyma.

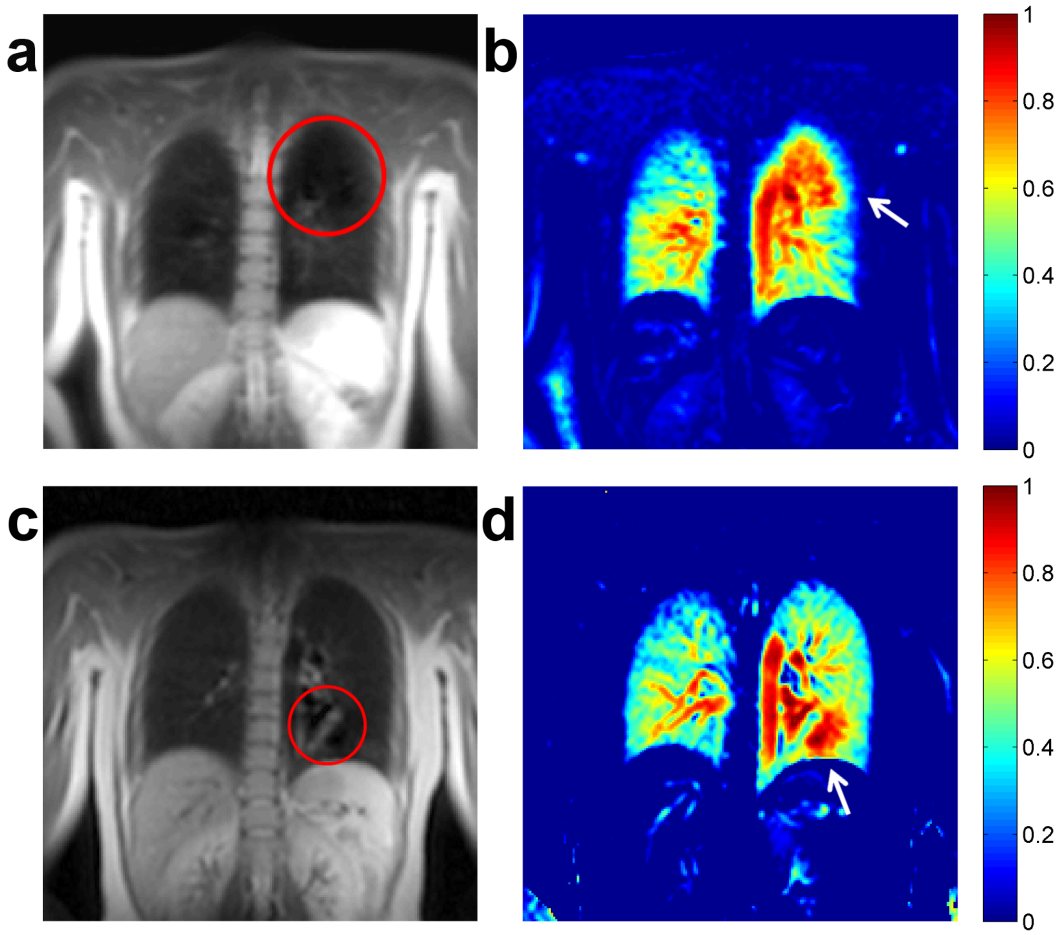

Figure 4.14: Example of the typical through plane deformation artifacts obtained with both conventional IVIM based on DWI (a,b) and the STEAM-prepared HASTE sequence (c,d) on the native images S_2 (a,c) and on the blood volume fraction maps (b,d). The artifacts are indicated by the arrows and the circles. a,b: With conventional IVIM, a through-plane deformation artifact due to physiologic bulk motion can be observed in the upper left lung. This results in an overestimation of the blood volume fraction. c,d: With the STEAM-prepared HASTE sequence, the images show a through-plane deformation artifact well localized in the region of the heart.

tion maps obtained with both sequence variants (Figure 4.13 b,d) and the corresponding histograms of the statistical distribution within the lung parenchyma (Figure 4.13 c,e) demonstrate that similar values of the blood volume fractions are obtained with both techniques. The resulting MVs were: 35.3% with IR and 38.6% without IR, with a relative difference of approximately 0.085.

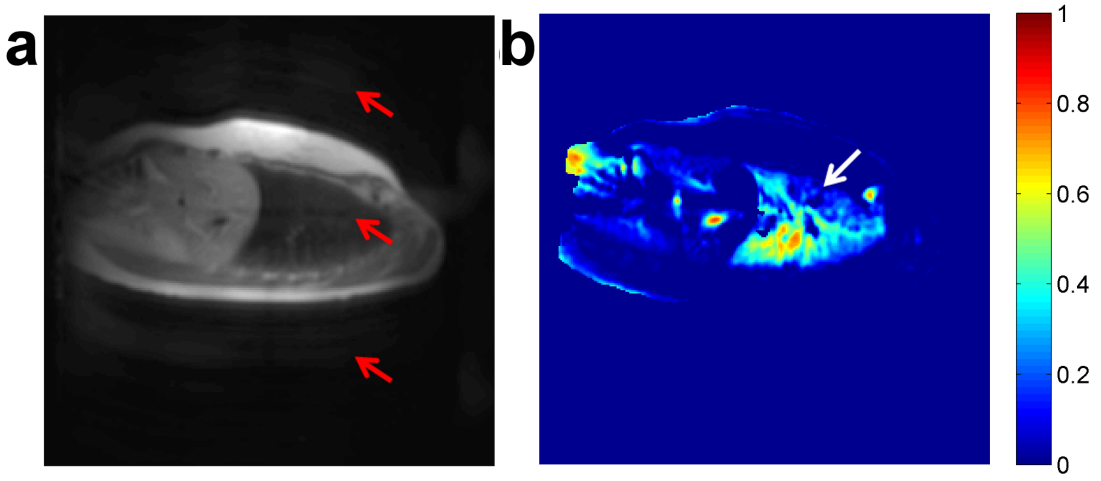

Figure 4.15: Example of the typical ghosting artifacts which are obtained with the non-CPMG HASTE sequence on both the native images (a) and the blood volume fraction maps (b). The artifacts are indicated by the arrows. a: The native images (in this case S_2) show ghosting artifacts due to the sensitivity of the non-CPMG HASTE sequence to inhomogeneities of the flip angle of the refocusing pulses. b: The quantification of the blood volume fraction in some regions of the lung may be over- or underestimated (like in the case of this figure), due to the presence of the ghost.

4.4 Discussion

In this chapter, it was shown how the presence of strong internal magnetic field gradients in the human lung can be exploited for the in-vivo quantification of the blood volume fraction. The proposed technique is based on the IVIM approach [59, 60, 61]. In the conventional IVIM technique, the modulation of the signal amplitude of blood in the capillaries is achieved by applying strong diffusion sensitizing gradients. In the presented technique, as the internal gradients are always active and thus they cannot be switched on or off, sensitization to blood microcirculation is obtained by changing both the time interval TM and the cardiac phase used for acquisition in an ECG-synchronized STEAM-prepared HASTE sequence.
The advantages offered by the elimination of diffusion sensitizing gradients are: 1) the possibility to use shorter TE and 2) the reduced sensitivity to bulk motion. A more detailed description of these advantages is given below:

1. The use of a shorter TE is beneficial for two reasons: 1) the reduction of signal losses induced by the T_2 decay, which results in increased signal amplitude, as well as 2) the better accuracy in the determination of the blood volume fraction. The model of equation (2.52), in fact, assumes that both the intra- and the extravascular water

compartments have the same T_2. If this is not the case, the effects on the calculation of f are negligible only if TE $<<$ T_2 for both water compartments. Otherwise, an over- or an underestimation of the blood volume fraction may occur, depending on the respective T_2 values in the two water compartments.
The absence of diffusion sensitizing gradients allows to reduce TE by a few tens of ms compared to conventional IVIM. This is of particular importance in the lungs considering that the signal component with the longest T_2 in the lung parenchyma has a relaxation time of approximately 80 ms [70, 112]. This was also the motivation for the use of centric reordering of the phase encoding lines in order to obtain a TE as short as possible, at the cost of increased blurring in the phase encoding direction. However, this effect was minimized by using a relatively high receiver bandwidth and a very short inter-echo time.
The different T_2-weighting of the two water compartments, together with the assumptions made on T_1 and D of the lung parenchyma, might be the reason for the systematically larger values of the blood volume fraction obtained in this work with conventional IVIM in comparison to the STEAM-prepared HASTE technique, for the reasons discussed above.

2. Because the typical velocities of physiological bulk motion are much higher than those of blood microcirculation, the diffusion gradients are strongly sensitive to bulk motion. Therefore, directional incoherencies of physiological motion within the voxel can give rise to signal voids in the lung space called "through-plane deformation artifacts" [203, 204, 206] which may corrupt the quantification of the blood volume fraction. This problem could be mitigated with the use of motion compensated diffusion gradients at the cost of even longer TEs [207]. This was also the approach adopted in this work for the comparison between the proposed technique and conventional IVIM. Even with motion compensated diffusion gradients, however, through-plane deformation artifacts were observed within the lung parenchyma in most subjects on the blood suppressed image S_2 when using conventional IVIM. An example of through-plane deformation artifacts obtained with conventional IVIM on image S_2 and of the corresponding influence on the quantification of the blood volume fraction is shown in Figures 4.14 a and b.
With the proposed technique, the external gradients are designed to be sensitive only to fast blood flow in the large vessels, which has a larger velocity compared to most of the other physiological motions. With this approach, through-plane deformation artifacts were only observed in close proximity of the heart and did not affect the quantification of the blood volume fraction in the lung parenchyma, as shown in the example of Figures 4.14 c and d.

Another relevant advantage of the proposed technique over conventional IVIM is the compatibility with a HASTE readout based on the CPMG conditions. As already discussed in Chapter 3, conventional IVIM requires the use of special approaches in order to overcome the violation of the CPMG conditions, which is due to the sensitivity of diffusion-sensitizing

gradients to bulk motion. The solution adopted in this work is based on a non-CPMG HASTE sequence with quadratic RF-phase increase during the refocusing pulse train, as proposed by Le Roux [165] and described in Chapter 3. The drawbacks of this approach are: 1) the need for a pulse train of double length compared to the CPMG sequence or, alternatively, the need to use parallel imaging techniques in order to reduce the pulse train length, as well as 2) the presence of ghosting artifacts if the flip angle of the refocusing pulses deviates significantly from the ideal 180°. An example of these ghosting artifacts and of their influence on the quantification of the blood volume fraction is illustrated in Figure 4.15.

Two main drawbacks can be identified for the STEAM-prepared HASTE technique with respect to the conventional IVIM approach: 1) because of the STEAM preparation, the signal amplitude is halved compared to a Stejskal-Tanner diffusion preparation, 2) the use of different TMs introduces also a T_1 dependent term in the calculation of f. Generally, the first drawback is actually negligible as the signal amplitude is completely recovered or even increased, thanks to the shorter TE allowed. The presence of the T_1 dependent term has a minor impact on the calculation of f, as the relatively long T_1 of the lung parenchyma permits the use of TM $<<$ T_1. Therefore, explicit knowledge of T_1 is not strictly necessary: the assumption of a homogeneous T_1 within the lung parenchyma would merely result in a slight over- or underestimation of f if this condition is not fulfilled. Furthermore, the influence of T_1 on the quantification of the blood volume fraction could be strongly and easily reduced by means of an additional IR preparation to regulate the T_1-weighting, as demonstrated by the results above.

Another difference with respect to conventional IVIM is the role of diffusion. The diffusion weighting which is due to the presence of external gradients is negligible in the proposed technique, while the effect of diffusion within the internal magnetic field gradients must be taken into account for an accurate quantification. In fact, not only the signal of flowing blood is attenuated when increasing TM, but also the signal of the diffusing spins in the extravascular compartment. This signal attenuation depends on the amplitude of the internal gradients and thus, on microstructural properties of the lung such as the alveolar size. If this effect were not taken into account, it would result in an overestimation of f. In this work, a typical value of the internal magnetic field gradients in healthy subjects was used for this correction, as discussed in Chapter 2.

The impact of the assumptions made on both T_1 and on the diffusion effects was estimated by using a mathematical model of the error propagation. In the case of a deviation of 50% on both assumptions, the absolute error on the blood volume fraction would be $\Delta f \approx 5\%$. Because the T_1 and diffusion corrections in equation (4.5) were performed using parameters which refer to the lung parenchyma only, the values obtained in the blood vessels are slightly smaller than expected ($f = 1$). Nevertheless, the presence of medium sized blood vessels could lead to an overestimation of the blood volume fraction of the lung parenchyma, due to partial volume effects. In fact, only large vessels are efficiently removed from the ROI, while signals from vessels which are smaller than the voxel size are difficult to separate from the lung parenchyma tissue. This effect could be mitigated by

using a thinner slice thickness and/or a higher in-plane resolution, at the cost of reduced SNR and increased blurring due to the longer inter-echo time required. However, this approach is limited by the low proton density of the lung tissue, which requires relatively large voxel sizes in order to obtain a detectable MR-signal and an acceptable SNR for the quantification of f.

Another drawback, which is common to most quantitative lung imaging techniques, is that any kind of motion which occurs within the lung space between the acquisition of the two images S_1 and S_2, such as imperfect breath-holding, can lead to image misregistration and result in erroneous quantification. This problem was observed in a limited number of acquisitions. The regions which are mostly subject to misregistration are the anterior part of the lung and the region of the diaphragm.

It is important to discuss here also the role of the static magnetic field B_0 on the presented technique. Equation (4.3) states that the values of TM and TE which enable the suppression of the blood signal from the capillaries is reduced when using higher magnetic field strengths, due to the stronger internal gradients. This means that the technique would benefit from the use of higher magnetic fields, as this would reduce the required TM and/or TE. This would result in a reduced influence of T_1 and/or T_2 on the calculation of f, as already discussed.

The values of f observed within the lung parenchyma with the presented technique in all subjects (MV $\pm$ STD $\approx 36 \pm 16\%$) are in good agreement with the results which were previously obtained by Lehmann et al. [186] by using contrast-enhanced MR angiography (MV $\approx 33\%$). The large standard deviation obtained in this work can be associated with the heterogeneity observed in the blood volume fraction maps between the inner part of the lung, with a higher f, and the periphery, with a lower f. The results obtained from the repeatability study demonstrate a relatively good reproducibility of the presented technique, with a coefficient of variation which was smaller than 0.03 in all subjects.

The gravitational dependence of the blood volume fraction shows a rather homogeneous distribution in the anterior-posterior direction, with a larger f in the central region of the lung. This indicates that the increase of perfusion towards the bottom of the lung, which is due to the effect of gravitation [208], is compensated by the increase of extravascular lung water, which is due to the compression of the lung parenchyma ("Slinky effect" [209]). This is in agreement with what was previously reported by Hopkins et al. in reference [209]. The dependence of f on the breathing state demonstrates that the blood volume fraction decreases with inflation, in agreement with the reduction of perfusion observed by Hopkins et al. [210].

In this work, most measurements were performed on healthy volunteers and the results are consistent with other studies. An in-depth assessment of the performance of the presented technique on patients with lung diseases requires further investigation and could be an interesting topic for future research. However, it could be useful to remark here some characteristics of this technique in order to identify possible clinical applications. The presented technique is designed for studies of the lung parenchyma and is not suited for investigation of tissues with high proton density and with negligible internal magnetic field gradients such

as lung tumors, as it was demonstrated in this work with experiments on patients. This represents one of the main differences between the proposed technique and other perfusion imaging methods, such as conventional IVIM, ASL, SEEPAGE and Fourier-decomposition. Nevertheless, in the presence of lung tumors, the presented technique could be useful for the assessment of perfusion defects as well as edema of the lung parenchyma, which may be induced by the pathology itself or by cancer treatment [52, 187, 211]. In fact, a reduction of the blood volume fraction in the lung parenchyma was clearly observed in at least three of the five investigated patients by applying the proposed technique. In other lung diseases, such as COPD and emphysema, it has been shown that the lung microstructure can be altered in comparison to healthy subjects [55]. A quantitative measurement of the effect of such diseases on the internal magnetic field gradients of the lung cannot be found yet in literature. However, studies conducted with hyperpolarized gases seem to indicate a change of the internal gradients in the presence of emphysema, due to the destruction of the alveolar walls [55]. Therefore, in the case of a reduction of the internal gradients it may be necessary to increase TM in order to obtain the desired blood suppression in the lung capillaries at the cost of the already discussed implications of a longer TM. As soon as a complete blood suppression can be achieved, the heterogeneous distribution of internal gradients within the lung has a small impact on the quantification of the blood volume fraction, as demonstrated by equations (4.5) and (4.9).
In conclusion, the presented technique represents a robust method to quantify the blood volume fraction of the lung parenchyma without the need for contrast agents. Image acquisition can be accomplished in a single breath-hold of approximately 10 s duration, which may be compatible with clinical studies on patients with lung diseases as well as with the clinical routine. The technique has the potential to detect a variety of pulmonary diseases which alter the water balance between the intra- and extravascular compartments. In this regard, deeper clinical investigations are necessary in order to assess the performance in the presence of lung diseases which can modify the lung microstructure and consequently the amplitude of the internal magnetic field gradients.

Chapter 5

Transverse Relaxation Enhancement and Alveolar Size Imaging

5.1 Introduction

The lung tissue is a heterogeneous systems in which the diffusion of spins through the internal magnetic field gradients enhances the loss of phase coherence in the transverse magnetization [64, 131, 150]. This results in a shortening of the transverse relaxation time that is typically indicated with $T_{2,\mathsf{diff}}$, as discussed in Chapter 2.
The microstructure of the lung can be modeled as a densely packed array of spheres which represent the air-filled alveoli. These generate magnetic field gradients in the surrounding lung tissue where the water molecules diffuse, as described by Case et al. [67]. The transverse relaxation enhancement of such a system has been experimentally studied by Weisskoff et al. [157]. Based on their results, a model for the relaxation time $T_{2,\mathsf{diff}}$ has been empirically developed by Yung [152], as indicated by equations (2.50) and (2.51). $T_{2,\mathsf{diff}}$ depends on several interesting parameters with regard to lung imaging. These are: 1) a parameter which characterizes the lung microstructure (R), 2) a parameter which depends on lung inflation (η) and 3) tissue-specific parameters ($\Delta\chi$ and D). As already mentioned in Chapter 2, the typical values of R, η, $\Delta\chi$ and D in the lung lead to the assumption that $T_{2,\mathsf{diff}}$ of the lung tissue can be approximated by equation (2.50).
The dependence of $T_{2,\mathsf{diff}}$ on R is of particular interest because it could be exploited for the quantification of the alveolar size, as recently demonstrated by Kurz et al. [65]. The alveolar size, in fact, is a parameter of paramount importance in the lung, as it represents an indicator of possible microstructural injuries. These might be induced by several lung diseases such as emphysema, Chronic Obstructive Lung Disease (COPD) and Acute Lung Injury (ALI), as well as by mechanical ventilation [55, 218, 221, 222]. Moreover, a non-invasive quantification of the alveolar size could help to develop a better understanding of the alveolar dynamics during respiration [135, 212, 213, 214, 215], which still represents an open issue of primary interest in the field of lung research [216, 217, 218, 219, 220, 221].

While several techniques are available to determine the alveolar size ex-vivo [137, 213, 214], non-invasive quantification in-vivo is still very challenging. In this regard, a possible approach is represented by the application of DWI in combination with hyperpolarized gas MRI [8, 53, 55, 56, 57, 135, 136, 212, 222, 223]. Nevertheless, the usage of this technique has not expanded to the clinical routine yet, as it is hampered by the requirement of dedicated hardware and complex workflows, which are typical of hyperpolarized gas MRI.
In this chapter, a technique based on proton MRI is presented which allows to quantify $T_{2,\mathrm{diff}}$ of the lung in-vivo in a single breath-hold. In addition to this, the possibility to exploit the knowledge of $T_{2,\mathrm{diff}}$ for the quantification of the alveolar size is investigated.
In the past, studies on the transverse relaxation enhancement which is induced by diffusion through the internal gradients have been performed in porous materials, with the aim of obtaining information about the pore size [151, 224]. To this end, the single spin-echo (or Hahn-echo) pulse sequence was used. In the slow diffusion regime, in fact, the signal amplitude decay of the Hahn-echo is directly related to the statistical distribution of the internal gradients [131, 134, 151], as described by equation (2.49). Measurement of the signal amplitude at different TEs can be used in combination with a Laplace inversion to generate a plot of the distribution of internal gradients [134, 151] and of the corresponding size of the magnetic field perturbers. For this, a mathematical model like that of equation (2.22) could be used. This approach, however, is highly time consuming as it normally requires the acquisition of a large number of points at different TEs with relatively long acquisition times. Furthermore, a-priori knowledge of $T_{2,0}$ is required in order to separate the signal decay component induced by spin-spin interactions from $T_{2,\mathrm{diff}}$.
Another possible approach to quantify $T_{2,\mathrm{diff}}$ consists in the analysis of the dependence of T_2 on the inter-pulse time in a CPMG pulse sequence [65, 70]. This technique, which has been used for ex-vivo studies of the lung, requires multiple quantifications of T_2 with different values of the inter-pulse time in a multi-echo CPMG sequence. This results in relatively long acquisition times as well as in a high sensitivity to physiological motion, thus making the technique incompatible with in-vivo studies.
The technique proposed here allows to quantify $T_{2,\mathrm{diff}}$ of the lung in a single breath-hold of approximately 10 s duration without the need for a-priori knowledge of $T_{2,0}$. To this end, a HASTE sequence with Hahn-echo preparation is used. The underlying idea to quantify $T_{2,\mathrm{diff}}$ is to exploit the Carr-Purcell mechanism described in Chapter 2 by acquiring two or more images with identical TE, but with a different number of refocusing pulses between excitation and signal acquisition.
In this work, the ability of the Hahn-prepared HASTE sequence to quantify $T_{2,\mathrm{diff}}$ was first validated in phantom by using the conventional Hahn-echo approach as a reference. In-vivo experiments were then conducted in order to investigate the influence of lung inflation and perfusion on $T_{2,\mathrm{diff}}$. Finally, the alveolar size was estimated by means of equation (2.50) from the $T_{2,\mathrm{diff}}$ maps which were obtained in-vivo. In order to compensate for the influence of lung inflation on $T_{2,\mathrm{diff}}$, which is expressed by the air volume fraction η, a proton density weighted image was additionally acquired by using a UTE sequence.

5.2 Materials and Methods

5.2.1 Signal Decay Model

For a system composed of spherical magnetic field perturbers, the signal amplitude decay in the Hahn-echo experiment is well described by the following mono-exponential function [157]:

$$S\left(\mathrm{TE}\right) \propto \exp\left[-\left(\frac{1}{T_{2,0}} + \frac{1}{T_{2,\mathrm{diff}}}\right) \cdot \mathrm{TE}\right] \tag{5.1}$$

where $T_{2,\mathrm{diff}}$ in the slow diffusion regime can be approximated by equation (2.50), as discussed in Chapter 2. This means that, in order to obtain $T_{2,\mathrm{diff}}$, the model of equation (5.1) can be used to fit the signal amplitude data acquired at different TEs.

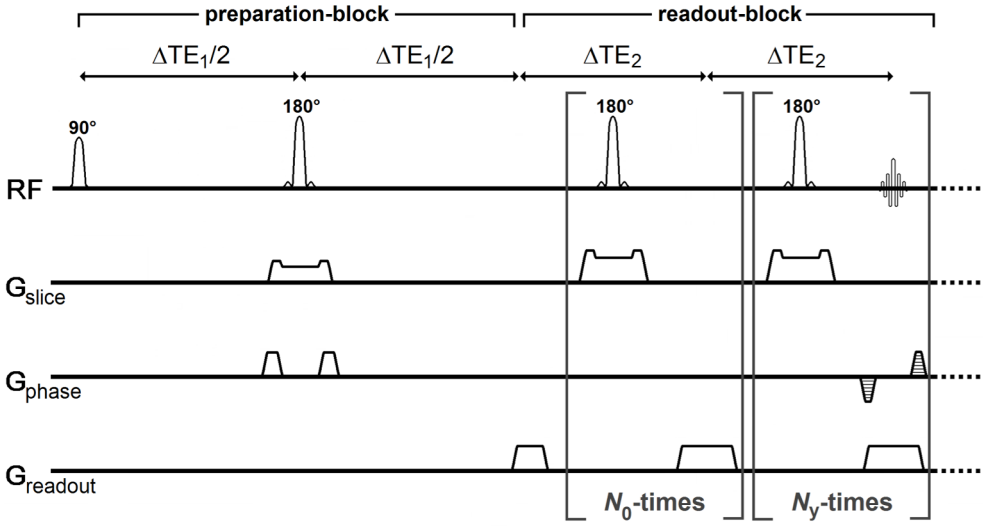

Figure 5.1: Timing diagram of the Hahn-prepared HASTE sequence which was used to quantify $T_{2,\mathrm{diff}}$ of the lung. The transverse magnetization is first prepared by means of a 180° refocusing pulse ("preparation-block"), similarly to the conventional Hahn-echo sequence. Signal refocusing is repeated N_0 times before actual image acquisition by applying a series of dummy-pulses. The following train of 180° refocusing pulses ("readout-block") allows the readout of the full k-space in a single shot (HASTE). Data readout is repeated, in combination with signal refocusing, for N_y-times (with N_y = number of acquired phase-encoding lines). The phase-encoding lines were acquired with linear reordering. The inter-pulse times of the preparation-block ($\Delta\mathrm{TE}_1$) and of the readout-block ($\Delta\mathrm{TE}_1$) are defined as shown.

5.2.2 Pulse Sequence

As already mentioned, the conventional Hahn-echo experiment presents two main drawbacks with regard to the quantification of $T_{2,\text{diff}}$ of the lung in-vivo:

1. knowledge of $T_{2,0}$ a-priori, or from a separate measurement, is required in order to extract $T_{2,\text{diff}}$ from equation (5.1);

2. for the acquisition of each image, relatively long acquisition times of the order of several minutes are required.

In order to solve both of these problems, the use of a Hahn-prepared HASTE sequence is proposed here. A diagram of the pulse sequence is shown in Figure 5.1. The magnetization preparation module ("preparation-block") consists of a non-slice-selective RF-pulse with 90° flip-angle, followed by a 180° slice-selective refocusing pulse. The time distance between excitation pulse and echo-signal is ΔTE_1. The subsequent HASTE readout ("readout-block") is composed of train of 180° slice-selective refocusing pulses with inter-pulse time ΔTE_2. This allows for the readout of the full k-space in a single shot. The values of ΔTE_1 and ΔTE_2 can be changed independently from each other. Another important parameter of the sequence that can be arbitrarily chosen is the number of refocusing pulses N_0 in the readout-block, which can be applied as dummy-pulses before actual image acquisition (i.e. without acquiring the corresponding echo signals).
Formation of unwanted echoes generated by the residual longitudinal magnetization which is available at the end of the preparation-block was prevented by using different directions and amplitudes for the spoiling gradients in the preparation-block (phase-encoding and slice-selection directions used) and those in the readout-block (readout and slice-selection direction used). In order to minimize the signal loss which is due to the elimination of the residual longitudinal magnetization, the slice thickness which was used for the refocusing pulse of the preparation-block was twice the slice thickness of the refocusing pulses in the readout-block.
Linear reordering of the phase-encoding steps was used together with partial Fourier acquisition. Image reconstruction was accomplished using the Margosian algorithm [158]. The sequence includes also ECG synchronization, as the resulting signal in the lungs depends strongly on the cardiac phase [34, 38].

5.2.3 Quantification of $T_{2,\text{diff}}$

The key feature of the sequence described above is the possibility to directly quantify the components of the transverse relaxation time $T_{2,0}$ or $T_{2,\text{diff}}$ without the need for extra measurements, as previously shown by Deichmann et al. [225]. $T_{2,0}$-weighting and $T_{2,\text{diff}}$-weighting, in fact, are dictated by different time variables, as further described below:

- Signal decay due to spin-spin interactions, with relaxation time $T_{2,0}$, is dictated by the time distance between excitation pulse and signal acquisition (i.e. the echo time TE). After n refocusing pulses in the readout-block, TE is:

$$\text{TE} = \Delta\text{TE}_1 + n \cdot \Delta\text{TE}_2 \tag{5.2}$$

- Signal decay due to diffusion through the internal gradients, with relaxation time $T_{2,\mathsf{diff}}$, is dictated by an effective echo time ($\mathrm{TE}_{\mathsf{eff}}$) given by [225]:

$$\mathrm{TE}_{\mathsf{eff}}^3 = \Delta\mathrm{TE}_1^3 + n \cdot \Delta\mathrm{TE}_2^3 \tag{5.3}$$

  as established by the Carr-Purcell mechanism described in Chapter 2.

This means that the effect of $T_{2,\mathsf{diff}}$ does not only depend on TE, but also on the specific inter-pulse times $\Delta\mathrm{TE}_1$ and $\Delta\mathrm{TE}_2$ used. Hence, the signal decay which is due to transverse relaxation can be factorized in two separate terms, each depending on either TE or $\mathrm{TE}_{\mathsf{eff}}$:

$$S\left(\mathrm{TE}, \mathrm{TE}_{\mathsf{eff}}\right) \propto \exp\left(-\frac{\mathrm{TE}}{T_{2,0}} - \frac{\mathrm{TE}_{\mathsf{eff}}}{T_{2,\mathsf{diff}}}\right) \tag{5.4}$$

Direct quantification of $T_{2,\mathsf{diff}}$ can be performed by acquiring several images with different values of $\mathrm{TE}_{\mathsf{eff}}$ but identical TE. This would result in identical $T_{2,0}$-weighting in all images, but different $T_{2,\mathsf{diff}}$-weighting. In order to achieve this, the values of $\Delta\mathrm{TE}_1$ and N_0 in the sequence shall be properly regulated, as further explained below.
The parameter n in equations (5.2) and (5.3) is given by:

$$n = N_0 + N_{y,\mathsf{center}} \tag{5.5}$$

where $N_{y,\mathsf{center}}$ is the number of phase-encoding lines acquired before the k-space center is reached. Its value depends on the partial Fourier factor and must be identical for all images. From equation (5.2), the allowed values for $\Delta\mathrm{TE}_1$ are:

$$\Delta\mathrm{TE}_1\left(n\right) = \mathrm{TE} - n \cdot \Delta\mathrm{TE}_2 \tag{5.6}$$

where n can assume discrete values only. The corresponding values for $\mathrm{TE}_{\mathsf{eff}}$ are (from equation (5.3)):

$$\mathrm{TE}_{\mathsf{eff}}\left(n\right) = \sqrt[3]{\left(\mathrm{TE} - n \cdot \Delta\mathrm{TE}_2\right)^3 + n \cdot \Delta\mathrm{TE}_2^3} \tag{5.7}$$

This means that different values of $\mathrm{TE}_{\mathsf{eff}}$ can be obtained by changing n, while keeping TE and $\Delta\mathrm{TE}_2$ fixed. $\Delta\mathrm{TE}_1$ and N_0 must be correspondingly adjusted according to equations (5.5) and (5.6). The data acquired with different values of $\mathrm{TE}_{\mathsf{eff}}$ can then be fitted by using the following model (from equation (5.4)) in order to obtain $T_{2,\mathsf{diff}}$:

$$S\left(\mathrm{TE}_{\mathsf{eff}}\right) \propto \exp\left(-\frac{\mathrm{TE}_{\mathsf{eff}}}{T_{2,\mathsf{diff}}}\right) \tag{5.8}$$

It is important to note that, according to equation (5.7), only a discrete and limited number of points within a fixed range of values of $\mathrm{TE}_{\mathsf{eff}}$ can be acquired when TE and $\Delta\mathrm{TE}_2$ are fixed. This is due to the fact that, according to equation (5.6), the allowed values for n, and consequently N_0, are discrete and limited by $0 \leq n < \mathrm{TE}/\Delta\mathrm{TE}_2$, as $\Delta\mathrm{TE}_1$ must be positive. Therefore, in order to achieve the desired $T_{2,\mathsf{diff}}$-weighting, it is necessary to prospectively select a set of parameters (TE, $\Delta\mathrm{TE}_1$, $\Delta\mathrm{TE}_2$ and N_0) that allows for the acquisition of an appropriate range of values of $\mathrm{TE}_{\mathsf{eff}}$, which in turn depends on the expected $T_{2,\mathsf{diff}}$.

5.2.4 The Influence of Stimulated Echoes on the Quantification

An important characteristic of the Hahn-prepared HASTE sequence, as compared to the conventional Hahn-echo, is the presence of stimulated-echoes in the signal, due to multiple signal refocusing [160, 169, 171, 226]. This has two main consequences:

1. If the flip-angle of the refocusing pulses deviates from the ideal 180°, then the signal is a mix of spin-echoes and stimulated-echoes. In this case, signal oscillations would occur in the first few echoes before a balance between the signal contributions of spin-echoes and stimulated-echoes is reached [160, 169]. In order to guarantee that the contribution of spin-echoes and stimulated-echoes was similar for all images, the minimum value used for n was 3.

2. The values of $T_{2,\mathsf{diff}}$ which are measured with the Hahn-prepared HASTE sequence may be slightly different compared to those which are obtained with the conventional Hahn-echo. This is due to the fact that stimulated-echoes and spin-echoes are differently sensitive to diffusion [227]. This effect was taken into account by means of the proportionality constant β in equation (2.50), which can be empirically determined to fit simulations or experimental data as originally proposed by Yung [152]. The value of the constant β for the Hahn-prepared HASTE was experimentally obtained by means of phantom experiments using the conventional Hahn-echo as a reference, as further described in the next section.

5.2.5 Phantom Experiments

Phantom experiments were performed to:

1. verify the ability of the Hahn-prepared HASTE to discriminate signals with different values of $T_{2,\mathsf{diff}}$;

2. determine the value of the proportionality constant β in equation (2.50) for the Hahn-prepared HASTE, which will be indicated in the following as β_{HASTE}.

Knowledge of β_{HASTE} would allow to quantitatively relate the measured $T_{2,\mathsf{diff}}$ to the other parameters underlying transverse relaxation enhancement (R, η, $\Delta\chi$ and D), according to equation (2.50). The Hahn-echo experiment was used as reference for this calibration by assuming that the value of the constant β for the conventional Hahn-echo sequence is $\beta_{\mathsf{Hahn}} \simeq 3.8$, as found by Yung [152].
A phantom composed of six samples was prepared. Five of the samples were filled with a mixture of water and glass microspheres. Each of them was filled with microspheres of a different size. Their nominal diameters were on the same order of magnitude as the alveolar diameter: 50, 100, 400, 700 and 1000 μm. The remaining sample was filled with water only. All samples had the same $T_{2,0}$, corresponding to T_2 of water ($T_{2,\mathsf{water}}$), but different $T_{2,\mathsf{diff}}$ according to equation (2.50). This is due to the fact that each series of microspheres has a different radius R and, possibly, a different susceptibility difference

Hahn-echo	Hahn-prepared HASTE					
	Dataset 1 (TE = 82.2 ms)			Dataset 2 (TE = 154.2 ms)		
TE (ms)	Δ TE_1 (ms)	N_0	TE_{eff} (ms)	Δ TE_1 (ms)	N_0	TE_{eff} (ms)
6.0	3.0	17	7.85	–	–	–
8.0	7.8	15	9.67	–	–	–
10	12.6	13	13.4	–	–	–
13	17.4	11	17.8	–	–	–
16	22.2	9	22.4	–	–	–
19	27.0	7	27.1	–	–	–
22	31.8	5	31.9	–	–	–
26	36.6	3	36.7	–	–	–
30	–	–	–	41.4	31	41.5
35	–	–	–	46.2	29	46.3
40	–	–	–	51.0	27	51.0
45	–	–	–	55.8	25	55.8
50	–	–	–	60.6	23	60.6
55	–	–	–	65.4	21	65.4
60	–	–	–	70.2	19	70.2
65	–	–	–	75.0	17	75.0
70	–	–	–	79.8	15	79.8
75	–	–	–	84.6	13	84.6
80	–	–	–	89.4	11	89.4
85	–	–	–	94.2	9	94.2
90	–	–	–	99.0	7	99.0
95	–	–	–	103.8	5	103.8
100	–	–	–	108.6	3	108.6

Table 5.1: List of sequence parameters used for phantom experiments with both the conventional Hahn-echo and the Hahn-prepared HASTE sequences.

$\Delta\chi$ with respect to water. The diffusion coefficient D is expected to be the same for all samples, as restriction effects are negligible at the used TEs (of the order of tens of ms) with the mentioned sphere diameters. The volume fraction η occupied by the microspheres is independent from the sphere radius, according to the theory of randomly and densely packed spheres [228] for which $\eta \approx 0.6$.
Imaging experiments were performed using both the conventional Hahn-echo and the Hahn-prepared HASTE sequences. A four element receiver head array coil was used for signal detection. The following imaging parameters were used for all experiments: FOV = 500×500 mm^2, slice thickness = 15 mm, matrix size = 128×128 (zero-filled to 256×256), partial Fourier factor = 5/8 (which resulted in 80 phase-encoding lines and, consequently, $N_{y,\mathsf{center}} = 16$), receiver bandwidth = 1500 Hz/Px. A single slice that included all samples in the phantom was acquired in the sagittal orientation. A Hamming

filter was applied to all acquired images, in order to avoid Gibbs ringing.
For the conventional Hahn-echo experiment, 23 images were acquired at different TEs (between 6 and 100 ms). Exact values are reported in Table 5.1. For all experiments, the same repetition time TR = 2000 ms was used. This resulted in a total acquisition time of 160 s for each image.
For the experiments with the Hahn-prepared HASTE, 23 images were acquired with different values of $\mathrm{TE}_{\mathsf{eff}}$ and fixed TE. Because the range of allowed values for $\mathrm{TE}_{\mathsf{eff}}$ is limited, as already discussed, two datasets with different TEs were acquired in order to cover a broader range of values of $\mathrm{TE}_{\mathsf{eff}}$. One dataset with TE = 82.2 ms was used to cover the region of short $\mathrm{TE}_{\mathsf{eff}}$. This included 8 points with $\mathrm{TE}_{\mathsf{eff}}$ between 7 and 40 ms. A second dataset with TE = 154.2 ms was used to cover the region of larger $\mathrm{TE}_{\mathsf{eff}}$. This included 15 points with $\mathrm{TE}_{\mathsf{eff}}$ between 40 and 110 ms. The overall range of $\mathrm{TE}_{\mathsf{eff}}$ values was similar to that used for TE in the conventional Hahn-echo experiment. The values of $\Delta\mathrm{TE}_1$ and N_0 used for both datasets and the corresponding values of $\mathrm{TE}_{\mathsf{eff}}$ are reported in Table 5.1. The inter-pulse time used for the readout-block was $\Delta\mathrm{TE}_2 = 2.4$ ms for all experiments. Ten averages were acquired with TR = 5000 ms. This resulted in an acquisition time of 50 s for each image.

5.2.6 Data Analysis

For all experiments, a ROI was manually drawn around each sample of the phantom. The corresponding mean signal within the ROI was calculated. Data obtained from the conventional Hahn-echo experiment were plotted against TE and fitted using the following model:

$$S\left(\mathrm{TE}\right) = S_0 \ \exp\left(-\frac{\mathrm{TE}}{T_2}\right) + S_{\mathsf{offset}} \tag{5.9}$$

where the parameter S_0 represents the signal amplitude at TE = 0 ms while S_{offset} is a signal offset reflecting the background noise level [229, 230]. All parameters in the fit could assume positive values only. For each sample, the corresponding T_2 was obtained from the fit, as shown in Figure 5.2 a.
Data obtained from the experiments with the Hahn-prepared HASTE sequence were plotted against $\mathrm{TE}_{\mathsf{eff}}$ and fitted using the following model:

$$S\left(\mathrm{TE}_{\mathsf{eff}}\right) = S_0 \ \exp\left(-\frac{\mathrm{TE}_{\mathsf{eff}}}{T_{2,\mathsf{diff}}}\right) + S_{\mathsf{offset}} \tag{5.10}$$

For each sample, $T_{2,\mathsf{diff}}$ was obtained from the fit, as shown in Figure 5.2 b. The two datasets acquired with different TEs were separately evaluated, as they presented different $T_{2,0}$-weighting. The dataset obtained with TE = 82.2 ms was used to study the samples with shorter $T_{2,\mathsf{diff}}$ (sphere diameters 50 and 100 μm) while the dataset obtained with TE = 154.2 ms was used for the samples with longer $T_{2,\mathsf{diff}}$ (sphere diameters 400, 700 and 1000 μm).

Each of the five samples which contained a mixture of water and glass microspheres was used to calculate β_{HASTE} by using the following formula:

$$\beta_{\mathsf{HASTE}} = \frac{T_{2,\mathsf{diff}}^{-1}}{T_2^{-1} - T_{2,\mathsf{water}}^{-1}} \beta_{\mathsf{Hahn}} \tag{5.11}$$

where $\beta_{\mathsf{Hahn}} = 3.8$ [152]. This formula was obtained from equation (2.50) by assuming that R, η, $\Delta\chi$ and D are independent from the pulse sequence used (conventional Hahn-echo or Hahn-prepared HASTE). $T_{2,\mathsf{water}}$ was obtained from the conventional Hahn-echo experiment in the sample which contained pure water only. For this sample, in fact, it can be assumed that $T_{2,\mathsf{water}} = T_{2,0}$ because $\eta = 0$.
The final value for β_{HASTE} and its associated error were calculated as the mean value and the standard deviation of the results obtained in the five samples from equation (5.11).

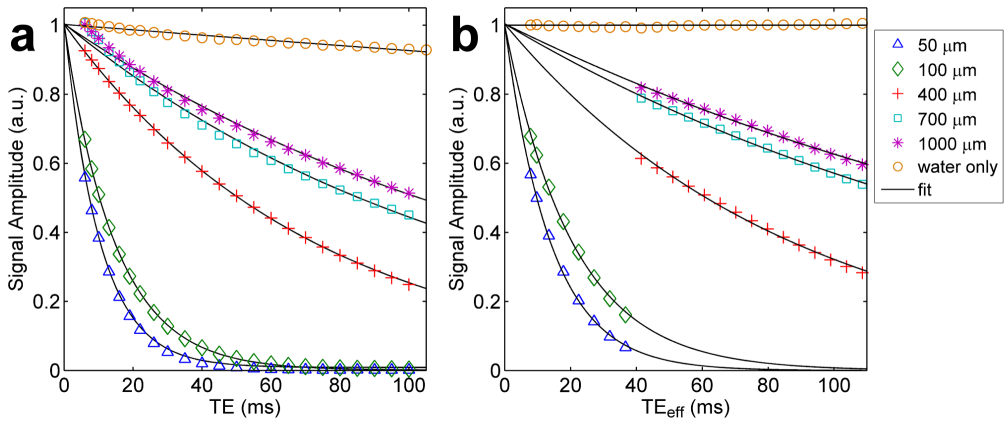

Figure 5.2: Signal attenuation curves obtained for each sample of the phantom with both the conventional Hahn-echo (a) and the Hahn-prepared HASTE (b) sequences. Both the experimentally acquired data and the curves obtained from the fit are shown. The values of the microsphere diameters which correspond to each curve are reported in the legend.

5.2.7 In-Vivo Experiments

Imaging experiments on the human lung were performed in-vivo by using the Hahn-prepared HASTE sequence. Eight healthy subjects (6 male and 2 female, age range $27 - 39$ years) without any known history of pulmonary disease were investigated.
All images were acquired with the volunteer in the supine position. A six element body array coil was used in combination with an eight channel spine matrix for signal detection. The following imaging parameters were used for all experiments: FOV $= 500 \times 500$ mm^2, slice thickness $= 15$ mm, matrix size $= 128 \times 128$ (zero-filled to 256×256), partial Fourier factor $= 5/8$ (which resulted in 80 phase-encoding lines and, consequently, $N_{y,\mathsf{center}} = 16$), receiver bandwidth $= 1500$ Hz/Px.

Two images were acquired in a single breath-hold of approximately 10 s duration: one image (S_1) was acquired with $N_0 = 13$ and $\Delta\text{TE}_1 = 3.0$ ms; the other image (S_2) was acquired with $N_0 = 3$ and $\Delta\text{TE}_1 = 27$ ms. For both images $\Delta\text{TE}_2 = 2.4$ ms and, consequently, TE = 72.6 ms. This resulted in effective echo times $\text{TE}_{\text{eff},1} = 7.54$ ms for S_1 and $\text{TE}_{\text{eff},2} = 27.1$ ms for S_2, according to equation (5.7). A separation time of 6 s was included between the two acquisitions, in order to allow for the full recovery of the longitudinal magnetization (assuming that $T_1 \approx 1000$ ms in the lung [201]). A Hamming filter was applied to all acquired images, in order to avoid Gibbs ringing.
Several experiments were performed, as further described below:

1. The dependence of $T_{2,\text{diff}}$ on the cardiac phase and on lung inflation was studied. The reason behind the investigation of the influence of the cardiac phase on $T_{2,\text{diff}}$ is that the diffusion coefficient which determines $T_{2,\text{diff}}$ does not only depend on the diffusivity of water molecules in the parenchymal tissue of the lung but also on blood microcirculation in the alveolar capillaries, through the pseudo-diffusion coefficient D^* [59] described in Chapters 2 and 4. D^* depends on the blood velocity and, consequently, on the cardiac phase.
   In one of the volunteers, coronal image acquisition was performed at both FRC and TLC in ten different cardiac phases. To this end, the cardiac period was divided in ten intervals of equal duration. The trigger delay between the ECG pulse and the start of image acquisition was manually adjusted. In the seven remaining volunteers, coronal image acquisition at FRC was performed in two cardiac phases only: systole and diastole. These provided the maximum variation of blood velocity. Additionally, in four of these volunteers, image acquisition at TLC was performed in the diastolic phase, which corresponds to minimum blood velocity.

2. In one of the volunteers, a reproducibility study was performed by repeating the acquisition of one coronal slice through the aorta for a total of ten measurements in separate breath-holds. For this study, all images were acquired at FRC in the diastolic phase.

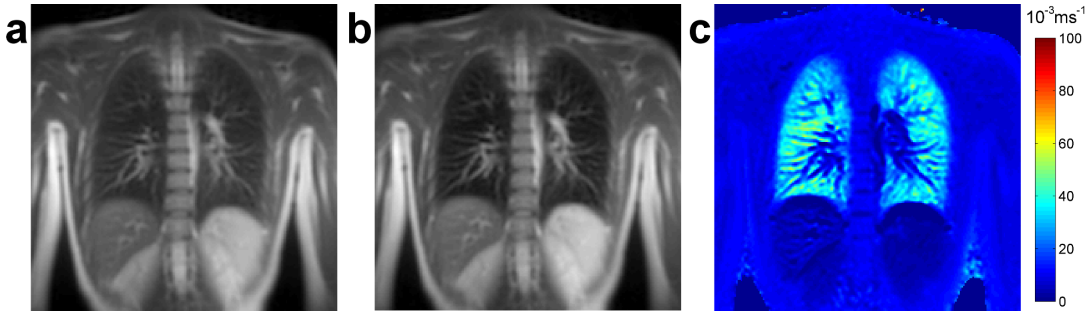

Figure 5.3: Example of the magnitude images S_1 (a) and S_2 (b) acquired in the human lung by using the Hahn-prepared HASTE sequence and corresponding map of $T_{2,\text{diff}}^{-1}$ (c).

3. In one of the volunteers, a sagittal slice of the right lung was acquired at both FRC and TLC in order to qualitatively assess the dependence of the transverse relaxation enhancement on gravitation in the A-P direction.

4. In three volunteers, the alveolar size was estimated at both FRC and TLC. Images of one coronal slice were acquired in the diastolic phase, in order to minimize the influence of possible perfusion heterogeneities. Perfusion, in fact, may be inhomogeneous throughout the lung and slightly different at FRC and TLC, as found by Hopkins et al. [210] and Henderson et al. [231]. In order to account for variations of η with inflation, a proton density weighted image (S_p) was additionally acquired in the same breath-hold as S_1 and S_2 by using a UTE sequence. For this acquisition, identical FOV, slice thickness, matrix size and receiver bandwidth were used as for S_1 and S_2, whereas TR = 2.5 ms and flip-angle = 2°. The total breath-hold duration was approximately 15 s.

5.2.8 Image Analysis

For all experiments, maps of the relaxivity $T_{2,\mathsf{diff}}^{-1}$ were calculated on a voxel-by-voxel basis from the two images S_1 and S_2 which were acquired with the Hahn-prepared HASTE sequence, as shown in Figure 5.3. To this end, the following formula was used (from equation (5.8)):

$$\frac{1}{T_{2,\mathsf{diff}}} = \frac{1}{\mathrm{TE}_{\mathsf{eff},2} - \mathrm{TE}_{\mathsf{eff},1}} \ln\left(\frac{S_1}{S_2}\right) \tag{5.12}$$

The results obtained in the lung parenchyma were systematically evaluated, as described below:

1. A ROI was drawn around the lung parenchyma. The procedure described in Chapter 4 was used to discard large vessels and other tissues with high proton density from the ROI and ensure that primarily data from the lung parenchyma are evaluated.

2. Histograms of the statistical distribution of $T_{2,\mathsf{diff}}^{-1}$ within the ROI were generated and the corresponding mean values (MV) and standard deviations (STD) were calculated.

For the analysis of the dependence of $T_{2,\mathsf{diff}}$ on lung inflation, the relative difference between the mean values obtained in the same coronal slice at FRC and TLC, defined as $(\mathrm{MV_{TLC}} - \mathrm{MV_{FRC}})/\mathrm{MV_{FRC}}$, was calculated. Values of the MV, STD and relative difference obtained in different volunteers were compared.
For the analysis of the influence of the cardiac phase, mean values obtained at FRC in systole and diastole were compared in all volunteers. The dataset acquired in ten different cardiac phases was used to generate a plot of the dependence of $T_{2,\mathsf{diff}}^{-1}$ on the time delay between the ECG peak and image acquisition, for both FRC and TLC.
For the repeatability study, the average mean value ($\mathrm{MV_{tot}}$) calculated over the performed ten measurements and its standard deviation (σ_{MV}) were calculated. The resulting CoV, defined as the ratio $\sigma_{\mathrm{MV}}/\mathrm{MV_{tot}}$, was quantified and used as a measure of reproducibility.

The gravitational dependence of $T_{2,\mathsf{diff}}$ was analyzed by averaging in the horizontal direction the sagittal maps which were obtained in one of the volunteers. To this end, it was assumed that each line of the image represents an isogravitational plane [49]. The result of this calculation was used to generate a plot of the profile of $T_{2,\mathsf{diff}}^{-1}$ in the A-P direction.
The air volume fraction η was estimated on a voxel-by-voxel basis from the images S_p acquired with the UTE sequence. For this calculation it was assumed that large vessels consist of 100% water, such that:

$$\eta \approx 1 - \frac{S_p}{S_{p,\mathsf{aorta}}} \tag{5.13}$$

where $S_{p,\mathsf{aorta}}$ is the mean signal within a ROI including the aorta only.

5.2.9 Estimation of the Alveolar Size

Maps of the alveolar diameter (d_{alveolus}) were calculated from a combination of the $T_{2,\mathsf{diff}}^{-1}$ and of the η maps on a voxel-by-voxel basis. The following formula was used for this calculation (from equation (2.50)):

$$d_{\mathsf{alveolus}} = 2\,\beta_{\mathsf{HASTE}} \frac{\eta}{T_{2,\mathsf{diff}}^{-1}} \sqrt{\gamma \frac{\Delta\chi}{3} B_0 D} \tag{5.14}$$

Other parameters in equation (5.14) were assumed to be homogeneous within the lung, with following values: $\Delta\chi \approx 9.1$ ppm [45, 121] and $D \approx 2.3 \cdot 10^{-3}$ mm^2/s (diffusion coefficient of water).
The mean values of the alveolar diameter obtained in the different volunteers at both FRC and TLC were calculated and compared.

Ex-vivo Experiments in Porcine Lungs

In order to get rid of the influence of perfusion on $T_{2,\mathsf{diff}}$, ex-vivo experiments were performed on four porcine lungs. In order to reproduce similar internal magnetic field gradients as in-vivo, the lungs were inflated by using the artiCHEST system (PROdesign Gesellschaft für Produktentwicklung mbH, Heiligkreuzsteinach, Germany) [232]. Imaging experiments were performed with the Hahn-prepared HASTE sequence by using the same imaging parameters as in-vivo. Maps of $T_{2,\mathsf{diff}}^{-1}$ as well as the corresponding MVs and STDs within the lung parenchyma were calculated as described above. In this case, η could not be estimated on a voxel-by-voxel basis, due to the absence of a reference tissue such as the blood in the aorta. The mean alveolar size was thus calculated from equation (5.14) by assuming that $\eta \approx 0.6$, as commonly observed at FRC [29].

	Conventional Hahn-echo		Hahn-prepared HASTE		
Diameter (μm)	T_2 (ms)	T_2^{-1} (10^{-3} ms^{-1})	$T_{2,\text{diff}}$ (ms)	$T_{2,\text{diff}}^{-1}$ (10^{-3} ms^{-1})	β_{HASTE}
50	10.3	97.4	14.0	71.4	2.8
100	14.7	67.9	20.7	48.3	2.7
400	72.6	13.8	87.4	14.4	3.3
700	122	8.22	176	5.67	2.9
1000	147	6.79	211	4.74	3.0
water only	1410	0.71	$> 10^5$	< 0.01	–
MV $\pm$ STD	–	–	–	–	2.9 ± 0.2

Table 5.2: Transverse relaxation times (T_2 and $T_{2,\text{diff}}$) and corresponding relaxivities (T_2^{-1} and $T_{2,\text{diff}}^{-1}$) obtained in phantom for different sphere diameters. The values obtained by using both the conventional Hahn-echo and the Hahn-prepared HASTE sequences are reported. The parameter β_{HASTE} was calculated for each sample using equation (5.11).

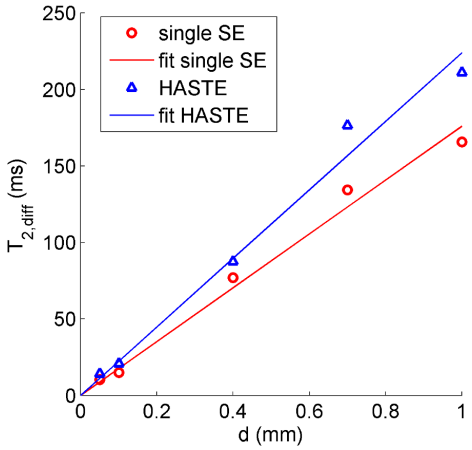

Figure 5.4: Dependence of $T_{2,\text{diff}}$ on the nominal sphere diameter for different samples of the phantom. The results obtained with both the conventional Hahn-echo (red) and the Hahn-prepared HASTE (blue) sequences are shown. For the conventional Hahn-echo, $T_{2,\text{diff}}$ was calculated as $1/(T_2^{-1} - T_{2,\text{water}}^{-1})$. A nearly linear relationship can be observed between $T_{2,\text{diff}}$ and the nominal sphere diameter. The increase rate is approximately 176 ms/mm for the conventional Hahn-echo and 224 ms/mm for the Hahn-prepared HASTE sequence.

5.3 Results

Phantom Experiments

The signal decay curves obtained for each sample of the phantom with both the conventional Hahn-echo and the Hahn-prepared HASTE sequences are shown in Figure 5.2. Both

the experimentally acquired data and the curves obtained from the fit are shown. Good agreement can be observed between the experimental data and the theoretical models for both sequences. A different transverse relaxation time was obtained in each sample, demonstrating a discrimination of signals with different $T_{2,\mathsf{diff}}$. The values of T_2 (for the conventional Hahn-echo) and $T_{2,\mathsf{diff}}$ (for the Hahn-prepared HASTE) which resulted from the fit are reported in Table 5.2, together with the corresponding relaxivities T_2^{-1} and $T_{2,\mathsf{diff}}^{-1}$. Shorter relaxation times were obtained in samples containing smaller microspheres. A monotonic increase of both T_2 and $T_{2,\mathsf{diff}}$ was observed with the sphere diameter, as shown in Figure 5.4. The relaxation times range from approximately 10 ms (for a microsphere diameter of 50 μm) to 200 ms (for a microsphere diameter of 1000 μm). In the sample containing pure water only, the conventional Hahn-echo experiment showed a signal decay with relaxation time $T_{2,\mathsf{water}} = T_{2,0} \approx 1400$ ms, while the Hahn-prepared HASTE sequence showed a negligible signal attenuation ($T_{2,\mathsf{diff}} > 10^5$ ms). This demonstrates a relatively good insensitivity of the proposed method to spin-spin relaxation.
For each sample, the values of β_{HASTE} calculated from equation (5.11) are reported in Table 5.2. For all samples, $\beta_{\mathsf{HASTE}} < \beta_{\mathsf{Hahn}}$, meaning that the transverse relaxation enhancement measured with the Hahn-prepared HASTE is systematically smaller than that obtained from the conventional Hahn-echo. Similar values of β_{HASTE}, between 2.7 and 3.3, were obtained for all samples. No correlation was observed with the sphere diameter. The calculation of the mean value and standard deviation of β_{HASTE} resulted in $\beta_{\mathsf{HASTE}} = 2.9 \pm 0.2$.

In-Vivo Experiments

A representative example of the magnitude images S_1 and S_2 which were acquired in one of the volunteers in the diastolic cardiac phase and coronal orientation is shown in Figures 5.3 a,b. A non-linear scaling was applied to both magnitude images in order to enhance the visualization of the lung parenchyma. Attenuation of the signal amplitude within the lung parenchyma can be observed in image S_2 compared to S_1. The resulting parametric map of the relaxivity $T_{2,\mathsf{diff}}^{-1}$ is shown in Figure 5.3 c. The lung parenchyma presents a stronger transverse relaxation enhancement compared to tissues with higher proton density, with a quite homogeneous spatial distribution within the coronal slice. Figures 5.5 a,d show the maps of $T_{2,\mathsf{diff}}^{-1}$ obtained in a different subject in the diastolic phase, at both FRC and TLC.
An example of the ROI obtained after segmentation of the lung parenchyma is shown in Figures 5.5 b,e. The resulting histogram of the statistical distribution of $T_{2,\mathsf{diff}}^{-1}$ within the lung parenchyma is shown in Figures 5.5 c,f, for both FRC and TLC. A distribution of values ranging from 0 to $80 \cdot 10^{-3}$ ms^{-1} can be observed. For each subject, the corresponding MVs and STDs are given in Table 5.3. In all subjects, MVs between 28 and $40 \cdot 10^{-3}$ ms^{-1} were found in diastole at FRC. The mean $T_{2,\mathsf{diff}}^{-1}$ calculated over all volunteers was $34.6 \cdot 10^{-3}$ ms^{-1}. This corresponds to a transverse relaxation time $T_{2,\mathsf{diff}} \approx 29$ ms. For all volunteers, it was observed that the transverse relaxation enhancement is larger at TLC than at FRC. The mean $T_{2,\mathsf{diff}}^{-1}$ calculated over all volunteers at TLC was $41.0 \cdot 10^{-3}$ ms^{-1}.

This corresponds to a transverse relaxation time $T_{2,\text{diff}} \approx 24$ ms. The relative difference of $T_{2,\text{diff}}^{-1}$ observed between FRC and TLC was strongly dependent on the volunteer, with values ranging from 11% to 28% and a mean relative increase of 18%.

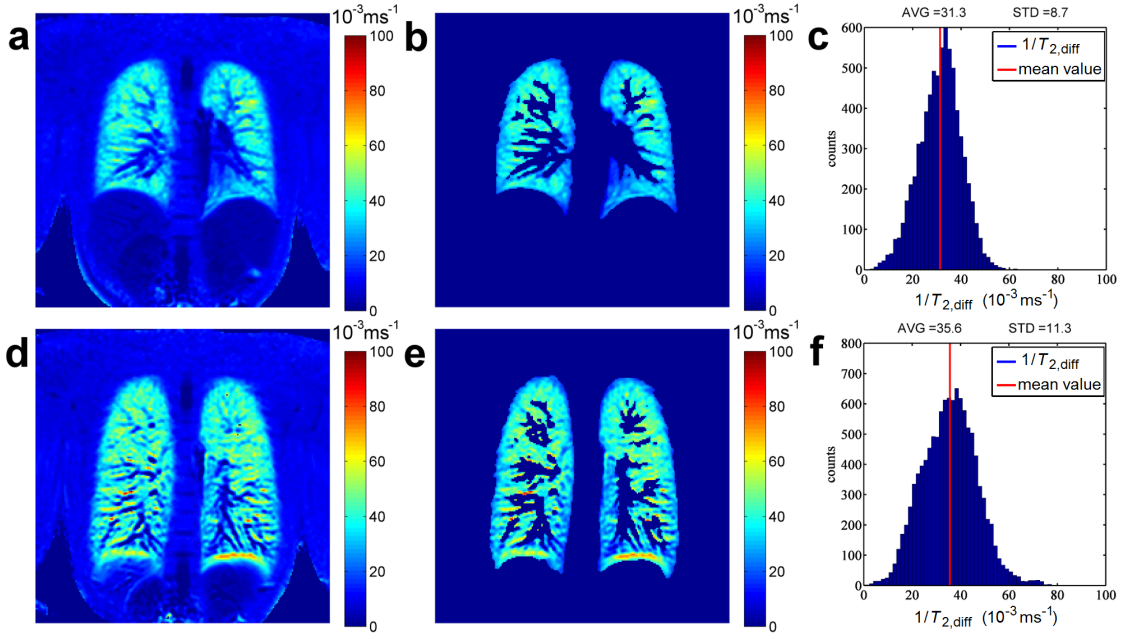

Figure 5.5: a,d: Coronal maps of $T_{2,\text{diff}}^{-1}$ of the human lung acquired in-vivo with the Hahn-prepared HASTE sequence. b,e: ROIs which include the region of the lung parenchyma, as obtained after image segmentation. c,f: Corresponding histograms of the statistical distribution of $T_{2,\text{diff}}^{-1}$ within the lung parenchyma. A comparison between the results obtained in the diastolic cardiac phase at both FRC (top) and TLC (bottom) is shown.

Subject	MV ± STD ($T_{2,\text{diff}}^{-1} 10^{-3}$ ms^{-1}) Expiration (FRC)	Inspiration (TLC)	($\text{MV}_{\text{TLC}} - \text{MV}_{\text{FRC}}$)/ MV_{FRC}
1	39.1 ± 11	43.4 ± 20	12%
2	34.9 ± 12	44.7 ± 17	28%
3	32.2 ± 8.4	35.6 ± 11	11%
4	32.3 ± 9.4	37.6 ± 17	16%
5	34.3 ± 9.2	43.8 ± 15	28%
Mean	34.6 ± 11	41.0 ± 16	18%

Table 5.3: Values of the transverse relaxation enhancement $T_{2,\text{diff}}^{-1}$ of the human lung obtained in different volunteers using the Hahn-prepared HASTE sequence: comparison between the results obtained at FRC and at TLC in the diastolic cardiac phase.

The plot of $T_{2,\text{diff}}^{-1}$ as a function of the delay time between the peak of the ECG signal and the image acquisition is shown in Figure 5.6, for both FRC and TLC. The cardiac cycle of the volunteer was approximately 800 ms. The transverse relaxation enhancement presents

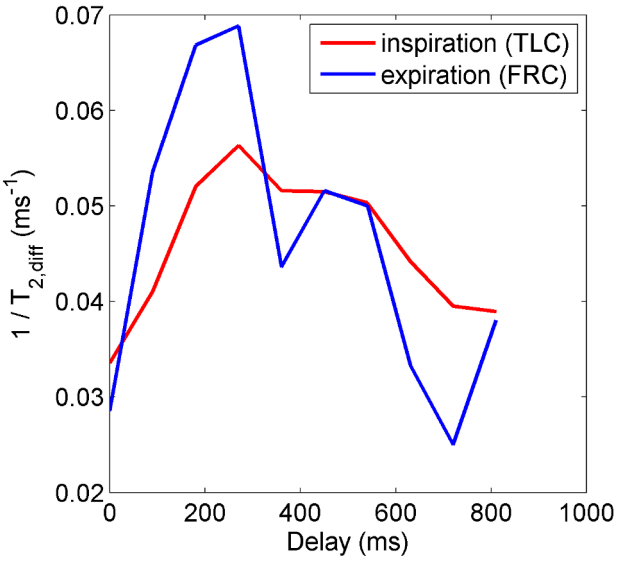

Figure 5.6: Variation of $T_{2,\text{diff}}^{-1}$ in the lung parenchyma with the time delay between the peak of the ECG signal and the image acquisition, at both FRC (blue line) and TLC (red line).

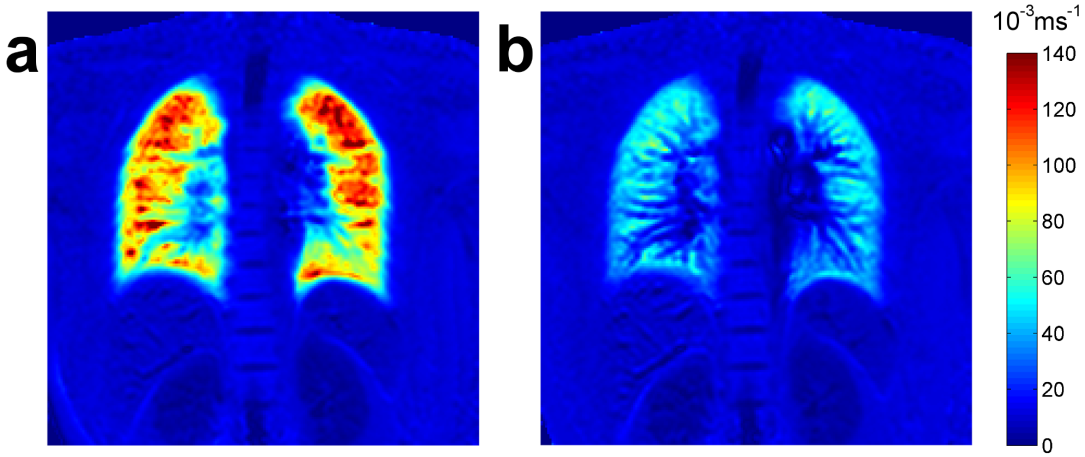

Figure 5.7: Coronal maps of $T_{2,\text{diff}}^{-1}$ of the human lung obtained in both the systolic (a) and the diastolic (b) cardiac phases at FRC.

a maximum in correspondence of systole and a minimum in diastole, for both FRC and TLC. The minimum value which was observed at FRC is smaller than the minimum value which was observed at TLC, in agreement with the results of the study on the dependence of $T_{2,\mathrm{diff}}^{-1}$ on lung inflation. The maximum value, instead, is larger at FRC than at TLC.
An example of the $T_{2,\mathrm{diff}}^{-1}$ maps which were acquired in one volunteer at FRC in both the systolic and the diastolic cardiac phases is shown in Figure 5.7. MVs and STDs obtained within the lung parenchyma for different volunteers are reported in Table 5.4. In all subjects, the transverse relaxation enhancement was larger in systole than in diastole. The mean $T_{2,\mathrm{diff}}^{-1}$ calculated over all volunteers in systole is $72.2 \cdot 10^{-3}$ ms^{-1}, indicating an increase of the transverse relaxation enhancement by approximately a factor 2 compared to diastole. The corresponding transverse relaxation time is reduced to $T_{2,\mathrm{diff}} \approx 14$ ms.

	MV $\pm$ STD ($T_{2,\mathrm{diff}}^{-1} 10^{-3}$ ms^{-1})	
Subject	Diastole	Systole
1	39.1 ± 11	79.7 ± 27
2	34.9 ± 12	67.7 ± 28
3	32.2 ± 8.4	77.6 ± 29
4	32.3 ± 9.4	60.0 ± 20
5	34.3 ± 9.2	81.9 ± 29
6	28.4 ± 9.9	65.7 ± 25
7	39.0 ± 14	83.2 ± 30
8	33.1 ± 12	61.5 ± 23
Mean	34.2 ± 11	72.2 ± 26

Table 5.4: Values of the transverse relaxation enhancement $T_{2,\mathrm{diff}}^{-1}$ of the human lung obtained in different volunteers by using the Hahn-prepared HASTE sequence: comparison between the results obtained in the systolic and in the diastolic cardiac phases at FRC.

The results of the repeatability study are reported in Table 5.5 and Figure 5.8. The standard deviation of the mean value σ_{MV} calculated over ten measurements was approximately $2.3 \cdot 10^{-3}$ ms^{-1}. The corresponding CoV is approximately 0.06.
The gravitational dependence of the transverse relaxation enhancement obtained in one of the volunteers from a sagittal slice is shown in Figure 5.9. The distribution of $T_{2,\mathrm{diff}}^{-1}$ in the A-P direction is rather homogeneous at FRC, while a gravitational dependence is observed at TLC with an increase of the transverse relaxation enhancement in the posterior region of the lung and a decrease in the anterior part. A similar effect can be observed in the coronal dataset of Figure 5.10, which includes six slices acquired in a different volunteer at several positions in the A-P direction.

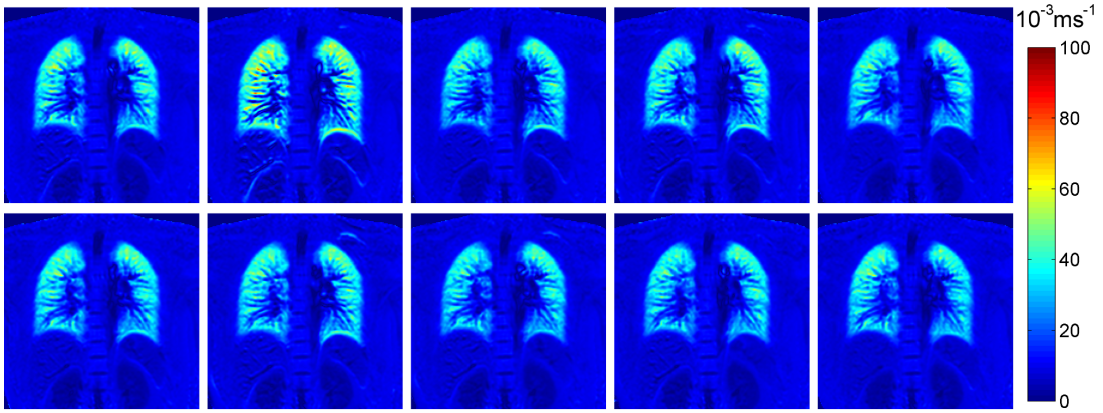

Figure 5.8: Set of ten coronal maps of $T_{2,\text{diff}}^{-1}$ of the human lung obtained in the same volunteer from ten repeated measurements. All images were acquired in the diastolic cardiac phase at FRC.

Measurement	MV ± STD ($T_{2,\text{diff}}^{-1}10^{-3}$ ms^{-1}) Expiration (FRC)
1	39.2 ± 11
2	44.0 ± 14
3	36.6 ± 10
4	39.2 ± 11
5	37.0 ± 10
6	37.9 ± 11
7	38.7 ± 11
8	36.1 ± 10
9	36.6 ± 10
10	36.5 ± 10
Mean	38.2 ± 11
σ_{MV}	2.3
CoV	0.06

Table 5.5: Mean values and standard deviations of $T_{2,\text{diff}}^{-1}$ obtained within the lung parenchyma in ten repeated measurements. The corresponding coefficient of variation (CoV $= \sigma_{\text{MV}}/\text{MV}$) is also reported.

A representative example of the results of the estimation of the air volume fraction η and of the alveolar size d_{alveolus} is shown in Figure 5.11. The magnitude images acquired with the UTE sequence at both FRC and TLC are shown in Figures 5.11a,d. The resulting η maps are shown in Figures 5.11 b,e. These maps present inhomogeneities with low spatial frequency towards the periphery of the image, as the UTE images from which they orig-

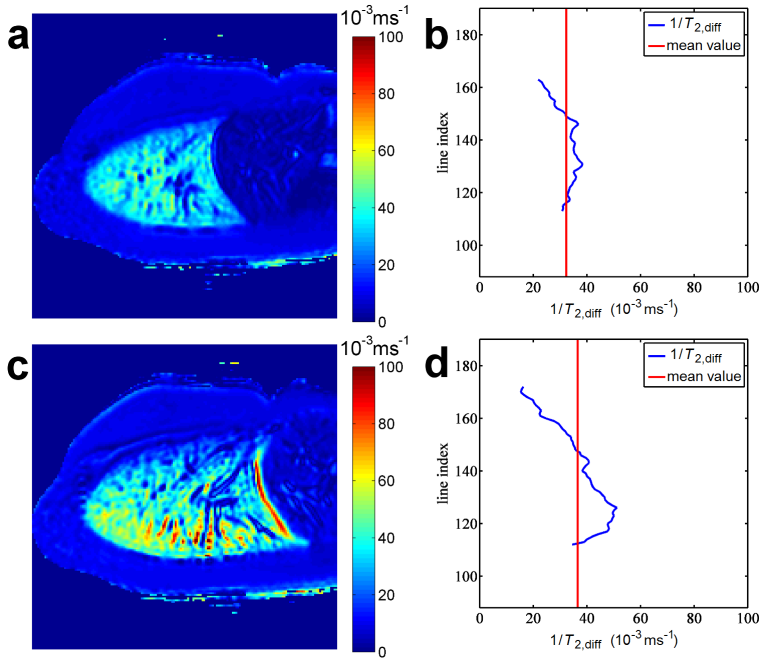

Figure 5.9: a,c: Sagittal maps of $T_{2,\text{diff}}^{-1}$ of the human lung acquired in-vivo with the Hahn-prepared HASTE sequence. b,d: Gravitational dependence of $T_{2,\text{diff}}^{-1}$ obtained by averaging the sagittal data sets in the horizontal direction after image segmentation. A comparison between the results obtained at both FRC (top) and TLC (bottom) is shown.

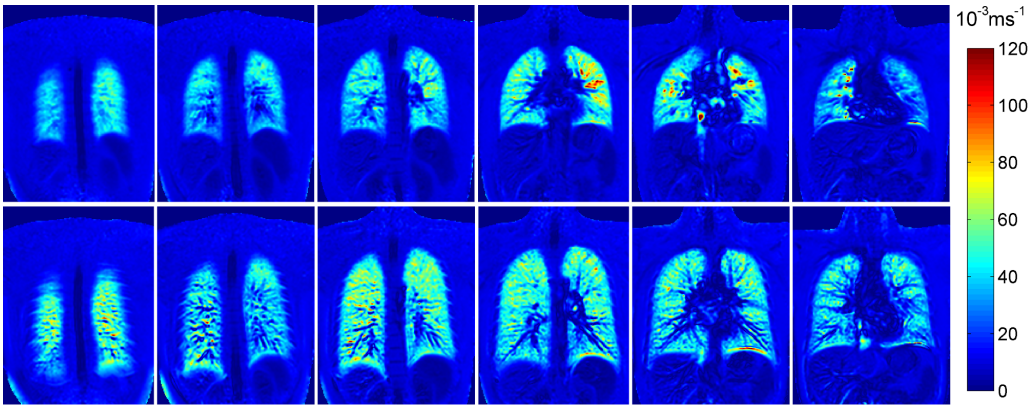

Figure 5.10: Coronal maps of $T_{2,\text{diff}}^{-1}$ of the human lung acquired in-vivo with the Hahn-prepared HASTE sequence: a set of six slices obtained at both FRC (top) and TLC (bottom) in different regions of the lung is shown.

inate are sensitive to inhomogeneities in the spatial sensitivity of both the transmit and the receive coils. Nevertheless, a sufficient homogeneity is obtained in the region of the lung to estimate η. As expected, the air volume fraction increases with lung inflation. The corresponding maps of the alveolar size which resulted from the combination of $T_{2,\mathrm{diff}}^{-1}$ and η are shown in Figures 5.11 c,f. Another example of alveolar size maps can be observed in the coronal dataset of Figure 5.12, which includes a set of six coronal slices acquired in a different volunteer.
Mean values and standard deviations obtained within the lung parenchyma for all parameters ($T_{2,\mathrm{diff}}^{-1}$, η and d_{alveolus}) are given in Table 5.6. For all subjects, similar values of η were obtained at both FRC and TLC, with a mean relative increase of approximately 18%, from 0.72 at FRC to 0.85 at TLC. The values of the alveolar size present variations among the different subjects, in a range between 172 and 237 μm. In all volunteers, these values do not change strongly with lung inflation: in one of the volunteers, a decrease of approximately 9% was observed between FRC and TLC, from 188 to 172 μm; in the other two volunteers, a substantial invariance to lung inflation was observed. The mean d_{alveolus} calculated over all volunteers is 209 μm at FRC and 202 μm at TLC.

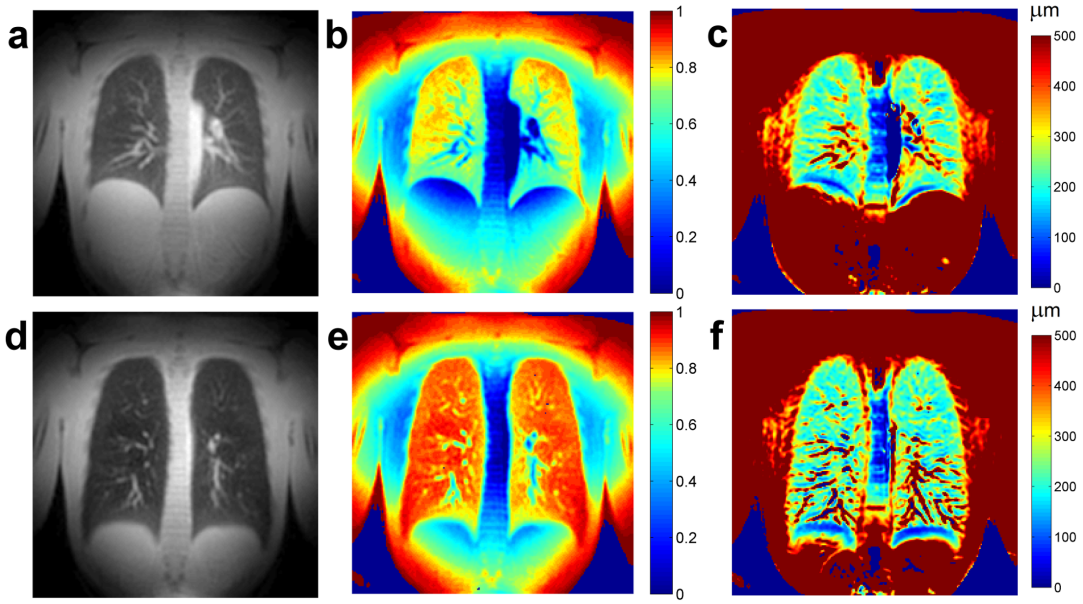

Figure 5.11: a,d: Example of proton density weighted images of the human lung acquired in coronal orientation by using a UTE sequence. b,e: Corresponding maps of the air volume fraction η calculated from equation (5.13). c,f: Maps of the alveolar diameter d_{alveolus} obtained from equation (5.14) by combining the maps of both $T_{2,\mathrm{diff}}^{-1}$ and η. A comparison between the results obtained at FRC (top) and TLC (bottom) is shown.

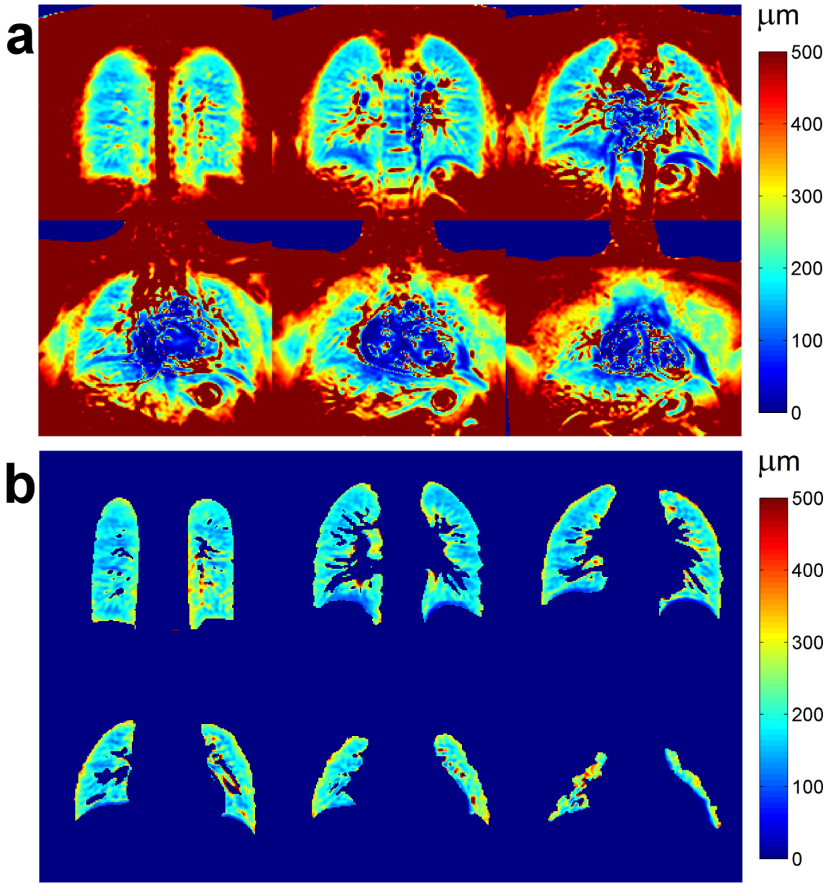

Figure 5.12: Coronal maps of the alveolar diameter d_{alveolus} of the human lung: a set of six coronal slices obtained in different regions of the lung is shown, before (a) and after (b) image segmentation.

	Expiration (FRC)			Inspiration (TLC)		
Subject	$T_{2,\text{diff}}^{-1}$ (10^{-3} ms^{-1})	η	d_{alveolus} (μm)	$T_{2,\text{diff}}^{-1}$ (10^{-3} ms^{-1})	η	d_{alveolus} (μm)
1	38.1 ± 10	0.70 ± 0.07	188 ± 82	51.8 ± 19	0.87 ± 0.10	172 ± 110
2	31.3 ± 8.7	0.72 ± 0.08	237 ± 99	35.6 ± 11	0.82 ± 0.09	237 ± 100
3	37.0 ± 11	0.73 ± 0.08	203 ± 94	43.7 ± 15	0.85 ± 0.11	198 ± 88
Mean	35.5 ± 9.9	0.72 ± 0.08	209 ± 92	43.7 ± 15	0.85 ± 0.10	202 ± 99

Table 5.6: Mean values and standard deviations of the transverse relaxation enhancement $T_{2,\text{diff}}^{-1}$, air volume fraction η and alveolar diameter d_{alveolus} obtained in the lung parenchyma of different subjects at both FRC and TLC.

Ex-vivo Experiments in Porcine Lungs

Figure 5.13 shows an example of image S_1 obtained in the porcine lungs ex-vivo, together with the corresponding map of $T_{2,\text{diff}}^{-1}$ and with the histogram of its statistical distribution in the lung parenchyma. The mean values of $T_{2,\text{diff}}^{-1}$ in the lung parenchyma and the corresponding values of the alveolar size obtained for all examined lungs are reported in Table 5.7. The mean $T_{2,\text{diff}}^{-1}$ calculated over all examined lungs is $26.2 \cdot 10^{-3}$ ms^{-1}. This corresponds to a transverse relaxation time $T_{2,\text{diff}} \approx 38.2$ ms. In the assumption of $\eta = 0.6$, the corresponding mean alveolar diameter is $d_{\text{alveolus}} \approx 223$ μm.

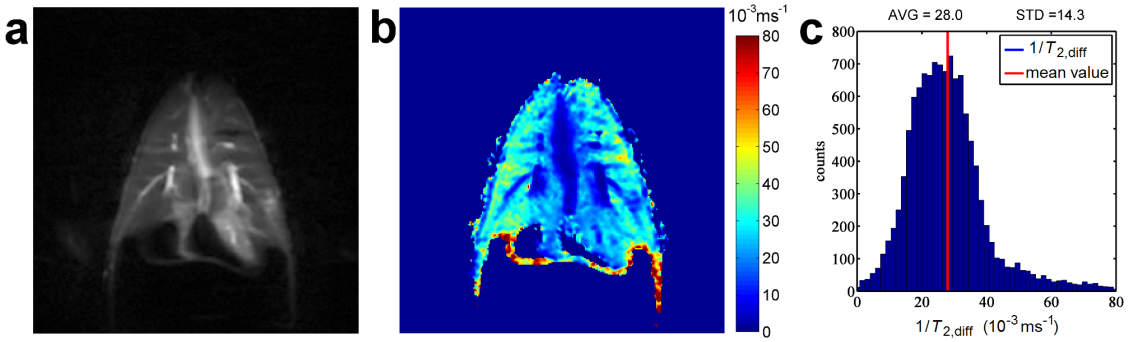

Figure 5.13: a: Example of magnitude image S_1 acquired in a porcine lung ex-vivo by using the Hahn-prepared HASTE sequence. b: Corresponding map of the transverse relaxation enhancement $T_{2,\text{diff}}^{-1}$. c: Histogram of the statistical distribution of $T_{2,\text{diff}}^{-1}$ within the lung parenchyma.

Subject	$T_{2,\text{diff}}^{-1}$ (10^{-3} ms^{-1})	d_{alveolus} (μm)
1	28.0 ± 14	208
2	25.6 ± 13	227
3	24.0 ± 13	243
4	27.2 ± 12	214
Mean	26.2 ± 13	223

Table 5.7: Mean values and standard deviations of the transverse relaxation enhancement $T_{2,\text{diff}}^{-1}$ obtained in the lung parenchyma of inflated porcine lungs ex-vivo. The corresponding value of the alveolar diameter d_{alveolus} was obtained from equation (5.14) by assuming that $\eta = 0.6$.

5.4 Discussion

In this chapter, a method to quantify the transverse relaxation time $T_{2,\text{diff}}$, which is due to diffusion through the internal magnetic field gradients of the lung, was presented. The proposed technique is based on a HASTE sequence with Hahn-echo preparation. Compared to the conventional Hahn-echo sequence, this technique presents two major advantages with regard to lung imaging: 1) direct quantification of $T_{2,\text{diff}}$ is possible without the need for a-priori knowledge of $T_{2,0}$; 2) acquisition of several images within a single breath-hold is possible, thanks to the reduced acquisition times. The Hahn-prepared HASTE sequence was used to conduct studies on the dependence of $T_{2,\text{diff}}$ on lung perfusion and inflation. Furthermore, the feasibility of exploiting the knowledge of $T_{2,\text{diff}}$ for the quantification of the alveolar size was demonstrated.
Phantom experiments showed that the Hahn-prepared HASTE sequence is capable of discriminating signals with different $T_{2,\text{diff}}$, similarly to the conventional Hahn-echo. The experiments also demonstrated that the proposed technique, in contrast to the conventional Hahn-echo, is insensitive to $T_{2,0}$ and, thus, it allows for direct quantification of $T_{2,\text{diff}}$. However, the values of $T_{2,\text{diff}}$ obtained with the Hahn-prepared HASTE are systematically larger compared to those obtained with the conventional Hahn-echo sequence, as shown in Figure 5.4. A possible reason for this effect is the presence of stimulated-echoes in the signal generated by the Hahn-prepared HASTE if the flip angle of the refocusing pulses deviates from the ideal 180°. Stimulated-echoes, in fact, present a different sensitivity to diffusion with respect to spin-echoes [227]. At a given echo time, spin-echoes experience a diffusion-induced attenuation which is dictated by a decay constant proportional to TE^3, as indicated in equation (2.48). For stimulated-echoes, instead, this decay constant is proportional to TE [227]. Another important aspect to consider is the possible T_1-weighting introduced by stimulated-echoes. The signal contribution due to stimulated-echoes, in fact, is modulated along the echo-train by T_1 decay [160, 226]. Stronger T_1-weighting is obtained in later echoes of the echo-train. This means that images acquired with different values of N_0 in the preparation-block might present a different T_1-weighting. In principle, this could affect the quantification of $T_{2,\text{diff}}$. However, because the T_1 of both water (of the order of a few seconds) and lung tissue (of the order of 1000 ms [201]) is much longer than the echo times used in this work (approximately 150 ms for phantom experiments and 73 ms for in-vivo experiments), this effect can be neglected.
The transverse relaxation enhancement of a system of densely packed spheres, such as the model which is commonly used to represent the lung tissue [67], depends on a combination of several parameters, as stated by equation (2.50). These are: 1) the diffusion coefficient D, 2) the sphere radius R, 3) the susceptibility difference $\Delta\chi$ between the spheres and the surrounding environment and 4) the volume fraction occupied by the spheres η. Phantom experiments confirmed, as already found by Weisskoff et al. [157], that in the slow diffusion regime $T_{2,\text{diff}}$ increases with the sphere radius. This demonstrates that $T_{2,\text{diff}}$ is a good indicator for microstructural changes. In-vivo, two additional factors which can influence the transverse relaxation enhancement of the lung were identified. These are: perfusion and lung inflation. The results of in-vivo experiments showed that $T_{2,\text{diff}}$ of the

lung decreases by approximately a factor 2 in systole compared to diastole, from 29 ms to 14 ms at FRC. This can be attributed to the increase of blood velocity in systole, which in turn results in a larger pseudo-diffusion coefficient of blood D^* according to the theory of Le Bihan et al. [59], as described in Chapter 2. The transverse relaxation enhancement due to diffusion through the internal gradients, in fact, is directly proportional to the square root of the diffusion coefficient, as indicated by equation (2.50). The studies on the influence of lung inflation on $T_{2,\mathsf{diff}}$ were performed in the diastolic phase. This, in fact, corresponds to slower blood velocity and allows to minimize the influence of both perfusion heterogeneities throughout the lung and perfusion differences at different breathing states. Under this condition, the results showed a decrease of $T_{2,\mathsf{diff}}$ with lung inflation to approximately 24 ms at TLC.

The proposed technique relies on the acquisition of two points only, with different values of $\mathrm{TE}_{\mathsf{eff}}$, for the quantification of $T_{2,\mathsf{diff}}$. This allows to keep the acquisition time as short as possible. However, it also reduces the sensitivity of the technique to a limited range of values of $T_{2,\mathsf{diff}}$. For this reason, it is important to prospectively choose appropriate values of $\mathrm{TE}_{\mathsf{eff}}$ for the image acquisition. In this work, $\mathrm{TE}_{\mathsf{eff},1} \simeq 7.5$ ms and $\mathrm{TE}_{\mathsf{eff},2} \simeq 27$ ms were used for all in-vivo experiments, at a field strength of 1.5 T. These values were empirically found and specifically chosen to obtain an optimal sensitivity to the typical range of values of $T_{2,\mathsf{diff}}$ observed at FRC and TLC in diastole. Under different experimental conditions, the use of different values of $\mathrm{TE}_{\mathsf{eff}}$ might be beneficial. For example, the optimal values for $\mathrm{TE}_{\mathsf{eff}}$ would decrease with larger magnetic field strengths as $T_{2,\mathsf{diff}}$ is inversely proportional to the square root of the magnetic field, as stated by equation (2.50). In this regard, the use of stronger static magnetic fields might be beneficial for the presented technique in terms of SNR, but at the cost of increased blurring due to the T_2 shortening effect at stronger magnetic fields.

One of the limitations of the proposed technique is that TE is always larger than $\mathrm{TE}_{\mathsf{eff}}$, as demonstrated by equation (5.7). This means that for tissues with $T_{2,0} < T_{2,\mathsf{diff}}$ strong signal losses would be induced by spin-spin interactions at the optimal $\mathrm{TE}_{\mathsf{eff}}$. However, this is not the case for the lung tissue as the results of this work indicate that diffusion through the internal gradients contributes to the transverse signal decay with a relaxation time $T_{2,\mathsf{diff}}$ of approximately 30 ms in diastole and 15 ms in systole (see Table 5.4). These values are relatively short compared to $T_{2,0}$ of the lung (of the order of 80 ms, as found by Shioya et al. [70, 112]).

One of the drawbacks of the presented technique, which is common also to the other acquisition techniques proposed in this thesis, is that any kind of motion which occurs within the lung space during image acquisition, such as instable breath-holding, can lead to image misregistration and corrupt the quantification. This problem was observed in a very limited number of acquisitions in volunteer experiments. Nevertheless, it could play a major role in clinical applications on critical patients, who may not be able to hold the breath for more than a few seconds. In this case, the use of navigators to control respiratory motion during free breathing and trigger the acquisition at the desired respiratory phase might be beneficial. In this regard, one possibility is offered by the Prospective Acquisition CorrEction (PACE) technique proposed by Thesen et al. [116].

The possibility of applying the Hahn-prepared HASTE sequence to the quantification of the alveolar size was investigated by combining the maps of $T_{2,\mathsf{diff}}^{-1}$ with the maps of the air volume fraction η, in order to correct for variations of $T_{2,\mathsf{diff}}$ with inflation. The η maps were estimated from a proton density weighted image acquired in the same breath-hold as the $T_{2,\mathsf{diff}}^{-1}$ map by using a UTE sequence. For the same reasons described above, the $T_{2,\mathsf{diff}}^{-1}$ maps used for the estimation of the alveolar size were acquired in the diastolic cardiac phase. Assumptions were made on the other parameters in equation (5.14) for the estimation of the alveolar size d_{alveolus}. The susceptibility difference $\Delta\chi$ was assumed to be approximately 9 ppm, as proposed by Pracht et al. [45]. Possible heterogeneities of this parameter throughout the lung are expected to have a minor impact on the quantification of the alveolar size, due to the square-root dependence of d_{alveolus} on $\Delta\chi$ in equation (5.14). The diffusion coefficient was assumed to be equal to the diffusion coefficient of water, as for most biological tissues D is of the same order of magnitude as the diffusion coefficient of water. Heterogeneities and deviations of the diffusion coefficient of the lung parenchyma from the assumed value should have a minor impact on the quantification of the alveolar size, due to the square-root dependence in equation (5.14). In this regard, however, the main issue is represented by perfusion, which affects the pseudo-diffusion coefficient of blood D^* as already discussed. D^*, in fact, strongly depends on the cardiac phase and might achieve values which are about 10 times larger than the diffusion coefficient of water, as previously shown by Le Bihan et al. [59]. The strong dependence of D^* and, consequently, $T_{2,\mathsf{diff}}$ on perfusion represents the main obstacle to the estimation of the alveolar size from $T_{2,\mathsf{diff}}$. Ideally, an effective diffusion coefficient should be calculated on a voxel-by-voxel basis, depending on the cardiac phase, as the weighted sum of the diffusion coefficients of the different lung compartments (lung parenchyma and flowing blood) and used for the estimation of the alveolar size. In this work, instead, the alveolar size was estimated in the assumption that the value of D^* in diastole is much smaller than in systole and, thus, it is close to the diffusion coefficient of water. This hypothesis is supported by the fact that the transverse relaxation enhancement decreases by approximately a factor 2 in diastole compared to systole, which indicates a decrease of at least a factor 4 in the pseudo-diffusion coefficient of blood, due to the square root dependence on D in equation (2.50). Moreover, ex-vivo experiments showed that the values of $T_{2,\mathsf{diff}}^{-1}$ in the inflated porcine lungs are of the same order of magnitude as those obtained in the human lung in the diastolic cardiac phase. This indicates that the assumption made on D is nearly correct. However, because the values of $T_{2,\mathsf{diff}}^{-1}$ are systematically smaller ex-vivo, it can be supposed that D was slightly underestimated in-vivo. This can be mainly attributed to the fact that even in diastole perfusion contributes to increase the effective diffusion coefficient.

One of the aims of this study was to explore the feasibility of estimating the alveolar size of the human lung in-vivo with proton MRI by exploiting the knowledge of $T_{2,\mathsf{diff}}$. In this regard, the results obtained for the alveolar diameter, between 170 and 240 μm, are in good agreement with the values obtained in the human lung in-vivo by Hajari et al. [135] (between 157 and 179 μm at FRC) and by Parra-Robles et al. [136] (between 135 and 190 μm at FRC). The mentioned studies were conducted by using hyperpolarized ^{3}He diffusion MRI. Similar values were obtained ex-vivo by Ochs et al. [137] by using light

microscopy. In this case, the average alveolar volume was estimated in $4.2 \cdot 10^6$ μm^3, which corresponds to an alveolar diameter of approximately 200 μm in the assumption of a spherical shape. The data acquired at FRC and TLC indicate a substantial independence of the alveolar size on lung inflation. This is supported by the theory of alveolar recruitment [215, 218, 219, 233, 234]. In this regard, however, open discussions are still ongoing in the scientific community [216, 217, 218, 219, 220, 221], as the mechanisms of alveolar dynamics during respiration have not been fully understood yet, due to the lack of a gold standard method for the quantification of the alveolar size in-vivo. For example, opposite results were obtained by different investigators by using hyperpolarized ^{3}He diffusion MRI: an increase of the alveolar size with lung inflation was observed by Parra-Robles et al. [136], whereas a decrease was observed by Hajari et al. [135].
Phantom and in-vivo experiments, together, seem to indicate that $T_{2,\mathsf{diff}}$ of the lung depends on a combination of functional (perfusion through D^* and inflation through η), microstructural (alveolar size d_{alveolus}) and tissue-specific properties of the lung ($\Delta\chi$ and D). The lung function and microstructure can be altered by several lung pathologies such as tumors, pulmonary fibrosis or emphysema. This makes $T_{2,\mathsf{diff}}$ an interesting parameter, which could be used to identify possible alterations and mismatches between the mentioned properties of the lung: perfusion, alveolar size and inflation. Moreover, the variation of $T_{2,\mathsf{diff}}$ observed between systole and diastole could be used as an indicator of the blood velocity in the alveolar capillaries and it could be used to detect perfusion defects. The quantification of the alveolar size, instead, could be useful for the investigation of lung injuries induced by pulmonary diseases such as emphysema, COPD and ALI, or by mechanical ventilation [55, 218, 221, 222]. This is known as Ventilator Induced Lung Injury (VILI). As already discussed, the main obstacle to the estimation of the alveolar size is represented by the strong dependence of $T_{2,\mathsf{diff}}$ on lung perfusion. In this work, it was assumed that perfusion is homogeneous within the lung and that D^* of blood in diastole is close to the diffusion coefficient of water. This assumption is realistic, as demonstrated by the results, for healthy volunteers with a regular and relatively slow cardiac rate (> 800 ms), such as those used for this study. In this case, perfusion heterogeneities have a negligible impact on the results and a relatively good reproducibility can be obtained (the repeatability experiment resulted in CoV $\simeq 0.06$). Nevertheless, the scenario could be different in patients with perfusion defects and/or fast or irregular cardiac rate (arrhythmia). In this case, additional corrections might be required for the estimation of the alveolar size, in order to take into account the influence of perfusion on $T_{2,\mathsf{diff}}$.
In conclusion, the presented technique represents a robust method to quantify $T_{2,\mathsf{diff}}$ of the lung parenchyma in-vivo. Data acquisition can be accomplished in a single breath-hold of approximately 10 s duration. This might be compatible with clinical studies on patients with lung diseases as well as with the clinical routine. The technique can be potentially used to quantify the alveolar size. For this, additional information about the air volume fraction η is required, which could be obtained from the separate acquisition of a proton density weighted image. In patients with lung diseases, further information about perfusion may be necessary for a correct estimation of the alveolar size. In this regard, however, a deeper clinical investigation is necessary.

Chapter 6

Quantification of the Spectral Line Broadening

The work presented in this chapter has been published on a peer-reviewed journal and presented at international conferences, as indicated by references [A2,A6,A10] in the list of publications.

6.1 Introduction

As already discussed in Chapter 2, the microscopic magnetic field inhomogeneities that occur at the alveolar air/tissue interfaces result in a broad NMR spectral line [63, 66, 126] and thus, in a short FID signal [28, 71, 111, 138]. It has been previously shown by means of both numerical calculations [67, 118, 120] and experiments [45, 63, 109, 114, 120, 124] that the broadening of the NMR spectral line in the lung increases with the following parameters, in agreement with equation (2.20):

1. the fractional volume of gas in the lung η [63, 67, 118, 120, 124];
2. the susceptibility difference between lung tissue and gas in the alveoli $\Delta\chi$; [45, 109]
3. the strength of the static magnetic field B_0 [114].

Considering the assumption of a uniform magnetic susceptibility of the lung tissue, the spectral line broadening can be regarded as a quantitative fingerprint for lung inflation, as proposed by Case et al. [67] and Christman et al. [120]. This makes the knowledge of the spectral line broadening of the lung of interest, first for the further characterization of lung tissue and, second, for the diagnosis of pulmonary diseases which might alter the local air content in the lung, such as: pulmonary edema, pulmonary fibrosis or emphysema [118, 138, 140, 235, 236]. In this regard, the quantification of the spectral line broadening itself, at a given breathing state, might help to detect local morphological changes, such as the loss or the compression of lung tissue due to emphysema as well as the accumulation of interstitial fluids or connective tissue. Furthermore, by comparing the line broadening

of the lung at different breathing states it would be possible to detect abnormal lung expansion and thus, to diagnose pulmonary functional disorders such as air trapping and ventilation defects, which might be induced by a variety of lung diseases [2, 10, 183, 237]. Another interesting application of the line broadening quantification is the assessment of local ventilation by means of oxygen-enhanced imaging [43]. It has been previously shown, in fact, that $\Delta\chi$ is directly proportional to the concentration of O_2 in the alveoli [45, 109]. This would result in a broader NMR spectral line when increasing the concentration of O_2 in the inhaled gas. Because dissolved O_2 has a negligible influence on the magnetic susceptibility of the lung tissue, the dependence of the spectral line broadening on the oxygen concentration can be regarded as a measure for local ventilation [45, 109].
The use of the Asymmetric Spin-Echo (ASE) sequence has been proposed in the past for the quantification of the spectral line broadening of the lung [71]. On the one hand, in-vivo applications of this technique would require relatively long acquisition times that are not suitable for investigations on patients with lung diseases. On the other hand, the violation of the CPMG conditions [68, 69], which is induced by static signal dephasing in the presence of magnetic field inhomogeneities, hampers the use of TSE-based sequences [22].
In this chapter, the feasibility of quantifying the spectral line broadening of the human lung in-vivo within a single breath-hold is demonstrated. To this end, the use of a fast and robust technique based on a HASTE sequence with ASE preparation is proposed. It is shown here that the violation of the CPMG conditions can be overcome by means of RF-phase cycling [166] in combination with GRAPPA reconstruction [26]. The possibility of exploiting the quantification of the spectral line broadening to obtain information about lung inflation and oxygen uptake is also investigated by means of in-vivo experiments on healthy volunteers.

6.2 Materials and Methods

6.2.1 The Asymmetric Spin Echo

Studies on the spectral line broadening of the lung have been previously performed ex-vivo using the ASE sequence [63, 71, 125]. This technique is a modification of the conventional SE sequence, in which the refocusing pulse between excitation and signal readout can be shifted in time relatively to the center of the spin-echo [128]. A diagram of the sequence showing both the standard and the asymmetric SE is given in Figure 6.1.
The key parameter of the sequence is the asymmetry time (τ), which corresponds to twice the time shift of the refocusing pulse. For $\tau \neq 0$, the time distances between excitation pulse, refocusing pulse and signal readout are asymmetric. This allows to the static signal dephasing which is due to magnetic field inhomogeneities to contribute to the signal decay [128]. The conventional SE sequence is a particular case of the ASE obtained for $\tau = 0$, in which the symmetry in the sequence timing provides full signal refocusing.

The echo time of the sequence is given by the total time distance between excitation and signal read-out, like in the conventional SE. One of the peculiarities of the ASE sequence is the possibility to acquire signals with different values of τ and identical TE. Thereby, the signal decay is independent from the transverse relaxation time T_2 and is only dictated by the static signal dephasing.

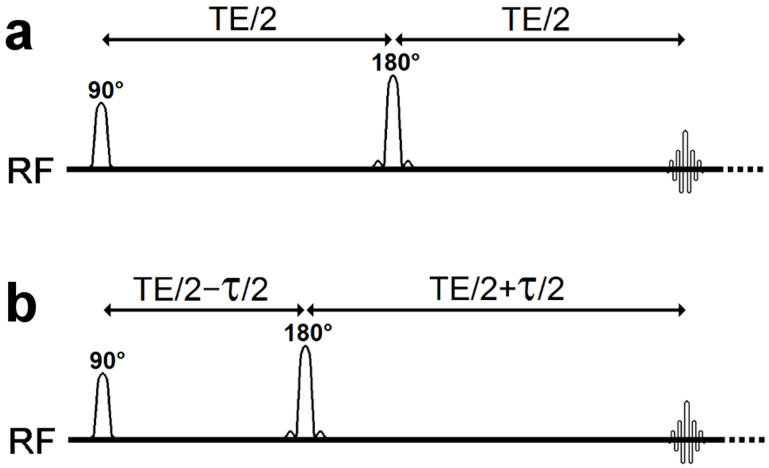

Figure 6.1: Diagrams of the ASE sequence in both the symmetric (a) and asymmetric (b) configurations. Reproduced with permission from reference [A2].

6.2.2 Signal Decay Model

The model for the signal amplitude decay in the ASE sequence is given by [125]:

$$S(\tau, \mathrm{TE}) \propto \exp\left(-\frac{\mathrm{TE}}{T_2}\right) \int P(\omega, \mathrm{TE}) \cos(\omega\tau)\, d\omega \tag{6.1}$$

where $P(\omega, \mathrm{TE})$ is the line shape at time TE.
In general, the line shape depends on the specific microstructural geometry of the considered system [117, 119] and so does the signal amplitude decay, according to equation (6.1). Nevertheless, it has been previously demonstrated by Stables et al. [128] that, at a fixed TE, the signal amplitude decay in a region of τ close to zero is given by:

$$S(\tau) \propto \exp\left(-\frac{\langle\omega^2\rangle\tau^2}{2}\right) \tag{6.2}$$

for a variety of microstructural geometries. This means that the spectral line broadening can be quantified by fitting the signal amplitude data acquired at different values of the asymmetry time τ, with fixed TE, by using the model of equation (6.2).

Ganesan et al. [125] showed that, at $B_0 = 0.94$ T, the signal decay of the lung tissue is well approximated by the Gaussian model of equation (6.2) for $0 < \tau < 4$ ms. Because the spectral line broadening increases linearly with the magnetic field strength [114, 127], in this work it will be assumed that at $B_0 = 1.5$ T the Gaussian model holds at least in the time region $0 < \tau < 2.5$ ms.

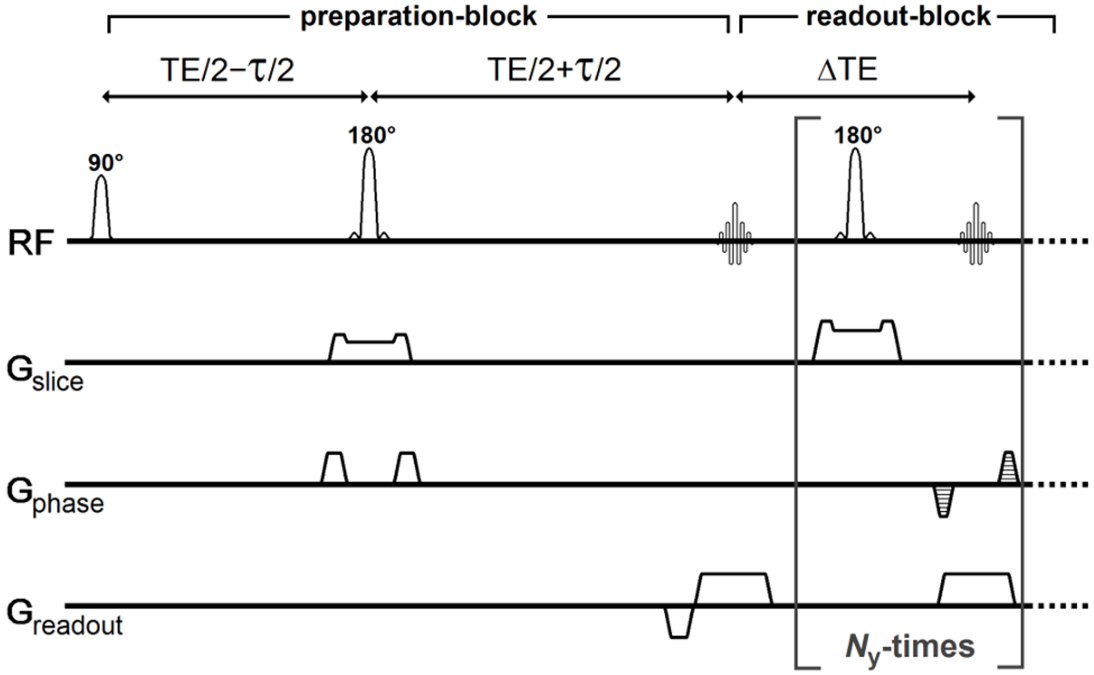

Figure 6.2: Timing diagram of the ASE-prepared HASTE sequence which was used to quantify the spectral line broadening of the lung. The transverse magnetization is prepared like in a standard ASE sequence ("preparation-block"). The following train of 180° refocusing pulses ("readout-block") allows to acquire the full k-space in a single shot (HASTE). Echo-time (TE), asymmetry time (τ) and inter-echo time (ΔTE) are defined as shown. Signal refocusing and readout are repeated N_y-times (with N_y = number of phase-encoding steps). Linear reordering of the phase-encoding steps was used. Reproduced with permission from reference [A2].

6.2.3 Pulse Sequence

The conventional ASE experiment presents a main drawback with regard to the in-vivo quantification of the spectral line broadening in the lung: for each image, relatively long acquisition times, of the order of a few minutes, are required [235]. For this reason, the

technique is prone to motion artifacts and is not suitable for clinical applications. Alternatively, TSE-based sequences could be used, as soon as the limitations imposed by the CPMG conditions could be overcome. Here, the use of a fast technique based on an ASE-prepared HASTE sequence is proposed for the quantification of the spectral line broadening of the human lung in-vivo. This sequence is particularly interesting because it allows for image acquisition in a single shot, which is especially beneficial for this application, due to the possibility to acquire several images in a single breath-hold.
A diagram of the ASE-prepared HASTE sequence is shown in Figure 6.2. The magnetization preparation ("preparation-block") consists of a non-slice-selective RF-pulse with 90° flip-angle followed by a 180° slice-selective refocusing pulse. The phase shift between the excitation pulse and the refocusing pulse in the preparation-block is $\pi/2$. The preparation-block is characterized by an asymmetry time τ and by an echo time TE. The subsequent HASTE readout ("readout-block") is composed of a train of 180° slice-selective refocusing pulses with inter-pulse time ΔTE, which allows to acquire the full k-space in a single shot. Another important parameter of the sequence is the phase ϕ of refocusing pulses in the readout-block, which can be arbitrarily chosen. The value of ϕ is constant during the whole pulse train.
Formation of unwanted echoes generated by the residual longitudinal magnetization which is available at the end of the preparation-block was prevented by using different directions and amplitudes for the crushing gradients in the preparation-block (phase-encoding and slice-selection directions used) and those in the readout-block (readout and slice-selection directions used). In order to minimize the signal loss which is due to the elimination of the residual longitudinal magnetization, the slice thickness which was used for the refocusing pulse of the preparation-block was twice the slice thickness of the refocusing pulses in the readout-block.
Linear reordering of the phase-encoding steps was used together with partial-Fourier acquisition. Image reconstruction was accomplished using the Margosian algorithm [158]. The sequence includes also ECG synchronization, as the resulting signal in the lungs depends strongly on the cardiac phase [34, 38].

6.2.4 Image Acquisition and Reconstruction

For $\tau \neq 0$ the transverse magnetization at the time of signal acquisition can present a phase shift, due to static dephasing in the presence of magnetic field inhomogeneities. This results in a violation of the CPMG conditions in the ASE-prepared HASTE, which could corrupt the image quality. In this case, the image would present the following characteristics: the in-phase signal ($S_{\parallel}$), corresponding to the magnetization component with phase $\phi \pm \pi$, generates the main image; the out-of-phase signal ($S_{\perp}$), corresponding to the magnetization component with phase $\phi \pm \pi/2$, generates a ghost shifted by half FOV, due to phase reversing between odd and even echoes.
The basic idea of the proposed technique is to acquire two images when $\tau \neq 0$, with the phase of the refocusing pulses in the readout-block cycled by $\pi/2$ [166]: one image ($S_{\parallel}$)

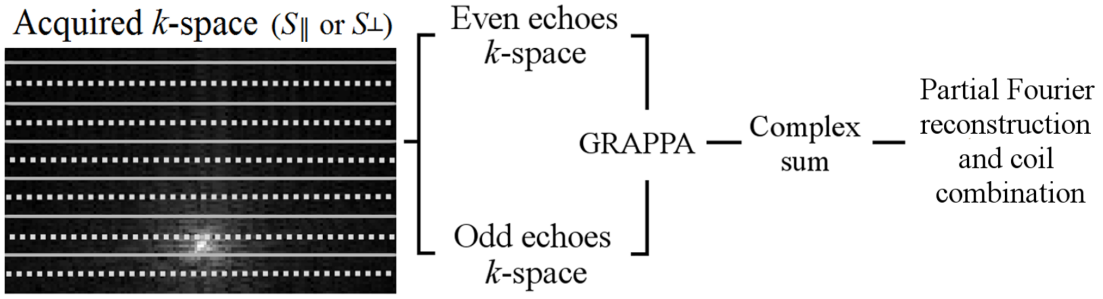

Figure 6.3: Image reconstruction procedure used to remove the ghosting artifact from $S_{\parallel}$ and $S_{\perp}$ in case $\tau \neq 0$. For each acquisition ($S_{\parallel}$ and $S_{\perp}$), two k-spaces are separately generated from the odd and the even lines using GRAPPA. The complex sum of two k-spaces is calculated and used for image reconstruction. Reproduced with permission from reference [A2].

is acquired with $\phi = 0$ while the other one ($S_{\perp}$) is acquired with $\phi = \pi/2$. The ghosting artifact is eliminated in both acquisitions as described below (see Figure 6.3):

1. for each receive channel, GRAPPA reconstruction [26] with AF = 2 is used to generate two separate k-spaces from the odd and the even echoes of the original partially acquired k-space;

2. the complex sum of the two obtained k-spaces is calculated, in order to cancel the signal components which present opposite phases in odd and even echoes, such as the ghost;

3. images $S_{\parallel}$ and $S_{\perp}$ are reconstructed from the summed k-spaces, for each of the two acquisitions, using the Margosian algorithm [158] in conjunction with adaptive coil combination [238];

4. finally, the signal amplitude image $S(\tau)$ is obtained as a combination of $S_{\parallel}$ and $S_{\perp}$ from the following formula (see Figure 6.4):

$$S(\tau) = \frac{1}{2}\sqrt{\left|S_{\parallel}(\tau)\right|^2 + \left|S_{\perp}(\tau)\right|^2} \tag{6.3}$$

For $\tau = 0$ the out-of-phase component $S_{\perp}$ is negligible, due to full signal refocusing. Therefore, only the in-phase component $S_{\parallel}$ is acquired. This acquisition is used also as calibration scan for the GRAPPA reconstruction.

6.2.5 Phantom Experiments

Phantom experiments were performed to demonstrate ghost elimination when using the proposed reconstruction procedure (see Figure 6.5). A water phantom with dimensions of

approximately $36 \times 28 \times 15$ cm^3 was used to mimic the human chest. A six element body array coil was used in combination with an eight channel spine matrix for signal detection. Imaging experiments were performed with the ASE-prepared HASTE sequence. The following imaging parameters were used for all experiments: FOV $= 500 \times 500$ mm^2, slice thickness $= 15$ mm, matrix size $= 128 \times 128$ (zero-filled to 256×256), PFF $= 5/8$ (corresponding to 80 phase encoding lines), receiver bandwidth $= 1500$ Hz/Px, inter-pulse time ΔTE $= 2.4$ ms. A single slice was acquired in the coronal orientation.
Three images were acquired: one image ($S_{\parallel}$) was acquired with $\tau = 0$ ms and two images ($S_{\parallel}$ and $S_{\perp}$) were acquired with $\tau = 10$ ms. A Hamming filter was applied to all images in order to avoid Gibbs ringing. Because the datasets acquired in phantom were not used to quantify the spectral line broadening but only to validate the image reconstruction procedure, the value of τ was arbitrarily chosen. For all images TE $= 15$ ms. A separation time of 20 s was included between the different acquisitions, in order to allow for the full recovery of the longitudinal magnetization. The image $S(\tau)$, given by equation (6.3), was reconstructed using the proposed reconstruction technique. The corresponding result was compared to that obtained from the conventional reconstruction procedure, which consists in the direct application of the Margosian algorithm on the partially acquired k-spaces followed by the calculation in equation (6.3). The signal amplitude of the ghost at half FOV in the images $S(\tau)$, which were obtained from both reconstruction procedures, was qualitatively assessed. To this end, a non-linear scaling was applied to both images in order to enhance the visualization of the ghost.

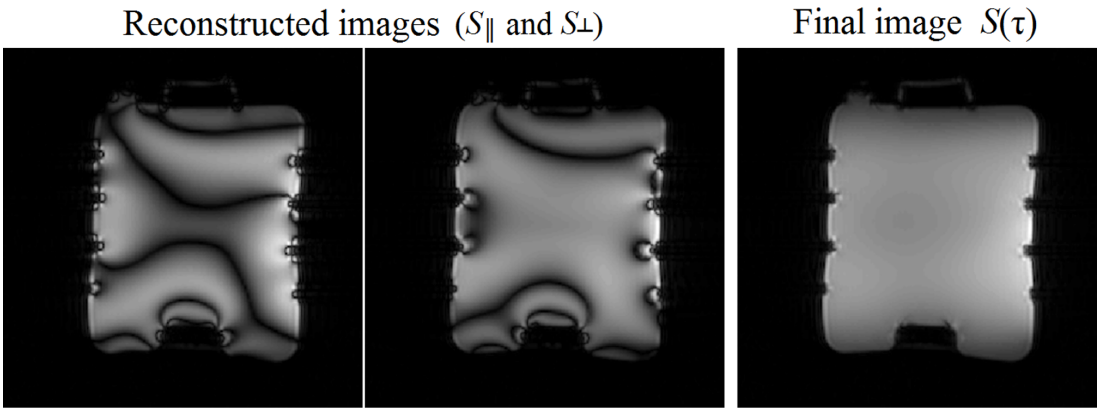

Figure 6.4: Magnitude images obtained in phantom, after the proposed reconstruction procedure, using the ASE-prepared HASTE sequence with $\tau = 10$ ms. Left: in-phase image ($S_{\parallel}$). Center: out-of-phase image ($S_{\perp}$). Right: combined image $S(\tau)$ obtained from equation (6.3). The signal voids in $S_{\parallel}$ and $S_{\perp}$, which are due to the violation of the CPMG conditions, are effectively removed in $S(\tau)$. Reproduced with permission from reference [A2].

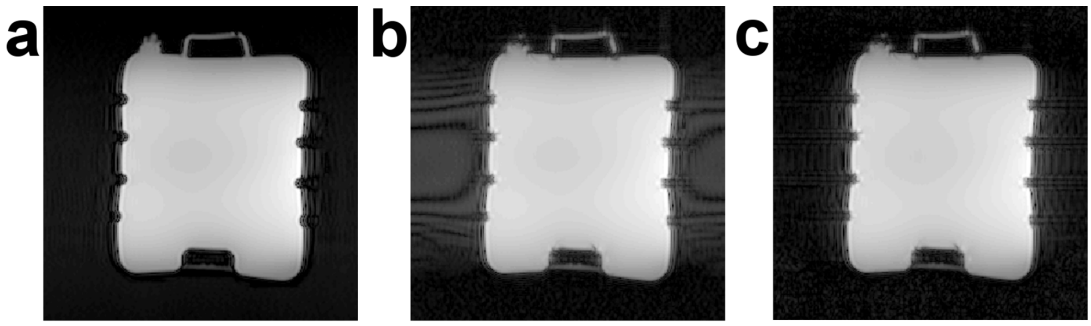

Figure 6.5: Comparison between the magnitude images obtained using the proposed reconstruction procedure and the conventional* reconstruction. a: Reference image $S(0)$ acquired with $\tau = 0$ ms. b: Combined image $S(\tau)$ obtained using the conventional reconstruction. c: Combined image $S(\tau)$ obtained using the proposed reconstruction procedure, showing effective ghost elimination. Reproduced with permission from reference [A2].

6.2.6 In-vivo Experiments

Imaging experiments by use of the ASE-prepared HASTE sequence were performed to quantify the spectral line broadening of the human lung in-vivo. Fourteen healthy subjects (11 male and 3 female, age range $22 - 32$ years) without any known history of pulmonary disease were investigated.
Three images were acquired in a single breath-hold of approximately 15 s duration: one image ($S_{\parallel}$) was acquired with $\tau = 0$ ms and two images ($S_{\parallel}$ and $S_{\perp}$) were acquired with $\tau = 2.0$ ms. For all images TE $= 5.0$ ms and ΔTE $= 2.4$ ms. This resulted in an actual echo time at the k-space center of 43.4 ms, due to the use of linear reordering of k-space lines. A separation time of 6 s was included between the different acquisitions, in order to allow for the full recovery of the longitudinal magnetization (assuming that $T_1 \approx 1000$ ms in the lung [201]). Receive coils and other imaging parameters were the same as for phantom experiments.
The trigger delay between the ECG pulse and the excitation pulse was manually adjusted, in order to acquire all images in the diastolic cardiac phase, which provides less signal sensitivity to blood flow in the pulmonary vessels and higher signal amplitude [38]. Image $S(\tau)$ was reconstructed using the procedure described above. A Hamming filter was applied to all images, in order to avoid Gibbs ringing.
Three series of experiments were performed with the volunteers in the supine position, as described below:

1. In eleven of the volunteers, the dependence of the spectral line broadening on lung inflation was analyzed by acquiring one coronal slice, through the aorta, at both an expiratory state (FRC) and an inspiratory state (TLC).

2. In six of the volunteers, a repeatability study was performed to demonstrate the robustness of the presented technique: acquisition of one coronal slice, through the aorta, was repeated in separate and consecutive breath-holds at FRC, for a total of ten measurements in each subject.

3. In six of the volunteers, the influence of oxygen concentration on the line broadening was investigated by acquiring one coronal slice, through the aorta, under both room air (21% O_2) and pure oxygen (100% O_2) conditions at FRC. The inhalation gases were administrated by means of a dedicated system provided with a breathing mask. A waiting time of approximately 5 min was included between the two acquisitions to avoid wash-in effects [43, 45, 109]. In order to minimize the influence of oxygen consumption during the breath-hold on the results, the two images $S_{\parallel}$ and $S_{\perp}$, with $\tau = 2$ ms, were acquired first in the series while the reference image $S(0)$ was acquired at last.

In addition to the experiments described above, in four of the volunteers imaging experiments were performed in both the supine and the prone position in order to assess the dependence of the spectral line broadening on gravitation in the A-P direction. To this end, four sagittal slices of the right lung were acquired at both FRC and TLC.

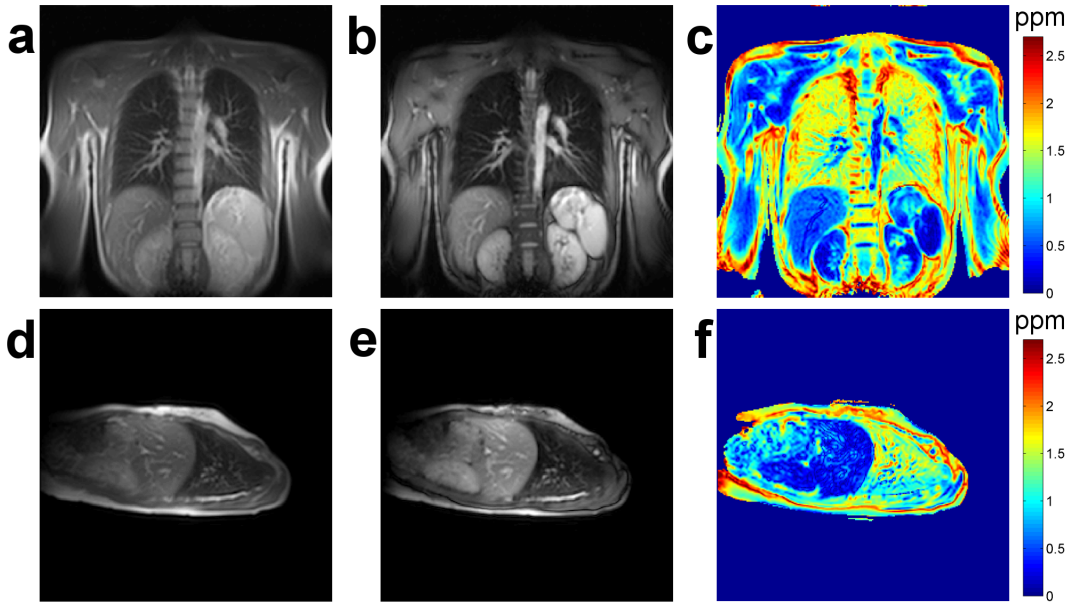

Figure 6.6: Example of the magnitude images $S_{\parallel}$ (a,d) and $S_{\perp}$ (b,e) obtained in the lung using the ASE-prepared HASTE sequence in combination with the proposed reconstruction procedure. Corresponding map of the spectral line broadening (c,f). Reproduced with permission from reference [A2].

6.2.7 Quantification and Image Analysis

Maps of the spectral line broadening, in ppm, were calculated from the acquired images on a voxel-by-voxel basis using the following equation:

$$\frac{\sqrt{\langle\omega^2\rangle}}{\gamma B_0} = \frac{1}{\gamma B_0 \tau}\sqrt{2\ln\left[\frac{S(0)}{S(\tau)}\right]} \tag{6.4}$$

For all in-vivo experiments, the results obtained in the lung parenchyma were systematically evaluated as described below:

1. A ROI was drawn around the lung parenchyma on the reference image $S(0)$. The procedure described in Chapter 4 was used to discard large vessels and other tissues with high proton density from the ROI and ensure that primarily data from the lung parenchyma are evaluated.

2. Histograms of the statistical distribution of the spectral line broadening within the ROI were generated and the corresponding MVs and STDs were calculated.

For the analysis of the influence of lung inflation on the spectral line broadening, the relative difference between the MVs obtained in the same coronal slice at FRC and TLC, defined as $(\mathrm{MV_{TLC}} - \mathrm{MV_{FRC}})/\mathrm{MV_{FRC}}$, was calculated. MVs, STDs and relative difference obtained in different volunteers were compared.
For the repeatability study, the average mean value ($\mathrm{MV_{tot}}$) calculated over the ten performed measurements and its standard deviation (σ_{MV}) were calculated. The resulting CoV, defined as the ratio $\sigma_{\mathrm{MV}}/\mathrm{MV_{tot}}$, was quantified and used as a measure of reproducibility.
For the assessment of the dependence of the line broadening on the oxygen concentration, the relative difference between the MVs obtained when breathing room air and pure oxygen, defined as $(\mathrm{MV_{oxygen}} - \mathrm{MV_{air}})/\mathrm{MV_{air}}$, was calculated. A Student's t-test was performed to assess the statistical significance of the similarity between the two groups (P_{oxygen}), in the assumption of homogeneity of variance. The null-hypothesis was rejected for $P_{\mathrm{oxygen}} < 0.05$. For this calculation, the largest CoV obtained from the reproducibility study in all volunteers, which represents the case with the most statistical variability, was used.
The gravitational dependence of the spectral line broadening was also analyzed: the sagittal datasets were averaged in the horizontal direction assuming that each line of the image represents an isogravitational plane [49, 239]. The result of this calculation was used to generate a plot of the spectral line broadening profile in the A-P direction. The mean slope of the line broadening change with gravitation, in %/cm, was calculated by fitting the obtained profiles with a least squares linear regression. To this end, the profiles of the spectral line broadening were rescaled, before applying the fit, by the MV calculated over the four acquired slices and plotted against the distance in cm from the bottom of the lung (with respect to gravitation).

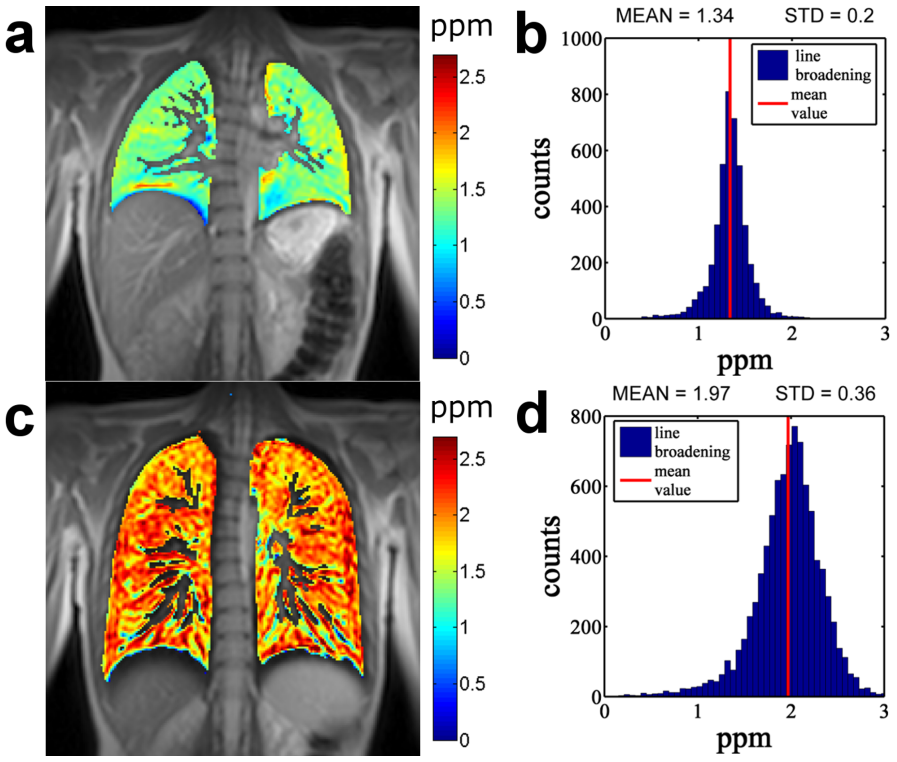

Figure 6.7: a,c: Coronal images of the human lung acquired with the ASE-prepared HASTE sequence in-vivo in a healthy volunteer. The parametric maps of the spectral line broadening of the lung parenchyma, obtained after image segmentation, are overlapped to the magnitude images $S(0)$. Each map was obtained in a single breath-hold, at either FRC (a) or TLC (c). b,d: Corresponding histograms of the statistical distribution of the spectral line broadening within the lung parenchyma. Reproduced with permission from reference [A2].

6.3 Results

The magnitude images obtained from the phantom experiments are shown in Figure 6.4. For $\tau \neq 0$, the in-phase and the out-of-phase images ($S_{\parallel}$ and $S_{\perp}$) present signal modulations throughout the FOV in the form of banding artifacts. This is due to the violation of the CPMG conditions in the presence of magnetic field inhomogeneities. In the combined image $S(\tau)$, obtained from equation (6.3), these modulations are canceled. Figure 6.5 shows the comparison between the results obtained with the conventional and with the proposed reconstruction procedures. A ghost artifact shifted by half FOV can be observed when using the conventional reconstruction (Figure 6.5 b). The ghost is effectively eliminated by the proposed reconstruction procedure (Figure 6.5 c).

A representative example of the magnitude images $S(0)$ and $S(\tau)$ (with $\tau = 2$ ms) which were acquired in two different volunteers at FRC, in both the coronal and the sagittal orientations, is shown in Figure 6.6. A non-linear scaling was applied to all magnitude images in order to enhance the visualization of the lung parenchyma. Attenuation of the signal amplitude within the lung parenchyma can be observed in image $S(\tau)$ compared to $S(0)$. The resulting parametric maps of the spectral line broadening are shown in Figures 6.6 c,f. Figures 6.7 a,c show a representative example of the coronal in-vivo maps of the spectral line broadening obtained within the lung parenchyma at both FRC and TLC. Homogeneous increase of the line broadening throughout the lung can be observed at TLC compared to FRC. This confirms normal lung inflation. The resulting histograms of the statistical distribution of the spectral line broadening within the lung parenchyma are shown in Figures 6.7 b,d A distribution of values ranging from 0.5 to 3.0 ppm can be observed, with an increase of both MV and STD with lung inflation. For each subject, the corresponding MVs and STDs obtained at both FRC and TLC are reported in Table 6.1. Mean values between 1.30 and 1.60 ppm were found at FRC and between 1.80 and 2.10 ppm at TLC, with a relative increase between 25% and 47% depending on the subject. The mean line broadening calculated over all volunteers is 1.48 ppm at FRC and 1.95 ppm at TLC, with a relative increase of approximately 33%.

	MV ± STD (ppm)		Relative
Subject	Expiration (FRC)	Inspiration (TLC)	Difference
1	1.34 ± 0.20	1.97 ± 0.36	47%
2	1.30 ± 0.27	1.85 ± 0.46	42%
3	1.56 ± 0.23	2.00 ± 0.31	28%
4	1.43 ± 0.35	1.89 ± 0.38	32%
5	1.49 ± 0.22	1.89 ± 0.33	27%
6	1.59 ± 0.27	2.05 ± 0.39	29%
7	1.49 ± 0.29	2.02 ± 0.36	36%
8	1.54 ± 0.23	1.92 ± 0.36	25%
9	1.54 ± 0.27	2.01 ± 0.43	31%
10	1.37 ± 0.27	1.94 ± 0.56	42%
11	1.56 ± 0.29	1.99 ± 0.52	28%
Mean	1.48 ± 0.29	1.95 ± 0.44	33%

Table 6.1: Mean values and standard deviations of the spectral line broadening of the lung parenchyma obtained in-vivo at FRC and TLC. Reproduced with permission from reference [A2].

The results of the repeatability study are reported in Table 6.2. The standard deviation of the mean value σ_{MV}, calculated over the ten performed measurements, was between 0.01 and 0.04 ppm for all volunteers. The corresponding CoV is below 0.03 in all cases, with a maximum of 0.028 and a mean calculated over all volunteers of 0.018.

Subject	MV (ppm)	σ_{MV} (ppm)	CoV (σ_{MV}/MV)
1	1.49	0.019	0.013
2	1.39	0.039	0.028
3	1.56	0.015	0.0097
4	1.49	0.034	0.023
5	1.54	0.010	0.0067
6	1.56	0.040	0.026
Mean	1.50	0.026	0.018

Table 6.2: Reproducibility of the mean values of the spectral line broadening in the lung parenchyma obtained from ten repeated measurements at FRC. Reproduced with permission from reference [A2].

Figure 6.8 shows a representative example of the maps obtained under room air and pure oxygen conditions. An increase of the spectral line broadening of the lung parenchyma can be observed with higher oxygen concentration. MVs and STDs obtained for both experimental conditions are reported in Table 6.3 together with the P-values obtained from the statistical analysis.
The comparison between room air and pure oxygen shows a significant increase of the spectral line broadening with the oxygen concentration, with $P_{\text{oxygen}} < 0.0001$ for all volunteers. The relative increase was between 9% and 20%. The mean relative increase, calculated over all volunteers, was 14%.

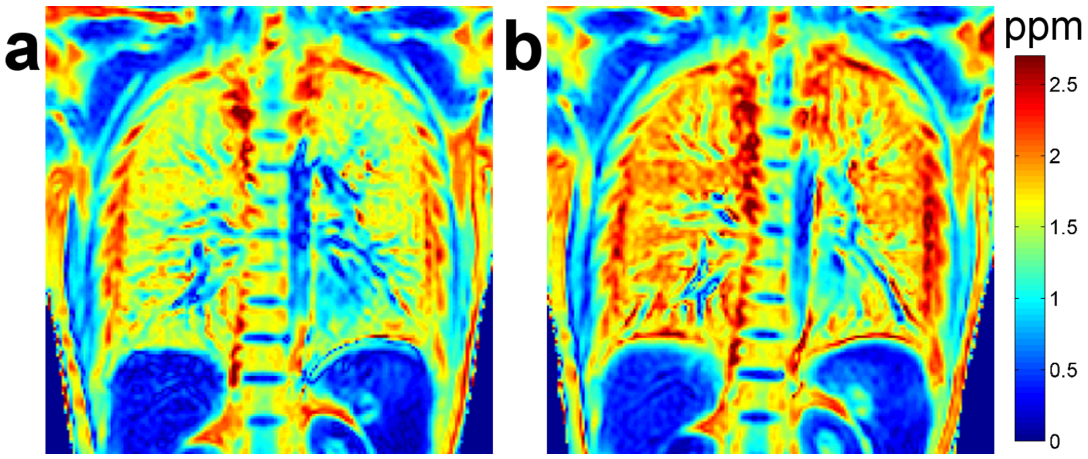

Figure 6.8: Coronal maps of the spectral line broadening of the human lung acquired with the ASE-prepared HASTE sequence in-vivo, under room air (a) and pure oxygen (b) conditions. Reproduced with permission from reference [A2].

Subject	MV ± STD (ppm) Room Air (21% O_2)	Pure Oxygen (100% O_2)	Relative Difference	P_{oxygen}
1	1.40 ± 0.28	1.63 ± 0.28	16%	< 0.0001
2	1.49 ± 0.29	1.79 ± 0.28	20%	< 0.0001
3	1.54 ± 0.23	1.68 ± 0.23	9%	< 0.0001
4	1.54 ± 0.27	1.75 ± 0.22	14%	< 0.0001
5	1.37 ± 0.27	1.57 ± 0.32	15%	< 0.0001
6	1.56 ± 0.29	1.73 ± 0.36	10%	< 0.0001
Mean	1.48 ± 0.27	1.69 ± 0.28	14%	< 0.0001

Table 6.3: Mean values and standard deviations of the spectral line broadening of the lung parenchyma obtained in-vivo under room air and pure oxygen conditions at FRC. Reproduced with permission from reference [A2].

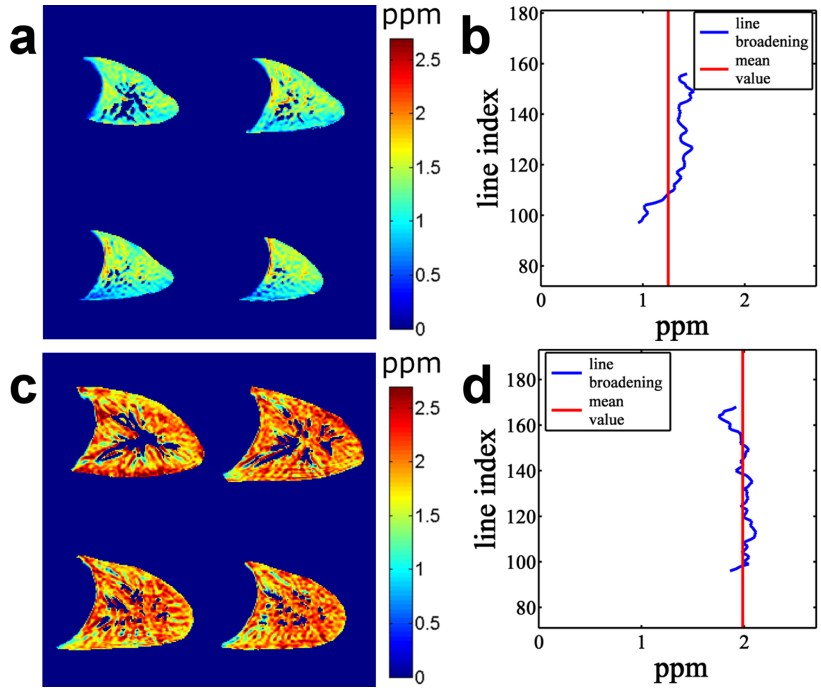

Figure 6.9: a,c: Sagittal maps of the spectral line broadening of the human lung acquired in-vivo, with the volunteer in the supine position, using the ASE-prepared HASTE sequence. Two sets of four slices each which were obtained at both FRC (a) and TLC (c) are shown. b,d: Gravitational dependence of the spectral line broadening obtained by averaging the whole sagittal data sets in the A-P direction after segmentation of the lung parenchyma. Reproduced with permission from reference [A2].

Figures 6.9 a,c show a set of four sagittal slices of the right lung acquired in one of the volunteers (indicated as subject 1 in Table 6.1) in the supine position, at both FRC and TLC. The corresponding plot of the gravitational dependence of the spectral line broadening is shown in Figures 6.9 b,d. The distribution in the A-P direction demonstrates a gravitational dependence of the spectral line broadening at FRC, with a decrease towards the bottom of the lung indicating a reduced inflation. This effect is strongly reduced at TLC, at which a quite homogeneous line broadening throughout the lung can be observed. MVs and STDs of the whole data sets were 1.26 ± 0.33 ppm at FRC and 1.99 ± 0.38 ppm at TLC, with a relative increase of 58%. A similar gravitational effect was observed with the same volunteer in the prone position, as shown in Figure 6.10.
Figure 6.11 shows an example of the linear regression fit performed on the line broadening profiles in the A-P direction. The slopes obtained from this calculation, in %/cm, are reported in Table 6.4. At FRC, the line broadening increased with the distance from the

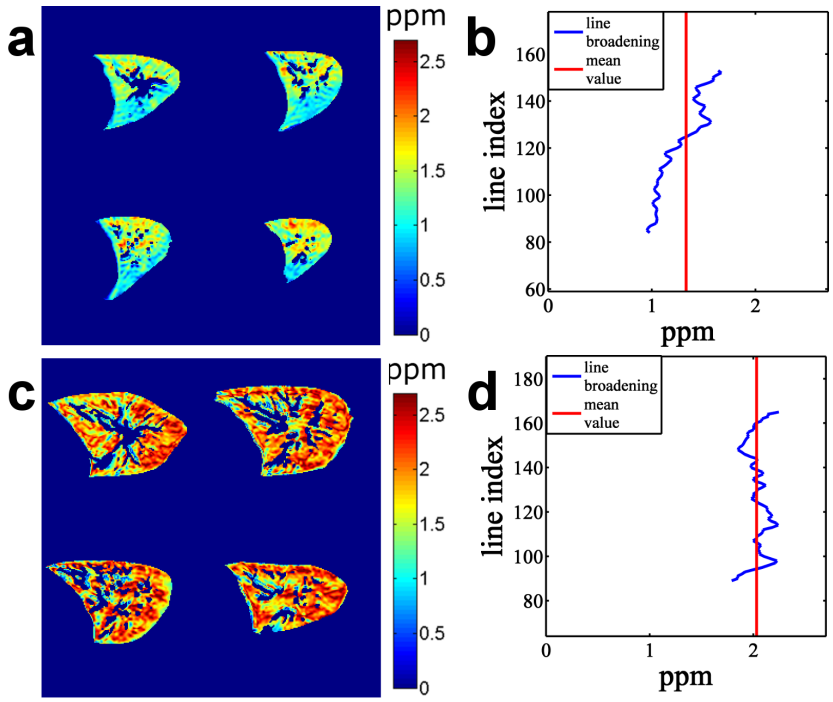

Figure 6.10: a,c: Sagittal maps of the spectral line broadening of the human lung acquired in-vivo, with the volunteer in the prone position, using the ASE-prepared HASTE sequence. Two sets of four slices each which were obtained at both FRC (a) and TLC (c) are shown. b,d: Gravitational dependence of the spectral line broadening obtained by averaging the whole sagittal data sets in the A-P direction after segmentation of the lung parenchyma. Reproduced with permission from reference [A2].

bottom of the lung in all volunteers, in both the supine and the prone positions, as indicated by the positive sign of the slope. In all cases, the gravitational dependence of the line broadening strongly decreased or completely disappeared (negative sign of the slope) at TLC.

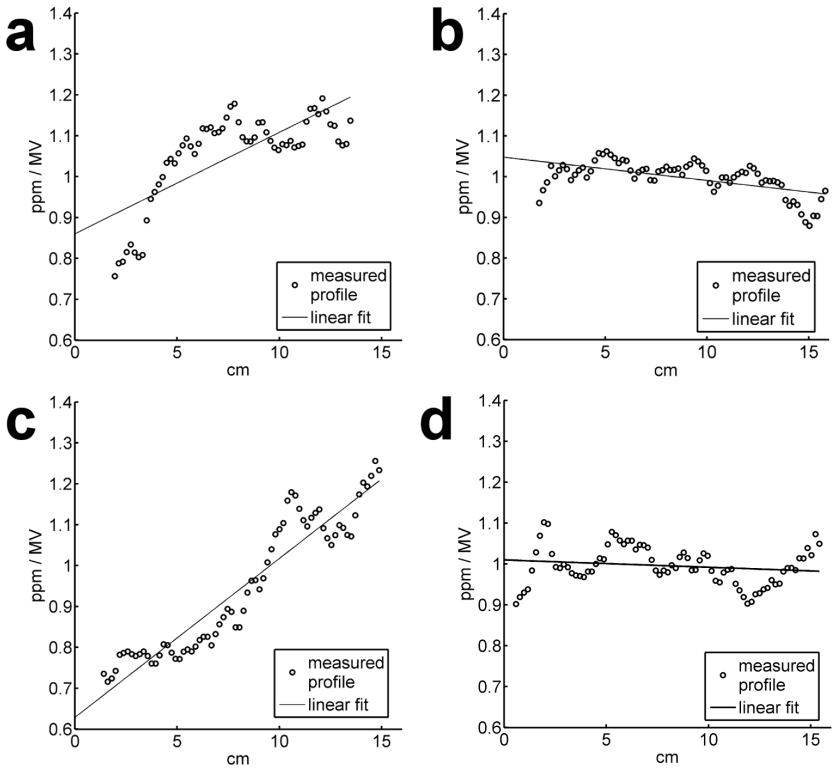

Figure 6.11: Profiles of the spectral line broadening in the A-P direction obtained in different experimental conditions and corresponding results of the linear regression fit. a: Supine, FRC; b: Supine, TLC; c: Prone, FRC; d: Prone, TLC. The line broadening profiles correspond to the data sets of Figs. 6 and 7 rescaled by the MV of the line broadening calculated over the four slices and plotted against the distance from the bottom of the lung in cm. Reproduced with permission from reference [A2].

6.4 Discussion

In this chapter, the feasibility of quantifying the spectral line broadening of the human lung in-vivo within a single breath-hold was demonstrated. To this end, a technique based on the ASE approach [63, 71, 125] was used. In the proposed technique, the ASE module is integrated in a HASTE sequence, which allows to acquire the images in a single shot

Subject	Slope in supine position (%/cm) FRC	TLC	Slope in prone position (%/cm) FRC	TLC
1	3.88	−0.57	2.48	−0.16
2	1.40	−0.63	1.82	−0.12
3	2.23	0.52	1.19	0.34
4	2.73	0.45	2.01	0.19
Mean	2.56	−0.057	1.88	0.063

Table 6.4: Values of the line broadening slope in the A-P direction (in %/cm) obtained with the volunteers in both the supine and prone positions, at FRC and TLC. Reproduced with permission from reference [A2].

and thus presents a significant advantage for lung imaging in comparison to the conventional ASE, namely: reduced acquisition times and consequently, a reduced sensitivity to motion. This results in a robust method which presents excellent reproducibility in the quantification, as demonstrated by the repeatability study with a coefficient of variation calculated over ten measurements smaller than 0.03 in all subjects.
The quantification of the spectral line broadening of the lung can be used to obtain two kinds of information about the lung functionality, namely: 1) lung inflation and 2) oxygen uptake. A significant increase of the line broadening was observed with both lung inflation and oxygen concentration. In this regard, the presented technique has some similarities with T_2^* mapping [45, 109, 110, 111]. However, some substantial differences between the two techniques can be identified, as described below:

- T_2^* mapping is not only sensitive to static signal dephasing due to the magnetic field inhomogeneities (usually expressed by T_2' [28]), but also to the intrinsic transverse relaxation dictated by T_2. The ASE approach, instead, is insensitive to T_2, owing to the possibility to acquire images with different values of τ and same TE. Even though the typical T_2 of the lung is much longer than T_2', it must be considered that the lung presents a multi-exponential T_2 decay [112], with short lived components dominating at the short echo times that are typically used for T_2^* mapping [45, 109]. Furthermore, the T_2 decay can be further accelerated in-vivo by the effect of pseudo-diffusion of the blood through the internal magnetic field gradients, as discussed in Chapter 5. This means that the contribution of short lived T_2 components to the measured T_2^* of the lung might not be negligible. In this case, the ASE technique would allow to obtain a better sensitivity to variations of the spectral line broadening, which carry the desired information on lung inflation and on oxygen uptake.

- T_2^* mapping is typically performed using GRE-based sequences. These techniques can generate either T_1 or proton density weighted images. The HASTE sequence used in this work, instead, allows for T_2 weighted imaging. This can have an impact

on the quantification, due to the multi-compartmental nature of the lung tissue [112]. The different lung compartments, in fact, have different T_2^* values, as recently demonstrated by Triphan et al. [192]. Consequently, image weighting acts as a filter on the spectral domain. Presumably, this may result in a different sensitivity to changes of the spectral line broadening in the two techniques. In the ASE sequence, the longer TE required in comparison to GRE-based sequences results in a different weighting of signal components with different T_2. The impact of this effect on the measured line broadening is described by the dependence of the line shape $P(\omega, \mathrm{TE})$ on TE in equation (6.1). This means that both following factors might have an impact on the quantification: 1) the presence of signal components with different values of $T_{2,0}$ due to spin-spin interactions and 2) the presence of lung compartments with different $T_{2,\mathrm{diff}}$ due to diffusion through the internal gradients of the lung, such as blood and lung parenchyma.

The results of this work suggest that the ASE approach provides a slightly increased sensitivity to oxygen uptake with respect to T_2^* mapping, as demonstrated by comparing the results obtained here with those of Pracht et al. [45] and Triphan et al. [109]. The relative increase of the line broadening, averaged over all volunteers, was approximately 14%, while with T_2^* mapping it was approximately 10%. Both effects described above including the insensitivity to the T_2 decay and the different image weighting may contribute to this result.

One of the drawbacks of the presented technique in comparison to T_2^* mapping, however, is the requirement for ECG-triggering. This is due to the sensitivity of the HASTE sequence to blood in- and outflow [38] as well as to the pseudo-diffusion of blood through the internal gradients of the lung. By triggering all images at the same cardiac phase, differences in the contribution of blood signal among the different acquisitions are minimized. In this work, the diastolic cardiac phase was used for all experiments, which corresponds to slower blood flow and, therefore, to a higher signal as well as to a better reproducibility [38].

Another drawback, which is common also to the other image acquisition techniques which have been presented in this thesis, is that any kind of motion which occurs within the lung space during image acquisition, such as instable breath-holding, can lead to image misregistration and corrupt the quantification. This problem was observed in a very limited number of acquisitions in volunteer experiments and might be overcome with the use of navigators, as discussed in Chapter 5.

Another characteristic of the presented technique is that the comparison between room air and pure oxygen conditions must be performed at the same breathing state, because of the strong influence of lung inflation on the line broadening. Due to the difficulty for the volunteers to reproduce the TLC respiratory state in different breath-holds, oxygen enhanced imaging was performed at FRC only, where a CoV below 0.03 was found for all volunteers.

The proposed technique relies on the acquisition of two points with different values of τ for the quantification of the spectral line broadening. This allows to keep the acquisition time

as short as possible. However, it also reduces the sensitivity of the technique to a limited range of values of the line broadening. For this reason, it is important to prospectively choose an appropriate value for τ. In this work, $\tau = 2$ ms was used for all in-vivo experiments at a field strength of 1.5 T. This value was empirically found and specifically chosen to obtain an optimal sensitivity to the typical range of values of the line broadening that was observed at FRC and TLC when breathing room air. Under different experimental conditions, the use of a different value of τ may be beneficial. For example, measurements at TLC when breathing pure oxygen might require the use of smaller values of τ, due to the increase of the line broadening. Because the magnetic field inhomogeneities linearly increase with the magnetic field strength [114], the optimal value for τ should linearly decrease with B_0. This would not introduce any penalties on the technique, because each image is acquired in a separate scan. The use of stronger static magnetic fields might be beneficial for the presented technique in terms of SNR, at the cost of an increased blurring, due to the effect of T_2 shortening at stronger magnetic fields [114].
Because the phase difference between fat and water, which is induced by chemical shift, depends on both τ and B_0, cancellation of the two signal components might lead to signal voids in some regions outside the lungs for $\tau \neq 0$, depending on the experimental settings. However, the impact of this effect on the quantification of the spectral line broadening of the lung tissue can be neglected, due to the absence of fat in the lung.
The values of the spectral line broadening observed within the lung parenchyma with the presented technique, averaged over all subjects, were: MV $\pm$ STD $\simeq 1.48 \pm 0.29$ ppm at FRC and 1.95 ± 0.43 ppm at TLC. These values are in good agreement with the results obtained by Case et al. [67] and by Christman et al. [120] from numerical simulations and experiments.
The gravitational dependence of the spectral line broadening showed a decrease towards the bottom of the lung at FRC, in both the supine and the prone positions. This is in perfect agreement with the increase of proton density which is due to the compression of the lung parenchyma in this region ("Slinky effect" [209]), as previously observed by several investigators [111, 209, 239]. At TLC this effect is strongly reduced, suggesting that the bottom of the lung expands more than the top. This also means that the relative difference between the values obtained at FRC and TLC depends on gravitation, which probably explains the large variations observed among all volunteers in the relative differences of Table 6.1 between FRC and TLC.
In this work, all measurements were performed on healthy volunteers and the results are consistent with prior studies [67, 120, 45, 109, 240, 209]. An in-depth assessment of the performance of the presented technique on patients with lung diseases requires further investigation and could be an interesting topic for future work. In this regard, it could be useful to remark here some characteristics of the technique in order to identify potential clinical applications. The line broadening maps represent a quantitative fingerprint for lung inflation [67, 118, 120] and therefore, they could be used to detect local morphological changes in the air content of the lung [118, 138, 235, 236], similarly to proton density imaging [32, 140, 240, 241, 242, 243] but with the advantage of relying on quantitative data, as

previously described by Theilmann et al. [140]. Furthermore, the comparison between the results obtained at different breathing states might be used to detect functional disorders, such as anomalous lung expansion which may occur in case of air trapping, obstructive lung diseases or ventilation defects [2, 10, 43, 183, 237]. The comparison between the results obtained under room air and pure oxygen conditions might be used to detect a local deficit in the oxygen uptake, which reflects local ventilation [45, 109].
The studies conducted in this work were subject to some limitations, though. All repeatability measurements were conducted in coronal slices placed at the height of the aorta, with the volunteers lying in the supine position. This experimental setting represents a well defined reference that can be applied and reproduced with good approximation in all volunteers. However, as the line broadening depends primarily on lung inflation, the region of the lung at which the slice is acquired can have a slight impact on the resulting CoV, as demonstrated by the gravitational study. The difference between the line broadening at the top and at the bottom of the lung, of the order of 40% at FRC, may result in similar variations of the CoV, in relative terms, throughout the whole lung. A similar effect can be expected also on a simple coronal acquisition of the line broadening map at FRC when shifting the slice in the A-P direction. Measurements at TLC, instead, are relatively insensitive to gravitation. Nevertheless, stronger variations should be expected among different acquisitions, compared to the CoV found in this work, due to the major difficulty for the volunteers to reproduce inspiratory breathing states.
Clinical application of quantitative MRI techniques remains very challenging for a body region such as the lung, due to several factors, namely: the low proton density, the short transverse relaxation times and physiological motion. The proposed technique represents a further step towards potential clinical applications of line broadening imaging, as compared to the state of the art. However, all results presented in this work were obtained from healthy volunteers. Further investigations are required to demonstrate the clinical applicability and the eventual benefits of the proposed technique in the characterization of lung diseases. In this regard, the quantitative line broadening data provided in this work could be used as a reference for future studies.
In conclusion, the presented technique represents a robust method to quantify the spectral line broadening of the lung parenchyma in-vivo. Data acquisition can be accomplished in a single breath-hold of approximately 15 s duration and may be compatible with clinical studies on patients with lung diseases as well as with the clinical routine. The technique can be potentially used to detect a variety of pulmonary diseases that alter the local air content of the lung, the lung expansion and the oxygen uptake. In this regard, deeper clinical investigations are necessary.

Summary

Magnetic Resonance Imaging (MRI) represents a unique tool in the field of diagnostic imaging, as it provides a large variety of diagnostic information without the use of ionizing radiations. Application of MRI in the lung allows to obtain and to combine spatially resolved information about morphological, functional and microstructural properties of the lung which are of primary interest for the diagnosis and the characterization of lung pathologies. However, lung imaging remains a challenging branch of MRI. This is due to the low proton density of the lung parenchyma as well as to the relatively short transverse relaxation times (T_2 and T_2^*), which hamper both image resolution and Signal-to-Noise Ratio (SNR). Furthermore, the multiple sources of physiological motion in the lungs, which include respiration, cardiac beat and blood flow in the pulmonary vessels, require the use of fast and relatively motion-insensitive acquisition techniques in order to reduce the risks of image artifacts. For these reasons, Computed Tomography (CT) and nuclear medicine are still considered the gold standard modalities to obtain spatially resolved information respectively about lung morphology and functionality. Nevertheless, lung MRI represents a promising alternative to the other imaging modalities as well as a potential source of additional diagnostic information thanks to its flexibility.

In recent years, a number of valuable technical developments have been proposed in the field of lung MRI to improve the image quality, to reduce the acquisition times and to expand the diagnostic information provided. For example, techniques such as oxygen-enhanced MRI [43], Fourier-decomposition [46], Arterial Spin Labeling (ASL) [48] and hyperpolarized gas MRI [53] have given access to spatially resolved knowledge about pulmonary perfusion, ventilation, gas-exchange and microstructural properties of the lung tissue, together with minimal invasivity as well as clinically acceptable image quality. This has led to the increase of potential clinical applications of lung MRI as well as to a remarkable approach to the clinical needs.

The goal of this work was to contribute to the further expansion of lung imaging methodologies based on proton MRI, with the development of a series of image acquisition techniques that aimed at the quantification of functional and microstructural parameters of the lung tissue. Additionally, with the in-vivo application of the developed techniques in the human lung, this work contributes to a better understanding about some properties of the lung tissue. The core of this dissertation is divided into three main parts (Chapters 4 to 6), each dedicated to a different parameter, namely: 1) the blood volume fraction, 2) the transverse

relaxation enhancement caused by molecular diffusion through the internal magnetic field gradients of the lung and 3) the spectral line broadening. These parameters are closely related to lung properties of primary diagnostic interest such as perfusion, alveolar size, inflation and ventilation.
Each technique was specifically designed to allow data acquisition within a single breath-hold of maximum duration of 15 s. All presented techniques make use of the Half-Fourier Acquisition Single-shot Turbo spin-Echo (HASTE) pulse sequence [33, 34], in different variants, for image acquisition. With the HASTE sequence, in fact, signal losses induced by the relatively short T_2^* of the lung tissue are minimized, thanks to signal refocusing. Furthermore, because the images are acquired in a single-shot, the HASTE sequence presents a relatively low sensitivity to physiological motion and allows the acquisition of multiple images in one breath-hold. For all in-vivo experiments, the slice-selective technique was used with a relatively large slice thickness of 15 mm and in-plane resolution of approximately 4 mm in order to obtain acceptable SNR for the quantification. In addition to this, cardiac synchronization based on ECG triggering was used to acquire the images at the desired cardiac phase and thus to reduce the influence of cardiac motion and blood flow on the quantification.
All proposed techniques are based on existing methodologies. However, substantial novelties were introduced to make them suitable for in-vivo application in the lung. In this regard, a key role for all techniques is played by the internal magnetic field inhomogeneities that characterize the lung tissue as well as by the corresponding magnetic field gradients. These originate from the difference between the magnetic susceptibilities of lung tissue and air in the alveoli. Usually, the internal magnetic field inhomogeneities and the corresponding gradients are regarded as a drawback for lung imaging, as they represent the origin of the short transverse relaxation times T_2 and T_2^*. In this work, however, their presence is exploited as a source of information, which turns an actual drawback into an advantage, as it is further described below.

Blood Volume Fraction

In Chapter 4 the possibility of quantifying the blood volume fraction of the human lung in-vivo by using the Intra-Voxel Incoherent Motion (IVIM) approach proposed by Le Bihan et al. in 1986 [60] was investigated. The blood volume fraction is defined as the ratio between intravascular lung water and total lung water. Therefore, it can be regarded as a perfusion parameter that reflects the water balance between the intra- and the extravascular compartments. Consequently, the blood volume fraction is not only capable of indicating perfusion defects that might be induced by pulmonary vascular diseases such as embolism, but it also permits to detect the accumulation of fluids and tissues in the extravascular compartment. Such phenomena can be induced by edema, Acute Lung Injury (ALI) and interstitial lung disease [2].
In comparison to other perfusion imaging techniques, the IVIM approach is particularly

interesting because it does not require the use of contrast agents. This is beneficial for applications on patients with kidney dysfunction. Furthermore, the invasivity of the investigation is reduced. The basic principle behind IVIM is that blood microcirculation in the capillaries mimics a diffusion process because of the incoherent spatial orientation of the capillary segments. Therefore, the conventional IVIM approach makes use of Diffusion Weighted Imaging (DWI) in order to obtain multiple images in which the signal contribution of flowing blood is progressively attenuated. The blood volume fraction is then calculated on a voxel-by-voxel basis from the signal amplitude difference between the acquired images. The application of this approach in the lung is particularly challenging due to the following factors: 1) the long echo times (TE) which are required by the use of diffusion sensitizing gradients and 2) the high sensitivity of DWI to motion. Both of these effects can lead to signal losses in the lung which could compromise the quantification due to the relatively short T_2 of the lung tissue and to the presence of physiological motion. An additional drawback of conventional IVIM is represented by the violation of the Carr-Purcell-Meiboom-Gill (CPMG) conditions [68, 69]. Such violations can be induced by motion when using DWI in combination with Turbo Spin-Echo (TSE) based sequences such as the HASTE. This effect is particularly relevant for lung imaging because the use of other approaches to perform DWI, such as Echo-Planar Imaging (EPI), is not suitable due to the relatively short T_2^* of the lung tissue [29]. In order to obtain artifact-free images, special countermeasures (or non-CPMG approaches) are required when using the HASTE sequence for DWI. This could degrade the image quality under other aspects, such as SNR and resolution [165, 170, 171].

In this work, it was shown how the presence of internal magnetic field gradients in the lung can be exploited to eliminate the need for external diffusion sensitizing gradients with the IVIM approach. This reduced the required TE as well as the sensitivity to motion and allowed to overcome the need for non-CPMG approaches. To this end, a HASTE sequence with STimulated Echo Acquisition Mode (STEAM) [96, 97] preparation and ECG-synchronization was developed and used for image acquisition. Two images with different values of the middle time (TM) delay in the STEAM preparation were acquired at different cardiac phases in a single breath-hold of approximately 10 s duration. One image (reference image) was acquired in the diastolic cardiac phase with a relatively short TM of 2 ms; the other image (blood-suppressed image) was acquired in the systolic phase with a longer TM of 40 ms. The blood volume fraction was quantified from the acquired images on a voxel-by-voxel basis using a two compartmental signal decay model, as given by the IVIM theory.

In-vivo experiments were performed on eight healthy volunteers, in order to evaluate the ability of the proposed technique to quantify the blood volume fraction as well as to investigate its reproducibility. To this end, the results obtained using the STEAM-prepared HASTE sequence were compared with those obtained from conventional IVIM as well as with previous reports. For the comparison with conventional IVIM, a non-CPMG HASTE sequence, as proposed by Le Roux in 2002 [165], was developed and used for image acquisition. For the reproducibility study, the acquisition was repeated for a total of ten

consecutive measurements in all volunteers. The resulting Coefficient of Variation (CoV) was calculated and used as a measure of reproducibility. Furthermore, a first application of the proposed technique on five patients with lung cancer was performed.
The results showed Mean Values (MV) of the blood volume fraction within the lung parenchyma between 27% and 41% in all volunteers. This is in accordance with previous reports (33% obtained by Lehmann et al. [186] using a contrast-enhanced technique) as well as with conventional IVIM (values between 32% and 40% obtained in this work). The CoV obtained from the repeatability study was below 0.03 for all volunteers, which indicated a relatively good reproducibility. In most cases, the results obtained in patients with lung tumors showed a decrease of the blood volume fraction in regions of the lung parenchyma which are close to the tumor, revealing an increase of extravascular lung water. Due to the reduced strength of the internal magnetic field gradients in tissues with higher proton density, the tumor itself could not be evaluated.
In conclusion, the presented technique offers a fast and reproducible way to quantify the blood volume fraction of the human lung parenchyma in-vivo without the use of contrast agents. The presence of internal gradients in the lung parenchyma was exploited to eliminate the need for strong diffusion sensitizing gradients which are typically required by the IVIM approach. This allowed 1) to shorten TE, 2) to diminish motion sensitivity and 3) to avoid the need for non-CPMG approaches in the HASTE sequence. With the proposed technique, image acquisition can be accomplished in a single breath-hold of approximately 10 s duration. Because the presence of relatively strong internal magnetic field gradients is required, the proposed technique is suitable for investigations of the lung parenchyma only. This is not the case for tissues with higher proton density, such as lung tumors and nodules.

Transverse Relaxation Enhancement and Alveolar Size

In Chapter 5 a novel imaging technique was presented, which allows to quantify the transverse relaxation time $T_{2,\mathsf{diff}}$ in a single breath-hold. This parameter is associated with the diffusion of water molecules through the internal magnetic field gradients of the lung. The amplitude of the internal gradients is related to the alveolar size [64] because the magnetic field inhomogeneities from which they originate present spatial modulations on the length scale of the alveolar diameter. Considering this, the possibility of exploiting the knowledge of $T_{2,\mathsf{diff}}$ for the quantification of the alveolar size was investigated. The alveolar size, in fact, is a parameter of paramount importance in the lung, as it could help to develop a better understanding about the alveolar dynamics during respiration. This still represents an open issue in the field of lung research [216, 217, 218, 219, 220, 221]. Another possible application of alveolar size imaging is the non-invasive detection of microstructural injuries that could be induced by several lung diseases such as emphysema, Chronic Obstructive Lung Disease (COPD) and Acute Lung Injury (ALI) as well as by mechanical ventilation. These microstructural injuries, in fact, are very difficult to identify in-vivo [137, 213, 214].

In this regard, one possibility is offered by the application of DWI in combination with hyperpolarized gas MRI [55, 135, 136, 212, 222, 223]. However, this technique has not expanded to the clinical field yet, as it requires the use of dedicated hardware and complex workflows.

In the past, it was observed that the T_2 of the lung tissue strongly depends on the time distance between two consecutive refocusing pulses (inter-pulse time) in TSE-based sequences [70]. This indicated that diffusion of water molecules through the internal gradients of the lung has a relevant contribution in the transverse relaxation mechanism. The relaxation time $T_{2,\mathsf{diff}}$, which is associated with this phenomenon, depends on several parameters including [64, 65, 152]: 1) the fractional amount of air in the lung (i.e. the lung inflation level), 2) the amplitude of the internal magnetic field gradients, which changes with the alveolar size, and 3) the diffusion coefficient of water molecules in the lung tissue. In order to obtain the alveolar size from $T_{2,\mathsf{diff}}$, the empirical mathematical model proposed by Yung in 2003 [152] was used. This defines the relationship between $T_{2,\mathsf{diff}}$ and the mean radius of a system of densely packed spheres, which have a different magnetic susceptibility with respect to the surrounding environment where the water molecules diffuse. Such a model is commonly used to represent the lung tissue [30, 67].

Quantification of $T_{2,\mathsf{diff}}$ of the lung is very challenging in-vivo, as it normally requires multiple quantifications of the relaxation time T_2 with different values of the inter-pulse time in a multi-echo CPMG sequence [65]. This approach is highly time consuming and sensitive to motion. Alternatively, a single quantification of T_2 by means of a conventional spin-echo (or Hahn-echo) pulse sequence would be sufficient. Thereby, a-priori knowledge of the native component $T_{2,0}$ of the transverse relaxation time, which is exclusively to ascribe to spin-spin interactions, is required [151]. This is usually not the case in-vivo.

The technique proposed in this work allows to quantify $T_{2,\mathsf{diff}}$ in a single breath-hold without the need for a-priori knowledge of $T_{2,0}$. For this purpose, a HASTE sequence with Hahn-echo preparation was implemented and used for image acquisition. Quantification of $T_{2,\mathsf{diff}}$ was performed by acquiring two (or more) images with identical TE, though with a different number of refocusing pulses between excitation and signal acquisition. This was achieved by properly changing the timing of the Hahn-echo preparation in each image acquisition, together with the number of refocusing pulses in the HASTE scan which were applied as dummy pulses before actual data acquisition. $T_{2,\mathsf{diff}}$ was quantified on a voxel-by-voxel basis from the signal attenuation in the different acquisitions.

In a first step, phantom experiments were performed as a prove-of-principle, in order to evaluate the ability of the proposed technique to discriminate signals with different $T_{2,\mathsf{diff}}$ as well as to verify the dependence of $T_{2,\mathsf{diff}}$ on the sphere diameter. To this end, six samples containing a mixture of water and glass microspheres of different nominal diameters were used. The results of this study were also compared with those obtained from the conventional Hahn-echo experiment. In a second step, in-vivo experiments were performed to investigate the dependence of $T_{2,\mathsf{diff}}$ on both lung inflation and perfusion. For this, data were acquired in eight healthy volunteers in different experimental conditions. These included 1) different breathing states: functional residual capacity (FRC) and total lung

capacity (TLC); and 2) different cardiac phases: systole and diastole. The reason behind the investigation of the influence of perfusion is that the diffusion coefficient which determines $T_{2,\mathrm{diff}}$ does not only depend on the diffusivity of water molecules in the parenchymal tissue of the lung but also on blood microcirculation in the alveolar capillaries, through the pseudo-diffusion coefficient D^* described by Le Bihan et al. [59].
The alveolar size was quantified by means of the mathematical model proposed by Yung [152] from the $T_{2,\mathrm{diff}}$ maps. In order to compensate the variations of the air volume in the lung with the level of inflation, which affects $T_{2,\mathrm{diff}}$, a proton density image was additionally acquired in the same breath-hold and used for a voxel-by-voxel correction. For this acquisition, the Ultrashort Echo Time (UTE) sequence was used. Other parameters that affect $T_{2,\mathrm{diff}}$ such as the diffusion coefficient and the susceptibility difference between lung tissue and air were assumed to be homogeneous throughout the lung. In order to reduce the influence of perfusion, the $T_{2,\mathrm{diff}}$ maps that were used for the calculation of the alveolar size were acquired in the diastolic cardiac phase.
The results of the phantom study showed an excellent discrimination between signal components which are characterized by different $T_{2,\mathrm{diff}}$. A monotonic increase of $T_{2,\mathrm{diff}}$ with the sphere diameter was obtained, in agreement with the results of the Hahn-echo experiment. In-vivo studies showed a rather homogeneous distribution of $T_{2,\mathrm{diff}}$ throughout the lung, with a slight dependence on inflation. In diastole, MVs throughout the lung parenchyma calculated over all volunteers were 29 ms at FRC and 24 ms at TLC. In systole, the MV at FRC was 14 ms, which indicates a strong dependence of $T_{2,\mathrm{diff}}$ on perfusion and in particular a shortening with larger blood velocities.
The quantification of the alveolar diameter provided similar values of approximately 200 μm in all volunteers, at both FRC and TLC. These values are very close to those reported in previous works by several investigators, which were obtained by using either hyperpolarized gas MRI in-vivo [135, 136] or light microscopy ex-vivo [137].
In conclusion, the technique presented in this work allows to quantify $T_{2,\mathrm{diff}}$ in a single breath-hold of approximately 10 s duration without the need for a-priori knowledge of $T_{2,0}$. Quantification of the alveolar size from $T_{2,\mathrm{diff}}$ is feasible by acquiring an extra proton density image in order to take into account the influence of inflation on $T_{2,\mathrm{diff}}$. However, because of the very strong dependence of $T_{2,\mathrm{diff}}$ on perfusion, additional corrections might be required in patients with lung diseases in order to compensate for possible perfusion inhomogeneities throughout the lung. This would make the method more robust. The $T_{2,\mathrm{diff}}$ maps themselves could be used to detect mismatches between functional and microstructural parameters such as perfusion, inflation and alveolar size.

Spectral Line Broadening

In Chapter 6 a technique to quantify the broadening of the NMR spectral line (or spectral line broadening) of the lung in-vivo was presented. The parenchymal tissue of the lung presents a relatively broad NMR peak in the frequency domain due to the presence

of strong internal magnetic field inhomogeneities, as already described. The spectral line broadening of the lung tissue represents an interesting parameter as it can provide information about important lung properties. In fact, the line broadening itself represents a quantitative fingerprint for lung inflation [67, 120]; apart from that, it can be used in combination with oxygen enhancement to obtain information about lung ventilation [43]. Considering these peculiarities, the quantification of the spectral line broadening could help to detect several pathological conditions of the lung such as: tissue accumulation in the alveolar and interstitial spaces, tissue destruction due to emphysema, air trapping or ventilation defects induced by obstructive lung diseases.
The use of the Asymmetric Spin-Echo (ASE) was proposed in the past for quantifying the spectral line broadening of the lung [71]. However, this technique is not suitable for in-vivo investigations because of the relatively long acquisition times and of the consequent sensitivity to physiological motion which might corrupt the quantification. The technique proposed in this work integrates the ASE approach with the HASTE sequence, in order to reduce the acquisition times and to allow the quantification of the spectral line broadening of the lung in-vivo. With this technique, violations of the CPMG conditions deriving from spatial inhomogeneities of the static magnetic field may occur, thus generating image artifacts. In this dissertation it was shown how to overcome these violations by means of RF-phase cycling [166] and GRAPPA reconstruction [26].
Imaging experiments were performed on fourteen healthy volunteers in order to investigate the dependence of the spectral line broadening on several factors, namely: 1) lung inflation, 2) gravitation and 3) oxygen concentration in the breathing gas. To this end, data were acquired in different experimental conditions. These included 1) different breathing states: FRC and TLC; 2) different volunteer positions: supine and prone; and 3) different breathing gases: room-air and pure-oxygen. Furthermore, the reproducibility of the technique was analyzed by repeating the acquisition for a total of ten consecutive measurements in six of the volunteers. The resulting CoV was used as a measure of reproducibility. The spectral line broadening was quantified on a voxel-by-voxel basis from two images acquired with different settings of the asymmetry time in the ASE preparation. The image acquisition was accomplished within a single breath-hold of approximately 15 s duration.
The results showed a significant increase of the spectral line broadening with both lung inflation and oxygen concentration. Values of the spectral line broadening obtained within the lung parenchyma at different breathing states (1.48 ± 0.29 ppm at FRC and 1.95 ± 0.43 ppm at TLC) are in agreement with those obtained in previous reports using either numerical calculations [67] or ex-vivo measurements [120]. The CoV obtained from the repeatability study was below 0.03 for all volunteers, which indicated a relatively good reproducibility. With oxygen-enhancement, a mean relative increase of the line broadening of approximately 14 % was observed.
The study of the gravitational effect showed a decrease of the line broadening towards the bottom of the lung at FRC, with the patient lying in both the supine and the prone positions. The gradient of the line broadening in the direction of gravitation was approximately 2.56 %/cm in the supine position and 1.88 %/cm in the prone position. The influence of

gravitation on the line broadening was strongly reduced at TLC, with gradients of the order of 0.5 %/cm or smaller.
In conclusion, the technique proposed here allows to quantify the spectral line broadening of the human lung in-vivo in a single breath-hold of approximately 15 s duration. The technique could be useful for the detection of morphological and functional abnormalities such as lung tissue destruction, accumulation of fluids or tissue in the lung and ventilation defects.

Future Perspectives

Currently, clinical application of quantitative MRI is still very limited. This applies even to body regions that are more suitable for MRI than the lung. Depending on the specific application, in fact, quantitative MRI could be prone to the influence of several factors that might corrupt the quantification. Apart from that, quantitative MRI usually requires longer acquisition times and is more sensitive to motion in comparison to conventional MRI. Due to low SNR and physiological motion, the application of quantitative MRI is even more challenging in a body region such as the lung. The techniques proposed in this work represent a further step towards potential clinical applications of quantitative MRI methodologies in the lung compared to the state of the art. In fact, for all proposed techniques, image acquisition can be accomplished in a single breath-hold of maximum duration of 15 s and with a relatively low sensitivity to motion. This could make the presented techniques suitable for the usage in the clinical routine as well as for clinical studies on patients with lung diseases. Furthermore, all techniques are also compatible with respiratory triggering techniques such as the Prospective Acquisition CorrEction (PACE) [116]. This may be beneficial for applications on critical patients who cannot hold the breath for more than a few seconds.
In this work, most experiments were performed on healthy volunteers. With this, a quantitative characterization of the healthy lung tissue is provided in terms of the parameters described above. Further investigations with the proposed techniques might regard the application on patients with lung diseases in order to characterize the pathological lung tissue and to evaluate the quality of diagnostic information that the mentioned parameters can provide to the clinicians. Considering this, the results obtained in this work can serve as a reference for the comparison between healthy and pathological lung tissue.
A further interesting aspect to investigate might be the influence of the magnetic field strength on the image quality, with all proposed techniques. In this work, a field strength of 1.5 T was used for all experiments with volunteers. In general, a better SNR can be expected with the use of higher magnetic field strengths thanks to the increase of signal amplitude. However, the use of higher magnetic field strengths also corresponds to a shortening of the transverse relaxation times T_2 and T_2^* in the lung, because of the stronger internal field inhomogeneities. This might have a negative impact on the image resolution. Nevertheless, all techniques presented in this work exploit the presence of internal mag-

netic field inhomogeneities in the lung as a source of information. For this reason, the use of higher field strengths might be beneficial for all proposed techniques.

Zusammenfassung

Die Magnetresonanztomographie (MRT) stellt ein einzigartiges Verfahren im Bereich der diagnostischen Bildgebung dar, da sie es ermöglicht, eine Vielzahl an diagnostischen Informationen ohne die Verwendung von ionisierenden Strahlen zu erhalten. Die Anwendung von MRT in der Lunge erlaubt es, räumlich aufgelöste Bildinformationen über Morphologie, Funktionalität sowie über die Mikrostruktur des Lungengewebes zu erhalten und diese miteinander zu kombinieren. Für die Diagnose und Charakterisierung von Lungenkrankheiten sind diese Informationen von höchstem Interesse. Die Lungenbildgebung stellt jedoch einen herausfordernden Bereich der MRT dar. Dies liegt in der niedrigen Protondichte des Lungenparenchyms begründet sowie in den relativ kurzen Transversal-Relaxationszeiten T_2 und T_2^*, die sowohl die Bildauflösung als auch das Signal-zu-Rausch Verhältnis beeinträchtigen. Des Weiteren benötigen die vielfältigen Ursachen von physiologischer Bewegung, welche die Atmung, den Herzschlag und den Blutfluss in den Lungengefäßen umfassen, die Anwendung von schnellen sowie relativ bewegungsunempfindlichen Aufnahmeverfahren, um Risiken von Bildartefakten zu verringern. Aus diesen Gründen werden Computertomographie (CT) und Nuklearmedizin nach wie vor als Goldstandardverfahren gehandhabt, um räumlich aufgelöste Bildinformationen sowohl über die Morphologie als auch die Funktionalität der Lunge zu erhalten. Dennoch stellt die Lungen-MRT aufgrund ihrer Flexibilität sowohl eine vielversprechende Alternative zu den anderen Bildgebungsverfahren als auch eine mögliche Quelle zusätzlicher diagnostischer Informationen dar.

In den letzten Jahren wurde eine Vielzahl von relevanten technischen Entwicklungen im Bereich der Lungen-MRT vorgeschlagen. Diese zielten darauf ab, die Bildqualität zu verbessern, die Aufnahmezeiten zu verkürzen sowie die bereitgestellte diagnostische Information zu erweitern. So gewähren beispielsweise Techniken wie sauerstoffgestützte MRT [43], Fourier-Decomposition [46], Arterial Spin Labeling (ASL) [48] und hyperpolarisiertes-Gas MRT [53] Zugang zu räumlich aufgelöstem Wissen über Lungenperfusion, Ventilation, Gasaustausch und mikrostrukturelle Eigenschaften des Lungengewebes, zusammen mit einer minimalen Untersuchungsinvasivität und einer klinisch geeigneten Bildqualität. Dies führte zu einem Anstieg von potentiellen klinischen Anwendungen von Lungen-MRT sowie zu einer bemerkenswerten Annäherung dieses Verfahrens an die klinischen Bedürfnisse.

Ziel dieser Arbeit war es, einen wissenschaftlichen Beitrag zu der Erweiterung von Proton-MRT basierten Lungenbildgebungsmethoden mithilfe der Entwicklung einer Reihe von

Bildaufnahmetechniken zu leisten. Diese zielten darauf ab, die Quantifizierung von funktionellen und mikrostrukturellen Parametern des Lungengewebes zu ermitteln. Darüberhinaus liefert diese Arbeit einen zusätzlichen Beitrag zur Erkenntnis über einige Eigenschaften des Lungengewebes, die mithilfe von in-vivo Anwendungen der entwickelten Techniken in der menschlichen Lunge erhalten werden konnten. Der Hauptteil dieser Doktorarbeit ist in drei größere Bereiche aufgeteilt (Kapitel 4 bis 6), wobei jeder einzelne unterschiedliche Parameter behandelt. Diese sind: 1) der Blutvolumenanteil, 2) die Transversale Relaxationsverstärkung, die von der Diffusion durch die internen Magnetfeldgradienten der Lunge verursacht worden sind, und 3) die Spektrallinienverbreiterung. Diese Parameter stehen mit Lungeneigenschaften von höchstem diagnostischem Interesse in Verbindung, wie etwa Perfusion, Alveolengröße, Lungeninflation und Ventilation.
Jede Technik wurde eigens gestaltet, um die Datenakquisition innerhalb eines einzigen Atemzugs von einer maximalen Länge von 15 Sekunden zu ermöglichen. Alle dargestellten Methoden verwenden die Half-Fourier Acquisition Single-shot Turbo spin-Echo (HASTE) Pulssequenz [33, 34] in verschiedenen Varianten zur Bilderstellung. Durch die HASTE-Sequenz wurden Signalverluste, die durch das relativ kurze T_2^* des Lungengewebes hervorgerufen wurden, aufgrund der Signalrefokusierung minimiert. Des Weiteren ist die HASTE-Sequenz relativ unempfindlich in Bezug auf physiologische Bewegung und erlaubt es, mehrere Bilder innerhalb eines einzigen Atemzugs aufzunehmen. Für alle in-vivo Experimente wurde die Schicht-selektive Technik mit einer relativ großen Schichtdicke von 15 mm und einer *in-plane* Auflösung von ca. 4 mm angewandt, um eine akzeptable SNR für die Quantifizierung zu erhalten. In Ergänzung dazu wurde eine Herzsynchronisation mithilfe der EKG-Triggerung angewendet. Diese diente dazu, Bilder in der erwünschten Herzphase zu erstellen und damit den Einfluss der Herzbewegung sowie des Blutflusses auf die Quantifizierung zu verringern.
Alle hier vorgeschlagenen Techniken beruhen auf bereits bestehenden Methoden. Jedoch wurden hierbei erhebliche Neuerungen eingeführt, um sie für in-vivo Anwendungen in der Lunge geeigneter zu machen. In dieser Hinsicht spielen die internen Magnetfeldinhomogenitäten sowie die dazugehörigen Magnetfeldgradienten, die das Lungengewebe charakterisieren, für alle Techniken eine Schlüsselrolle. Diese Inhomogenitäten entstammen aus der Differenz zwischen den magnetischen Suszeptibilitäten des Lungengewebes und der Luft in den Alveolen. Gewöhnlich werden die internen Magnetfeldinhomogenitäten sowie die dazugehörigen Magnetfeldgradienten als Hindernis für die Lungenbildgebung betrachtet, da sie die kurzen Transversal-Relaxationszeiten T_2 und T_2^* verursachen. Jedoch wird ihr Vorhandensein in dieser Arbeit als eine Informationsquelle genutzt, die den eigentlichen Nachteil in einen Vorteil umwandelt, wie es im weiteren Verlauf beschrieben wird.

Blutvolumenanteil

In Kapitel 4 wurde die Möglichkeit untersucht, den Blutvolumenanteil der menschlichen Lunge in-vivo mittels der Methode der Intra-Voxel Incoherent Motion (IVIM) zu quan-

tifizieren, die 1986 von Le Bihan et al. [60] vorgeschlagen wurde. Der Blutvolumenanteil ist als das Verhältnis zwischen dem intravaskulären Lungenwasser und dem gesamten Lungenwasser definiert. Daher kann er als Perfusionsparameter betrachtet werden, der die Wasserbilanz zwischen intra- und extravaskulären Kompartimenten aufzeigt. Folglich ist der Blutvolumenanteil nicht nur fähig, Perfusionsdefekte anzuzeigen, die durch pulmonale Gefäßkrankheiten wie etwa Embolie, ausgelöst sein könnten, sondern auch die Ansammlung von Flüssigkeiten und Geweben im extravaskulären Kompartiment festzustellen. Solche Phänomene können etwa durch Ödeme, akute Lungenverletzung (ALI) sowie durch interstitielle Lungenkrankheiten hervorgerufen werden [2].
Im Vergleich zu anderen Perfusionsbildgebungstechniken ist der IVIM Ansatz von besonderem Interesse, da er keine Gabe von Kontrastmitteln erfordert. Dies ist für Anwendungen an Patienten mit Nierenfunktionsstörungen besonders geeignet. Des Weiteren wird die Invasivität der Untersuchung reduziert. Dem IVIM liegt das Prinzip zugrunde, dass die Blutmikrozirkulation in den Kapillaren einen Diffusionsprozess nachahmt, aufgrund der inkohärenten Raumorientierung der Kapillarensegmente. Daher wendet der konventionelle IVIM Ansatz die Diffusionswichtungsbildgebung (DWI) an, um mehrfache Bilder zu erhalten, in denen der Signalbeitrag des fließenden Blutes schrittweise abgeschwächt wird. Der Blutvolumenanteil wird dann auf einer *voxel-by-voxel* Basis aus der Differenz der Signalamplitude in den aufgenommenen Bildern errechnet. Die Anwendung dieser Vorgehensweise in der Lunge ist aufgrund der folgenden Faktoren besonders auspruchsvoll: 1) der langen Echozeiten, die durch den Gebrauch von diffusionsempfindlichen Gradienten benötigt werden, sowie 2) der hohen Bewegungsempfindlichkeit von DWI. Diese beiden Effekte können zu Signalauslöschungen in der Lunge führen, welche die Quantifizierung aufgrund des relativ kurzen T_2 des Lungengewebes und des Auftretens von physiologischer Bewegung beeinträchtigen könnten. Einen zusätzlichen Nachteil der herkömmlichen IVIM Methode stellt die Verletzung der Carr-Purcell-Meiboom-Gill (CPMG) Bedingungen [68, 69] dar. Solche Verletzungen können durch Bewegung induziert werden, wenn die DWI in Verbindung mit Turbo-Spin-Echo (TSE) basierten Sequenzen wie HASTE angewandt wird. Dieser Effekt ist besonders relevant für die Lungenbildgebung, da der Gebrauch von anderen Ansätzen zur Durchführung von DWI, wie etwa die Echo-Planar Bildgebung (EPI), wegen des relativ kurzen T_2^* des Lungengewebes [29] nicht geeignet ist. Um Artefakt-freie Bilder zu erhalten, werden spezielle Gegenmaßnahmen (oder non-CPMG Methoden) benötigt, wenn die HASTE-Sequenz für DWI benutzt wird. Dies könnte eine negative Auswirkung auf die Bildqualität haben, wie auf das Signal-zu-Rausch Verhältnis und auf die Auflösung [165, 170, 171].
In dieser Arbeit wurde aufgezeigt, wie das Vorhandensein der internen Magnetfeldgradienten in der Lunge genutzt werden kann, um den Bedarf der IVIM Methode an externen diffusionsempfindlichen Gradienten zu beseitigen. Dies verringerte das benötigte TE sowie die Bewegungsempfindlichkeit und ermöglichte es, den Bedarf an non-CPMG Ansätzen zu überwinden. Zu diesem Zweck wurde eine HASTE-Sequenz mit STimulated Echo Acquisition Mode (STEAM) Präparation [96, 97] sowie mit EKG-Synchronisierung entwickelt und folglich für die Bildgebung angewandt. Zwei Bilder wurden mit unterschiedlichen

Werten der Zeitverzögerung (TM) in der STEAM-Präparation in einem einzigen Atemzug von ca. 10 Sekunden bei verschiedenen Herzphasen aufgenommen. Ein Bild, das Referenzbild, wurde in der diastolischen Herzphase mit einem relativ kurzen TM von 2 ms aufgenommen; das andere Bild, das blutunterdrückte Bild, wurde in der systolischen Phase mit einem längerem TM von 40 ms aufgenommen. Der Blutvolumenanteil wurde von den akquirierten Bildern auf einer *voxel-by-voxel* Basis mithilfe eines zwei-Kompartimente-Signalzerfallmodells, gemäß der IVIM Theorie, quantifiziert.
Die in-vivo Experimente wurden an acht gesunden Probanden durchgeführt, um die Fähigkeit dieser Methode in der Quantifizierung des Blutvolumenanteils sowie dessen Reproduzierbarkeit zu untersuchen. Zu diesem Zweck wurden die Ergebnisse, die durch die STEAM-präparierte HASTE-Sequenz erlangt wurden, mit denen verglichen, die mithilfe der konventionellen IVIM Methode sowie mit vorangehenden Studien erstellt wurden. Für den Vergleich mit dem herkömmlichen IVIM Ansatz wurde eine non-CPMG HASTE-Sequenz, wie sie von Le Roux 2002 [165] vorgeschlagen wurde, entwickelt und für die Bildgebungsanwendung angewandt. Für die Reproduzierbarkeitsstudie wurde die Bildakquisition in insgesamt zehn aufeinanderfolgenden Messungen bei allen Probanden wiederholt. Der daraus resultierende Variationskoeffizient (CoV) wurde berechnet und als ein Maß zur Reproduzierbarkeit verwendet. Darüber hinaus wurde eine erste Anwendung der vorgeschlagenen Technik an fünf Lungenkrebspatienten durchgeführt.
Die Ergebnisse zeigten bei allen Probanden Durchschnittswerte (MV) des Blutvolumenanteils innerhalb des Lungenparenchyms zwischen 27% und 41%. Dies stimmt mit früheren Studien überein. So wurden 33% bei Lehmann et al. [186] durch den Gebrauch der Kontrastmitteltechnik erhalten. Außerdem wurden in dieser Arbeit mittels der konventionellen IVIM Methode Werte zwischen 32% und 40% ermittelt. Der durch die Reproduzierbarkeitsstudie erhaltene CoV war bei allen Probanden unter 0.03; dieser deutet auf eine relativ gute Reproduzierbarkeit hin. Die Ergebnisse, die anhand von Patienten mit Lungenkrebs ermittelt wurden, zeigten in den meisten Fällen eine Verringerung des Blutvolumenanteils in den Bereichen des Lungenparenchyms nahe des Tumors, wobei sich ein Anstieg des extravaskulären Lungenwassers feststellen ließ. Aufgrund der reduzierten Stärke der internen Magnetfeldgradienten, die in den Geweben mit einer höheren Protondichte vorhanden sind, konnte der Tumor nicht bestimmt werden.
Zusammenfassend bietet die dargestellte Technik eine schnelle und reproduzierbare Möglichkeit, den Blutvolumenanteil des menschlichen Lungenparenchyms in-vivo ohne die Anwendung von Kontrastmittelagenten zu quantifizieren. Das Auftreten von internen Gradienten im Lungenparenchym wurde genutzt, um den Gebrauch von starken diffusionsempfindlichen Gradienten auszuschließen, die bei der Anwendung der IVIM Methode gewöhnlich verwendet werden. Dieses Verfahren ermöglichte die Verkürzung von TE und führte zu einer Verringerung der Bewegungsempfindlichkeit sowie zu einer Vermeidung des Bedarfs für non-GPMG Anwendungen in der HASTE-Sequenz. Mit der dargestellten Technik kann die Bilderstellung innerhalb eines einzigen Atemzugs von ca. 10 Sekunden Dauer ausgeführt werden. Da die Anwesenheit von relativ starken internen Magnetfeldgradienten benötigt wird, ist die vorgestellte Methodik nur für Untersuchungen des Lungenparenchyms

geeignet. Dies ist bei Geweben mit einer höheren Protondichte, wie Lungentumoren und Knoten, nicht der Fall.

Transversale Relaxationsverstärkung und Alveolengröße

In Kapitel 5 wurde eine neuartige Bildgebungstechnik vorgestellt, die es ermöglicht, die transversale Relaxationszeit $T_{2,\mathsf{diff}}$ innerhalb eines einzigen Atemzugs zu quantifizieren. Dieser Parameter ist mit der Diffusion der Wassermoleküle durch die internen Magnetfeldgradienten der Lunge verbunden. Die Amplitude der internen Gradienten bezieht sich auf die Alveolengröße [64], da die Magnetfeldinhomogenitäten, denen sie entstammen, räumliche Modulationen auf der Längenskala der alveolaren Durchmesser aufzeigen.
In Anbetracht dieser Tatsache wurde die Möglichkeit untersucht, die Kenntnis von $T_{2,\mathsf{diff}}$ für die Quantifizierung der Alveolengröße zu nutzen. Die Alveolengröße ist tatsächlich ein Lungenparameter von höchster Wichtigkeit, da er helfen könnte, ein besseres Verständnis für die alveolaren Dynamiken während der Atmung zu entwickeln. Im Bereich der Lungenforschung werfen diese nach wie vor ungeklärte Fragen auf [216, 217, 218, 219, 220, 221]. Eine weitere mögliche Anwendung der Quantifizierung der Alveolengröße ist die nicht-invasive Feststellung von mikrostrukturellen Verletzungen, die durch verschiedene Lungenkrankheiten wie Emphysem, chronisch-obstruktiver Lungenerkrankung (COPD), akute Lungenverletzung (ALI) sowie durch die mechanische Ventilation verursacht worden sein können. Diese mikrostrukturellen Verletzungen sind in-vivo in der Tat schwierig festzustellen [137, 213, 214]. In diesem Zusammenhang ist eine Möglichkeit mittels der Anwendung von DWI in Verbindung mit hyperpolarisiertem-Gas MRT gegeben [55, 135, 136, 212, 222, 223]. Diese Technik hat sich bisher jedoch noch nicht im klinischen Bereich durchgesetzt, da sie die Verwendung von dedizierter Hardware sowie von komplexen Arbeitsabläufen erfordert.
In der Vergangenheit wurde beobachtet, dass die Relaxationszeit T_2 des Lungengewebes stark vom Zeitabstand zwischen zwei aufeinanderfolgenden Refokusierungspulsen in TSE-basierten Sequenzen abhängt [70]. Dies deutet darauf hin, dass die Diffusion der Wassermoleküle durch die internen Gradienten der Lungen zum transversalen Relaxationsmechanismus beiträgt. Die Relaxationszeit $T_{2,\mathsf{diff}}$, die mit diesem Phänomen in Verbindung steht, hängt von verschiedenen Parametern ab. Diese sind [64, 65, 152]: 1) Der Mengenanteil von Luftvolumen in der Lunge (d.h. der Lungeninflationslevel), 2) die Amplitude der internen Magnetfeldgradienten in der Lunge, die mit der Alveolengröße variiert, sowie 3) der Diffusionskoeffizient von Wassermolekülen im Lungengewebe. Um die Alveolengröße von $T_{2,\mathsf{diff}}$ zu erhalten, wurde das empirische mathematische Modell von Yung von 2003 [152] angewandt. Dieses definiert die Beziehung zwischen $T_{2,\mathsf{diff}}$ und dem durchschnittlichen Radius eines Systems von dicht gepackten Kugeln, welche eine unterschiedliche magnetische Suszeptibilität im Bezug auf die Umgebung besitzen, in der die Wassermoleküle diffundieren. Ein solches Modell wird gewöhnlich zur Darstellung des Lungengewebes angewandt [30, 67].

Die Quantifizierung von $T_{2,\text{diff}}$ der Lunge in-vivo ist besonders herausfordernd, da normalerweise mehrere Quantifizierungen der Relaxationszeit T_2 mit der Anwendung von verschiedenen Werten des Zeitabstandes zwischen den Refokusierungspulsen einer Multi-Echo CPMG-Sequenz nötig sind [65]. Diese Methode ist sehr zeitaufwendig und bewegungsempfindlich. Ersatzweise würde eine einzige T_2 Quantifizierung mithilfe einer herkömmlichen Spin-Echo (oder Hahn-Echo) Pulssequenz ausreichen. Dadurch wird jedoch die a-priori Kenntnis der nativen Komponente $T_{2,0}$ der transversalen Relaxationszeit, die auf die Spin-Spin Interaktionen zurückzuführen ist, benötigt [151], was in-vivo gewöhnlich nicht der Fall ist.
Die Technik, die in dieser Arbeit vorgeschlagen wurde, ermöglicht es, $T_{2,\text{diff}}$ in einem einzigen Atemzug und ohne die a-priori Kenntnis von $T_{2,0}$ zu quantifizieren. Zu diesem Zweck wurde eine HASTE-Sequenz mit Hahn-Echo Präparation implementiert und für die Bildgebung verwendet. Die Quantifizierung von $T_{2,\text{diff}}$ wurde durch die Aufnahme von zwei oder mehreren Bildern mit identischem TE durchgeführt, jedoch mit einer unterschiedlichen Anzahl von Refokusierungspulsen zwischen Anregung und Signalakquisition. Dies wurde durch eine dedizierte Anpassung der Zeiteinstellungen der Hahn-Echo Präparation in jeder Bildaufnahme erreicht, zusammen mit der Änderung der Anzahl der Refokusierungspulse im HASTE-Scan, die als Dummy-Pulse vor der eigentlichen Datenakquisition benutzt wurden. $T_{2,\text{diff}}$ wurde auf einer *voxel-by-voxel* Basis von dem Signalzerfall in den verschiedenen aufgenommenen Bilder quantifiziert.
In einem ersten Schritt wurden Phantomexperimente als ein proof-of-principle durchgeführt, um die Fähigkeit der vorgestellten Technik festzustellen, Signale mit verschiedenen $T_{2,\text{diff}}$ zu unterscheiden, sowie, um die Abhängigkeit des $T_{2,\text{diff}}$ vom Kugeldurchmesser zu überprüfen. Zu diesem Zweck wurden sechs Proben verwendet, die eine Mischung aus Wasser und Glas-Mikrosphären mit unterschiedlichen nominalen Durchmessern enthielten. Die Ergebnisse dieser Untersuchung wurden mit denen verglichen, die mithilfe des herkömmlichen Hahn-Echo Experiments erlangt wurden. In einem zweiten Schritt wurden in-vivo Versuche ausgeführt, um die Abhängigkeit des $T_{2,\text{diff}}$ sowohl von der Lungeninflation als auch von der Perfusion zu untersuchen. Um dies zu erreichen, wurden Daten von acht gesunden Probanden in unterschiedlichen Versuchsbedingungen erfasst. Diese beinhalteten 1) verschiedene Atemphasen: funktionelle Residualvolumen (FRC) und totale Lungenkapazität (TLC); sowie 2) verschiedene Herzphasen: Systole und Diastole. Der Grund, der die Untersuchung des Einflusses der Perfusion hervorrief, liegt darin, dass der Diffusionskoeffizient, der $T_{2,\text{diff}}$ bestimmt, nicht nur von der Beweglichkeit der Wassermoleküle im Lungenparenchymgewebe abhängt, sondern auch von der Blutzirkulation in den alveolaren Kapillaren. Dies ist auf den Pseudodiffusionskoeffizienten D^* zurückzuführen, der von Le Bihan et al. [59] beschrieben wurde.
Die Alveolengröße wurde mittels des mathematischen Modells von Yung [152] aus den $T_{2,\text{diff}}$ Karten quantifiziert. Um die Abweichungen des Luftvolumens in der Lunge mit dem Inflationslevel auszugleichen, die das $T_{2,\text{diff}}$ beeinflussen, wurde ein zusätzliches Bild der Protondichte in der selben Atemanhaltphase aufgenommen. Dies wurde für eine *voxel-by-voxel* Korrektur verwendet. Für diese Anwendung wurde die Ultrashort Echo Time

(UTE) Sequenz eingesetzt. Andere Parameter, die $T_{2,\text{diff}}$ beeinflussen, wie der Diffusionskoeffizient und die Suszeptibilitätsdifferenz zwischen dem Lungengewebe und der Luft, wurden als homogen in der ganzen Lunge angenommen. Um den Einfluss der Perfusion zu vermindern, wurden die $T_{2,\text{diff}}$ Karten, die für die Berechnung der Alveolengröße verwendet wurden, in der diastolischen Herzphase akquiriert.
Die Ergebnisse der Phantomstudie zeigten eine sehr gute Unterscheidung zwischen Signalkomponenten, die verschiedenen $T_{2,\text{diff}}$ hatten. $T_{2,\text{diff}}$ zeigte einen monotonen Anstieg mit dem Kugeldurchmesser auf. Dies stimmt mit dem Hahn-Echo Experiment überein. Die in-vivo Studien zeigten eine eher homogene Verteilung von $T_{2,\text{diff}}$ in der ganzen Lunge, mit einer leichten Abhängigkeit vom Inflationslevel. In der diastolischen Herzphase waren die Mittelwerte im ganzen Lungenparenchym, die bei allen Probanden berechnet wurden, 29 ms bei FRC und 24 ms bei TLC. In der systolischen Phase war der Mittelwert bei FRC bei 14 ms. Dies deutet auf eine starke Abhängigkeit des $T_{2,\text{diff}}$ von der Perfusion hin.
Die Quantifizierung des alveolaren Durchmessers ergab bei allen Probanden ähnliche Werte von ca. 200 μm, sowohl bei FRC als auch bei TLC. Diese sind sehr nah an den Ergebnissen, die in früheren Arbeiten von verschiedenen Forschern beschrieben wurden und die entweder durch den Gebrauch von hyperpolarisiertem-Gas MRT in-vivo [135, 136] oder mithilfe der Lichtmikroskopie ex-vivo [137] erhalten wurden.
Abschließend ermöglicht die in dieser Arbeit vorgestellte Technik die Quantifizierung von $T_{2,\text{diff}}$ in einem einzigen Atemzug von ca. 10 Sekunden Dauer ohne die Notwendigkeit einer a-priori Kenntnis von $T_{2,0}$. Die Quantifizierung der Alveolengröße von $T_{2,\text{diff}}$ ist durch die Aufnahme eines zusätzlichen Bildes der Protondichte durchführbar, um den Einfluss der Inflationslevel auf $T_{2,\text{diff}}$ zu berücksichtigen. Aufgrund der sehr starken Abhängigkeit des $T_{2,\text{diff}}$ von der Perfusion könnten jedoch zusätzliche Korrekturen bei Patienten mit Lungenkrankheiten benötigt werden, um eventuelle Perfusionsungleichheiten in der Lunge zu kompensieren. Dies würde die Methode robuster machen. Die $T_{2,\text{diff}}$ Karten selbst könnten angewendet werden, um mögliche Ungleichgewichte zwischen funktionellen und mikrostrukturellen Parametern wie Perfusion, Inflation und Alveolengröße aufzudecken.

Spektrallinienverbreiterung

Kapitel 6 stellte eine Technik vor, um die Verbreiterung der NMR Spektrallinie (oder Spektrallinienverbreiterung) der Lunge in-vivo zu quantifizieren. Aufgrund des bereits beschriebenen Vorhandenseins der starken internen Magnetfeldinhomogenitäten weist das Lungenparenchymgewebe eine relativ breite NMR Linie im Frequenzbereich auf. Die Spektrallinienverbreiterung des Lungengewebes ist ein interessanter Parameter, da er Informationen über wichtige Lungeneigenschaften geben kann. Tatsächlich stellt die Spektrallinienverbreiterung ein quantitatives Kennzeichnen für die Lungeninflation dar [67, 120]. Abgesehen davon kann es in Verbindung mit sauerstoffgestützten Messungen angewandt werden, um Informationen über die Lungenventilation zu erhalten [43]. Betrachtet man diese Eigenheiten, könnte die Quantifizierung der Spektrallinienverbreiterung helfen, ver-

schiedene pathologische Zustände der Lunge festzustellen, wie etwa: Gewebeansammlung in den alveolaren und interstitiellen Bereichen, Gewebszerstörung aufgrund von Emphysemen, Luft-einfangen (*air trapping*) oder Ventilationsdefekte, die durch obstruktive Lungenerkrankungen hervorgerufen werden.
Der Gebrauch des Asymmetrischen Spin-Echos (ASE) wurde in der Vergangenheit für die Quantifizierung der Spektrallinienverbreiterung der Lunge vorgeschlagen [71]. Diese Technik ist jedoch nicht für in-vivo Untersuchungen geeignet, da sie relativ lange Aufnahmezeiten erfordert, und die daraus folgende Empfindlichkeit gegenüber physiologischer Bewegung die Quantifizierung beeinflussen kann. Die in dieser Arbeit vorgestellte Methode integriert den ASE-Ansatz mit der HASTE-Sequenz, um die Aufnahmezeiten zu verringern und die Spektrallinienverbreiterung der Lunge in-vivo zu quantifizieren. Mit dieser Technik können Verletzungen der CPMG-Bedingungen auftreten, die den räumlichen Inhomogenitäten des statischen Magnetfeldes entstammen und die zur Generierung von Bildartefakten führen können. In dieser Arbeit wurde aufgezeigt, wie diese Verletzungen mithilfe eines Phasenzyklus der Hochfrequenz-Pulse [166] zusammen mit der GRAPPA-Rekonstruktion [26] überwunden werden können.
Bildgebungsexperimente wurden an vierzehn gesunden Probanden durchgeführt, um die Abhängigkeit der Spektrallinienverbreiterung auf die folgenden Faktoren hin zu untersuchen: 1) Lungeninflation, 2) Gravitation und 3) Sauerstoffkonzentration im eingeatmeten Gas. Zu diesem Zweck wurden Daten in verschiedenen Versuchsbedingungen erfasst. Diese umfassten 1) unterschiedliche Atemphasen: FRC und TLC; 2) verschiedene Liegepositionen der Probanden: Bauch- und Rückenlage; sowie 3) unterschiedliche eingeatmete Gase: Raumluft und reiner Sauerstoff. Des Weiteren wurde die Reproduzierbarkeit der Technik durch die Wiederholung der Datenakquisition für insgesamt zehn aufeinanderfolgende Messungen bei sechs Probanden analysiert. Die Spektrallinienverbreiterung wurde auf einer *voxel-by-voxel* Basis von zwei Bildern quantifiziert, die mit unterschiedlichen Einstellungen der Zeitasymmetrie in der ASE Präparation aufgenommen wurden. Die gesamte Bildakquisition wurde mit einem einzigen Atemzug von ca. 15 Sekunden vervollständigt.
Die Ergebnisse zeigten einen signifikanten Anstieg der Spektrallinienverbreiterung sowohl mit der Lungeninflation als auch mit der Sauerstoffkonzentration. Die Werte der Spektrallinienverbreiterung, die innerhalb des Lungenparenchyms bei unterschiedlichen Atemphasen erhalten wurden (1.48 ± 0.29 ppm bei FRC und 1.95 ± 0.43 ppm bei TLC), stimmen mit denen aus früheren Berichten überein. Diese wurden entweder durch numerische Berechnungen [67] oder durch ex-vivo Messungen ermittelt [120]. Der aus der Reproduzierbarkeitsstudie erhaltene CoV war bei allen Probanden unter 0.03; dies lässt auf eine relativ gute Reproduzierbarkeit schließen. Durch die sauerstoffgestützten Messungen wurde ein relativer Anstieg der Spektrallinienverbreiterung von ca. 14% beobachtet. Die Studie des Gravitationseffekts wies bei FRC eine Verringerung der Spektrallinienverbreiterung in Richtung des unteren Lungenbereichs auf, wobei der Proband sich sowohl in Bauch- als auch Rückenlage befand. Der Gradient der Linienverbreiterung in die Richtung der Gravitation war ca. 2.56%/cm in der Rückenlage und 1.88%/cm in der Bauchposition. Der Einfluss der Schwerkraft auf die Spektrallinienverbreiterung war bei TLC stark verringert,

wobei die Gradienten bei ca. 0.5%/cm oder kleiner waren.
Abschließend ermöglicht die hier vorgestellte Technik die in-vivo Quantifizierung der Spektrallinienverbreiterung der menschlichen Lunge in einem einzigen Atemzug von ca. 15 Sekunden. Diese Methode könnte bei der Feststellung von morphologischen und funktionalen Anomalien wie Gewebszerstörung, Ansammlung von Flüssigkeiten sowie Geweben in der Lunge oder von Ventilationsdefekten nützlich sein.

Ausblick

Heutzutage ist die klinische Anwendung des quantitativen MRT noch sehr begrenzt. Dies gilt ebenso für die Untersuchung von Körperregionen, die für die Kernspintomographie besser als die Lunge geeignet sind. Die quantitative MRT kann, von der spezifischen Anwendung abhängend, anfällig für verschiedene Faktoren sein, die die Quantifizierung beeinflussen könnten. Davon abgesehen benötigt die quantitative MRT längere Aufnahmezeiten und ist im Vergleich zur konventionellen MRT bewegungsempfindlicher. Aufgrund des niedrigen SNR und der physiologischen Bewegung stellt die Anwendung der quantitativen MRT eine besondere Herausforderung in einer Körperregion wie der Lunge dar. Die Methoden, die in dieser Arbeit vorgeschlagen wurden, sollen dabei ein weiterer Schritt zu möglichen klinischen Anwendungen der quantitativen MRT in der Lunge sein, im Vergleich zum aktuellen Stand der Entwicklung. Tatsächlich kann die Bildaufnahme bei allen vorgestellten Techniken innerhalb eines einzigen Atemzugs von einer maximalen Dauer von 15 Sekunden sowie mit einer relativ niedrigen Bewegungsempfindlichkeit vervollständigt werden. Dies könnte die vorgestellten Methoden für den Gebrauch in der klinischen Routine geeignet machen, ebenso wie für klinische Studien an Patienten mit Lungenkrankheiten. Zudem sind alle vorgeschlagene Techniken auch mit Atemtriggerverfahren wie der Prospective Acquisition CorrEction (PACE) [116] vereinbar. Dies kann nützlich für Anwendungen an kritischen Patienten sein, die ihren Atem nicht länger als ein paar Sekunden anhalten können.
In dieser Arbeit wurden die meisten Experimente an gesunden Probanden durchgeführt. Damit wurde eine quantitative Charakterisierung des gesunden Lungengewebes in Bezug auf die oben beschriebenen Parameter ermöglicht. Weitere Untersuchungen mit den hier vorgeschlagenen Techniken könnten etwa die Anwendung an Patienten mit Lungenkrankheiten berücksichtigen, um das pathologische Lungengewebe zu charakterisieren sowie um die Qualität der diagnostischen Informationen zu bewerten, die die erwähnten Parameter Klinikern bereitstellen können. Zieht man dies in Betracht, können die Ergebnisse, die in dieser Arbeit erhalten wurden, als eine Referenz für den Vergleich zwischen gesundem und pathologischem Lungengewebe dienen.
Ein weiterer, interessanter Forschungsaspekt könnte die Untersuchung des Einflusses der Magnetfeldstärke auf die Bildqualität für alle vorgeschlagenen Techniken sein. In dieser Arbeit wurde eine Feldstärke von 1.5 T für alle Probandenversuche verwendet. Im Allgemeinen kann durch den Gebrauch von höheren Magnetfeldstärken ein besseres SNR

erwartet werden. Jedoch entspricht die Anwendung einer höheren Magnetfeldstärke auch einer Verkürzung der transversalen Relaxationszeit T_2 und T_2^* in der Lunge, die auf die internen Magnetfeldinhomogenitäten zurückzuführen ist. Dies kann einen negativen Einfluss auf die Bildauflösung haben. Jedoch nutzen alle in dieser Arbeit dargestellten Techniken das Vorhandensein der internen Magnetfeldinhomogenitäten in der Lunge als Informationsquelle. Daher könnte die Verwendung von höheren Feldstärken nützlich für alle vorgestellten Methoden sein.

Bibliography

[1] World Health Organisation (WHO). Global Health Observatory (GHO) data - World Health Statistics Reports 2006-2015 (http://www.who.int/gho/publications/world_health_statistics/en/).

[2] Baert AL, Kauczor HU. MRI of the Lung. Springer Berlin Heidelberg; 2008.

[3] Hopkins SR, Wielpütz MO, Kauczor HU. Imaging lung perfusion. J Appl Physiol 2012; 113:328-339.

[4] Wild JM, Marshall H, Bock M, et al. MRI of the lung (1/3): methods. Insights into imaging 2012; 3:345-353.

[5] Biederer J, Beer M, Hirsch W, et al. MRI of the lung (2/3). Why ... when ... how? Insights into imaging 2012; 3:355-371.

[6] Biederer J, Mirsadraee S, Beer M, et al. MRI of the lung (3/3) - current applications and future perspectives. Insights into imaging 2012; 3:373-386.

[7] Mills GH, Wild JM, Eberle B, Van Beek EJR. Functional magnetic resonance imaging of the lung. Br J Anaesth 2003; 91:16-30.

[8] Miller GW, Mugler JP, Sá RC, Altes TA, Prisk GK, Hopkins SR. Advances in functional and structural imaging of the human lung using proton MRI. NMR Biomed 2014; 27:1542-1556.

[9] Hopkins SR, Levin DL, Emami K, et al. Advances in magnetic resonance imaging of lung physiology. J Appl Physiol 2007; 102:1244-1254.

[10] Kauczor HU, Chen XJ, van Beek EJ, Schreiber WG. Pulmonary ventilation imaged by magnetic resonance: at the doorstep of clinical application. Eur Respir J 2001; 17:1008-1023.

[11] Ley S, Ley-Zaporozhan J. Pulmonary perfusion imaging using MRI: clinical application. Insights into imaging 2012; 3:61-71.

[12] Webb S. The Physics of Medical Imaging. CRC Press; 1988.

[13] Bloch F. Nuclear Induction. Physical Review 1946; 70:460-474.

[14] Bloch F, Hansen WW, Packard M. The Nuclear Induction Experiment. Physical Review 1946; 70:474-485.

[15] Purcell EM, Torrey HC, Pound RV. Resonance Absorption by Nuclear Magnetic Moments in a Solid. Physical Review 1946; 69:37-38.

[16] Lauterbur PC. Image Formation by Induced Local Interactions: Examples Employing Nuclear Magnetic Resonance. Nature 1973; 242:190-191.

[17] Mansfield P, Grannell PK. NMR 'diffraction' in solids? Journal of Physics C: Solid State Physics 1973; 6:L422.

[18] Garroway AN, Grannell PK, Mansfield P. Image formation in NMR by a selective irradiative process. Journal of Physics C: Solid State Physics 1974; 7:L457.

[19] Kumar A, Welti D, Ernst RR. NMR Fourier zeugmatography. Journal of Magnetic Resonance (1969) 1975; 18:69-83.

[20] Geva T. Magnetic resonance imaging: historical perspective. Journal of cardiovascular magnetic resonance: official journal of the Society for Cardiovascular Magnetic Resonance 2006; 8:573-580.

[21] Haase A, Frahm J, Matthaei D, Hanicke W, Merboldt KD. FLASH imaging. Rapid NMR imaging using low flip-angle pulses. J Magn Reson 1986; 67:258-266.

[22] Hennig J, Nauerth A, Friedburg H. RARE imaging: A fast imaging method for clinical MR. Magn Reson Med 1986; 3:823-833.

[23] Hahn EL. Spin Echoes. Physical Review 1950; 80:580-594.

[24] Sodickson DK, Manning WJ. Simultaneous acquisition of spatial harmonics (SMASH): Fast imaging with radiofrequency coil arrays. Magn Reson Med 1997; 38:591-603.

[25] Pruessmann KP, Weiger M, Scheidegger MB, Boesiger P. SENSE: Sensitivity encoding for fast MRI. Magn Reson Med 1999; 42:952-962.

[26] Griswold MA, Jakob PM, Heidemann RM, et al. Generalized autocalibrating partially parallel acquisitions (GRAPPA). Magn Reson Med 2002; 47:1202-1210.

[27] Breuer FA, Blaimer M, Heidemann RM, Mueller MF, Griswold MA, Jakob PM. Controlled aliasing in parallel imaging results in higher acceleration (CAIPIRINHA) for multi-slice imaging. Magn Reson Med 2005; 53:684-691.

[28] Bergin CJ, Glover GM, Pauly J. Magnetic resonance imaging of lung parenchyma. J Thorac Imaging 1993; 8:12-17.

[29] Hatabu H, Chen Q, Stock KW, Gefter WB, Itoh H. Fast magnetic resonance imaging of the lung. Eur J Radiol 1999; 29:114-132.

[30] Cutillo AG. Application of Magnetic Resonance to the Study of Lung. Wiley; 1996.

[31] Wielputz M, Kauczor HU. MRI of the lung: state of the art. Diagnostic and interventional radiology (Ankara, Turkey) 2012; 18:344-353.

[32] Kauczor HU, Kreitner KF. MRI of the pulmonary parenchyma. Eur Radiol 1999; 9:1755-1764.

[33] Patel MR, Klufas RA, Alberico RA, Edelman RR. Half-fourier acquisition single-shot turbo spin-echo (HASTE) MR: comparison with fast spin-echo MR in diseases of the brain. American Journal of Neuroradiology 1997; 18:1635-1640.

[34] Hatabu H, Gaa J, Tadamura E, et al. MR imaging of pulmonary parenchyma with a half-Fourier single-shot turbo spin-echo (HASTE) sequence. Eur J Radiol 1999; 29:152-159.

[35] Bergin CJ, Pauly JM, Macovski A. Lung parenchyma: projection reconstruction MR imaging. Radiology 1991; 179:777-781.

[36] Robson MD, Gatehouse PD, Bydder M, Bydder GM. Magnetic resonance: an introduction to ultrashort TE (UTE) imaging. J Comput Assist Tomogr 2003; 27:825-846.

[37] Paley M, Bydder GM, and GDF, Young IR. MRI of tissues with short T_2 s and T_2^* s. NMR Biomed 2013; 26:1336-1337.

[38] Knight-Scott J, Keilholz-George SD, Mai VM, Christopher JM. Temporal dynamics of blood flow effects in half-Fourier fast spin echo ^{1}H magnetic resonance imaging of the human lungs. J Magn Reson Imaging 2001; 14:411-418.

[39] Hatabu H, Gaa J, Kim D, Li W, Prasad PV, Edelman RR. Pulmonary perfusion: qualitative assessment with dynamic contrast-enhanced MRI using ultra-short TE and inversion recovery turbo FLASH. Magn Reson Med 1996; 36:503-508.

[40] Hatabu H, Tadamura E, Levin DL, et al. Quantitative assessment of pulmonary perfusion with dynamic contrast-enhanced MRI. Magn Reson Med 1999; 42:1033-1038.

[41] Ohno Y, Hatabu H, Murase K, et al. Quantitative assessment of regional pulmonary perfusion in the entire lung using three-dimensional ultrafast dynamic contrast-enhanced magnetic resonance imaging: Preliminary experience in 40 subjects. J Magn Reson Imaging 2004; 20:353-365.

[42] Hochhegger B, Marchiori E, Irion K, Souza AS, Jr., Volkart J, Rubin AS. Magnetic resonance of the lung: a step forward in the study of lung disease. Jornal brasileiro de pneumologia: publicacao oficial da Sociedade Brasileira de Pneumologia e Tisilogia 2012; 38:105-115.

[43] Edelman RR, Hatabu H, Tadamura E, Li W, Prasad PV. Noninvasive assessment of regional ventilation in the human lung using oxygen-enhanced magnetic resonance imaging. Nat Med 1996; 2:1236-1239.

[44] Jakob PM, Wang T, Schultz G, Hebestreit H, Hebestreit A, Hahn D. Assessment of human pulmonary function using oxygen-enhanced T_1 imaging in patients with cystic fibrosis. Magn Reson Med 2004; 51:1009-1016.

[45] Pracht ED, Arnold JF, Wang T, Jakob PM. Oxygen-enhanced proton imaging of the human lung using T_2^*. Magn Reson Med 2005; 53:1193-1196.

[46] Bauman G, Puderbach M, Deimling M, et al. Non-contrast-enhanced perfusion and ventilation assessment of the human lung by means of fourier decomposition in proton MRI. Magn Reson Med 2009; 62:656-664.

[47] Kjørstad Å, Corteville DMR, Fischer A, et al. Quantitative lung perfusion evaluation using fourier decomposition perfusion MRI. Magn Reson Med 2013; 72:558-562. doi:10.1002/mrm.24930.

[48] Mai VM, Hagspiel KD, Christopher JM, et al. Perfusion imaging of the human lung using flow-sensitive alternating inversion recovery with an extra radiofrequency pulse (FAIRER). Magn Reson Imaging 1999; 17:355-361.

[49] Fischer A, Pracht ED, Arnold JF, Kotas M, Flentje M, Jakob PM. Assessment of pulmonary perfusion in a single shot using SEEPAGE. J Magn Reson Imaging 2008; 27:63-70.

[50] Jakob PM, Wang T, Schultz G, et al. Magnetization transfer short inversion time inversion recovery enhanced ^{1}H MRI of the human lung. Magnetic Resonance Materials in Physics, Biology and Medicine 2002; 15:10-17.

[51] Arnold JFT, Kotas M, Pyzalski RW, Pracht ED, Flentje M, Jakob PM. Potential of magnetization transfer MRI for target volume definition in patients with non-small-cell lung cancer. J Magn Reson Imaging 2008; 28:1417-1424.

[52] Henzler T, Schmid-Bindert G, Schoenberg SO, Fink C. Diffusion and perfusion MRI of the lung and mediastinum. Eur J Radiol 2010; 76:329-336.

[53] Mugler JP, Altes TA. Hyperpolarized ^{129}Xe MRI of the human lung. J Magn Reson Imaging 2013; 37:313-331.

[54] Horn FC, Deppe MH, Marshall H, Parra-Robles J, Wild JM. Quantification of regional fractional ventilation in human subjects by measurement of hyperpolarized ^{3}He washout with 2D and 3D MRI. J Appl Physiol 2014; 116:129-139.

[55] Yablonskiy DA, Sukstanskii AL, Leawoods JC, et al. Quantitative in vivo assessment of lung microstructure at the alveolar level with hyperpolarized ^{3}He diffusion MRI. Proceedings of the National Academy of Sciences 2002; 99:3111-3116.

[56] Sukstanskii AL, Yablonskiy DA. In vivo lung morphometry with hyperpolarized ^{3}He diffusion MRI: Theoretical background. J Magn Reson 2008; 190:200-210.

[57] Parra-Robles J, Ajraoui S, Deppe MH, Parnell SR, Wild JM. Experimental investigation and numerical simulation of ^{3}He gas diffusion in simple geometries: Implications for analytical models of ^{3}He MR lung morphometry. J Magn Reson 2010; 204:228-238.

[58] Wild JM, Fichele S, Woodhouse N, Paley MN, Kasuboski L, van Beek EJ. 3D Volume-Localized pO_2 Measurement in the Human Lung With ^{3}He MRI. Magn Reson Med; 53:1055-1064, 2005.

[59] Le Bihan D, Breton E, Lallemand D, Aubin ML, Vignaud J, Laval-Jeantet M. Separation of diffusion and perfusion in intravoxel incoherent motion MR imaging. Radiology 1988; 168:497-505. doi:10.1148/radiology.168.2.3393671.

[60] Le Bihan D, Breton E, Lallemand D, Grenier P, Cabanis E, Laval-Jeantet M. MR imaging of intravoxel incoherent motions: application to diffusion and perfusion in neurologic disorders. Radiology 1986; 161:401-407.

[61] Le Bihan D, Turner R. The capillary network: a link between IVIM and classical perfusion. Magn Reson Med 1992; 27:171-178.

[62] Hardy P, Henkelman RM. On the Transverse relaxation rate enhancement induced by diffusion of spins through inhomogeneous fields. Magn Reson Med 1991; 17:348-356.

[63] Cutillo AG, Ganesan K, Ailion DC, et al. Alveolar air-tissue interface and nuclear magnetic resonance behavior of lung. J Appl Physiol 1991; 70:2145-2154.

[64] Ziener CH, Kampf T, Jakob PM, Bauer WR. Diffusion effects on the CPMG relaxation rate in a dipolar field. J Magn Reson 2010; 202:38-42.

[65] Kurz FT, Kampf T, Buschle LR, et al. Microstructural Analysis of Peripheral Lung Tissue through CPMG Inter-Echo Time R_2 Dispersion. PloS one 2015; 10:e0141894.

[66] Morris AH, Blatter DD, Case TA, et al. A new nuclear magnetic resonance property of lung. Journal of applied physiology (Bethesda, Md : 1985) 1985; 58:759-762.

[67] Case TA, Durney CH, Ailion DC, Cutillo AG, Morris AH. A mathematical model of diamagnetic line broadening in lung tissue and similar heterogeneous systems: Calculations and measurements. Journal of Magnetic Resonance (1969) 1987; 73:304-314. doi:10.1016/0022-2364(87)90202-2.

[68] Carr HY, Purcell EM. Effects of Diffusion on Free Precession in Nuclear Magnetic Resonance Experiments. Physical Review 1954; 94:630-638.

[69] Meiboom S, Gill D. Modified Spin-Echo Method for Measuring Nuclear Relaxation Times. Rev Sci Instrum 1958; 29:688-691.

[70] Shioya S, Kurita D, Haida M, et al. Dependence of transverse relaxation time T_2 of biologic tissues on the interpulse delay time in Carr-Purcell-Meiboom-Gill (CPMG) measurements. Tokai J Exp Clin Med 1997; 22:27-31.

[71] Blatter DD, Morris AH, Ailion DC, Cutillo AG, Case TA. Asymmetric spin echo sequences. A simple new method for obtaining NMR ^{1}H spectral images. Invest Radiol 1985; 20:845-853.

[72] Abragam A. The Principles of Nuclear Magnetism. Clarendon Press; 1961.

[73] Bernstein MA, King KF, Zhou XJ. Handbook of MRI Pulse Sequences. Elsevier Science; 2004.

[74] Callaghan PT. Principles of Nuclear Magnetic Resonance Microscopy. Clarendon Press; 1993.

[75] Haacke EM, Brown RW, Thompson MR, Venkatesan R. Magnetic Resonance Imaging: Physical Principles and Sequence Design. Wiley; 1999.

[76] Levitt MH. Spin Dynamics: Basics of Nuclear Magnetic Resonance. Wiley; 2013. ISBN:9781118681848.

[77] Cohen-Tannoudji C, Diu B, Laloe F. Quantum Mechanics. Wiley; 1991.

[78] Segrè E. Nuclei and particles: an introduction to nuclear and subnuclear physics. W. A. Benjamin; 1977.

[79] Jin J. Electromagnetic Analysis and Design in Magnetic Resonance Imaging. CRC Press, 1999.

[80] https://en.wikipedia.org/wiki/Composition_of_the_human_body

[81] Alvarez LW, Bloch F. A Quantitative Determination of the Neutron Moment in Absolute Nuclear Magnetons. Physical Review 1940; 57:111-122.

[82] Wolbarst AB. Physics of Radiology. Appleton & Lange; 1993.

[83] Bloembergen N, Purcell EM, Pound RV. Relaxation Effects in Nuclear Magnetic Resonance Absorption. Physical Review 1948; 73:679-712.

[84] Rabi II, Ramsey NF, Schwinger J. Use of Rotating Coordinates in Magnetic Resonance Problems. Reviews of Modern Physics 1954; 26:167-171.

[85] Ernst RR, Anderson WA. Application of Fourier Transform Spectroscopy to Magnetic Resonance. Rev Sci Instrum 1966; 37:93-102.

[86] Mansfield P. Multi-planar image formation using NMR spin echoes. Journal of Physics C: Solid State Physics 1977; 10:L55.

[87] Mansfield P, Maudsley AA. Medical imaging by NMR. Br J Radiol 1977; 50:188-194.

[88] Bottomley PA, Foster TH, Argersinger RE, Pfeifer LM. A review of normal tissue hydrogen NMR relaxation times and relaxation mechanisms from 1-100 MHz: dependence on tissue type, NMR frequency, temperature, species, excision, and age. Med Phys 1984; 11:425-448.

[89] Morris GA, Freeman R. Selective excitation in Fourier transform nuclear magnetic resonance. Journal of Magnetic Resonance (1969) 1978; 29:433-462.

[90] http://www.my-ms.org/mri_plane_math.htm

[91] http://creativecommons.org/licenses/by/3.0/legalcode

[92] Zur Y, Wood ML, Neuringer LJ. Spoiling of transverse magnetization in steady-state sequences. Magn Reson Med 1991; 21:251-263.

[93] Chavhan GB, Babyn PS, Jankharia BG, Cheng HL, Shroff MM. Steady-state MR imaging sequences: physics, classification, and clinical applications. Radiographics 2008; 28:1147-1160.

[94] Haacke EM, Wielopolski PA, Tkach JA. A Comprehensive Technical Review of Short TR, Fast, Magnetic Resonance Imaging. Pergamon Press; 1991.

[95] Burstein D. Stimulated echoes: Description, applications, practical hints. Concepts Magn Reson 1996; 8:269-278.

[96] Frahm J, Haase A, Matthaei D, Merboldt KD, Hänicke W. Rapid NMR imaging using stimulated echoes. J Magn Reson 1985; 65:130-135.

[97] Frahm J, Merboldt KD, Hänicke W, Haase A. Stimulated echo imaging. J Magn Reson 1985; 64:81-93.

[98] Zhou X, Liang Z-P, Cofer GP, Beaulieu CF, Suddarth SA, Johnson GA. Reduction of ringing and blurring artifacts in fast spin-echo imaging. J Magn Reson Imaging 1993; 3:803-807.

[99] Hoult DI, Richards RE. The signal-to-noise ratio of the nuclear magnetic resonance experiment. Journal of Magnetic Resonance (1969) 1976; 24:71-85.

[100] Constable RT, Henkelman RM. Contrast, Resolution, and Detectability in MR Imaging. J Comput Assist Tomogr 1991; 15.

[101] Edelstein WA, Glover GH, Hardy CJ, Redington RW. The intrinsic signal-to-noise ratio in NMR imaging. Magn Reson Med 1986; 3:604-618.

[102] Beachey W. Respiratory Care Anatomy and Physiology: Foundations for Clinical Practice. Elsevier Mosby; 2007.

[103] Larsen R, Ziegenfuß T. Beatmung: Grundlagen und Praxis. Springer; 2009.

[104] Schwartzstein RM, Parker MJ. Respiratory Physiology: A Clinical Approach. Lippincott Williams & Wilkins; 2006.

[105] Tortora GJ, Derrickson BH. Principles of anatomy and physiology: Maintenance and continuity of the human body. Volume 2. John Wiley & Sons, Inc.; 2009.

[106] Gilroy AM, MacPherson BR, Ross LM. Atlas of Anatomy Latin Nomenclature version. Thieme; 2012.

[107] S. Karger AG, Medical and Scientific Publishers, Allschwilerstrasse 10, 4009 Basel, Switzerland, www.karger.com.

[108] Burri PH. Morphology and respiratory function of the alveolar unit. Int Arch Allergy Appl Immunol 1985;76 Suppl 1:2-12. doi:10.1159/000233728.

[109] Triphan SMF, Breuer FA, Gensler D, Kauczor HU, Jakob PM. Oxygen enhanced lung MRI by simultaneous measurement of T_1 and T_2^* during free breathing using ultrashort TE. J Magn Reson Imaging 2015; 41:1708-1714.

[110] Stock KW, Chen Q, Hatabu H, Edelman RR. Magnetic resonance T_2^* measurements of the normal human lung in vivo with ultra-short echo times. Magn Reson Imaging 1999; 17:997-1000.

[111] Hatabu H, Alsop DC, Listerud J, Bonnet M, Gefter WB. T_2^* and proton density measurement of normal human lung parenchyma using submillisecond echo time gradient echo magnetic resonance imaging. Eur J Radiol 1999; 29:245-252.

[112] Shioya S, Haida M, Fukuzaki M, et al. Nuclear magnetic resonance study of lung water compartments in the rat. Am J Physiol 1997; 272:L772-778.

[113] Mayo JR, McKay A, Mueller NL. T_2 relaxation time in MR imaging of normal and abnormal lung parenchyma. United States: Radiological Society of North America Inc; 1990.

[114] Kveder M, Zupancic I, Lahajnar G, et al. Water proton NMR relaxation mechanisms in lung tissue. Magn Reson Med 1988; 7:432-441.

[115] Alsop DC, Hatabu H, Bonnet M, Listerud J, Gefter W. Multi-Slice, Breathhold Imaging of the Lung with Submillisecond Echo Times. Magn Reson Med 1995; 33:678-682.

[116] Thesen S, Heid O, Mueller E, Schad LR. Prospective acquisition correction for head motion with image-based tracking for real-time fMRI. Magn Reson Med 2000; 44:457-465.

[117] Durney CH, Bertolina J, Ailion DC, et al. Calculation and interpretation of inhomogeneous line broadening in models of lungs and other heterogeneous structures. Journal of Magnetic Resonance (1969) 1989; 85:554-570.

[118] Durney CH, Cutillo AG, Ailion DC. Magnetic resonance behavior of normal and diseased lungs: spherical shell model simulations. J Appl Physiol 2000; 88:1155-1166.

[119] Bertolina JA, Durney CH, Ailion DC, Cutillo AG, Morris AH, Goodrich KC. Experimental verification of inhomogeneous line-broadening calculations in lung models and other inhomogeneous structures. Journal of Magnetic Resonance (1969) 1992; 99:161-169.

[120] Christman RA, Ailion DC, Case TA, et al. Comparison of calculated and experimental NMR spectral broadening for lung tissue. Magn Reson Med 1996; 35:6-13. doi:10.1002/mrm.1910350103.

[121] Spees WM, Yablonskiy DA, Oswood MC, Ackerman JJH. Water proton MR properties of human blood at 1.5 Tesla: Magnetic susceptibility, T_1, T_2, T_2^*, and non-Lorentzian signal behavior. Magn Reson Med 2001; 45:533-542.

[122] Audoly B, Sen PN, Ryu S, Song YQ. Correlation functions for inhomogeneous magnetic field in random media with application to a dense random pack of spheres. J Magn Reson 2003; 164:154-159.

[123] Ailion DC. Potential industrial applications of inhomogeneous broadening imaging. Magn Reson Imaging 1992; 10:799-808.

[124] Pillai RP, Buescher PC, Pearse DB, Sylvester JT, Eichhorn GL. ^{31}P NMR spectroscopy of isolated perfused lungs. Magn Reson Med 1986; 3:467-472.

[125] Ganesan K, Ailion DC, Cutillo AG, Goodrich KC. New Technique for Obtaining NMR Linewidth Images of Lung and Other Inhomogeneously Broadened Systems. Journal of Magnetic Resonance, Series B 1993; 102:293-298.

[126] Ailion DC, Case TA, Blatter DD, et al. Applications on NMR Spin Imaging to the Study of Lungs. Bulletin of Magnetic Resonance 1984; 6:130-139.

[127] Yablonskiy DA, Haacke EM. Theory of NMR signal behavior in magnetically inhomogeneous tissues: The static dephasing regime. Magn Reson Med 1994; 32:749-763.

[128] Stables LA, Kennan RP, Gore JC. Asymmetric spin-echo imaging of magnetically inhomogeneous systems: theory, experiment, and numerical studies. Magn Reson Med 1998; 40:432-442.

[129] Song YQ. Using internal magnetic fields to obtain pore size distributions of porous media. Concepts Magn Reson A 2003; 18A:97-110.

[130] Hürlimann MD. Effective Gradients in Porous Media Due to Susceptibility Differences. J Magn Reson 1998; 131:232-240.

[131] Dunn K-J. Enhanced Transverse Relaxation in Porous Media due to Internal Field Gradients. J Magn Reson 2002; 156:171-180.

[132] Cho H, Ryu S, Ackerman JL, Song YQ. Visualization of inhomogeneous local magnetic field gradient due to susceptibility contrast. J Magn Reson 2009; 198:88-93.

[133] Winkler M, Zhou M, Bernardo M, Endeward B, Thomann H. Internal magnetic gradient fields in glass bead packs from numerical simulations and constant time diffusion spin echo measurements. Magn Reson Imaging 2003; 21:311-315.

[134] Sun B, Dunn K-J. Probing the internal field gradients of porous media. Physical Review E 2002; 65:051309.

[135] Hajari AJ, Yablonskiy DA, Sukstanskii AL, Quirk JD, Conradi MS, Woods JC. Morphometric changes in the human pulmonary acinus during inflation. J Appl Physiol 2012; 112:937-943.

[136] Parra-Robles J, Ajraoui S, Marshall H, Deppe MH, Xu X, Wild JM. The influence of field strength on the apparent diffusion coefficient of ^{3}He gas in human lungs. Magn Reson Med 2012; 67:322-325.

[137] Ochs M, Nyengaard JR, Jung A, et al. The Number of Alveoli in the Human Lung. Am J Respir Crit Care Med 2004; 169:120-124.

[138] Bergin CJ, Glover GH, Pauly JM. Lung parenchyma: magnetic susceptibility in MR imaging. Radiology 1991; 180:845-848.

[139] Brown RJS. Distribution of Fields from Randomly Placed Dipoles: Free-Precession Signal Decay as Result of Magnetic Grains. Physical Review 1961; 121:1379-1382.

[140] Theilmann RJ, Arai TJ, Samiee A, et al. Quantitative MRI measurement of lung density must account for the change in T_2^* with lung inflation. J Magn Reson Imaging 2009; 30:527-534.

[141] Brownstein KR, Tarr CE. Importance of classical diffusion in NMR studies of water in biological cells. Physical Review A 1979; 19:2446-2453.

[142] Stejskal EO. Use of Spin Echoes in a Pulsed Magnetic-Field Gradient to Study Anisotropic, Restricted Diffusion and Flow. The Journal of Chemical Physics 1965; 43:3597-3603.

[143] Kopf M, Corinth C, Haferkamp O, Nonnenmacher TF. Anomalous diffusion of water in biological tissues. Biophys J 1996; 70:2950-2958.

[144] Torrey HC. Bloch Equations with Diffusion Terms. Physical Review 1956; 104:563-565.

[145] Stejskal EO, Tanner JE. Spin Diffusion Measurements: Spin Echoes in the Presence of a Time-Dependent Field Gradient. The Journal of Chemical Physics 1965; 42:288-292.

[146] Froeling M, Strijkers G, Nederveen A, Luijten P. Whole heart DTI using asymmetric bipolar diffusion gradients. Journal of Cardiovascular Magnetic Resonance 2015; 17:P15.

[147] http://creativecommons.org/licenses/by/4.0/legalcode

[148] Tanner JE, Stejskal EO. Restricted Self-Diffusion of Protons in Colloidal Systems by the Pulsed-Gradient, Spin-Echo Method. The Journal of Chemical Physics 1968; 49:1768-1777.

[149] Packer KJ. The effects of diffusion through locally inhomogeneous magnetic fields on transverse nuclear spin relaxation in heterogeneous systems. Proton transverse relaxation in striated muscle tissue. Journal of Magnetic Resonance (1969) 1973; 9:438-443.

[150] Majumdar S, Gore JC. Studies of diffusion in random fields produced by variations in susceptibility. Journal of Magnetic Resonance (1969) 1988; 78:41-55.

[151] Hürlimann MD, Helmer KG, Sotak CH. Dephasing of hahn echo in rocks by diffusion in susceptibility-induced field inhomogeneities. Magn Reson Imaging 1998; 16:535-539.

[152] Yung K-T. Empirical models of transverse relaxation for spherical magnetic perturbers. Magn Reson Imaging 2003; 21:451-463. doi:10.1016/S0730-725X(02)00640-9.

[153] Hürlimann MD, Helmer KG, Deswiet TM, Sen PN. Spin Echoes in a Constant Gradient and in the Presence of Simple Restriction. Journal of Magnetic Resonance, Series A 1995; 113:260-264.

[154] Hayden ME, Archibald G, Gilbert KM, Lei C. Restricted diffusion within a single pore. J Magn Reson 2004; 169:313-322.

[155] Sen PN. Time-dependent diffusion coefficient as a probe of geometry. Concepts in Magnetic Resonance Part A 2004; 23A:1-21.

[156] Washburn KE, Eccles CD, Callaghan PT. The dependence on magnetic field strength of correlated internal gradient relaxation time distributions in heterogeneous materials. J Magn Reson 2008; 194:33-40.

[157] Weisskoff R, Zuo CS, Boxerman JL, Rosen BR. Microscopic susceptibility variation and transverse relaxation: Theory and experiment. Magn Reson Med 1994; 31:601-610.

[158] Margosian P, Schmitt F, Purdy D. Faster MR imaging: imaging with half the data. Health Care Instrum 1986; 1:195.

[159] McGibney G, Smith MR, Nichols ST, Crawley A. Quantitative evaluation of several partial fourier reconstruction algorithms used in MRI. Magn Reson Med 1993; 30:51-59.

[160] Hennig J. Multiecho imaging sequences with low refocusing flip angles. J Magn Reson 1988; 78:397-407.

[161] Hennig J. Echoes-how to generate, recognize, use or avoid them in MR-imaging sequences. Part I: Fundamental and not so fundamental properties of spin echoes. Concepts in Magnetic Resonance 1991; 3:125-143.

[162] Hennig J. Echoes-how to generate, recognize, use or avoid them in MR-imaging sequences. Part II: Echoes in imaging sequences. Concepts in Magnetic Resonance 1991; 3:179-192.

[163] Norris DG, Börnert P, Reese T, Leibfritz D. On the application of ultra-fast rare experiments. Magn Reson Med 1992; 27:142-164.

[164] Beaulieu CF, Zhou X, Cofer GP, Johnson GA. Diffusion-weighted MR microscopy with fast spin-echo. Magn Reson Med 1993; 30:201-206.

[165] Le Roux P. Non-CPMG Fast Spin Echo with Full Signal. J Magn Reson 2002; 155:278-292. doi:10.1006/jmre.2002.2523.

[166] Fransson A, Ericsson A, Jung B, Sperber GO. Properties of the PHase-Alternating Phase-Shift (PHAPS) multiple spin-echo protocol in MRI: A study of the effects of imperfect RF pulses. Magn Reson Imaging 1993; 11:771-784.

[167] Pipe JG, Farthing VG, Forbes KP. Multishot diffusion-weighted FSE using PROPELLER MRI. Magn Reson Med 2002; 47:42-52.

[168] Williams CFM, Redpath TW, Smith FW. The influence of stimulated echoes on contrast in fast spin-echo imaging. Magn Reson Imaging 1996; 14:419-428.

[169] Le Roux P, Hinks RS. Stabilization of echo amplitudes in FSE sequences. Magn Reson Med 1993; 30:183-190.

[170] Alsop DC. The sensitivity of low flip angle RARE imaging. Magn Reson Med 1997; 37:176-184.

[171] Norris DG, Bornert P. Coherence and Interference in Ultrafast RARE Experiments. J Magn Reson A 1993; 105:123-127.

[172] Alsop DC. Phase insensitive preparation of single-shot RARE: Application to diffusion imaging in humans. Magn Reson Med 1997; 38:527-533.

[173] Schick F. SPLICE: Sub-second diffusion-sensitive MR imaging using a modified fast spin-echo acquisition mode. Magn Reson Med 1997; 38:638-644.

[174] Brockstedt S, Thomsen C, Wirestam R, Holtås S, Ståhlberg F. Quantitative diffusion coefficient maps using fast spin-echo MRI. Magn Reson Imaging 1998; 16:877-886.

[175] Bastin ME, Le Roux P. On the application of a non-CPMG single-shot fast spin-echo sequence to diffusion tensor MRI of the human brain. Magn Reson Med 2002; 48:6-14.

[176] Gullion T, Baker DB, Conradi MS. New, compensated Carr-Purcell sequences. J Magn Reson 1990; 89:479-484.

[177] Le Roux P. Non-CPMG fast spin echo MRI method. Patent US6265873B1, DE60035143D1, DE60035143T2, EP1037067A1, EP1037067B1; 2001 (https://www.google.nl/patents/US6265873).

[178] Bulwer BE, Rivero JM, Solomon FSD. Echocardiography Pocket Guide: The Transthoracic Examination. Jones & Bartlett Learning; 2010.

[179] Stadler A, Stiebellehner L, Jakob PM, et al. Quantitative and O_2 Enhanced MRI of the Pathologic Lung: Findings in Emphysema, Fibrosis, and Cystic Fibrosis. International Journal of Biomedical Imaging 2007; 2007:23624.

[180] http://www.gimp.org

[181] Uematsu H, Levin DL, Hatabu H. Quantification of pulmonary perfusion with MR imaging: recent advances. Eur J Radiol 2001; 37:155-163.

[182] Schraml C, Schwenzer N, Martirosian P, et al. Non-invasive pulmonary perfusion assessment in young patients with cystic fibrosis using an arterial spin labeling MR technique at 1.5 T. Magn Reson Mater Phy 2012; 25:155-162.

[183] Jobst BJ, Wielputz MO, Triphan SM, et al. Morpho-Functional ^{1}H-MRI of the Lung in COPD: Short-Term Test-Retest Reliability. PloS one 2015; 10:e0137282.

[184] Bock JC, Pison U, Wlodarczyk W, et al. Magnetic resonance imaging of the degree of pulmonary edema using a macromolecular contrast medium. Rofo 1997; 167:509-515.

[185] Gaass T, Dinkel J, Bauman G, et al. Non-contrast-enhanced MRI of the pulmonary blood volume using two-compartment-modeled T_1-relaxation. J Magn Reson Imaging 2012; 36:397-404.

[186] Lehmann J, Bock JC, Podrabsky P, Wlodarczyk W, Felix R. Young Investigator Award presentation at the 13th annual meeting of the ESMRMB, September 1996, Prague. Quantification of pulmonary water compartments by magnetic resonance. MAGMA 1997; 5:3-11.

[187] Hocking DC, Phillips PG, Ferro TJ, Johnson A. Mechanisms of pulmonary edema induced by tumor necrosis factor-alpha. Circ Res 1990; 67:68-77.

[188] Groeneveld AB, Verheij J. Extravascular lung water to blood volume ratios as measures of permeability in sepsis-induced ALI/ARDS. Intensive Care Med 2006; 32:1315-1321.

[189] Chew MS, Ihrman L, During J, et al. Extravascular lung water index improves the diagnostic accuracy of lung injury in patients with shock. Critical care (London, England) 2012; 16:R1.

[190] Francová P, Carinci F, Triphan S, Jakob PM. Magnetization Transfer Effect in the Lung Parenchyma: Dependence on the Presence of the Blood Signal. In: Proceedings of the 22nd annual meeting of the ISMRM, Milan, Italy, 2014; #6513.

[191] Schwarzbauer C, Syha J, Haase A. Quantification of regional blood volumes by rapid T_1 mapping. Magn Reson Med 1993; 29:709-712.

[192] Triphan SMF, Jobst BJ, Breuer FA, et al. Echo time dependence of observed T_1 in the human lung. J Magn Reson Imaging 2015; 42:610-616.

[193] Song YQ. Determining pore sizes using an internal magnetic field. J Magn Reson 2000; 143:397-401.

[194] Newbould RD, Owen DR, Shalhoub J, Brown AP, Gambarota G. Motion-sensitized driven equilibrium for blood-suppressed T_2^* mapping. J Magn Reson Imaging 2011; 34:702-709.

[195] Nguyen TD, de Rochefort L, Spincemaille P, et al. Effective motion-sensitizing magnetization preparation for black blood magnetic resonance imaging of the heart. J Magn Reson Imaging 2008; 28:1092-1100.

[196] Ibrahim el SH, Weiss RG, Stuber M, et al. Stimulated-echo acquisition mode (STEAM) MRI for black-blood delayed hyperenhanced myocardial imaging. J Magn Reson Imaging 2008; 27:229-238.

[197] Karaus A, Merboldt KD, Graessner J, Frahm J. Black-blood imaging of the human heart using rapid stimulated echo acquisition mode (STEAM) MRI. J Magn Reson Imaging 2007; 26:1666-1671.

[198] Pawlik G, Rackl A, Bing RJ. Quantitative capillary topography and blood flow in the cerebral cortex of cats: an in vivo microscopic study. Brain Res 1981; 208:35-58.

[199] Horimoto M, Koyama T, Kikuchi Y, Kakiuchi Y, Murao M. Effect of transpulmonary pressure on blood-flow velocity in pulmonary microvessels. Respir Physiol 1981; 43:31-41.

[200] Horimoto M, Koyama T, Mishina H, Asakura T, Murao M. Blood flow velocity in pulmonary microvessels of bullfrog. Respir Physiol 1979; 37:45-59.

[201] Stadler A, Jakob PM, Griswold M, Barth M, Bankier AA. T_1 mapping of the entire lung parenchyma: Influence of the respiratory phase in healthy individuals. J Magn Reson Imaging 2005; 21:759-764.

[202] Merboldt K-D, Hänicke W, Frahm J. Diffusion imaging using stimulated echoes. Magn Reson Med 1991; 19:233-239.

[203] Fahmy AS, Pan L, Osman NF. Artifact-free black-blood cine cardiac imaging in a single breath-hold. Magn Reson Imaging 2006; 24:1303-1310.

[204] Fahmy AS, Pan L, Stuber M, Osman NF. Correction of through-plane deformation artifacts in stimulated echo acquisition mode cardiac imaging. Magn Reson Med 2006; 55:404-412.

[205] Wang Y, Yu Y, Li D, et al. Artery and vein separation using susceptibility-dependent phase in contrast-enhanced MRA. J Magn Reson Imaging 2000; 12:661-670.

[206] Wedeen VJ, Weisskoff RM, Poncelet BP. MRI signal void due to in-plane motion is all-or-none. Magn Reson Med 1994; 32:116-120.

[207] Ozaki M, Inoue Y, Miyati T, et al. Motion artifact reduction of diffusion-weighted MRI of the liver: Use of velocity-compensated diffusion gradients combined with tetrahedral gradients. J Magn Reson Imaging 2013; 37:172-178.

[208] Stock KW, Chen Q, Levin D, Hatabu H, Edelman RR. Demonstration of gravity-dependent lung perfusion with contrast-enhanced magnetic resonance imaging. J Magn Reson Imaging 1999; 9:557-561.

[209] Hopkins SR, Henderson AC, Levin DL, et al. Vertical gradients in regional lung density and perfusion in the supine human lung: the Slinky effect. J Appl Physiol 2007; 103:240-248.

[210] Hopkins SR, Arai TJ, Henderson AC, Levin DL, Buxton RB, Kim Prisk G. Lung volume does not alter the distribution of pulmonary perfusion in dependent lung in supine humans. J Physiol 2010; 588:4759-4768.

[211] Shioya S, Haida TM, Fukuzaki M, et al. A 1-year time course study of the relaxation times and histology for irradiated rat lungs. Magn Reson Med 1990; 14:358-368.

[212] Cereda M, Emami K, Kadlecek S, et al. Quantitative imaging of alveolar recruitment with hyperpolarized gas MRI during mechanical ventilation. J Appl Physiol 2011; 110:499-511.

[213] Chang S, Kwon N, Kim J, et al. Synchrotron x-ray imaging of pulmonary alveoli in respiration in live intact mice. Scientific Reports 2015; 5:8760.

[214] Chang S, Kwon N, Weon BM, et al. Tracking X-ray microscopy for alveolar dynamics in live intact mice. Scientific Reports 2013; 3:1304.

[215] Namati E, Thiesse J, de Ryk J, McLennan G. Alveolar Dynamics during Respiration. Am J Respir Cell Mol Biol 2008; 38:572-578.

[216] Smaldone GC, Mitzner W. Viewpoint: Unresolved mysteries. J Appl Physiol 2012; 113:1945-1947.

[217] Weibel ER, Nieman GF, Frazer DG, et al. Commentaries on Viewpoint: Unresolved mysteries. J Appl Physiol 2012; 113:1948-1949.

[218] Carney D, DiRocco J, Nieman G. Dynamic alveolar mechanics and ventilator-induced lung injury. Crit Care Med 2005; 33:S122-128.

[219] Roan E, Waters CM. What do we know about mechanical strain in lung alveoli? American Journal of Physiology - Lung Cellular and Molecular Physiology 2011; 301:L625-L635.

[220] Nieman GF. Amelia Earhart, alveolar mechanics, and other great mysteries. J Appl Physiol 2012; 112:935-936.

[221] Hubmayr RD. Perspective on Lung Injury and Recruitment. Am J Respir Crit Care Med 2002; 165:1647-1653.

[222] Salerno M, Altes TA, Brookeman JR, de Lange EE, Mugler JP. Rapid hyperpolarized ^{3}He diffusion MRI of healthy and emphysematous human lungs using an optimized interleaved-spiral pulse sequence. J Magn Reson Imaging 2003; 17:581-588.

[223] Habib D, Grebenkov D, Guillot G. Gas diffusion in a pulmonary acinus model: experiments with hyperpolarized helium-3. Magn Reson Imaging 2008; 26:1101-1113.

[224] Randall K, Rockliffe JW, Smith EG, Tiddy GJT. Magnetic relaxation in glass-bead/water dispersions. Journal of the Chemical Society, Faraday Transactions 1: Physical Chemistry in Condensed Phases 1983; 79:1901-1909.

[225] Deichmann R, Adolf H, Kuchenbrod E, Nöth U, Schwarzbauer C, Haase A. Compensation of Diffusion Effects in T_2 Measurements. Magn Reson Med 1995; 33:113-115.

[226] Constable RT, Anderson AW, Zhong J, Gore JC. Factors influencing contrast in fast spin-echo MR imaging. Magn Reson Imaging 1992; 10:497-511.

[227] Schick F. Signal losses in diffusion preparation: Comparison between spin-echo, stimulated echo and SEASON. Magnetic Resonance Materials in Physics, Biology and Medicine 1998; 6:53-61.

[228] Scott GD, Kilgour DM. The density of random close packing of spheres. Journal of Physics D: Applied Physics 1969; 2:863.

[229] Henkelman RM. Measurement of signal intensities in the presence of noise in MR images. Med Phys 1985; 12:232-233.

[230] Carneiro AAO, Vilela GR, Araujo DB de, Baffa O. MRI relaxometry: methods and applications. Brazilian Journal of Physics 2006; 36:9-15.

[231] Henderson AC, Prisk GK, Levin DL, Hopkins SR, Buxton RB. Characterizing pulmonary blood flow distribution measured using arterial spin labeling. NMR Biomed 2009; 22:1025-1035.

[232] Biederer J, Heller M. Artificial thorax for MR imaging studies in porcine heart-lung preparations. Radiology 2003;226:250-255.

[233] Escolar JD, Escolar MA, Guzman J, Roques M. Pressure volume curve and alveolar recruitment/de-recruitment. A morphometric model of the respiratory cycle. Histol Histopathol 2002; 17:383-392.

[234] Smaldone GC, Mitzner W, Itoh H. Role of alveolar recruitment in lung inflation: influence on pressure-volume hysteresis. J Appl Physiol Respir Environ Exerc Physiol 1983; 55:1321-1332.

[235] Cutillo AG, Goodrich KC, Ganesan K, et al. Alveolar air/tissue interface and nuclear magnetic resonance behavior of normal and edematous lungs. Am J Respir Crit Care Med 1995; 151:1018-1026.

[236] Olsson LE, Lindahl M, Onnervik PO, et al. Measurement of MR signal and T_2^* in lung to characterize a tight skin mouse model of emphysema using single-point imaging. J Magn Reson Imaging 2007; 25:488-494.

[237] Robertson HT, Buxton RB. Imaging for lung physiology: What do we wish we could measure? J Appl Physiol 2012; 113:317-327.

[238] Walsh DO, Gmitro AF, Marcellin MW. Adaptive reconstruction of phased array MR imagery. Magn Reson Med 2000; 43:682-690.

[239] Bankier AA, Storey P, Mai VM, Edelman RR, Chen Q. Gravity-dependent signal gradients on MR images of the lung in supine and prone positions: A comparison with isogravitational signal variability. J Magn Reson Imaging 2006; 23:115-122.

[240] Bankier AA, O'Donnell CR, Mai VM, et al. Impact of lung volume on MR signal intensity changes of the lung parenchyma. J Magn Reson Imaging 2004; 20:961-966.

[241] Holverda S, Theilmann RJ, Sá RC, et al. Measuring lung water: Ex vivo validation of multi-image gradient echo MRI. J Magn Reson Imaging 2011; 34:220-224.

[242] Carroll FE Jr., Loyd JE, Nolop KB, Collins JC. MR imaging parameters in the study of lung water. A preliminary study. Invest Radiol 1985; 20:381-387.

[243] Caruthers SD, Paschal CB, Pou NA, Harris TR. Relative quantification of pulmonary edema with noncontrast-enhanced MRI. J Magn Reson Imaging 1997; 7:544-550.

List of Publications

Publications Related to This Thesis

Peer Reviewed Articles

[A1] F. Carinci, C. Meyer, F. A. Breuer, S. Triphan, M. Choli, P. M. Jakob. Blood Volume Fraction Imaging of the Human Lung Using Intravoxel Incoherent Motion. Journal of Magnetic Resonance Imaging; 41(5):1454-1464. doi:10.1002/jmri.24669, 2014.

[A2] F. Carinci, C. Meyer, F. A. Breuer, P. M. Jakob. In-Vivo Imaging of the Spectral Line Broadening of the Human Lung in a Single Breath-Hold. Journal of Magnetic Resonance Imaging; published online. doi:10.1002/jmri.25192, 2016.

Conference Proceedings

[A3] F. Carinci, M. Choli, F. A. Breuer, P. M. Jakob. Application of a non-CPMG Single-Shot Turbo Spin-Echo Sequence to Multi-Contrast Imaging of the Human Lung at 1.5 T. In: Proceedings of the 21st Annual Meeting of the ISMRM, Salt Lake City, USA, abstract #3701, 2013.

[A4] S. Weick, F. Carinci, C. Meyer, F. A. Breuer, F. Mantel, P. Kleine, P. M. Jakob. Improved SNR in retrospective respiratory self-gated 3D human lung MRI using image registration. In: Proceedings of the 21st Annual Meeting of the ISMRM, Salt Lake City, USA, abstract #3718, 2013.

[A5] F. Carinci, C. Meyer, F. A. Breuer, S. Triphan, P. M. Jakob. Blood volume fraction imaging in the human lung using a diffusion weighted non-CPMG HASTE sequence. In: Proceedings of the 30th Annual Meeting of the ESMRMB, Toulouse, France, abstract #47306, 2013. (oral)

[A6] F. Carinci, S. Triphan, F. A. Breuer, M. Voelker, P. M. Jakob. Line broadening mapping in the human lung using a non-CPMG HASTE sequence. In: Proceedings of the 30th Annual Meeting of the ESMRMB, Toulouse, France, abstract #47816, 2013.

[A7] P. Francová, F. Carinci, S. Triphan, P. M. Jakob. Magnetization Transfer Effect in the Lung Parenchyma: Dependence on the Presence of the Blood Signal. In: Proceedings of the 22nd Annual Meeting of the ISMRM, Milan, Italy, abstract #3411, 2014.

[A8] F. Carinci, C. Meyer, F. A. Breuer, S. Triphan, P. M. Jakob. Blood volume fraction imaging of the human lung using a ECG-synchronized STEAM-prepared HASTE sequence. In: Proceedings of the 22nd Annual Meeting of the ISMRM, Milan, Italy, abstract #3411, 2014. ISMRM merit award: "magna cum laude". (oral)

[A9] F. Carinci, F. A. Breuer, P. M. Jakob. On the Estimation of the Alveolar Size in the Human Lung Using Proton MRI. In: Proceedings of the 23rd Annual Meeting of the ISMRM, Toronto, Canada, abstract #3394, 2015.

[A10] F. Carinci, C. Meyer, F. A. Breuer, S. Triphan, P. M. Jakob. In-Vivo Imaging of the Spectral Line Broadening of the Human Lung in a Single Breath-Hold. In: Proceedings of the 23rd Annual Meeting of the ISMRM, Toronto, Canada, abstract #3394, 2015. ISMRM merit award: "magna cum laude". (oral)

Other Publications

Peer Reviewed Articles

[A11] F. Carinci, D. Santoro, F. von Samson-Himmelstjerna, T. D. Lindel, M. A. Dieringer, T. Niendorf. Characterization of Phase-Based Methods Used for Transmission Field Uniformity Mapping: a Magnetic Resonance Study at 3.0 T and 7.0 T. PLoS ONE 8(3): e57982. doi:10.1371/journal.pone.0057982, 2013.

[A12] G. Lykowsky, F. Carinci, M. Düring, D. Weber, P. M. Jakob, D. Haddad. Optimization and comparison of two practical dual-tuned birdcage configurations for quantitative assessment of articular cartilage with sodium magnetic resonance imaging. Quantitative Imaging in Medicine and Surgery; 5(6):799-805. doi:10.3978/j.issn2223-4292.2015.11.06, 2015.

Conference Proceedings

[A13] L. Zanini, F. Carinci. Neutronic and nuclear calculations for the Pb/Au target option for ESS. In: Proceedings of the 19th Meeting of the International Collaboration on Advanced Neutron Sources (ICANS-XIX), Grindelwald, Switzerland, PSI-Proceedings 10-01, ISSN-Nr. 1019-6447, abstract #TP180, 2010.

[A14] L. Zanini, F. Carinci, D. Reggiani, K. Thomsen, M. Wohlmuther. Effects of the beam footprint on the neutron yield in SINQ. In: Proceedings of the 19th Meeting of the International Collaboration on Advanced Neutron Sources (ICANS-XIX),

Grindelwald, Switzerland, PSI-Proceedings 10-01, ISSN-Nr. 1019-6447, abstract #TO174, 2010. (oral)

[A15] F. Carinci, F. von Samson-Himmelstjerna, D. Santoro, T. Lindel, M. Dieringer, F. Seifert, J. Sobesky, T. Niendorf. Comparison of four phase-based methods for the B_1^+ mapping at 7 T. In: Proceedings of the 19th Annual Meeting of the ISMRM, Montreal, Canada, abstract #4418, 2011.

[A16] M. A. Dieringer, M. Deimling, D. Santoro, F. Carinci, J. Schulz-Menger, T. Niendorf. Implications of 2D slice profile deformations for rapid myocardial T_1/T_2 quantification using DESPOT. In: Proceedings of the 19th Annual Meeting of the ISMRM, Montreal, Canada, abstract #3411, 2011.

[A17] F. Carinci, D. Santoro, F. von Samson-Himmelstjerna, T. Lindel, M. Dieringer, T. Niendorf. Characterization of four phase-based methods for 3D B_1^+ mapping at 3 T and 7 T. 2nd Annual Scientific Symposium on Ultrahigh Field Magnetic Resonance: Clinical Needs, Research Promises and Technical Solutions, Berlin, Germany, 2011.

[A18] F. Carinci, D. Santoro, F. von Samson-Himmelstjerna, T. Lindel, M. Dieringer, T. Niendorf. Characterization of phase-based methods for B_1^+ mapping at 3.0 T and 7.0 T MRI. In: Programmbuch 14. Jahrestagung der Deutsche Sektion der ISMRM, Berlin, Germany, ISSN-Nr. 1863-6365, 2011. (oral)

[A19] F. Carinci, D. Santoro, F. von Samson-Himmelstjerna, T. Lindel, M. Dieringer, T. Niendorf. Characterization of phase-based methods for 3D B_1^+ mapping at 3.0 T and 7.0 T. In: Proceedings of the 28th Annual Meeting of the ESMRMB, Leipzig, Germany, abstract #59, 2011. (oral)

[A20] D. Santoro, F. von Samson-Himmelstjerna, F. Carinci, F. Hezel, M. Dieringer, T. Niendorf. Cardiac triggered B_1^+ mapping using Bloch Siegert in the heart at 3 T. In: Proceedings of the 20th Annual Meeting of the ISMRM, Melbourne, Australia, abstract #5161, 2012.

[A21] G. Lykowsky, F. Carinci, P. M. Jakob, D. Haddad. Development and performance evaluation of a dual tuned $^{23}Na/^{1}H$ knee coil. In: Proceedings of the 21st Annual Meeting of the ISMRM, Salt Lake City, USA, abstract #1043, 2013.

[A22] G. Lykowsky, F. Carinci, K. Hemberger, E. Munz, P. M. Jakob, D. Haddad. Quantitative sodium MRI in an osteoarthritis goat animal model: preliminary results. In: Proceedings of the 21st Annual Meeting of the ISMRM, Salt Lake City, USA, abstract #1197, 2013.

Acknowledgements

This work would have not been possible without the help and support of many people. Therefore, I would like to thank all of them who made it possible to accomplish this thesis.

First of all, I want to thank my doctoral advisor Prof. Dr. Peter M. Jakob for his constant guidance and advice through the whole period of work as well as the other members of the thesis advisory committee Prof. Dr. Bert Hecht and Prof. Dr. Dr. Wolfgang R. Bauer. My special thank goes to my supervisor Dr. Felix A. Breuer, who supported my project with his constructive collaboration, important teachings and discussions.

Further thanks go to my colleagues:

- Cord Meyer for his help in performing the experiments and providing relevant image material;
- Simon Triphan and Morwan Choli for the valuable discussions and the help with pulse sequence development;
- Stefan Weick for enabling the access to patient measurements;
- Dr. Karl-Heinz Hiller for the support with the financial aspects of the project;
- Melisa Okanovic and Michael Seethaler for having been wonderful officemates;
- Andreas Hopfgartner, Kathrin Hemberger, Gunthard Lykowsky, Martin Blaimer, Sabine Voll, Eberhard Munz, Michael Völker, Pavla Francová, Johannes Oberberger, Martin Ott, Thomas Benkert and all the others with whom I shared many pleasant moments during my stay in Würzburg, also outside the working environment.

I would also like to thank the whole Department of Experimental Physics 5 (EP5) and the Research Center Magnetic Resonance Bavaria (MRB) for the friendly and cordial working atmosphere. Further thanks go to all the volunteers who participated in the in-vivo experiments, for their patience, to Prof. Dr. Jürgen Biederer and his research group for their support with the experiments in the porcine lungs as well as to Dr. Stephan Schröder-Köhne for his precious help with the regulatory issues.

Moreover, I want to emphasize that this work was financially supported by the European project "Pulmonary Imaging NETwork (π-NET)", funded by the 7th Framework Program of the European Commission (grant number PITN-GA-2010-264864).

Finally, my special thanks go to my family and to my girlfriend Dorothea for their unconditional love and their constant encouragement. Without them none of this would have been possible.